A Numerical Approach: Broadband Technologies for Efficient Magnetic Resonance Imaging

by

Dimitrios Mitsouras

M.Sc. Electrical Engineering and Computer Science, MIT (2000)
B.Sc. Computer Science, Brown University (1998)

Submitted to the Department of Electrical Engineering and Computer Science
in partial fulfillment of the requirements for the degree of

Doctor of Philosophy

at the

MASSACHUSETTS INSTITUTE OF TECHNOLOGY

September 2004

Author____
Department of Electrical Engineering and Computer Science
September 2004

Certified by____
Alan Edelman
Professor of Applied Mathematics
Thesis Supervisor

Certified by____
Gary P. Zientara
Associate Professor of Radiology, Harvard Medical School
Thesis Supervisor

Accepted by____
Arthur C. Smith
Chairman, Department Committee on Graduate Students

A Numerical Approach: Broadband Technologies for Efficient Magnetic Resonance Imaging

by

Dimitrios Mitsouras

Submitted to the Department of Electrical Engineering and Computer Science
on September 2004, in partial fulfillment of the
requirements for the degree of
Doctor of Philosophy

Abstract

This dissertation investigates the use of matrix compression techniques to increase the efficiency of data acquisition in Magnetic Resonance Imaging (MRI) scanners, such as those routinely used in hospitals.

MRI is based on the Nuclear Magnetic Resonance (NMR) principle which states that nuclei with a non-zero spin may only attain specific quantum spin states when under the influence of a magnetic field. By absorbing a photon of energy equal to the difference between two spin states, nuclei are "excited", flipping spins to a higher energy state. Their classical sum, the *magnetization* vector, once tipped from the lowest energy state, precesses like a spinning top about the direction of the magnetic field. The frequency of its precession depends entirely upon the field's strength. Therefore, just as a camera detects reflected light, including associated color, MRI detects spin density and its associated surrounding chemical conditions via local effects on field strength. MRI, i.e., obtaining an image via localization of the NMR signal, is typically accomplished by manipulating the precession frequency based on location, casting MRI into a Fourier transform problem.

In order to increase MRI acquisition efficiency, we follow the proposition of extending the applicability of the physics that MRI is based on. That is, the MR signal content may be prospectively encoded at the excitation step by spatially manipulating both the amplitude and phase of the resonant excitation. In so doing, we create a novel application of algebraic matrix factorization technologies, casting them into broadband MRI signal compression technologies.

We examine recent literature to conclude that most fast MRI methods that employ e.g., additional encoding such as multiple independent receiver coils in parallel or time-axis compression, can be cast as complementary to broadband MRI encoding. This affords broadband non-Fourier MRI with time efficiencies over current fast MRI methods. Finally, we describe the first software and hardware implementation combining these mathematical and physical principles in a proof-of-concept practical broadband MRI system, shown to achieve one order of magnitude increase in efficiency for both 2D and 3D MR imaging.

Thesis Supervisor: Alan Edelman
Title: Professor of Applied Mathematics

Thesis Supervisor: Gary P. Zientara
Title: Associate Professor of Radiology, Harvard Medical School

Acknowledgments

First and foremost, I thank my family. This work is dedicated to them. Their sacrifices, love, support, and dreams, are the reasons I am here today, completing this manuscript. There is no book large enough to hold even a minute account of everything they have done for me, taught me and given me. My aunt, Eudokia Stoupis, gave up her life to raise my sister and me. I am the person I have become thanks to her. My mother, Dr. Valassia Stoupi-Mitsouras, sacrificed everything a person deserves without a moment's thought in order to give my sister and me the brightest future she could. She taught me what love, sacrifice and devotion really mean. My uncle, Emannuel Stoupis, through his perpetual smile from the bed he was confounded to, taught me that happiness exists even in the most adverse conditions – it is only a state of mind, and one that keeps us sane and able to love and give when all else is failing. My sister, Dr. Katherine Mitsouras-Irizarry, paved the path and set the bar high, encouraging and making it possible for me to follow her steps. My father, Dr. Konstantine Mitsouras supported me through my undergraduate career and for that I thank him. My grandfather, Dr. Joachim Stoupis, through his life taught me that you can go from everything to nothing in no time, and the only things that remain with you and that define you are the love of your family and the knowledge you have accumulated. My grandmother, Stavroula Stoupis, never asked for anything but always had something to give and always wanted to give everything she had. Without the love, devotion and support of my loving fiancée, Miss Cristina Marie De Silva, I would not have had the energy and sanity to keep on going. All the lonely nights working at the MR scanners in the basement of the Brigham and Women's Hospital, it was her loving voice that reminded me what I was working and fighting for. Her family has taken me as their child and I love them like my family. Words can not express my gratitude and love to all the members of my family. My love is with you in this world or wherever you are.

My deepest gratitude to my thesis advisors, Professors Gary Zientara and Alan Edelman. It is because of their insight, excitement, and their will to help me gain some of their understanding, that this work has flourished. Often, the answer to problems I encountered was easy to find by recalling their words. Their devotion to their work and their love for their respective fields was instilled in me and became the motivation to exceed my capacity. If there is one thing they taught me that I will always treasure, it is that the drive to understand something about the world gives purpose to one's life. I hope this work serves as my appreciation of, and gratitude to, them. I thank you both for believing in me and for encouraging me to pursue anything and everything I wanted and thought was worth pursuing. I know you would have done the same! The resources they made available to me through their funds made this work technologically possible and as easy as it could be made.

I wish to thank Drs. Larry Panych, Robert Mulkern and Frank Rybicki for offering their extremely valuable and useful opinion, support, and many bits of knowledge the escaped me, whenever I was in need.

Finally, I thank Ty Sealy, Mary-Ann Ladd and Frank Tilley of the Computer Resource Services at the Laboratory for Computer Science. Their valuable technical support and crash-recovery efforts were instrumental to the success of the technical aspects of my work and my mental health.

Contents

---

[1] Portions of this chapter have appeared in [88, 101]

[2] Portions of this chapter have appeared in [90, 89, 93, 102, 101]

---

[3] Portions of this chapter have appeared in [94, 95, 101]

[4] Portions of this chapter have appeared in [96]

---

[5] Portions of this chapter have appeared in [88, 91, 92, 101]

[6] Portions of this chapter have appeared in [100, 97, 98, 99]

List of Figures

List of Tables

Partial List of Symbols

The following list is meant to serve as a short introduction to some important symbols and concepts in MRI that are necessary to understand this work.

γ	Gyromagnetic ratio. Constant intrinsic to each nucleus, relating spin precession to magnetic field strength. $\gamma \approx 4257.6$ Hz/Gauss for Hydrogen.
$\vec{B}_0$	External magnetic field applied to sample. By convention points along z, i.e., $\vec{B}_0 = B_0\hat{k}$.
$\nu_L = \gamma\lVert B_0 \rVert$ $\omega_L = 2\pi\nu_L$	Larmor frequency. Equation relating spin precessional frequency to magnetic field strength.
$G_{\{x,y,z\}}$	Gradient strength along each physical axis, $\partial B_z/\partial\{x,y,z\}$, in Gauss/cm. Gradients are typically applied so as to modify the net magnetic field component along the axis of the external magnetic field, i.e., $G_x = \partial B_z/\partial x$.
$k_{\{x,y,z\}}$	k-space location (spatial frequency wavenumber) along each physical axis in 1/cm. If sampling of signal occurs at time t_{acq} and the spins generating it were excited at time t_{exc}, $k(t_{\text{acq}}) = \frac{\gamma}{2\pi}\int_{t_{\text{exc}}}^{t_{\text{acq}}} G(t)dt$.
S	MR signal acquired at a receiving coil.
$\rho(x, y, z)$	Spin density of sample in the MR scanner as function of spatial dimension.
$\text{FOV}_{\{x,y,z\}}$	Size of the Field of View of the MR Image along each dimension. Equal to the inverse of the k-space sampling increment, $1/\Delta k_{\{x,y,z\}}$.
$\vec{M}$	Classical magnetization vector composed of the sum of excess high energy spins in the sample.
M_z	*Longitudinal* magnetization. The component of the equilibrium magnetization aligned with the external static magnetic field (z by convention).

M_{xy}	*Transverse* magnetization. The component of the magnetization vector on the x–y plane, expressed on the complex plane as $M_{xy} = M_x + iM_y$. Transverse magnetization always precesses about the static magnetic field axis and produces the measured signal.
θ	*Flip Angle.* The angle by which radiation applied to the sample tilts longitudinal magnetization away from the static field axis.
T_1	*Longitudinal Relaxation.* Time constant characterizing the exponential return of transverse magnetization (M_{x+iy}) to realignment with the external magnetic field (M_z) by loss of energy to surrounding nuclei (spin-lattice relaxation).
T_2	*Transverse Relaxation.* Time constant characterizing the dephasing of transverse magnetization due to small differences in magnetic field strength experienced by spins, e.g. due to chemical surroundings (spin-spin relaxation). $T_2 << T_1$ (except in pure water where $T_2 = T_1$).
T_2^*	Observed T_2 time constant; includes main magnet and local magnetic field inhomogeneities and magnetic susceptibilities of the sample. $T_2^* < T_2$. In spin echo imaging, $T_2^* = T_2$.
TR	MRI experiment repetition time. The time between sequential repetitions of the encoding and sampling sequence. Typically long enough for full relaxation to occur before irradiating the sample again, or, short enough to attain a steady state of the magnetization vector.
TE	Echo Time. Time between excitation and signal acquisition. TE and TR are the main sources of contrast in MR image generation; the different relaxation constants of different particle species resuilt in different amounts of coherent signal remaining at different echo times (TE) while the time between subsequent excitations (TR) affects the amount of magnetization due to each species available for excitation.

Chapter 1

Foreword

Since shortly after its inception in 1973 by P.C. Lauterbur [69], Magnetic Resonance Imaging, is mostly performed using the same basic principle of using Fourier basis functions to sample the excited MR spin density [64]. Only recently has the notion of more complex signal encoding methods been adopted by the MRI community. In this regard, encoding methods such as parallel imaging [139] and UNaliasing by Fourier encoding the Overlaps using the temporaL Dimension (UNFOLD) [79] have succeeded where previous noteworthy approaches [12, 13, 72, 38, 71] have failed.

MRI is the art of directly controlling a physical system (the spin system) via a given set of parameters that are within our control, in order to form an image of it. An MR scanner, or, imager, allows us to control these parameters through imaging pulse sequences. In essence, the MR imager is to imaging pulse sequences what logic gates are to circuits: it provides the RF excitation antennae, the magnetic field gradient coils and the RF receiver coils. A pulse sequence is the diagram that describes when to "use" (activate) these in order to form an MR image. Forming the MR image using these elements involves inducing the sample to emanate an MR signal via RF excitation, which is then manipulated via magnetic field gradients to carry position information about the sample, and which is then sampled by RF receiver coils. Obtaining, analyzing, and manipulating a set of such signals finally produces the image. Then, to complete our parallelism, pulse sequences are to MRI what circuit diagrams are to electrical engineering.

The task of controlling the parameters, that is, the task of controlling the physical system via control of these elements, requires drawing knowledge from various diverse disciplines such as: physics, chemistry, engineering, mathematics and computer science. For the author, the task of understanding and connecting the various elements involved in producing an MR image, in an attempt to contribute to knowledge in this field, was formidable task far from being complete.

Like any physical system, Nuclear Magnetic Resonance is governed by a given set of principles, such as the relatively slow relaxation of magnetization. These manifest as intrinsic limitations of

MRI that cannot be overcome, i.e., that are beyond our control. Although these limitations of MRI may not be compromised, mathematics and computation can clearly become the tools via which these limitations are effectively circumvented for each and every specific task that a radiologist wishes to perform in order to image a patient. It is this conjecture that was the premise of this research, which demonstrates the capabilities available. This dissertation is then a numerical and computational approach because it is concerned with both the manipulation of the physical system as well as the manipulation of the resulting signal equations and the computing resources necessary in order to form an MR image more efficiently than is otherwise possible.

Our goal in this dissertation is to, as a physicist, figure out how to control the various parameters, offered by the MR imager, in order to enable the use of arbitrary complex encoding methods to sample the underlying physical system. Then, as a mathematician, to figure out how the use of these encoding methods can impact signal compression. Finally, as a computer scientist, to provide the complex implementations that control the system in order to apply the compression and finally reconstruct the MR image with unprecedented efficiency.

For a computer scientist efficiency naturally implies compression and problem subdivision. It is no accident then that the MR imaging efficiency we achieve in this work comes from employing each of these two approaches in the context of MRI. A large portion of this work is based on the approach of [117] in order to enable compressing the MR image, *prior* to acquiring it, by manipulating the very excitation of the imaged sample so that sampling the resulting signals then produces as much information about the sample as possible [164]. Here, our work aims to make this notion of compressing the acquisition of a series of dynamically acquired MR images useful in everyday MRI by controlling, extending, complementing and implementing it. The final portion of this work is again based on using the excitation of the sample, but this time in order to enable the sampled signals to resolve only the specific region of interest of the sample. This is the notion of problem subdivision; rather than wasting the time available for encoding to acquire an entire sample, we instead attempt to reduce the size of the sample being imaged, in order to create a practically useful MRI implementation.

With a single exception, this work does not resort to simulation. Every statement is backed by experimental results; every image presented in support of an argument was acquired on a commercial clinical MR scanner, using a real spin system, whether that was a plastic phantom filled with water, a slab of meat purchased at the local supermarket, or a trusted (and still alive and healthy) PhD thesis advisor.

It is our deepest hope that the (small) contributions in each of the aforementioned aspects, that are presented and painstakingly experimentally verified in this work, though may not be noteworthy to a physicist, mathematician or computer scientist, serve the purpose of teaching everyone involved in the field of MRI that as far as the aspect of efficiency (and inarguably clinical value) is concerned, MRI stands to gain by complementing the physics with mathematics and computation.

Chapter 2

Introduction

2.1 Overview of MRI

Magnetic Resonance Imaging (MRI) is the currently preferred non-invasive medical imaging modality of choice for many medical indications due to its use of non-ionizing radiation and its unprecedented ability to control tissue and pathology contrast. MRI, first proposed in 1973 by Lauterbur [69] and Damadian [21], is an application of the NMR principle [3, 4], that refers to enhanced energy absorption by certain atomic nuclei when they are under the influence of an external magnetic field (by convention $\vec{B} = B_0\hat{\mathrm{k}}$) at some resonance RF frequency, called the Larmor frequency,

$$\omega_L = 2\pi\gamma B_0, \tag{2.1}$$

where γ is a nucleus-dependent constant, called the gyromagnetic ratio.

Paramagnetic nuclei (nuclei with an unpaired spin), have a permanent dipole moment, i.e., are magnetically polarized, and act in a fashion analogous to tiny bar magnets. Per quantum mechanics, a nucleus of spin I can only attain $2I + 1$ possible quantum spin states. The spin number, I, is either zero, a half-integer, or an integer[1]. When placed in an external magnetic field[2], the $2I+1$ spin states undergo *energy splitting*, meaning that a nucleus in a given spin state possesses a different energy than the same nucleus in any other spin state.

For spin 1/2 nuclei, such as ^1H that is imaged in most clinical MRI, the two spin states represent spin orientations that are either aligned (i.e., the low energy state) or anti-aligned (i.e., the high energy state) with the field. By absorbing a photon of energy equal to the energy difference between these two energy levels[3], ^1H nuclei can be "excited", e.g., spins transition to the higher energy anti-

---

[1] Most clinical MRI is performed on ^1H whose spin is 1/2.

[2] Field strengths of 1.5 Tesla, that is, 15,000 Gauss, where the earth's magnetic field is approximately 0.5–1 G, are commonplace in clinical imaging.

[3] $\omega_L/2\pi$ is approximately 62.5 MHz for Hydrogen nuclei in a 1.5 T magnetic field.

aligned state. The classical sum of the nuclear moments over many molecules (i.e., many nuclei), is the *magnetization* vector. Once tipped from alignment, the magnetization vector precesses much like a spinning top, about the direction of the external magnetic field. The precession frequency (ω_L), depends entirely upon the strength of the external magnetic field the spins experience [3, 4]. If a coil is placed around the imaged sample, it will experience a magnetic flux due to the spin's precession and will therefore generate an alternating voltage in the coil.

Just as a camera detects reflected light including associated color, MRI detects nuclear spin density and, indirectly, the surrounding chemical environment of nuclear and electronic spins. However useful, Magnetic Resonance Imaging is an inherently slow process, requiring of the order of $O(n)$ repetitions of a spin excitation – spin evolution – signal acquisition process, with each repetition measured in the tens to hundreds of milliseconds, and often, to seconds.

Signal Mapping Physics. Unlike most other imaging modalities, the acquired MR signal is radiated rather than reflected from a sample. To achieve reconstruction (i.e., solve the inverse problem) the emanating signal needs to be localized in each spatial dimension. This is typically accomplished with the use of a magnetic field gradient,

$$G(\vec{r}) = \vec{\nabla} \times \vec{B}(\vec{r}), \tag{2.2}$$

imposed in the Field-of-View (FOV) of a MR scanner. Since the Larmor frequency of the magnetization depends linearly on the strength of the external magnetic field, a one-to-one mapping between the field strength and spatial location (linear being the simplest case) allows signal emanating from spins at different locations to be differentiated and uniquely reconstructed. This linear mapping is typically accomplished by using magnetic field gradient coils (see e.g., [133] for a self contained introduction). By using constant gradients in each physical axis along the direction of $\vec{B}$, i.e.,

$$G(\vec{r}) = \partial B_z/\partial x\hat{\mathrm{i}} + \partial B_z/\partial y\hat{\mathrm{j}} + \partial B_z/\partial z\hat{\mathrm{k}} = G_x\hat{\mathrm{i}} + G_y\hat{\mathrm{j}} + G_z\hat{\mathrm{k}}, \tag{2.3}$$

with $\hat{\mathrm{i}}$, $\hat{\mathrm{j}}$ and $\hat{\mathrm{k}}$ the unit vectors, the net magnetic field becomes linearly dependent on location along the net direction of the applied gradient:

$$\vec{B} = (\vec{B}_0 + \vec{G} \cdot \vec{r})\hat{\mathrm{k}}. \tag{2.4}$$

Accordingly, the Larmor frequency becomes linearly dependent on location as well. Experiencing such a magnetic field gradient, nuclei in different positions along the direction of the gradient precess at slightly different frequencies and hence induce alternating voltages of different frequencies in the receiver coil. When constant gradients are applied, knowledge of the frequency content of the signal and the direction of the applied gradient is equivalent to knowledge of the spatial distribution of the spin density and suffices to uniquely reconstruct it via Fourier transformation.

Fourier Encoding. Present day MRI experiments are dominated by the so-called "Fourier encoded" approach [26]. In such an MRI experiment, the signal matrix that we are attempting to acquire is simply the discretized value of the voltage induced on the surrounding coil(s) by the ensemble of spins in the sample. The rows and columns of this voltage matrix range angular frequency offsets imposed on the rotating spins by the gradients, linearly dependent along each physical axis. Thus the matrix can be most accurately called the "spatial-frequency space" representation of the imaged sample. That is, the matrix acquired in the MRI experiment represents the two-dimensional Discrete Fourier Transform (DFT) of the MR spin density of the sample. Enough "steps" of varying the gradients must be imposed in order for all desired locations in the sample to be spatially differentiated. This means that every location of the signal matrix, extending out to the desired resolution, must be filled by sampling the MR signal at the needed spatial frequencies through appropriate combinations of the magnetic field gradients.

Signal Loss via Relaxation. Following the spin excitation, during spin evolution, the sample loses the spin energy deposited by the absorbed radiation, with some spin energy radiating back to the environment, "relaxing" spins back into their low-energy aligned state. This relaxation process is an exponential return to thermal equilibrium, $\left(1 - e^{-t/T_1}\right)$, characterized by the time constant T_1[4]. Furthermore, spins still in their excited state lose phase coherence because of minuscule magnetic field variations they experience due to their chemical surroundings or magnet imperfections, causing destructive interference. This relaxation process (dephasing) is an exponential decay of the emanating signal, e^{-t/T_2^*}, characterized by the time constant T_2^*[5]. As time elapses after excitation, the number of spins that remain excited and phase-coherent diminishes, thereby reducing the acquired signal.

In human imaging it is not possible to exactly quantify this loss of signal strength due to tissue heterogeneity. It is in fact desirable, e.g., to make one species of spins brighter over another. Practically, then, most sampling schemes fill in only a small portion of the matrix per irradiation of the sample. Spins are then allowed to relax and return to equilibrium before they are irradiated again, and the next portion of the matrix can be filled. In human tissue, relaxation times can be of the order of 1 sec, making the process of filling in the entire matrix time consuming if performed naïvely.

State of the Art MRI. With few exceptions, the bulk of MRI studies performed in the clinical setting consist of the direct acquisition of the signal matrix, i.e., the Fourier coefficients of the spatial distribution of the MR signal, as was originally proposed by Kumar et. al. in 1975 [64]. In the past, various methods have been devised aiming to increase the efficiency of MRI, and more

---

[4] Also called longitudinal or spin-lattice relaxation.

[5] Also called transverse or spin-spin relaxation. Spin coherence can only be partially recovered, as it is partially a random process depending on the spin's chemical surroundings which vary in time.

are currently being developed. Nonetheless, the bulk of these "fast" MRI methods still depends on the direct Fourier encoding methodology. This is perhaps attributable to the immense complexity inherent in even the most simple MR imaging hardware and the complexity of modifying proprietary components of commercial MR scanners. Figure 2-1 shows a typical MR scanner and its associated electronics cabinets. Adding even more complexity to such a system for a particular imaging method is difficult from both the engineering and the economics points of view.

Figure 2-1: A typical MR scanner and associated computing & electrical hardware cabinets. In the right hand photograph, the three closet-size cabinets are, from left to right, the TPS computer, the RF amplifier, and the gradient magnetic field power supplies for each physical axis. The TPS computer is a collection of systems, including the real-time Integrated Pulse Sequence Generator controlling the timing of RF & gradient application, the RF receiver & exciter A/D converters, and the Array Processor image reconstruction board. This particular scanner is a 1.5 Tesla superconducting wire magnet, installed at the Brigham And Women's Hospital in Boston, MA, USA.

As a means of imposing a hierarchy on the taxonomy of diverse MRI data acquisition methods, we separate most fast MRI methods that have been proposed to-date into roughly three main categories:

(1.) *Accelerated Signal Sampling Methods.* By far the most popular, these methods simply aim to acquire more Fourier coefficients per unit time. We separate these methods into two classes;

  (1a.) *Multi-Echo Techniques.* For comprehensive reviews, the interested reader is referred to [152, 25, 34]. These methods employ optimized "echo-planar" trajectories [82] through k-space[6] (e.g., [83] or spiral trajectories [2, 160, 31]) to fill more than one line of k-space per excitation.

  These methods suffer numerous artifacts, primarily due to effects such as non-constant velocity through k-space, non-uniform signal intensity over the range of k-space due to relaxation [86, 105, 18] and/or non-Cartesian grid sampling. These artifacts lead to interpolation and signal weighting problems [143, 57, 70, 131, 123, 127], as well as non-

---

[6] k-space is a convenient space for the representation of acquired signal in MRI experiments [145, 74, 157]. The acquired signal data is considered as a function of spatial frequency variables k_x and k_y, inversely proportional to the corresponding spatial wavelengths. The acquired signal matrix ranges k_x and k_y.

linear gradient effects [1, 62] and pronounced off-resonance precession effects [108]. These methods also impose stringent hardware requirements, such as rate of gradient switching, receiver bandwidth, filter efficiency etc. Some of these can only be optimized to a certain practical limit when imaging human patients (e.g., high gradient switching rates needed to take sharp turns in k-space can cause peripheral nerve stimulation). In most cases, poor SNR and tissue contrast is a limitation of these methods.

(1b.) *Steady State Techniques.* These methods aim to find a steady state of the magnetization vector via fast periodic excitation. In between excitation of spins, the transverse component of the magnetization vector, which produces the signal[7], relaxes via the two exponential processes. The excitatory pulses in these methods are then crafted to partially account for these relaxation effects, therefore retaining a constant signal strength[8]. In the steady state of the magnetization vector that is achieved, one can scan separate locations of k-space without having to wait for the sample to fully relax. In general, steady state methods suffer primarily from reduced contrast and reduced signal as well as off-resonance effects. However, they have recently found widespread use in applications such as cardiac imaging [152]. This adoption is perhaps related to the fact that they do not require any additional hardware or associated software, over the already optimized options available in present-day MR scanners.

(2.) *Parallel Imaging Methods.* Proposed early on [55, 14, 15, 128], these methods are only now beginning to be implemented [139, 126, 33, 67] in the clinical setting, partly because their efficiency is practically unlimited. The position of a radiating nucleus with respect to a receiver coil leads to a weighting of the signal acquired by that coil due to that nucleus. When multiple receiver coils, each with an independent spatially varying sensitivity, are used in parallel to acquire the radiated signal, one can replace some of the signal encoding that is typically induced via magnetic field gradients with the natural encoding induced by the coils' sensitivity to spin location.

This can be explained by imagining each coil as filtering the radiated MR signal [147]. The "filter coefficients" that correspond to a given receiver coil are directly related to its spatial sensitivity and its placement around the sample. The MRI signal passes through these fixed "filters" that together form a filter bank. The down-sampling of the signal that is associated with any filter bank can be explicitly imposed by manipulating the magnetic field gradients to skip more than one row of the k-space matrix at a time. If the ensemble of filters possesses

---

[7] The component of the magnetization that is orthogonal to the external magnetic field, called the *transverse* magnetization, produces the acquired signal. The component of the magnetization aligned with the magnetic field is called the *longitudinal* component.

[8] The situation is much more complicated than the simple description given here. The interested reader is referred to the thorough treatment of the wealth of spin echoes that an MR signal is composed of, found in [46, 48, 47].

certain properties [141], the filtering process can then be inverted to recover the original signal, thus effectively completing the k-space matrix. In these so-called *parallel imaging* methods, the amount of data that needs to be acquired in order to reconstruct k-space is not reduced *per se*; the number of receiver coils times the number of signal samples acquired must be at least as large as the number of desired k-space locations. However, apart from the cost of replicating the associated RF receiver electronics, there is no intrinsic physical or electromagnetic limit on the number of coils that can be used in parallel.

(3.) *Data-Selective Methods.* Few methods in this third category have been proposed and even fewer have successfully demonstrated viability. These methods aim to make use of some form of *a priori* assumptions about the imaged object, or otherwise place acceptable constraints on the image reconstruction. Restricted FOV methods (e.g., [54, 68]) aim to image only a selected region of interest (ROI). Resolution can be maintained with fewer encoding steps. In general, data selection can be performed in a multitude of approximation spaces; the RIGR method expands a high resolution image as a generalized series of complex exponentials. Subsequent images are formed by acquiring only those Fourier coefficients which are found to carry the most information [72, 38, 71], and extrapolating the skipped samples. The "feature-recognizing" method [12], uses a large database of e.g., brain images, hypothesizing that any new brain image can be expressed as a linear combination of the initial set. Similarly to [72], only the Fourier coefficients which are determined best fit to the underlying expansion basis are acquired. A form of feature-recognizing MRI was also proposed in [149, 44], along with the proposition of using wavelet bases [45, 150] to increase imaging efficiency. In wavelet basis MRI, the contractions of wavelets with a small support (such as Haar wavelets) can be excited without affecting spins in other portions of the imaged object. In effect, one can excite multiple disjoint wavelets on the sample sequentially, within a short time of each other, and acquire their responses while the effective relaxation time in between excitation of the same spins is elongated. One approach to schedule a given set of wavelets for such "multiplexed" acquisition was developed in [43, 151].

In wavelet basis MRI [149, 44] and those author's description of the feature-recognizing MRI approach, a markedly different approach was suggested. Namely, it was re-emphasized that one is not limited to acquiring Fourier coefficients of the spin density. Rather, MR physics allows one to use any basis for encoding the signal. The acquired signal can be represented in a space other than k-space. Wavelet encoding was first experimentally demonstrated by Panych [112] and one of the methods used here, namely Singular Value Decomposition basis encoding, was first demonstrated in [164].

It is well known that MR physics allows signal content within the FOV to be arbitrarily selected prior to acquisition. This means, for example, that an MRI technician operating the MR scanner can localize a region of the brain and excite primarily that region. This can be a 2D plane (as routinely used in everyday clinical MRI), a line, or even a single 3D voxel. This approach is termed "Spatially Selective Radio Frequency Excitation." Every clinical MR imager today uses this capacity, typically for selection of the slice of interest through the sample. However, this capacity is not generally used to full advantage; weighted combinations of elemental regions can be excited when the superposition principle applies [117]. By coupling this ability of MR imagers with linear algebraic methods, the full potential of the MR signal acquisition process can be realized. Wavelet and SVD encoded MRI relies precisely on this approach in order to acquire a non-Fourier encoded signal from the MR system.

2.2 Basics of Spatial Encoding in MRI

The purpose of most MR imaging experiments is to produce a discretized form of the Fourier coefficients of the spin distribution of a sample. Subsequently, DFTs are applied to reconstruct an image with well known approximation errors [140]. Before we describe the use of broadband spatial excitations for signal encoding in MRI, a short review of the basics of Fourier basis imaging is useful. For more detailed introductions, from both the signal processing as well as the physics perspective, the interested reader is directed to the excellent reviews found in [155, 50, 130, 73].

2.2.1 Fourier Encoding Basics

2D Fourier basis MR imaging typically involves a *slice-selective excitation* followed by *phase encoding* and finally *frequency encoding* during sampling. Each of these three processes causes or leads to signal localization along one physical dimension.

A typical 2D MRI experiment begins by the excitation of the sample's magnetization within the slice $z = z_0 \pm \Delta z$. This is accomplished by means of a spatially selective radio frequency (RF) excitation. A spin in the aligned state needs a specific energy (delivered by a photon of energy $E = \hbar\omega_L$) to transition to the anti-aligned state, proportional to the Larmor frequency and therefore the strength of the external magnetic field it experiences. For magnetic field strengths used in clinical MRI, this energy is delivered by photons with frequencies in the RF range. During the application of this RF pulse, a magnetic field gradient imposes a linear dependent magnetic field component used for locating the spin in the sample. If the RF pulse contains only a short band of frequencies, while the sample's Larmor frequencies from edge to edge correspond to a larger bandwidth, only a slice of the sample's magnetization is excited. The excitatory RF pulse is crafted so as to contain a small bandwidth; a boxcar in frequency space, approximated by a sinc envelope in time. The amount of power delivered by the RF pulse tilts the magnetization vector away from the longitudinal axis onto the transverse plane by the *flip angle.*

The Spin Echo Experiment. A typical Kumar-Welti-Ernst spin-warp spin echo pulse sequence

[64] that produces one row of the 2D Fourier coefficients of a sample is shown in Fig. 2-2.1. This diagram describes the timing of the application of the gradients in the three physical axes ($G_{\{x,y,z\}}$), the deposition of RF power, and the locations at which samples from the receiver coils are obtained. Time starts at the beginning of the experiment on the left of the diagram and flows to the right. The pulse sequence represented in the diagram is typically initiated and completed in a few tens of milliseconds. A dead time follows, until the sample has relaxed. The two times together add to the experiment repetition time (called TR). At each TR, the sequence is repeated to obtain the next row of the Fourier coefficient matrix.

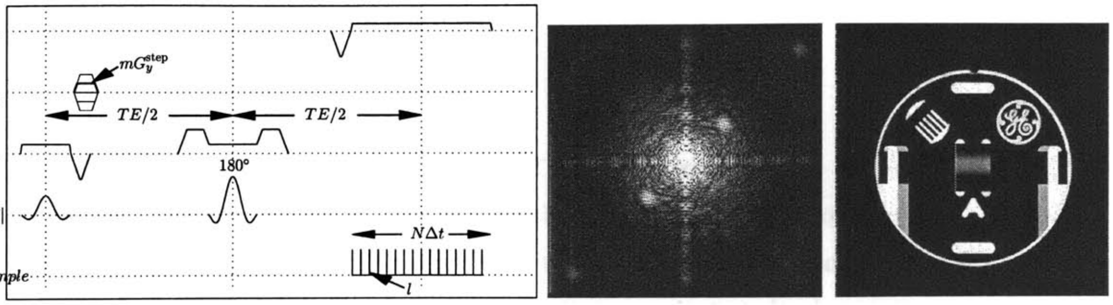

2-2.1: A simple 2D Fourier encoded spin echo pulse sequence using the spin-warp method of KWE [64].

2-2.2: Raw MR data signals (magnitude plot) collected with the pulse sequence.

2-2.3: Corresponding image after 2D DFT of the acquired signals

Figure 2-2: Execution of the pulse sequence diagram (left plot) for a fixed value of mG_y^{step} will yield signal samples that represent one row of the matrix of raw Fourier coefficients of the sample. A magnitude plot of this matrix, collected on a 1.5 T clinical MR imager, is shown in the middle image. The MR image that is produced by Fourier transformation of the acquired signal matrix is shown on the right. The complete matrix was acquired by 256 repetitions of the pulse sequence, with each repetition yielding one row of the raw signal data matrix, composed of 256 samples (i.e., matrix columns). Imaging parameters were TE = 60 ms, TR = 400 ms, 16 cm FOV and 10 mm Slice Thickness.

The term “spin echo” refers to the usage of a 180° flip angle RF pulse in between RF excitation and signal acquisition in order to null the part of phase coherence relaxation that is due to static local magnetic field inhomogeneities. Excited spins inside a voxel experience slightly different time-varying magnetic fields, due to both surrounding nuclei, which may possess magnetic fields, as well as static main magnet imperfections, causing them to precess at individually varying frequencies. The resulting loss of phase coherence of the transverse magnetization causes the *free induction decay* signal to diminish exponentially as e^{-t/T_2^*}. T_2^* relaxation incorporates the T_2 relaxation that is due to the local spin micro-environment inhomogeneities as well as contributions from main magnet inhomogeneities, i.e.,

$$\frac{1}{T_2^*} = \frac{1}{T_2} + \gamma \Delta B_0, \tag{2.5}$$

where ΔB_0 is a measure of magnetic field inhomogeneity. Considering transverse magnetization

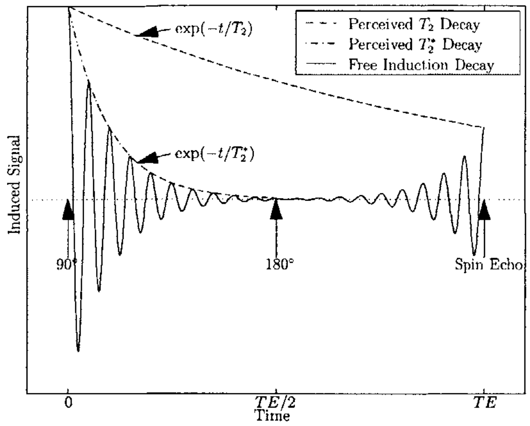

Figure 2-3: The spin echo formation induced by the rephasing of magnetization by application of a 180° pulse alters the observed signal decay at the sampling (echo) time.

as a rotating vector on the complex plane[9], a 180° RF pulse has the effect of conjugating that vector. Inside a voxel, spins that are precessing faster and have advanced over the slower ones, end up behind the slower ones after this conjugation. To the extent that the precessional frequencies remain constant (i.e., only that static magnetic field imperfection contributions), the faster spins start to catch up, causing coherence to rebuild (rephasing) and culminating in a *spin echo* [35]. The observed characteristic time for the transverse relaxation of spin echoes is then e^{-t/T_2}, with $T_2^* < T_2$. The difference between T_2^* and T_2 is depicted in Fig. 2-3

The signal produced by the excitation and rephasing of the magnetization is sampled at Δt-equidistant points under a constant gradient G_x which is applied (arbitrarily) along the x direction[10]. The general MR imaging equation for the pulse sequence in Fig. 2-2.1, for the lth sample, $l = 1, \ldots, N$, obtained at time $t = l\Delta t$ after sampling begins, is

$$S(t, G_y, z_0) = \int_z \int_y \int_x \rho(x, y, z) P(z - z_0) e^{-i2\pi(k_x x + k_y y)} dx\, dy\, dz, \tag{2.6}$$

$$P(z) \approx \begin{cases} 1, & -\Delta z \leq z \leq \Delta z, \\ 0, & \text{otherwise}, \end{cases} \tag{2.7}$$

where $\rho(x, y, z)$ is the MR spin density weighted by various imaging factors, such as relaxation terms and hardware characteristics, $P(z)$ is the achieved slice profile of the RF pulse envelope played under

---

[9] It is usual practice in MRI to consider the transverse x–y plane as the complex plane. The x axis is the real and the y axis the imaginary component.

[10] Other gradient waveforms may be used, e.g., half-period sinusoids which are easier to produce in hardware. In such cases, the sampling interval is irregular, and it is the gradient area in between any two sampling points that is held constant[25].

the gradient G_z [120] and

$$\begin{aligned} k_x &= \gamma G_x t - \gamma G_x (1/2N\Delta t) \\ &= \gamma G_x \left(l - 1/2N\right) \Delta t, \end{aligned} \tag{2.8}$$

$$k_y = \gamma G_y \tau, \tag{2.9}$$

where τ is the fixed duration of the G_y gradient and γ is the gyromagnetic ratio of the imaged nucleus. Note the $1/2N\Delta t$ factor in k_x due to the negative lobe of the G_x gradient which is applied prior to sampling, has half the area of the positive lobe, and is used to center the samples in Fourier space. Finally, we assumed that both excitatory RF pulses were slice selective in $z \in [z_0 - \Delta z, z_0 + \Delta z]$.

As shown in Eq. (2.6), once a slice has been selected at the excitation step, magnetic field gradients along the other two dimensions are used for signal localization. Leading up to and during signal acquisition, additional phase offsets to the precession of the sample's magnetization are imposed along each of the physical axes, i.e., the factors $\exp\{-i2\pi(k_x x + k_y y)\}$ (see e.g., [50]). These offsets are directly related to magnetic field gradients and hence the position of the magnetization along the gradient axes. These are precisely Fourier basis functions. Effectively, direct manipulation of the precession of the sample's magnetization, via application of the magnetic field gradients, produces its Fourier coefficients.

Frequency Encoding. During signal readout, the linear gradient applied along the x axis causes a linear phase increase at each x location of the magnetization in between sampling points. In between sampling points, magnetization in each different location of the sample will acquire a different amount of such phase that linearly depends on that location. This phase offset is captured by the encoding function $\exp(-i2\pi k_x x)$ in Eq. (2.6) which gives rise to the desired size of the FOV; the factor k_x is chosen so as to avoid aliasing by sampling an FOV_x-periodic function.

Letting $q = l - 1/2N$, the exponent for the lth sample must diminish to $-i\frac{2\pi}{\mathrm{FOV}_x}qx$. Thus,

$$\begin{gathered} \exp(-i2\pi k_x x) = \exp\left(-i\frac{2\pi}{\mathrm{FOV}_x}qx\right) \Rightarrow \\ k_x = q/\mathrm{FOV}_x \Rightarrow \\ \gamma G_x(l - 1/2N)\Delta t = (l - 1/2N)/\mathrm{FOV}_x \Rightarrow \\ \mathrm{FOV}_x = 1/(\gamma G_x \Delta t) \equiv 1/\Delta k_x. \end{gathered} \tag{2.10}$$

The desired FOV determines G_x, while the resulting spatial resolution, when N samples $l = 1, \ldots, N$ are acquired, is simply $\Delta x = \mathrm{FOV}_x/N$.

Phase Encoding. Each repetition of the pulse sequence of Fig. 2-2.1, allows only one value for the gradient G_y to be chosen, e.g., only one factor k_y for the encoding functions $\exp(-i2\pi k_y y)$, thus yielding one row of the k-space matrix per repetition. To obtain the entire 2D Fourier coefficient matrix at the desired resolution, the experiment must be repeated for different values of G_y. Using the gradient

$$\begin{aligned} G_y^{(m)} &= (1/2M - m)G_y^{\text{step}}, \\ m &= 1, \dots, M, \end{aligned} \tag{2.11}$$

in the mth repetition, yields the FOV along y given by the inverse of

$$\Delta k_y = \gamma G_y^{\text{step}} \tau. \tag{2.12}$$

The Fourier coefficients are then obtained from positive to negative order of spatial frequency, since

$$k_y^{(m)} = \gamma G_y^{(m)} \tau = \gamma(1/2M - m)G_y^{\text{step}} \tau \tag{2.13}$$

System Response Model. We can think of Eq. (2.6) as an "MR system" with RF pulses and gradient strengths as inputs, and spin echoes as responses. These inputs are manipulated in order to yield echoes that adequately sample the system response to produce the MR image with the desired resolution and FOV. By placing the lth sample of the mth experiment

$$s_l^{(m)} = S(l\Delta t, G_y^{(m)}, z_0) \tag{2.14}$$

in a matrix, we can build the 2D Fourier coefficient, or, *system response* matrix:

$$^{(\mathcal{F})}F_{m,l} = s_l^{(m)}. \tag{2.15}$$

A 2D DFT of the matrix $^{(\mathcal{F})}F$ produces the MR image with the well known approximation errors [140].

2.2.2 Non-Fourier "Broadband" Encoding Basics

Non-Fourier encoding [109, 150, 118] allows one to use arbitrary encoding functions to efficiently and accurately sample the FOV and fill the entries of the system response matrix. Suppose that instead of the first excitatory sinc-envelope pulse, an RF pulse defined by the envelope

$$p(t) = \sum_{m=1}^{M} p_m \Pi\left(\frac{t - (m-1)\Delta t}{\Delta t}\right), \tag{2.16}$$

$$\Pi(t) = \begin{cases} 1, & 0 \le t < 1, \\ 0, & \text{otherwise,} \end{cases} \tag{2.17}$$

is played out during the application of a gradient of strength G_y as in Fig. 2-4.1. This pulse sequence can be used to acquire practically the same results as the sequence in Fig. 2-2.1, e.g., Fourier encode the FOV, but can also encode it using any arbitrary basis [117] as we will now show.

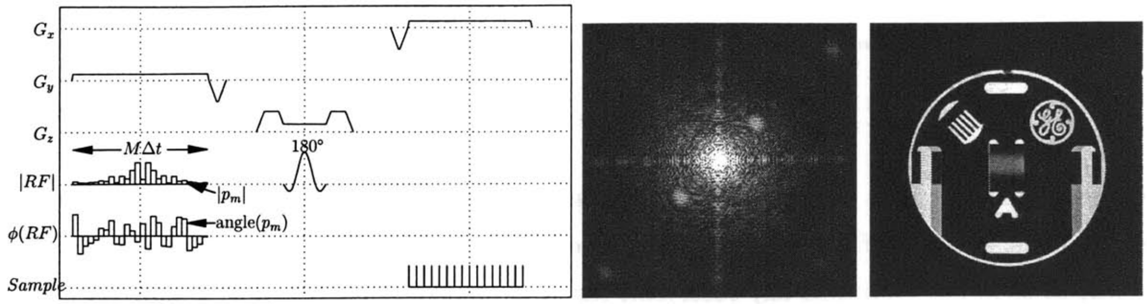

2-4.1: A simple 1D-spatial/1D-Fourier encoded "spin echo" pulse sequence.

2-4.2: MR data collected using the PSD in Fig. 2-4.1 and rows of the identity matrix as RF pulses.

2-4.3: Corresponding image after 2D DFT.

Figure 2-4: Image produced by the pulse sequence in Fig. 2-4.1 with 256 repetitions and 256 samples per repetition. Each repetition used a row of the identity matrix for the RF pulse. Imaging parameters where TE = 40ms, TR = 400ms, 16cm FOV, 10mm Slice Thickness and 15° flip angle. The x axis of the physical gradient coil system spans the vertical direction and the y axis spans the horizontal.

Any RF pulse $p(t)$, intrinsically discretized by the RF excitation process, can be placed in the form of Eq. (2.16), effectively composed of a train of *hard pulses* $p_m \in \mathbb{C}$, i.e., narrow boxcars. If Δt is sufficiently short[11], the effect of a hard pulse on the magnetization can be approximated by that of an impulse, occurring at time $m\Delta t$. An impulse (with infinite bandwidth), instantaneously flips magnetization to the transverse plane throughout the FOV by a flip angle proportional to its RF power. Once magnetization is excited by the mth impulse, it undergoes free precession under the influence of any remainder gradients. Let us assume for a moment that this transverse magnetization remains undisturbed by subsequent hard pulses in the RF pulse. Then, since the gradient of strength G_y and duration $M\Delta t$ in Fig. 2-4.1 is followed by a rephasing lobe of area $1/2M(-G_y)\Delta t$, magnetization excited at $m\Delta t$ after the beginning of excitation, acquires a phase offset proportional to the area of the remaining gradient, $((1/2M - m))G_y\Delta t)$, which leads to a rotation by $\exp(-i2\pi\gamma Ay)$.

Suppose the RF pulse train is composed of a single hard pulse p_m, excited at time $\tau = m\Delta t$ after the beginning of the excitation, and zeros everywhere else, i.e., $\vec{p} = (0, \ldots, 0, p_m, 0, \ldots 0)$. If we absorb the small differences due to the slight variation in echo time, and hence effective relaxation times, due to the placement of the hard pulse p_m within the RF pulse, into the spin density function,

---

[11] E.g., much smaller than the characteristic times of the two relaxation processes of the sample's magnetization.

the acquired signal at time $t = l\Delta t$ after sampling begins, is then given by

$$S_{\mathcal{SE}}(t, \vec{p}, z_0) = \int_{z_0-\Delta z}^{z_0+\Delta z} \int_y \int_x \rho(x,y,z) \left(p_m e^{-i2\pi k_y^{(m)} y}\right) e^{-i2\pi k_x x} dx\, dy\, dz, \tag{2.18}$$

$$k_x = \gamma G_x \left(l - 1/2N\right) \Delta t, \tag{2.19}$$

$$\begin{aligned} k_y^{(m)} &= \gamma G_y \left((M - m)\Delta t - 1/2M\Delta t\right) \\ &= \gamma G_y (1/2M - m)\Delta t, \end{aligned} \tag{2.20}$$

where the 180° RF pulse was used to refocus the signal only for $z \in [z_0 - \Delta z, z_0 + \Delta z]$. It is assumed, and experimentally verified, that all other magnetization in the sample will have dephased significantly so as to not contribute any observable signal at sampling time (c.f., Fig. 2-4.3). Effectively, the impulse at m produces the specific Fourier mode $\exp(-i2\pi k_y^{(m)} y)$ of the signal density, but scaled by the complex value p_m.

Let p_m equal unity, and compare Eq. (2.20) with Eq. (2.13). Letting $G_y \Delta t$ of this non-Fourier experiment equal $G_y^{\text{step}} \tau$ of the Fourier encoded experiment, we find that we obtain precisely the same spin echo as the mth step of the Fourier encoded experiment of Eq. (2.6). Repeating the non-Fourier experiment using the mth row of the identity matrix, $\vec{e}^{\,(m)}$, at the mth repetition, we can therefore obtain the system response matrix ${}^{(\mathcal{F})}F$: the lth sample of the kth repetition of the experiment, produces the signal

$$S_{\mathcal{SE}}(l\Delta t, \vec{e}^{\,(m)}, z_0) = S(l\Delta t, G_y^{(m)}, z_0) \equiv {}^{(\mathcal{F})}F_{m,l}, \tag{2.21}$$

where the last equation follows from the equivalence of Eqns. (2.20) and (2.13).

The discrete signal acquired from each repetition of the experiment using the identity matrix for the RF pulses defines the respective row of the system response matrix (equivalently the respective Fourier mode of the imaged sample). Linearity and superposition allow us to use those simple Fourier modes as building blocks in order to produce arbitrary complex 1D spatial excitation profiles, or, "modes", and acquire the signal produced by these modes. This ability to excite arbitrary spatial profiles will then allow us to treat the induced MR signal as the response of a linear system, as shown in [117]. As we will see in Chapter 3, efficient broadband encoding is the process of limiting MR signal acquisition to those spatial modes which are known *a priori* to have then strongest contributions in the imaged object. Via the linear system approach, these can then be obtained via linear algebraic matrix factorization approaches.

The necessary condition for this treatment is that each hard pulse produce a low flip angle tipping of the magnetization. Each impulse tilts magnetization down to the transverse plane by the flip angle, θ_m. If θ_m is small (e.g., $\theta_m < 2°$), two conditions hold: first, the longitudinal component (M_z) of the magnetization remains approximately the same after application of each impulse as prior to it. If $-$, $+$ indicate the times before and after a hard pulse application respectively,

$$M_z^+(x,y,z) = M_z^-(x,y,z)\cos(\theta_m) \approx M_z^-(x,y,z). \tag{2.22}$$

Therefore subsequent impulses can produce the same amount of transverse magnetization. Second, just as M_z^+ remains undisturbed, subsequent impulses do not appreciably disturb the transverse component of the magnetization that was generated from preceding impulses; the system reacts linearly to RF pulses. In general, it has been shown that if the entire RF pulse $p(t)$ produces a low flip angle tipping of the magnetization ($\theta(x,y,z) \leq 30°$), then the excitation behaves linearly [53, 50, 121].

Under this condition, a low flip angle RF pulse $p(t)$ expressed by the row vector $\vec{p}$ of hard pulses, $\vec{p} = (p_1, \ldots, p_M)$, produces a signal composed of the sum of the responses from all M discrete hard pulses [117]:

$$\begin{aligned} S_{\mathcal{SE}}(t,\vec{p},z_0) &= \int_{z_0-\Delta z}^{z_0+\Delta z} \int_y \int_x \rho(x,y,z) \left(\sum_{m=1}^{M} p_m e^{-i2\pi k_y^{(m)} y} \right) e^{-i2\pi k_x x} dx\, dy\, dz \\ &= \sum_{m=1}^{M} \left\{ p_m S_{\mathcal{SE}}(t, \vec{e}^{\,(m)}, z_0) \right\}. \end{aligned} \tag{2.23}$$

Equation (2.23) describes the readout signal samples that are acquired by the receiver coil when an arbitrary shaped RF excitation, described by the vector p, is applied in conjunction with a gradient applied along the y axis and the readout axis is x. During RF excitation, each hard pulse p_m contained in the shaped RF pulse produces some transverse magnetization. This magnetization subsequently experiences the remainder of the y gradient, causing it to acquire the phase offset described by $\exp\{-i2\pi k_y^{(m)} y\}$ by the end of the RF and gradient application. Because of the low flip condition, the transverse magnetization generated by each hard pulse simply coexists with transverse magnetization generated by preceding hard pulses, leading to the summation over these "modes" as shown in Eq. (2.23). The spin echo 180° RF pulse then selects a slice within $z \pm \Delta z$ whose transverse magnetization will rephase at the readout time, so that the signal acquired originates only from within that slice, leading to the outer integral over that extent of z. Frequency encoding finally produces the factors $\exp\{-i2\pi k_x x\}$, just as in the standard Fourier encoded experiment.

The expression in parentheses of Eq. (2.23) is the Fourier transform of the hard pulse train, i.e., the spatially selective profile that we excite, which in more standard notation is:

$$p(y) = \sum_{k=-1/2M}^{1/2M} \hat{p}_k e^{i(2\pi/\mathrm{FOV}_y)ky)}, \tag{2.24}$$

$$\hat{p}_k = p_{k+1/2M}, \tag{2.25}$$

with Eq. (2.25) mapping the standard-order coefficients to our RF vector (note the reverse order).

Spatial Profile ≡ Encoding Function. The spatial excitation profile, $p(y)$, is built by the ensemble of Fourier modes excited – or "activated" – by the scaled impulses in the RF train. In the spatial domain, taking the Fourier transform of Eq. (2.23) with respect to x produces the inner product of the spatial profile $p(x_0, y)$ with the spin density, $\rho(y)$ at every location x_0 throughout the x axis. This inner product is the necessary and sufficient condition to decompose any signal into its components onto any arbitrary basis given by the set of basis functions $p^{(m)}(y)$ [141]. Since we are not trying to resolve the Fourier coefficients of ρ more accurately than Fourier imaging (with its intrinsic sinc-like point spread function [111]), we proceed to express Eq. (2.23) as a sum of responses of the $m = 1, \ldots, M$ intrinsic Fourier modes of ρ. In other words, we employ the superposition property.

Transition from Encoding Functions to Linear System. The last equality of Eq. (2.23) is rewritten in matrix-vector notation as [164, 114, 117]:

$$s = p\left\{ {}^{(\mathcal{SE})}F \right\} = p\left\{ {}^{(\mathcal{F})}F \right\}. \tag{2.26}$$

Effectively, if we use an RF excitation that is spatially selective along what used to be the phase encode axis of the Fourier encoded MRI experiment, Eq. (2.26) defines the signal acquired by the MR scanner as a simple vector-matrix multiplication, where the length-M input vector p is the Fourier coefficient representation of the spatially selective excitation, and the M-by-N matrix ${}^{(\mathcal{F})}F$ is the Fourier coefficient representation of the MR image (i.e., of the spin density ρ). The sampled signal is then the length-N output vector s, whose entries define the inner product of the RF vector with the MR system response matrix, obtained via the readout frequency encoding process. By exchanging the x and y gradient directions one can also similarly obtain $\left\{ {}^{(\mathcal{F})}F \right\} p^T$ from the MR system.

2.2.3 Transition from Spatially Selective RF Excitation to Broadband MR Imaging

Equation (2.26) describes a linear process wherein a length-M input row vector, p, representing the digitized RF excitation waveform, operates on the M-by-N system response matrix F corresponding to the spin distribution, with frequency encoded readout samples along the columns, in order to produce a length-N output "response" row vector, s, of sampled data. One may now consider MR image encoding using arbitrary RF inputs p.

Given an arbitrary invertible matrix P, we can use each of its rows as the RF pulse in a repetition of the non-Fourier encoded experiment. Collecting these responses into the rows of the matrix S we can express the MR imaging process as [117]:

$$S = PF, \tag{2.27}$$

which can be inverted using an appropriate inverse for P, in order to yield the estimated k-space matrix

$$F_{\text{est}} = P^{\dagger} S. \tag{2.28}$$

Fourier transformation of F_{est} finally yields the desired spin density image.

Based on Eq. (2.28), Hadamard, Wavelet and SVD-based input vector sets have been studied [109, 150, 164] and used [112, 20, 116] for MRI. For example, Hadamard encoding derives the matrix P from the M-by-M Hadamard matrix H_M. For M a power of two, H_M is defined via the recurrence relation

$$H_M = \begin{bmatrix} H_{M/2} & H_{M/2} \\ H_{M/2} & -H_{M/2} \end{bmatrix}; \quad H_2 = \begin{bmatrix} 1 & 1 \\ 1 & -1 \end{bmatrix}, \tag{2.29}$$

with H_2 the boundary condition. In the low flip angle approximation this is done by taking the Fourier transform of each desired Hadamard spatial profile, i.e., the desired $p(y)$, are defined by the rows of H_M. Wavelet encoding similarly derived from the M-by-M Haar wavelet matrix [141] is another example. The SVD method [164] chooses a reduced set of $K \leq M$ input vectors

$$P_{\text{SVD}} = \begin{bmatrix} p^{(1)} \\ \vdots \\ p^{(K)} \end{bmatrix} \tag{2.30}$$

based on maximizing the power of F that is captured by these K vectors. The Singular Value Decomposition of an estimate of F (or reference image to, since the two are related by the unitary Fourier transform) yields a near optimal set of such vectors in the sense of minimizing the mean squared error function

$$e = \|F - F_{\text{est}}\|_F^2 = \|F - (P_{\text{SVD}}^H P_{\text{SVD}})F\|_F^2 \tag{2.31}$$

over any set of K vectors. The K-by-M matrix P_{SVD} completes the encoding of the rank-K estimate of F in K repetitions of the pulse sequence thereby yielding a speedup of M/K over *obliviously* encoded modalities such as Fourier or Hadamard encoding. However, the reconstructed image retains an intrinsic resolution of M along the non-Fourier encoded direction (i.e., k_y).

2.2.4 Linear Response Model Caveats

The MR imaging model described by Eqns. (2.27) and (2.28) embodies a number of unseen RF, electronic, and physics effects intrinsic to NMR. These (many) effects do not appear because of assumptions made in MRI theory, or they are considered intrinsic elements of the multi-stage imaging process.

Noise

Like any imaging system, MRI involves noise. In the model of Eq. (2.27), the sampled signal includes a noise component, resulting in the formulation

$$\tilde{S} = PF + \mathcal{N}, \tag{2.32}$$

where $\mathcal{N}$ is the random noise component, formed by samples of a zero mean random process. When the image estimate is formed by transforming the acquired samples via Eq. (2.28), the noise component is also transformed. This leads to the signal to noise ratio (SNR) of the imaging method. It has been shown that for any orthogonal encoding method defined by the (square) orthogonal encoding matrix P, the resulting noise energy is [111]

$$E_{\text{noise}} = \sigma^2_{\text{noise}} \text{Trace}\left(\{PP^H\}^{-1}\right), \tag{2.33}$$

where $\sigma^2_{\text{noise}} = \mathcal{E}[\mathcal{N}^2_{ij}]$ and $\mathcal{E}[\cdot]$ denotes expectation.

When non-Fourier encoding is performed with a set of orthogonal functions described by the rows of P, the difference in SNR between Fourier encoding and this arbitrary spatially selective RF encoding method originates from the fact that P may not be orthonormal, since orthonormality may be precluded by physical considerations. For example, the contractions of wavelets that are supported in a very small region need increasing amplitude in order to remain orthonormal. However, increasing the amplitude of the spatial excitation modeled after the wavelet is limited by the maximum flip angle which can never exceed 90°.

Off-Resonance Excitation

Another issue embodied within Eq. (2.23) and, by extension, Eq. (2.27), is the assumption of on-resonance excitation.

In general, the sample is composed of a continuous distribution of spin isochromats. A spin isochromat is the collection of spins that are resonant at a given frequency. Different spin isochromats arise both due to the imperfections of the main magnetic field as well as because of chemical shift and tissue susceptibility variations. An example of chemical shift is the 3.4 ppm difference (i.e., 220 Hz at 1.5 T) in the resonance frequency of hydrogen nuclei in fat molecules compared to water molecules because of the different molecular composition.

For a given low flip angle RF excitation, on a carrier frequency ω_0, the Fourier transform relation of the excitation profile only holds for the ω_0 spin isochromat. Other isochromats experience a different RF field, resulting in a different excitation. The overall assumption of linearity of the spatial RF excitation, and hence utility of Eq. (2.23), is maintained when the RF excitation is shorter than the spin-spin relaxation time constant, T_2^* [121, 117, 73]. In terms of a general impulse response that is independent of the image generated, even this assumption is not necessary [117]. That is, we can accept that the image we obtain includes complex contributions of relaxation and off-resonance effects.

2.3 Contributions of this thesis

Via spatially selective excitation *any* MR imaging system has the capacity to return Fv or $v^H F$ for any complex-valued column vector v, if F is the sample's Fourier coefficient matrix[12]. At the simplest level, just as the spatial distribution of spin density forms a Fourier transform pair with the MR signal produced using constant magnetic field gradients, so do the resulting spatial profiles of excited spins with the low flip angle RF pulses used to excite them, when the pulse is applied in tandem with a constant magnetic field encoding gradient. Effectively, spatially selective excitation allows us to obtain the signal produced by any desired spatial profile of transverse magnetization, simply by exciting the Fourier coefficients of the desired profile function under a linear encoding gradient.

The goal of any MRI method is to sample and reconstruct the contents of the FOV, i.e., acquire data in order to construct the k-space matrix, and by subsequent Fourier transformation, the image. Via the linear system of Eq. (2.27), linear algebra methods give us the tools to as best as possible acquire samples to construct this matrix. Associated with every matrix is a column and row space. In many cases, the useful information content may be concentrated in a relatively small part of these vector spaces. Other parts might contain little or no useful information. In matrix language, if Fv or $v^H F$ is large (small) relative to v, then v contains important (unimportant) information about F.

This thesis does away with Fourier imaging, instead approaching the MR image acquisition problem from the non-Fourier encoding perspective. Our work expands on the ability to acquire and reconstruct a good approximation to the FOV in a fraction of typical acquisition times by limiting the subspace spanned by the acquired data [168]. However, rather than focusing on the use of a specific set of encoding vectors $v^{(m)}$, our aim is to use the underlying physical principles in order to extend the theory of spatial encoding thus devising the technologies that enable *any* novel encoding method that does not rely on Fourier basis functions to be *efficiently* applied for fast dynamic MR imaging in two and three dimensions. Then, what we hope to have achieved is to produce the path that enables the MRI encoding problem to be solved efficiently while challenging current state of

---

[12] The low tip angle requirement may be relaxed by explicit numerical calculation of pulses that produce the required response but excite even all available magnetization (i.e., 90° RF pulses) [136, 137, 120, 65].

the art fast MRI methods.

In the process of accomplishing this task a large number of novel MRI technologies have been produced:

- *Strategies for Fast Non-Fourier MRI.* In every case we have examined, the physics upon which non-Fourier encoding is based, allows it to coexist with, take advantage of, or enables a direct analogue to, fast MRI methods. For each case, we describe the encoding strategy and show how it yields an efficient encoding methodology. In particular:
    - In Section 3.1, and with numerous dynamic imaging experiments throughout this dissertation, we settle the issue of applicability of compression in MR image encoding by considering the properties of the signal rather than relying on ad-hoc compression which has misled previous work to dismiss the use of compression in MRI encoding [24, 37].
    - In Section 4.1 we present a multi-echo non-Fourier encoded pulse sequence which builds on the simple notions of multiplexing and demultiplexing signals. Direct manipulation of the physical system, and particularly the spin echo formation mechanism, enables us to obtain more than one linear system response per sequence repetition. This is accomplished by multiplexing spatial excitations and subsequently demultiplexing the spin echoes.
    - In Section 4.4 we further generalize the general linear impulse response model of [117] in order to enable encoding by spatial excitation using arbitrary excitation and acquisition trajectories through k-space. Arbitrary trajectories can optimize the given imaging task by minimizing the time necessary to traverse the k-space necessary to obtain the desired image resolution. By generalizing the impulse response model to spatial encoding with arbitrary trajectories, we effectively enable an additional level of optimization in MR signal sampling; we can not only reduce the number of sequence repetitions, but the time necessary for each repetition as well.
    - In Chapter 5 we describe a general theoretical framework combining non-Fourier spatially encoded MRI with parallel multi-channel acquisition MR imaging. We show that the two spatial encoding mechanisms are physically and analytically separable, allowing non-Fourier encoding to be expressed as complementary to the inherent encoding imposed by RF receiver coil sensitivities. Consequently, the number of non-Fourier spatial encoding steps necessary to fully encode a FOV is reduced when parallel imaging methods are used. Furthermore, by casting parallel imaging techniques as a dimensionality reduction of the k-space that is non-Fourier encoded, a speedup of each digital non-Fourier spatial excitation may be obtained in addition to imaging acceleration.
    - Similar to the framework in Chapter 5, in Chapter 6 we present a framework combining non-Fourier spatially encoded MR imaging with UNaliasing by Fourier encoding the

Overlaps using the temporaL Dimension (UNFOLD) MRI. UNFOLD compresses spatial information into the time-axis, by enabling the time-dependent signal bandwidth of more than one spatial locations, over a dynamic series of images, to share a common frequency axis. We show that the compression of spatial information performed by UNFOLD can also be expressed as complementary to non-Fourier encoding, leading to the same efficiencies afforded by the parallel non-Fourier encoding framework.

- *Translation of Strategies to Pulse Sequence Implementations.* Prior to this work, only the simplest pulse sequences had been proposed and implemented for non-Fourier encoding [112, 114, 113]. Pulse sequence implementation is a non-trivial task because of the complexity of the physical system that is being manipulated; stated another way, apart from the typical math and programming bugs, one also has to deal with physics bugs. For example, even a trivial misalignment of the un-blanking of the RF and gradient applications, or the RF magnitude and phase applications, can lead to failure to obtain anything that even remotely resembles an image. With typical pulse sequences provided by our scanner manufacturer exceeding 25,000 lines of program code in a single source file, and with no documentation on the hardware and software semantics of support functions provided, this is a task not for the faint of heart. Nonetheless, we overcome the implementation complexity and largely rectify this lack for both 2D & 3D encoding functionality in Chapter 4. There, we produce sequences for a number of different imaging requirements. One example is a 3D sequence which is shown to acquire a dynamic series of 3D MR images at high resolution in 3 to 4 times faster than the currently fastest imaging sequence available to MRI (i.e., steady state imaging).

- *Real-Time System Implementation.* Performing non-Fourier MR imaging involves greatly increased implementation complexity, compared to presently used methods, in all the stages of the MR imaging process; from taking a set of encoding functions to the RF exciters, to receiving and reconstructing the sampled signals to displaying the MR image. To put this complexity in perspective, the only signal reconstruction presently offered in most commercial MR imagers is an FFT routine. In Chapter 7 we simplify the task of devising Broadband MRI encoding methods by presenting a fully functional and modular software and hardware system implementation that works in concert with a clinical MR imager. We then use this system to prove the viability of non-Fourier broadband encoding for real dynamic MR imaging experiments. Control issues for the dynamic truncation of the compression process are described in Section 3.1, while methods to ensure that the encoding process does not fall out of synchronization with the contents of the MR signal (e.g., loss of changes in the FOV that happen to have no projection onto the encoding basis) are discussed in Chapter 9.

- *3D Inner Volume UFSE.* Finally, in Chapter 8 we merge the power of non-Fourier excitations with the utility of Fourier sampling in order to increase the efficiency of Fourier sampling when it is most necessary: 3D spin echo morphological MR imaging. This particular solution was proposed to answer a problem raised by Dr. Frank Rybicki[13] and Dr. Robert Mulkern[14] concerning circumventing the inefficiency of 3D Fourier MRI, for targeted imaging applications wherein the pathology of interest is known in advance. Fourier encoding is undoubtedly best-suited for structural, or, morphological imaging, where signal compression could lead to loss of the detail whose very existence we are trying to determine. In particular, the interest was to use Ultra-Fast spin echo (UFSE) trains which achieve high quality 3D imaging by employing tightly packed, *non-selective*, refocusing RF pulses. Like all high flip angle spin echo methods, fast spin echo (FSE) is limited to very long repetition times. This, coupled with the non-selective feature of UFSE trains which limits them to imaging the entire sample within the coil sensitivity, severely sacrifices efficiency, rendering them practically useless. We use broadband excitation to limit the extent of magnetization that is excited in both Fourier phase encoded dimensions, and, although the combination of UFSE trains and Inner Volume imaging appears intrinsically incompatible, we formulate and analyze two general-purpose 3D IVUFSE methods. With 3D IVUFSE, the number of Fourier samples required to produce the desired resolution is greatly reduced thereby greatly increasing efficiency.

---

[13] Brigham And Women's Hospital, Boston, MA, USA.
[14] Children's Hospital, Boston, MA, USA.

Chapter 3

Efficient Compression via Broadband MRI[1]

The MR system response matrix (k-space matrix), denoted by F, may be Fourier encoded using a standard phase encoded pulse sequence such as that shown in Fig. 2-2.1. Alternatively, as described in Section 2.2.2, may be Fourier encoded using the rows of the identity matrix in a spatially selective pulse sequence such as that shown in Fig. 2-4.1. However, with spatially selective encoding sequences it is also possible to obtain the full system response by encoding it using any orthogonal or invertible matrix, as described in Section 2.2.3 and Eq. (2.28) [117].

In general, Eq. (2.28) provides the necessary mathematical capability to compress the MR image at the excitation step. For the purpose of MR imaging this will translate to fewer signal samples necessary in order to reconstruct a "good" approximation to the k-space matrix. Here we will be concerned with two issues: First, how many samples do we need (i.e., what is a "good" approximation)? That is, we ask what is the smallest number of spatially selective excitation encoding steps that we must employ so that the reconstructed approximation to F does not sacrifice pertinent image information. This, of course, is ultimately dependent on the medical application, since medical applications have widely varying requirements for spatial and temporal resolution and SNR to name a few. We answer this issue in the following section. Second, how fast can we obtain these samples? To rephrase this question, how short can we keep the TR without reaching a point of hysteresis wherein there is no available longitudinal magnetization for subsequent experiment repetitions to encode. We turn to this question in Section 3.2.

Regarding how many excitations we need, most image matrices tend to be compressible and MR images are no exception. Typically, the amount of compression can be based on dropping the acquisition of non-existent components of a particular image, dropping components too small

---

[1] Portions of this chapter have appeared in [88, 101]

to be significant with respect to noise, or even further, if one is willing to admit some loss in resolving power of the imaging system. In MRI, efficient encoding via compression of F can not sacrifice pertinent image information. On the other hand, the contents of the FOV are not known in advance, complicating application of any compression method. Nonetheless the very requirements of certain MRI applications can be beneficial in this respect, like the continuous imaging necessary in interventional MRI. We will first focus on adjusting the set of encoding vectors to the smallest possible subset of a given encoding basis so that using that particular subset for the acquisition of a known FOV *no significant image information is lost.* No assumptions will be made for an error metric. We will merely rely on the fact that for a given set of acquisition sequence parameters, the amount of *detectable* information must be acquired. In order to do this we will apply knowledge of the noise in the MRI system. This method applies to any encoding basis and for both compressed and uncompressed acquisitions. The issue of prospective encoding will be further visited in Chapters 7 and 9.

Regarding how fast we can excite the encoding functions sequentially, we must not forget that we are attempting to sample a physical system with rigid physical characteristics, one of which is the return of magnetization to thermal equilibrium (T_1 relaxation). If we do not allow sufficient time between RF excitations of the sample, after the first few samples are acquired, there will be no appreciable longitudinal magnetization available to encode with excitations. The same issue arises in Fourier basis imaging where imaging with short repetition times typically comes in two flavors [152]: spoiled steady state gradient recalled echo imaging (e.g., the so-called GRASS and SPGR sequences), and steady state free precession imaging (e.g., the SSFP sequence [119]).

Gradient recalled echo (GRE) imaging does not employ spin echoes, rather, it involves the *free induction decay* after excitation. That is, a phase encoded GRE pulse sequence looks exactly like that of Fig. 2-2.1 except without the 180° RF pulse and the associated slice-select gradient of that RF pulse. In order to use short repetition times, it is necessary to use low flip angle excitations so that longitudinal magnetization reaches a steady state in the sample. This is achieved by choosing a flip angle close to the so-called *Ernst angle* [26], that ensures the amount of longitudinal magnetization prior to each excitation is equal to the amount of longitudinal magnetization at the end of the experiment repetition for a given TR and the sample's (assumed uniform) T_1. The Ernst flip angle that maximizes the amount of longitudinal magnetization when $TR < T_1$ is given by [26]

$$\theta_E = \arccos\left(e^{-TR/T_1}\right). \tag{3.1}$$

In spoiled steady state GRE imaging (SPGR) any transverse magnetization remaining in the sample after signal sampling is destroyed, via e.g., dephasing imposed by a large gradient. If magnetization were allowed to remain on the transverse plane, the encoding gradients of subsequent experiment repetitions would add onto the modulations that it already carried from the experiment repetition that generated it (i.e., excited it), leading to an erroneous signal acquisition that would involve transverse magnetization components of various phase encoding gradient combinations [48, 47]. In contrast, steady state free precession imaging [119] additionally reuses all remaining transverse magnetization by removing all gradient-induced encoding information from it immediately after signal sampling, thus enabling its pure re-encoding on subsequent experiment repetitions. This is accomplished simply by gradient reversal until the 0th gradient moment is nulled.

For non-Fourier encoded MRI we will focus on the effect of spatially varying excitation of the FOV over time, and ask how that affects the steady state of longitudinal magnetization. We will not concern ourselves with reaching a steady state of transverse magnetization since encoding information imposed during excitation can not be as readily removed as with gradient moment nulling achieved by gradient reversal in Fourier imaging. This is however an issue of further research discussed in Chapter 9.

3.1 Compression Control

The columns of the M-by-N k-space matrix F reconstructed via Eq. (2.28) lie in the subspace spanned by the columns of the encoding matrix P. Using the columns of a K-by-M orthogonal matrix U as the discretized excitations in the spatially encoded experiment (c.f., Fig. 2-4.1), the set of responses acquired at time t is $S(t) = U^H F(t)$, when the contents of F (i.e., the FOV,) are time-varying. Inversion, using Eq. (2.28), reconstructs the estimate of $F(t)$, $F_{\text{est}}(t)$, as a projection onto the subspace spanned by the K columns of U:

$$F_{\text{est}}(t) = US(t) = \left\{UU^H\right\} F(t). \tag{3.2}$$

Careful selection of the subspace spanned by the encoding matrix P yields an acquisition and subsequent image reconstruction that can retain most pertinent information. Furthermore, careful selection of the encoding matrix itself yields a short-wide matrix that, when used for acquisition may require fewer encoding steps than phase encodes for the desired image resolution.

SVD encoded MRI [164] uses the reduced set of $K \leq M$ basis functions derived precisely from the first K left singular vectors of the k-space matrix or an estimate to it, i.e.,

$$P = U^H_{1:K,:}, \tag{3.3}$$

in MATLAB-style notation, when the SVD of $F(t)$ is

$$F(t) := U\Sigma V^H. \tag{3.4}$$

Using these singular vectors for acquisition, the power of $F(t)$ that is captured by the reduced set of encoding steps is maximized, i.e.,

$$e = \|F(t) - F_{\text{est}}(t)\|_F^2 = \|F(t) - \left(P^H P\right) F(t)\|_F^2 = \|F(t) - \left(U_{1:K,:} U_{1:K,:}^H\right) F(t)\|_F^2, \tag{3.5}$$

while it is assumed that this maximization is equivalent to capturing pertinent image information [167], which is not necessarily the desired criterion. Furthermore, it is assumed that the k-space matrix of the FOV contents is known *a priori*, since the encoding basis to encode $F(t)$ must be computed from $F(t)$ in order for Eq. (3.5) to hold. Nonetheless, the recent DATUM approach [52] proposed continually adapting the subspace used for each prospective image acquisition in a dynamic series by SVD encoding a simple linear prediction of the change in F, thus somewhat relaxing the latter assumption.

The coherent MR signal detected is always contaminated by white, zero mean, Gaussian noise due to the thermal radiation generated in the receiver by the sample [155]. Most MR images obtained today have an SNR of approximately between 5 (e.g., functional MRI studies) to 100 (e.g., morphological imaging). SNR is defined as the ratio of the signal energy to the standard deviation of noise, denoted by σ_{noise}. Using this simple fact, and irrespective of how an encoding basis is generated, it can be separated into significant and insignificant subspaces for a given k-space matrix F. For some unit vectors p we have that

$$\|pF\|_2 \leq \sigma_{\text{noise}}; \tag{3.6}$$

the projection of the columns of F along the direction of p is smaller than can be explained by the noise component alone and is therefore statistically insignificant. Note the lack of the $\sqrt{M}$ factor missing from the right-hand side of Eq. (3.6), since σ_{noise} is defined in the spatial rather than the spatial frequency domain.

According to Fig. 3-1.1, using 84 randomly selected MR images (256-by-256 matrix size) from a clinical MRI database, and assuming an SNR of 100, a 179-dimensional subspace contains information that is negligible compared to noise. If we choose phase encoded Fourier basis imaging, then 155 out of the 256 Fourier basis functions produce signal that contains information more significant than noise. Similarly, for an SNR of 30, a 218-dimensional subspace contains projections negligible compared to noise, but 65 Fourier basis functions produce significant information. For Hadamard encoding (c.f., Eq. (2.29)), although 254 basis functions produce significant signal for an SNR of 100, that dimensionality drops to 64 for an SNR of 30.

Two conclusions are reached by examining Fig. 3-1.1. First, typical Fourier encoded MRI experiments expend 40-85% of scanning time acquiring data that is indistinguishable from noise in the imaging equipment. Second, even if the amount of noise is used to drive choice of the subset of

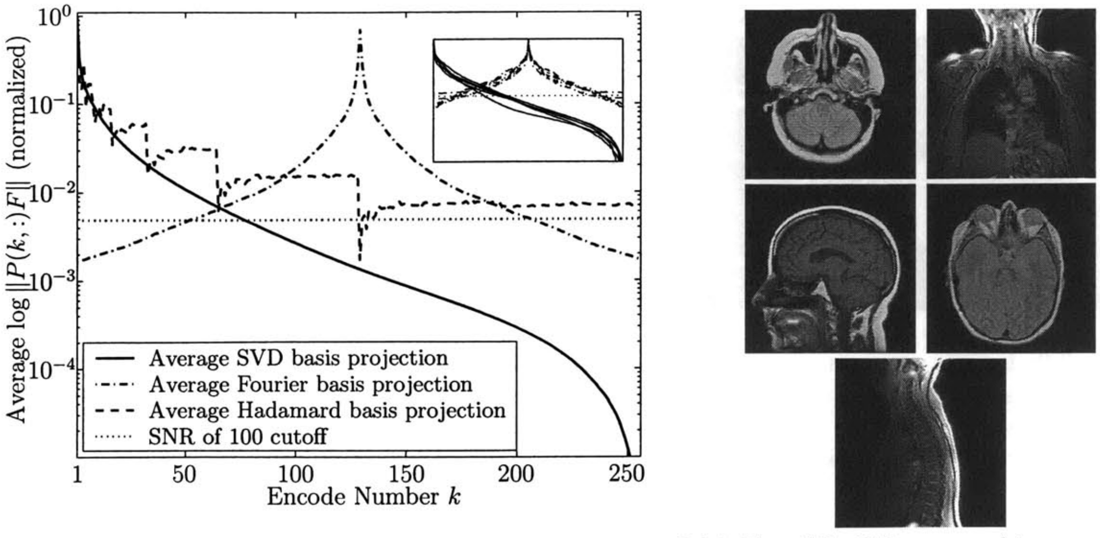

3-1.1: Plot of average singular values, phase encode and Hadamard encode projection norms of 84 clinical MR images, and cutoff for SNR of 100.

3-1.2: Five of the 84 images used to generate the plot in Fig. 3-1.1. Their individual projections appear in the inset plot in Fig. 3-1.1.

Figure 3-1: Statistical significance of projections of sample's k-space onto different encoding bases with respect to noise is established via the SNR.

the encoding basis [87, 148], the set of encoding vectors needed to resolve all statistically significant components is 40% to 50% larger for Fourier basis imaging compared to using the singular value decomposition basis.

Approaching the encoding problem in relation to image noise, we can always ignore any basis vectors of any encoding basis that form statistically insignificant subspaces of k-space, hence increasing imaging efficiency [87, 148]. For reduced basis imaging, the truncation of the encoding subspace, which intrinsically controls the level of compression, can also be driven in the same manner with this unified criterion, dropping the encoding basis functions that are below the noise threshold. The SVD example chooses the smallest K such that $\Sigma_{K,K} \geq \sigma_{\text{noise}}$. For typical MR images, this can translate to speedups of up to 8 over Fourier basis encoding. An experimental result of truncated SVD MRI is shown in Fig. 3-2. For this particular image, the standard deviation of noise approached the $40th$ singular value. Accordingly, the image reconstructed from samples acquired using 42–32 of the left singular vectors for excitation in the sequence of Fig. 2-4.1 led to a good approximation of the FOV.

Naturally, there are advantages to using fixed encoding bases that are independent of the contents of the FOV, such as Fourier, Hadamard or wavelet. Generating oblivious bases does not require any computational overhead. Furthermore, for reduced basis acquisitions based on e.g., the criterion set forth in Eq. (3.6), the trade-offs can be more easily identified and quantified with fixed encoding bases. For example, a reduced set of Fourier basis functions results in lower spatial resolution and Gibbs ringing [140] regardless of the FOV contents.

In contrast, the trade-offs of subspace projection in compressed non-Fourier imaging are not

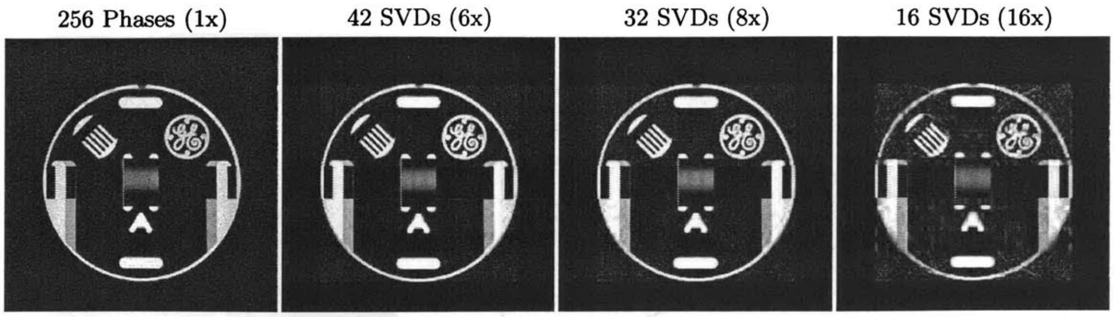

Figure 3-2: Images acquired on a 1.5T MR scanner using full phase encoding (1x speedup, far left image) and spatially selective encoding using the truncated SVD basis at 6, 8 and 16x speedups (same parameters as in Fig. 2-2.1). The standard deviation of the noise of the phase encoded image approached the 40th singular value.

as easily assessed. Of particular interest is the effect of changing the contents of the FOV while using an encoding basis that is matched to compress a prior representation of the FOV contents. Separating the time-varying F into an initial representation plus a time-dependent change, $F(t) = F(t_0) + \Delta F(t)$, when a truncated encoding basis described by the orthogonal matrix $U(t)$ is used to acquire the response $S(t)$ of the MR system's state at time t, the k-space estimate reconstructed is

$$\tilde{F}(t) = U(t)S(t) = \tilde{F}(t_0) + \left\{U(t)U^H(t)\right\}\Delta F(t). \tag{3.7}$$

Choosing the subspace and its dimensionality based on the SNR ensures than $\tilde{F}(t_0)$ contains all significant information that $F(t_0)$ does. However, changes are only acquired to the extent that they have a component in the subspace spanned by the given choice of encoding vectors. The principal angles analysis of [167] asserts that using an encoding basis computed to optimally encode the FOV contents at one time step to acquire an image at a subsequent time step is a well-defined proposition so long as the time-scale of the imaging step is not significantly larger than the time-scale of change. Alternatively, the encoding subspace can be designed specifically to minimize the expected difference as the DATUM method [52] demonstrates. Applicability is further suggested by our experimental results in Chapter 7.

3.2 Spoiled Steady States

When the non-Fourier spatially selective excitations that we use produce a low flip angle excitation, most of the longitudinal magnetization remains undisturbed during an excitatory encoding pulse. This longitudinal magnetization can be used for subsequent excitations without waiting for the sample to relax (in fact we will use this to further our advantage in section 4.1). In this section we particularly aim to analyze the steady state formation of longitudinal magnetization for low flip angle spin echo sequences with short TRs.

This analysis is necessary because of two complications. First, the spatial profiles used for encoding vary in each excitation, and hence the flip angle by which magnetization is disturbed at any one location in the FOV, varies with every repetition of the experiment. Second, every RF pulse disturbs all magnetization in a sample, and, in particular, the 180° refocuser RF pulse used in spin echo sequences has a destructive effect on our ability to use the remaining longitudinal magnetization.

In a spin echo pulse sequence, the 180° refocuser RF pulse is applied with its magnetic field component say along the y axis. Then, all magnetization begins to rotate about the y axis of a reference frame rotating at the resonance frequency of the external magnetic field, undergoing a 180° rotation. This rotation causes transverse magnetization to refocus into the signal echo. Unfortunately, since all magnetization undergoes this rotation, any remaining longitudinal magnetization that was still aligned with the z axis, also rotates about the y axis through 180° to the negative z axis.

The equations of motion of the magnetization vector [3, 4] dictate that when magnetization is aligned with the $-z$ axis, i.e. fully anti-aligned with the external magnetic field, the rate of return to alignment is maximal, making it difficult to obtain a steady state: from the Bloch equations neglecting T_2 relaxation [50],

$$\frac{d\vec{M}}{dt} = \gamma \vec{M} \times \vec{B} - \frac{(M_z - M_0)\hat{\mathrm{k}}}{T_1}, \tag{3.8}$$

and assuming the influence of the external static magnetic field only (e.g. $\vec{B} = B_0\hat{\mathrm{k}}$), the rate of change of the longitudinal component of magnetization, $M_z(t)$, becomes

$$\frac{dM_z(t)}{dt} = \frac{(M_0 - M_z(t))}{T_1}, \tag{3.9}$$

where M_0 is the equilibrium magnetization (i.e., magnetization aligned with the external magnetic field on the $+z$ axis). From Eq. (3.9) it is easy to see that the closer $M_z(t)$ is to $-M_0$, the larger the rate of change of longitudinal magnetization will be. In the case of interest, following a low flip angle spatially selective excitation, most magnetization remains aligned with z, i.e., $M_z \simeq M_0$. The subsequent 180° RF pulse of the spin echo sequence will force this to $M_z \simeq -M_0$, thus maximizing the rate of return of the longitudinal component of magnetization.

During the return to equilibrium, the longitudinal magnetization component must diminish to zero, i.e., $M_z(t') = 0$ for some t'. Non-Fourier excitations which need to convert longitudinal magnetization to transverse would need to wait for multiple T_1 periods for an acceptable amount of longitudinal magnetization to be available again. An alternative is to apply a second 180° pulse after the 180° refocuser, and as soon as the echo from the encoding excitation is sampled, thereby re-negating longitudinal magnetization, returning it to the positive z axis [152, 144]. In this case, $M_z(t_0)$, with t_0 now representing the time after this second refocuser RF pulse, will be close to M_0, and thus slowly relax to equal M_0 in the long time limit. This dual-inversion strategy was known to allow short-TR low flip angle spin echo sequences when all magnetization is perturbed by the same fixed flip angle by the first RF pulse in each series of excitations. To understand the effects of variable low flip angle RF pulses that are in general imposed by non-Fourier encoding, we thus turn to simulation.

In Fig. 3-3, we have computed the longitudinal component of magnetization just prior to the initial spatially selective excitation in each repetition interval using the solution to Eq. (3.9), [50]:

$$M_z(t) = M_z(t_0)e^{-(t-t_0)/T_1} + M_0\left(1 - e^{-(t-t_0)/T_1}\right), \tag{3.10}$$

where $M_z(t_0)$ is the component M_z at $t = 0$, which, for the purpose of this analysis, translates to the moment immediately after an instantaneous excitation.

The longitudinal component is computed for the cases of fixed and variable low flip angle excitations, the former to simulate Fourier encoding and those non-Fourier encoding methods that only use the phase of precession for encoding (such as Hadamard encoding), while the latter, simulated using a random sequence of flip angles, encapsulating general non-Fourier encoding methods.

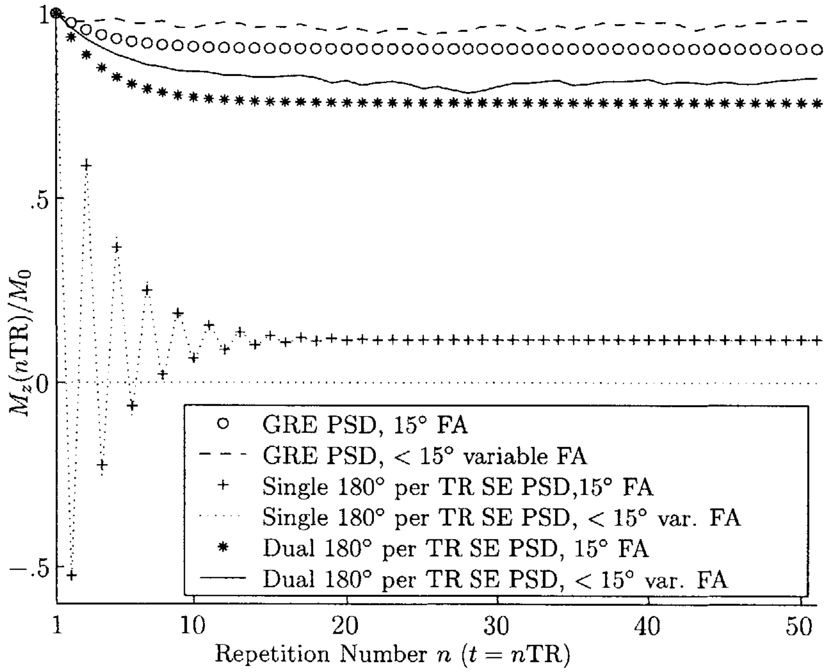

Figure 3-3: Fraction of longitudinal over equilibrium magnetization of a sample just prior to the first excitatory RF pulse in each repetition interval. Typical low flip angle steady state imaging (Gradient Recalled Echo – GRE) and variable flip angle non-Fourier encoding in GRE and Spin Echo (SE) sequences. The graph was computed based on a sample of 1s T_1 and a 280 ms TR and 50 ms TE pulse sequences.

The graph in Fig. 3-3 was computed by directly applying Eq. (3.10) between instances of RF pulses in each TR interval for a number of different pulse sequences. Once the value of M_z just prior to each RF pulse was known, this magnetization was perturbed by an appropriate flip angle corresponding to the next RF pulse. The transverse component was assumed to have dephased, while longitudinal magnetization was then relaxed via Eq. (3.10) until the occasion of the next RF pulse. If the next RF pulse was the first in a TR, the amount of longitudinal magnetization computed was added to the plot. This was done for the Spin Echo sequence of Fig. 2-4.1, both with the single refocuser as well as with a second refocuser right after the acquisition (sampling) window. Finally, for reference, we also show the steady state achieved by a typical low flip angle gradient recalled echo pulse sequence, which does not use refocusers. The results of this simulation suggest that use of a second RF refocuser in variable low flip angle spin echo pulse sequences can indeed yield steady states comparable to GRE sequences.

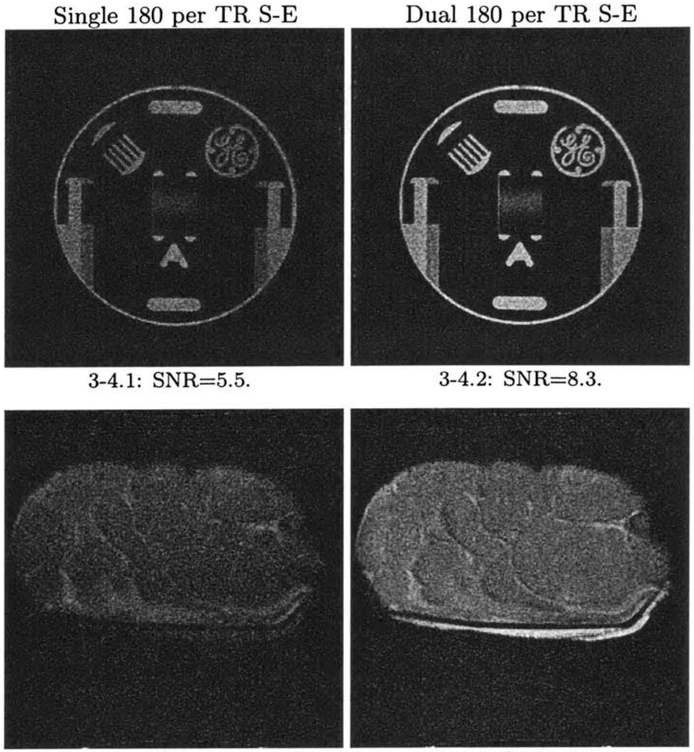

3-4.1: SNR=5.5.

3-4.2: SNR=8.3.

3-4.3: SNR=1.8.

3-4.4: SNR=9.8.

Figure 3-4: Top row: low-T_1 doped-water phantom, acquired with single 180° on the left, dual 180° on the right (TE = 20 ms, TR = 80 ms). Bottom row: animal tissue phantom, single 180° on the left, dual 180° on the right (TE = 30 ms, TR = 100 ms). A factor of 1.4 signal increase for the water phantom ($T1 \approx 100$ ms, 12° FA, second 180° 16 ms after TE) and a factor of 7 for the tissue phantom ($T1 \approx 800$ ms, 12° FA, second 180° 16 ms after TE) was expected by steady state analysis.

This is experimentally verified by the results shown in Fig. 3-4 that corroborate this simulation. In a typical case of a long T_1 tissue (animal tissue phantom) and fairly short TR, an SNR improvement of 5.4 is obtained, compared to the expected factor of 7 if we were to use an educated guess approximation for the tissue's T_1. Unless mentioned otherwise, all spin echo pulse sequences presented in this work follow this double-refocuser approach.

Chapter 4

Broadband Encoded Pulse Sequence Designs[1]

4.1 A Multi-Linear System Response "Fuzzy" Spin Echo Sequence

Through spatially selective RF excitation and application of linear algebraic techniques, an efficiency increase of almost an order of magnitude in acquisition time can be obtained for MRI experiments compared to fully phase encoded MRI. However, many practical Fourier encoding techniques obtain more than one row of k-space per repetition interval [49] thereby speeding up acquisition and increasing temporal resolution. Accordingly, it is desirable to have the same functionality available in the non-Fourier encoding toolbox. Here we show that it is possible to acquire more than one linear system response per repetition in a non-Fourier spatially encoded MRI experiment as well [90], thereby achieving further reductions in imaging times.

Let us collect the following facts:

- The use of low tip angle excitatory RF pulses leaves the longitudinal magnetization component largely unaffected and thus approximately equal to its state prior to each encoding RF pulse (see e.g., Fig. 3-3). This remaining magnetization can be used by subsequent RF excitations within the same experiment repetition.
- Immediately following excitation, the emanating signal decays due to T_2^* dephasing. In a spin echo sequence this dephasing is partially reversed by the refocuser RF pulse. This RF pulse precisely pinpoints when in time transverse magnetization will be in phase again, i.e., refocus, and thus produce the spin echo. If we excite a series of encoding RF pulses, followed by a

---

[1] Portions of this chapter have appeared in [90, 89, 93, 102, 101]

refocusing RF pulse, then we can allow sufficient time in between the encoding RF pulses so that at the moment when magnetization due to one RF pulse refocuses, magnetization due to all other RF pulses is adequately dephased. That is, a spin echo refocusing RF pulse can be used to demultiplex multiple spatial RF excitations that are applied in a single TR. This form of "demultiplexing" individual responses from multiple encoding RF pulses in a single TR is not very efficient since the time in between the encoding RF pulses must be of the order of the T_2^* time constant (e.g., 50ms for typical human tissue). Nonetheless, a refocuser RF pulse may still serve as one component of an echo demultiplexing process.

- Lastly, spatially selective RF profiles are composed of an ensemble of Fourier modes of transverse magnetization that are "activated", i.e., excited, by the hard pulses that a spatially selective RF pulse is composed of. These modes in turn depend on the rephasing of the gradients in order for the magnetization excited by each constituent hard pulse to form the specified Fourier mode. If the applied magnetic field gradient associated with an encoding RF pulse is not appropriately balanced, the magnetization produced by its constituent hard pulses still produces a signal, resulting in a response to be received by the system. However, the individual modes that compose this response are no longer centered about the DC component, i.e., are not centered in k-space. In particular, by controlling the gradient, we can selectively force the magnetization produced by a given set of a hard pulses to result in modes that correspond to very low energy outskirts of k-space, minimizing their resulting response and thus causing another form of "demultiplexing."

Careful combination of these facts enables us to use multiple spatial excitations in a single spin echo experiment repetition in order to acquire and reconstruct an image that closely resembles one acquired with a single excitation and subsequent single response sampling per repetition [90]. Consider a train of K distinct RF pulses, defined by the vectors $\vec{p}^{(j)}$, $j = 1, \ldots, K$, each composed of M constituent hard pulses, i.e., $\vec{p}^{(j)} = (p_{j,1}, \cdots, p_{j,M})$, thus composing a hard pulse train $p_{j,m}$ excited sequentially as shown in Fig. 4-1.

Transverse magnetization resulting from the constituent hard pulses of the jth RF pulse, (i.e., the $p_{j,m}$ for some fixed j) rephase exactly during the sampling interval $q_j = K - j + 1$ by virtue of the spin echo mechanism. Note that $q_j \in \{\text{sampling interval indices}\}$ while $j \in \{\text{excitation interval indices}\}$. At that sampling interval we wish to only receive a response from the transverse magnetization resulting from only the jth RF pulse, defined by the hard pulse vector $\vec{p}^{(j)} = (p_{j,1}, \cdots, p_{j,M})$, and ensure that no significant response from any transverse magnetization that resulted from hard pulses in other RF pulses ($\vec{p}^{(l)}$, $l \neq j$) is received. We accomplish this by relying both on dephasing, as well as unbalanced gradients to force the unwanted magnetization components far out to the edges of k-space so that their (partially dephased) contribution is indistinguishable from noise.

Separating the Individual Responses via Refocusing. For a sampling interval q_j, transverse mag-

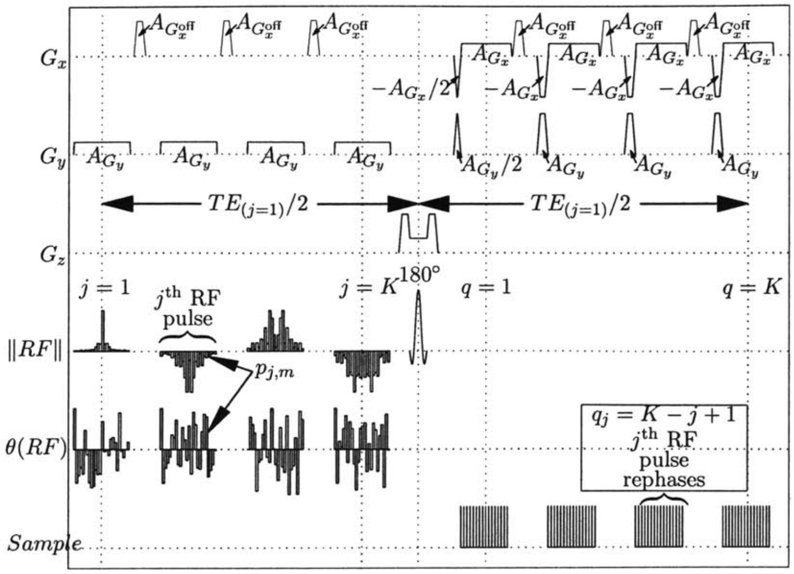

Figure 4-1: A multiple-excitation, multiple-echo, 1D-spatial/1D-Fourier encoded spin echo pulse sequence. The echo of each individual RF pulse is induced both via refocusing as well as gradient reversal in order to center it in k-space only at the symmetric readout (sampling) window. In this manner, the echo of each encoding RF pulse is formed at a different time thereby allowing sampling time to be used in addition to gradient-induced dephasing to demultiplex the set of responses.

netization generated by hard pulses in RF pulses $l \neq j$ will be dephased by an amount proportional to the time difference between the point of their excitation to the 180°, and the point of the 180° to the sampling interval in question. Let the time between consecutive RF pulses be Δt_{rf}, and the time between the last RF pulse and the 180° be $1/2\Delta t_{\text{rf}}$ (without loss of generality). Then, the first of these two times is $T = t_{180} - t_l = (K - l + 1/2)\Delta t_{\text{rf}}$. This is because this is the time difference between the time from excitation of RF pulse l, $t_l = l\Delta t_{\text{rf}}$, to the 180°, which occurs at time $t_{180} = t_K + 1/2\Delta t_{\text{rf}} = (K + 1/2)\Delta t_{\text{rf}}$. The second of these times, i.e., the time from the 180° to the sampling interval q_j will then be $t_{q_j} - t_{180}$. Note that because the interval q_j is where RF pulse j rephases, this time is the same as $t_{180} - t_j = (K - j + 1/2)\Delta t_{\text{rf}}$.

Now, the amount of dephasing of RF pulse l at a sampling interval q_j will be proportional to the difference between these two times, and thus equal to $(K-l+1/2)\Delta t_{\text{rf}} - (K-j+1/2)\Delta t_{\text{rf}} = (j-l)\Delta t_{\text{rf}}$. As expected, this time difference is the same as the time difference between the given sampling interval q_j, and the sampling interval q_l where the RF pulse l will in fact rephase. We define this time difference, proportional to the dephasing, as the *rephasing to sampling distance*, $d(l, q_j)\Delta t_{\text{rf}}$, using the "distance" construct

$$d(l, q_j) = l - j \equiv q_j - q_l. \tag{4.1}$$

Note that the first argument of $d(\cdot, \cdot)$, l, is an excitation index while its second argument, q_j, is a sampling interval index.

Separating the Individual Responses via Unbalanced Gradients. Suppose that this time, $d(l, q_j)\Delta t_{\text{rf}}$, is shorter than T_2^* and therefore at the sampling interval q_j some of these RF pulses ($l \neq j$) still account for some of the coherent magnetization. Because this dephasing can only aid in the demultiplexing of the signals, by lowering the unwanted contributions, we will now ignore it. Instead, we concentrate on the modulation functions produced by the gradients, in order to obtain the resulting composite response that describes the signal sample obtained at sampling location r of the q_lth sampling interval. This is the sample obtained at time $t = t_{q_l} + r\Delta t$, where t_{q_l} is the time point of the beginning of the sampling interval that RF pulse l rephases, and Δt is the digital sampling period for one sample. This response is given by

$$\begin{aligned} S_{\mathcal{MSE}}(q_l, r, \{\vec{p}_1, \ldots, \vec{p}_K\}, z_0) &= \int_{z_0-\Delta z}^{z_0+\Delta z} \iint \rho(x,y,z) \times \\ \sum_{j=1}^{K}\sum_{m=1}^{M} p_{j,m} e^{-i2\pi k_y(j,m,q_l)y} e^{-2\pi k_x(j,r,q_l)x} & dx\, dy\, dz, \end{aligned} \tag{4.2}$$

where the Fourier modes $k_y(j,m,q_l)$ and $k_x(j,r,q_l)$ are given by:

$$\begin{aligned} k_y(j,m,q_l) &= \gamma\Big(\overbrace{(M-m)}^{\substack{\text{remaining } G_y\\ \text{gradient in}\\ j\text{th RF pulse}}} + \overbrace{(K-j)M}^{\substack{\text{subsequent}\\ \text{RF pulses' } G_y\\ \text{gradients in RF train}}} \\ &\qquad - \underbrace{(q_l - 1/2)M}_{\substack{G_y \text{ rephasers until}\\ \text{sampling interval } q_l}}\Big) G_y \Delta t \\ &= \gamma\left((K-j-q_l+1)M + (1/2M - m)\right) G_y \Delta t \\ &= \gamma\left(d(j,q_l)M + (1/2M - m)\right) G_y \Delta t, \end{aligned} \tag{4.3}$$

and

$$\begin{aligned} k_x(j,r,q_l) &= \gamma\Big(\overbrace{(K-j)G_x^{\text{off}}\tau_{\text{off}}}^{\substack{\text{subsequent } G_x^{\text{off}}\\ \text{gradients in RF train}\\ \text{after excitation}}} - \overbrace{(q_l-1)G_x^{\text{off}}\tau_{\text{off}}}^{\substack{G_x^{\text{off}}\\ \text{rephasers until}\\ q_l\text{th sampling interval}}} \\ &\quad \underbrace{-(q_l-1/2)NG_x\Delta t}_{\substack{G_x \text{ rephasers}\\ \text{until } q_l\text{th sampling}\\ \text{interval}}} + \underbrace{\left((q_l-1)N + r\right)G_x\Delta t}_{\substack{G_x \text{ readout}\\ \text{gradients until } r\text{th}\\ \text{sample in } q_l\text{th interval}}}\Big) \\ &= \gamma\left((K-j-q_l+1)G_x^{\text{off}}\tau_{\text{off}} + (r - 1/2N)G_x\Delta t\right) \\ &= \gamma\left(d(j,q_l)G_x^{\text{off}}\tau_{\text{off}} + (r-1/2N)G_x\Delta t\right), \end{aligned} \tag{4.4}$$

assuming that the duration of the G_x^{off} gradient is τ_{off}.

Equations (4.4) and (4.3) relate the signal received in each sampling window of this multiple-response sequence to the desired signal of Eq. (2.23). Using Eq. (4.1), we find that when the sampling interval q_l is that corresponding to the RF pulse j, i.e., $q_l = q_j$, the rephasing to sampling distance $d(j,q_j) = 0$. But for all other pulses $j \neq l$, $d(j,q_j) \neq 0$. Accordingly, at the sampling interval at which RF pulse j rephases ($l = j$), the signal obtained contains the correct sum of modes for the hard pulses of the jth RF pulse since $k_y(j, m, q_j) = \gamma G_y(1/2M - m)\Delta t$ The signal at that sampling interval also contains a sum of modes from the hard pulses of the other RF pulses but they are offset by an additional $d(j, q_l)\gamma G_y M \Delta t$ in the k_y direction and an additional $d(j, q_l)\gamma G_x^{\text{off}}\tau_{\text{off}}$ in the k_x direction.

The $k_{\{x,y\}}$ are wavenumbers of the complex exponentials in the integrals of Eq. (4.2). These wavenumbers effectively lead to wavelengths that modulate the transverse magnetization generated by the hard pulses contained in each RF pulse. As we have seen, through Eqns. (4.3) and (4.4), at each sampling interval these wavenumbers become dependent on the RF pulse that produced the respective magnetization. That is, the further that an RF pulse is from the RF pulse that we desire to obtain a response from at that sampling interval, the larger the wavenumbers that modulate the transverse magnetization that it produced are. In particular, these wavenumbers become larger by multiples of $G_x^{\text{off}}\tau_{\text{off}}$, and $MG_y\Delta t$ proportionally to this distance. Because these wavenumbers translate to wavelengths, it is the possible to make the wavelengths small enough, for the unwanted RF pulses at each sampling interval, so that they represent information about oscillations of the sample's properties in minute scales, making them indistinguishable from thermal noise oscillations. In fact, if the multiples of $G_x^{\text{off}}\tau_{\text{off}}$ are insufficient to make the wavelengths small enough, we can even add such offset gradients along the y direction as well.

In our experiments we found no need for G_x^{off} offset gradients. The natural offset added in k_y due to the spatially selective excitation gradients appears enough to completely dephase any remaining undephased component for typical SNRs, as seen from the images reconstructed in Fig. 4-2. These images were acquired using the identity matrix for encoding with varying number of responses acquired per TR. Using the SVD as a general broadband encoding example, reconstructed images acquired using a relatively large number of encoding RF pulses per TR (4, with 8 being typical in Fourier-encoded FSE sequences) are shown in Fig. 4-3.

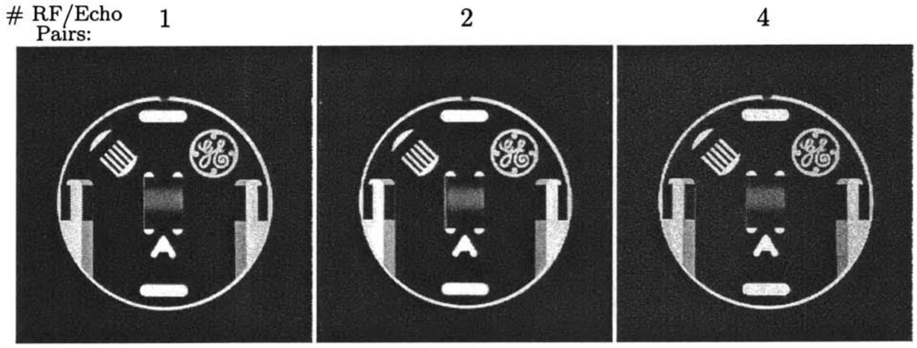

Figure 4-2: Images acquired with the pulse sequence in Fig. 4-1 and variable number of encoding RF pulses per repetition, using the rows of the identity matrix. Imaging parameters were Eff.TE = 40 ms, TR = 400 ms, 16 cm FOV, 10 mm Slice Thickness and 15° flip angle. Gradual loss of signal with increasing echo train length is observed, due to T_2 relaxation; to dramatize this effect, 16 KHz sampling filters were used, yielding 8.192 ms sampling windows, making the RF pulse spacing rather long.

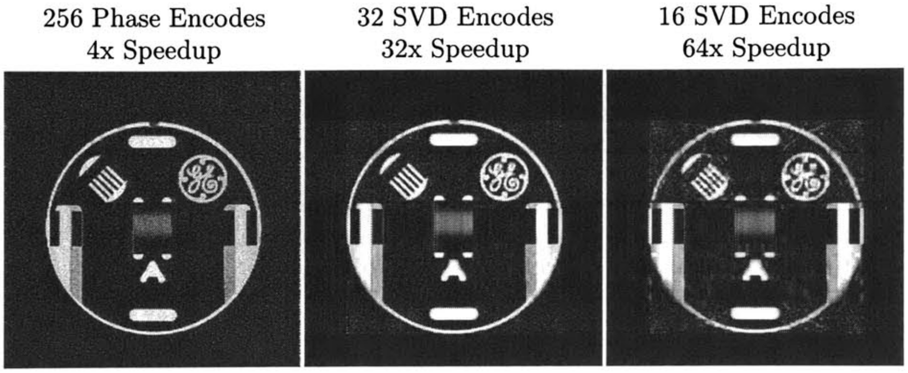

Figure 4-3: Images acquired using the multi-echo sequence of Fig. 4-1 with 4 RF/Echo pairs per TR. Full phase encoding via the identity matrix (left) and non-Fourier encoding using the truncated SVD basis (middle and right). Same imaging parameters as Fig. 4-2.

Summary of Demultiplexing in the Multi-Linear Response Sequence. The most effective demultiplexing of the responses in this multi-linear response pulse sequence is naturally performed via the 180° refocusing RF pulse. Gradient offsets that further dephase any remaining coherent magnetization produced by unwanted RF pulses are used to enhance the demultiplexing process, resulting in a nearly-linear MR system response. With this multi-linear response model, the broadband encoding model described by Eqns. (2.27) and (2.28) remains unchanged. However, it is now capable of the acquisition of the response to multiple broadband encoding RF pulses per experiment repetition, resulting in increased broadband MRI acquisition throughput. We have termed this pulse sequence "fuzzy" since, even in the absence of noise, one does not obtain the exact linear response expected from the Fourier coefficients of the sample that we are trying to reconstruct. Rather, the sampled response includes negligible contributions, from Fourier coefficients outside the spatial frequency region of interest.

Visualizing the Multi-Linear Response Model. It is useful to visualize the effect of using gradient offsets to drive the sum of Fourier modes generated by excited, but undesired, magnetization toward the edges of k-space in this pulse sequence. This effect is depicted in Fig. 4-4 for a dual-RF pulse sequence with the two corresponding sampling windows. The gradient applied during each RF pulse positions the excited magnetization produced by each hard pulse within that RF pulse so that it corresponds to (e.g., "activates") a Fourier mode that is separated by a single wavenumber (one Δk_y in k-space) from the previous hard pulse. However, because the magnetic field gradient associated with each spatially selective RF pulse in the train of RF pulses is not followed by any negative gradient lobe immediately following the RF pulse, any two d-distant RF pulses in the excitation pulse train are forced to activate modes that are placed at a vertical distance proportional to $dG_yM\Delta t$ from each other, or $dM\Delta k_y$ in k-space. Similarly, the x offset gradient forces coefficients activated in different RF pulses to a horizontal distance proportional to $dG_x^{\text{off}}\tau_{\text{off}}$. Following the excitation pulse train, the vertical and horizontal distances between any two RF pulses can not be modified, as any applied gradient will force the repositioning of all activated Fourier modes in unison.

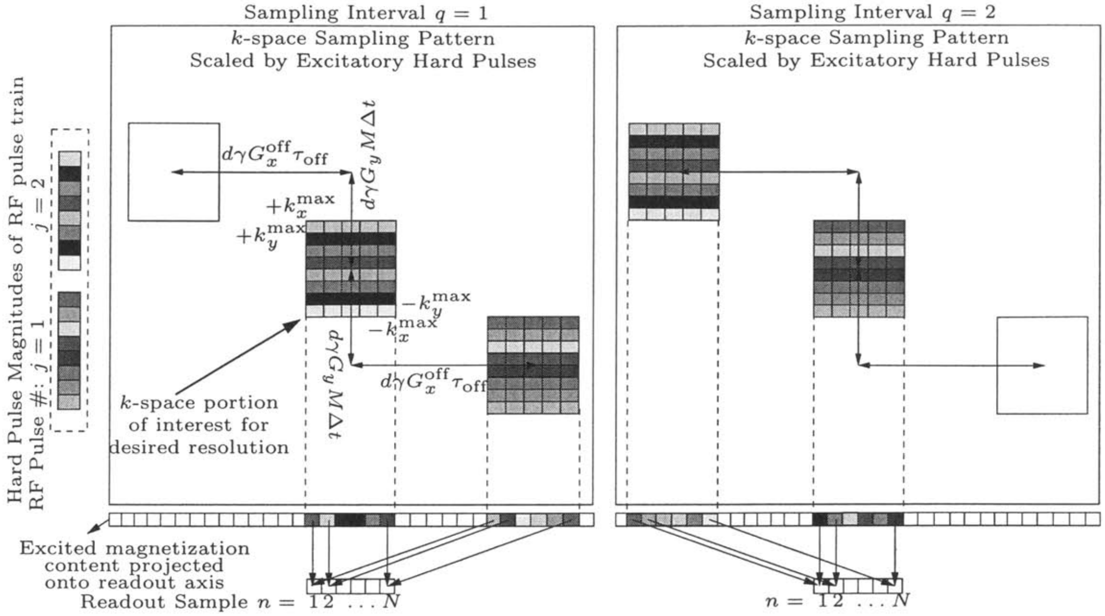

Figure 4-4: The sliding sampling window effect of the multiple excitation, multiple echo pulse sequence presented in Fig. 4-1. k-space extends indefinitely, with most signal energy centered at the origin. For a given spatial resolution, one must resolve the k-space centered about the origin and extending out to the wavenumbers corresponding to that resolution. The multiple excitation pulse sequence introduces "fuzziness" by allowing contributions from unwanted portions of k-space to corrupt the central k-space reconstruction, so long as those contributions are insignificant with respect to noise.

During sampling, all Fourier modes that are activate are added together in order to form the result sampled by the receiver, i.e., this is the effect of integrating over all transverse magnetization. Furthermore, as each sample is acquired, the frequency encoding gradient drives the active modes one wavenumber to the right, so that the next readout sample can be acquired. The k-space distance between modes activated by different RF pulses in the excitation pulse train is fixed once the excitation pulse train is completed. Accordingly, when we balance these gradients during the sampling intervals, only the transverse magnetization generated by the hard pulses of a single spatially selective RF pulse will be centered in k-space (i.e., the one we desire to receive the response of and for which $d = 0$). Therefore only that RF pulse will produce the most significant contribution to the sampled signal. At the following sampling interval, the additional intervening gradient applications will drive these modes, that were centered in k-space for the prior sampling interval, away from the center of k-space. In particular, the modes that were centered at the prior interval will now be a distance proportional to $\gamma G_y M\Delta t$ above the center and a distance proportional to $\gamma G_x^{\text{off}}\tau_{\text{off}}$ to the left, thus forcing them to diminish into a negligible contribution to the MR signal relative to noise. Instead, the new modes that are centered in k-space at the current sampling interval are the modes generated by the RF pulse that was excited just prior to that sampled in the prior interval.

Variable TE and Effective TE. Initially, this sequence poses a minor disadvantage compared to the single-echo sequence of Fig. 2-4.1, stemming from the different echo time (TE) at which the response to each encoding RF pulse is sampled. The fact that each spatial encoding profile produces a response at a different TE leads to a mix of T_2-induced contrasts (TE has a primary effect on image contrast). We note that this is a general issue that is well accepted in Fourier multi-echo sequences such as echo-planar (EPI) [83] and fast spin echo (FSE) [49].

However, in this particular sequence it is possible to remedy this limitation by adding a second refocusing RF pulse after the last profile rephases due to the first refocuser, i.e., after the last sampling window in the sequence of Fig. 4-1. By placing the sampling windows after this second refocuser, magnetization from each of the RF pulses will then rephase in the same order as excited, and thus each pulse will have the same effective TE. In this case, it has been shown that in order to avoid ghosting artifacts [113], either extreme care must be taken in order to ensure that the refocusing pulses are as close as possible to 180°, or that the spatial encoding profiles be real-valued. Restricting the spatial encoding profiles to be real-valued is possible for any general broadband imaging approach by considering the MR system response as $F' = [\mathcal{Re}\{F\} \;\; \mathcal{Im}\{F\}]$ and separately reconstructing the real and imaginary components from the acquired data. Accordingly, for adaptive broadband encoding, the encoding subspace can be computed by the matrix concatenation of the real and imaginary parts. If the different TE of each generated response is acceptable for practical use, as it often is the case, then the ordering of the sampling of encoding functions in the echo train shares the same concerns as the ordering of Fourier phase encodes in Fourier multi-echo sequences.

For this case, in general, a different signal energy is detected due to the different amount of T_2 relaxation in the response of each encoding function. This results in a perceived point spread function (PSF) that is the Fourier transform of the relative weighting of the phase encode lines [105, 86, 18]. In Fourier phase encoded imaging, one typically arranges the order of phase encodes in the echo train so that the central row of k-space is received at the sampling window that is closest to the desired effective TE (abbreviated Eff.TE) for the image. Neighboring phase encodes are acquired in neighboring sampling windows, in the same order as they fill the k-space matrix. That is, the phase encode at $-\Delta k_y$ is acquired at the sampling window preceding TE, while the encode $-2\Delta k_y$ is acquired at the sampling window prior to that, and so forth. This idea can be extended to cases when the entire set of phase encodes can not be acquired in a single echo train, e.g., if we desire 256 phase encodes but use an echo train of length 8 (abbreviated as 8 ETL). In this case the sequence must be repeated 32 times, necessitating that the phase encode set is segmented. That is, the central 32 rows of k-space will be separated and assigned to be acquired one at each of the 32 experiment repetitions. Doing so allows us to acquire each of these 32 rows at the same sampling window within the echo train of the experiment repetition that each is assigned to. The point spread function then becomes the Fourier transform of the staircase function which then describes the relative T_2

weighting of a segmented multi-echo acquisition. In some applications, such as Magnetic Resonance Angiography (MRA), the phase encode ordering in a multi-echo sequence is chosen to optimize a particular aspect of the induced PSF for the specific application [154].

Similar to Fourier multi-echo sequences, the multi-linear response sequence of this section orders the excitation of the encoding RF pulses in the excitation train based on the spatial frequency content that they encode. The ordering arranges for the excitations that encode the lowest frequency content to be placed at the RF pulse excitation j that will yield the time t_{q_j} that is closest to the desired Eff.TE. A set of spatial encoding functions can be ordered according to spatial frequency content with the method described in [166], for example.

4.2 3D Broadband MRI

Fast 2D Fourier encoded imaging sequences are ubiquitous in present-day clinical MRI. To-date, Fourier encoding methods have largely failed to produce useful fast dynamic 3D imaging approaches. This has created a lack of dynamic 3D MR imaging for clinical purposes. The main impetus of 3D imaging is the associated boost in SNR due to increased signal stemming from imaging a larger amount of spins concurrently. Furthermore, SNR, along with imaging time, are the main factors limiting resolution in present-day MRI. For example, if imaging time for a given resolution can be reduced, partial volume effects (stemming from low order Fourier encoding) can be reduced. Similarly, susceptibility artifacts are not an issue in spin echo imaging but, because of the long imaging times the latter requires, they can not be avoided. Accordingly, the limitations of SNR and imaging time are among those most sought after to improve in MRI.

3D MR imaging achieves higher SNR over slice-selective 2D imaging methods since the noise is the same regardless of how much of the available spin density is being imaged. The thermal EMF that composes the noise depends on the volume of the sample that is "visible" by a specific receiver coil, i.e., the volume that is within the spatial sensitivity of the coil, and is otherwise unrelated to what portion of that sample's magnetization will be producing the sampled MR signal [130, 77, 156]. On the other hand, the MR signal radiated is proportional not only to the fraction of the sample's magnetization within the coil's visible volume, but that is nutated as well, i.e., converted to transverse magnetization.

Unfortunately, the increase in SNR and achievable resolution, are accompanied by an increase in imaging time to $O(N^2)$ from the already long $O(N)$ acquisition time of 2D imaging. Especially for *in vivo* imaging, affected by physiological motion, $O(N^2)$ is often unattainable, even when the hidden constant (i.e., the TR) is ultra-short, such as when using SSFP.

Thus, most "3D imaging" performed today in fact employs 2D multi-slice Fourier acquisitions, sacrificing the higher SNR of acquiring a full 3D volume for reduced imaging time. Reduced acquisition time is possible because when multiple slices need to be acquired with a 2D imaging method, separate slices can be excited and acquired efficiently.

Because the desirable TR is typically much longer than the desired TE, the remaining transverse magnetization in one slice can be crushed (i.e., destroyed via dephasing by application of a large gradient) after sampling. Then, another slice can immediately be excited and acquired. That is, the excitation of slices is interleaved so that, within a single TR, multiple slices are excited, each producing a k-space line. The slice excitation/acquisition interleaving scheme is repeated in the same order after one TR has elapsed from the excitation of the first slice. This effectively enables the acquisition of all the 2D slices with the same TR for each slice and in the same amount of time as that required for imaging a single slice. The number of slices that can be interleaved within a single TR is only limited to: (1) the extent of fitting the TE's within the available TR, and, (2) satisfying the FDA *Specific Absorption Rate* (SAR) limits, which place a restriction on the amount of RF power deposition in a human patient per unit time during imaging.

The possibility of performing 3D imaging emerges with the increased efficiency of adaptive non-Fourier imaging via the rank-reduced encoding methodology described earlier in Section 2.2.2. The direct 3D non-Fourier approach has the potential of up to an order of magnitude increase in efficiency over a multi-slice non-Fourier approach. This is because all slices may be treated as a single subspace rather than separate slices with subspaces that would need to be individually spanned. In order to accomplish 3D spatially encoded compressed MRI, we can use two dimensional spatial excitations to encode two dimensions and frequency encoding to localize the third dimension [163]. In the following sections we will see examples of each of these approaches. Unfortunately, the subspace that is encoded with these sequences is relatively small compared to the dimensionality of the encoding space, leading to the likelihood that small FOV changes will induce a significant impact on the image subspace. In the language of Eq. (3.7), because the subspace spanned by the encoding functions is small, a change in the FOV, $\Delta F(t)$ is likely to have very small projections onto the encoding subspace. Subspace tracking and image extrapolation is likely to prove of utmost importance for such methods.

Rather than 2D non-Fourier encoding and 1D readout, we can also encode slices simultaneously along a single dimension via 1D non-Fourier encoding, and make use of a 2D readout method, such as EPI and spiral. Two-dimensional sampling methods have received an immense amount of optimization within the last decade in an attempt to enable 3D Fourier encoding or to provide near-instantaneous 2D imaging. Although returning to 1D non-Fourier encoding for 3D imaging allows us to avoid the problem of the thin encoding subspace, we must still face the hurdles of 2D echo-planar readout and reconstruction [143, 83, 159, 108, 1, 57, 134, 25, 76, 51, 70, 131, 81, 129, 123, 62, 132, 106, 127, 28].

In the process of producing instances of each of these two approaches, we will go through the exercise of producing a generalized linear system encoding model for arbitrary trajectories. This generalized model is additionally beneficial in that it will enable the division of the k-space coefficients that must be acquired into any arbitrary distinct acquisition and excitation sets. Effectively, we will be able to separate the imaging problem into a (3/2)-dimensional excitation and (3/2)-dimensional acquisition, as postulated in [117]. Moreover, any other division that we can imagine, on any arbitrary k-space trajectory we might use to actually perform this division, will be encapsulated by this model.

4.3 Pulse Sequences for 3D MRI I: 2D Echo-Planar Spatial Excitation in a GRE Pulse Sequence

The pulse sequence depicted in Fig. 4-5.1 excites a two-dimensional profile that is spatially selective along the x-y plane by employing an "echo-planar" k-space trajectory in the excitation step. The spatial profile is excited equally throughout the sample volume along the z axis. Subsequently, the signal emanating from this volume of excited magnetization is localized along z via Fourier frequency encoding [89]. Suppose that the RF train resulting in each 2D excitation is composed of K individual 1D RF excitations that we individually refer to as RF pulses. The RF train is composed of the ensemble of K RF pulses. Each RF pulse is in turn composed of M hard pulses. Each of the 1D RF excitation pulses is played out during a gradient applied in the x direction, of duration $M\Delta t$, and constant magnitude. Except for the gradient associated with the last RF pulse, each x spatial selection gradient is followed by a rephasing gradient of equal area. The last pulse is followed by a rephasing gradient of only half that area. We refer to the x direction spatial selection gradient followed by a rephaser gradient as an excitation-rephasing gradient "block".

With the exception of the last excitation-rephasing block, the 0th x-axis gradient moment of each excitation-rephasing block is nulled. Then consider a spin located at x_0, excited by the mth impulse in the jth RF pulse. At the end of the jth x-gradient excitation-rephasing block, the spin will have acquired a phase that has rotated it to $\exp(-i2\pi\gamma G_x(-m)x_0\Delta t)$, since only gradients after the moment of excitation (i.e., $(M-m)\Delta t$ from the mth impulse) affect the spin's phase. Subsequent excitation-rephasing blocks, except the last, will add no extra phase to this spin since the 0th gradient moment of each subsequent block is nulled. The last excitation's gradient block is, however, unbalanced by an excess additional area of $1/2M\Delta t$, which will contribute to the phase of all spins excited during the entire RF train. Therefore, the net effect of the ensemble of x gradients is that transverse magnetization excited by each RF pulse will be individually centered in k-space along the x direction at the end of the entire RF train. The net phase accumulated will be independent of the RF pulse position (i.e., j) in the RF train. That is, regardless of which RF pulse contained the impulse that excited the magnetization, it will cause the magnetization to rotate

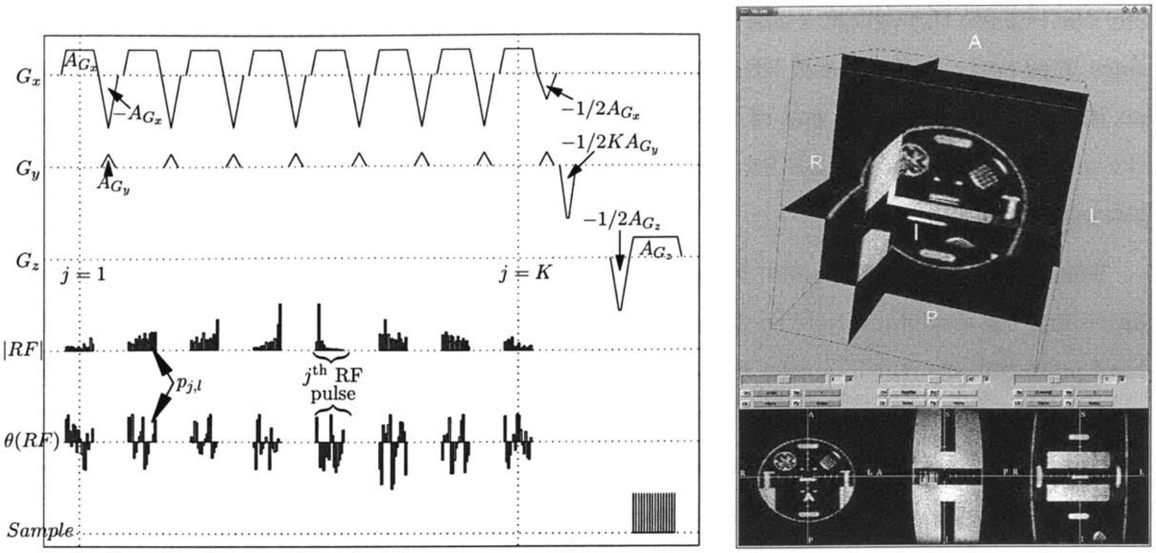

4-5.1: A 2D Echo-Planar Spatial/1D-Fourier encoded GRE pulse sequence. The RF excitation train is composed of K RF pulses, each composed of M hard pulses. These excite a 2D spatial profile in the $x-y$ plane. The train is manipulated so as to excite a $K \times M$ 2D spatial profile in the $x-y$ plane, equally throughout the z dimension of the sample. The response of the sample to this 2D profile along z is then obtained in each of N samples via frequency encoding.

4-5.2: 3D cube produced using the rows of the $(KM) \times (KM)$ identity matrix for the RF trains of the pulse sequence in Fig. 4-5.1, with $K = 64$, $M = 128$ and $N = 256$ readout samples.

Figure 4-5: The 2D Echo-Planar Spatial/1D-Fourier encoded GRE pulse manipulates the RF excitation train so as to produce a $K \times M$ spatial profile of transverse magnetization in the $x-y$ plane, excited equally throughout the z dimension of the sample. The response of the sample to this 2D profile along z is then obtained in each of N samples via frequency encoding. Repeating the process for a set of 2D profiles that span the encoding space allows reconstruction of the k-space cube, as shown in Fig. 4-5.2, where the rows of the $(KM) \times (KM)$ identity matrix were used for the RF trains. For this acquisition, TE was 10 ms, TR 200 ms, and a 16 KHz receive bandwidth was used for a 16 cm FOV. Total imaging time was 27 min, equivalent to a commercial 3D GRE or SPGR pulse sequence of the same TR.

through $\exp(-i2\pi\gamma G_x(1/2M - m)x\Delta t)$. Each hard pulse composing any of the RF pulses produces a single k_x Fourier mode of the sample, centered about $k_x = 0$.

Each RF pulse in the RF train excites a 1D spatial profile along x, while all the spatial profiles generated by the RF pulses coexist at the end of the RF train. However, the gradients along the G_y axis enforce the separation of these 1D profiles so as to lead to the production of separate Fourier modes along the second spatially selective direction (i.e., y).

Consider the case of a square FOV in the x-y dimensions, and a resolution of K along the y direction. In between RF pulses, we insert a gradient "blip" (i.e., a fixed duration and magnitude gradient) along the y direction of duration Δt and same magnitude as the x gradient. The effect of this gradient blip is to add phase to every spin that has been excited by any impulse prior to the blip. The phase added to those spins due to a single blip is equivalent to a rotation by $\exp(-i2\pi\gamma G_y y\Delta t)$. At the end of the RF train, a gradient rephaser, of area half the sum of the K blips, is applied along the y direction, causing a final rotation through $\exp(i2\pi\gamma G_y y(K/2)\Delta t)$. Magnetization excited by any one impulse throughout a single RF pulse will experience the same number of y gradient blips, since blips occur at the end of RF pulses. This quantizes the rotation of excited magnetization on an RF pulse basis. At the end of the gradient rephaser, a spin located at y_0 that was excited by the mth hard pulse in the jth RF pulse, will have been rotated by $\exp(-i2\pi\gamma G_y(K/2-j)y_0\Delta t)$, independent of m.

The position of a hard pulse within any RF pulse of Fig. 4-5.1 controls the k_x wavenumber describing the modulation of the transverse magnetization produced. That is, the position of the hard pulse controls which Fourier mode along x the impulse will effectively produce, independent of the position of the RF pulse in the RF train. Similarly, the position of an RF pulse in the RF train controls which Fourier mode of transverse magnetization along y is produced by the hard pulses that compose it, independent of their particular position in that RF pulse.

We are particularly interested in the signal produced when the RF pulses composing the RF pulse train are taken from the rows of a $K \times M$ matrix P, with elements $P_{j,m}$, $1 \leq j \leq K$, $1 \leq m \leq M$. We will interchangeably refer to the RF pule train that these RF pulses produce as a vector composed of the concatenation of the rows of the matrix P. That is, if the rows of the matrix P are used as the RF pulses in the sequence of Fig. 4-5.1, then the equivalent input RF vector p is formed by

$$p_l = P_{j,m}, \tag{4.5}$$

$$\text{where} \tag{4.6}$$

$$j = \lfloor l/M \rfloor, \quad m = \mathrm{mod}(l, M). \tag{4.7}$$

Following the development of previous sections (c.f., Section 2.2.2), the signal produced by the RF train $\tilde{P}$, that is composed of a single hard pulse located at the mth position in the jth RF pulse, and zeros elsewhere, contains a single Fourier mode of the sample scaled by the hard pulse. The signal due to that hard pulse for the qth signal sample obtained at time $t = q\Delta t$, $1 \leq q \leq N$ after sampling begins is [90, 92]:

$$S_{2DS\mathcal{E}}(t, \tilde{P}) = \int_z \int_y \int_x \rho(x, y, z) e^{-i2\pi k_z z} \tilde{P}_{j,m} e^{-i2\pi(k_y y + k_x x)} dx\, dy\, dz, \tag{4.8}$$

$$k_z = \gamma G_z(q - N/2)\Delta t, \tag{4.9}$$

$$k_y = \gamma G_y(K/2 - j)\Delta t, \tag{4.10}$$

$$k_x = \gamma G_x(M/2 - m)\Delta t, \tag{4.11}$$

where $\tilde{P}_{j,m}$ is the single non-zero impulse of $\tilde{P}$.

Remaining in the low flip angle regime, we again invoke superposition to obtain the MR imaging equation for the signal produced when the rows of any arbitrary complex-valued RF matrix P are used as the RF pulses [90, 117]:

$$S_{2DS\mathcal{E}}(t,P) = \int_z \int_y \int_x \rho(x,y,z) e^{-i2\pi k_z z} \left(\sum_{j=1}^{K} \sum_{m=1}^{M} P_{j,m} e^{-i2\pi(k_y y + k_x x)} \right) dx\, dy\, dz, \tag{4.12}$$

$$= \sum_{j=1}^{K} \sum_{m=1}^{M} P_{j,m} \left(\int_z \int_y \int_x \rho(x,y,z) e^{-i2\pi(k_z z + k_y y + k_x x)} dx\, dy\, dz \right), \tag{4.13}$$

with k_x, k_y and k_z as given in Eqns. (4.9)–(4.11). Equation (4.12) explicitly reveals the 2D DFT of the RF matrix P, that multiplies, in the spatial domain, the sample's spin density $\rho(x,y,z)$. In Eq. (4.13) this is recast as the sum of intrinsic Fourier modes of the signal density scaled by the corresponding elements of the 2D RF train matrix.

4.3.1 RF Pulse Train Segmentation

In echo-planar imaging the acquisition train is typically "segmented" i.e., divided among multiple sequence repetitions in order to reduce off-resonance induced distortions [108] (caused by chemical shift and susceptibility resonance offsets), T_2^* relaxation induced blurring [86, 18], as well as gradient and sampling requirements.

Distortions and relaxation affect an RF pulse excitation train much like they affect a readout echo train. Additionally, in order to deposit enough RF power on the sample to achieve a flip angle of say 20° using current RF amplifier hardware, it is necessary to use hard pulses of the order of 6 μsec. Thus, to obtain a resolution of 128 along the x direction, each RF pulse requires 768 μsec. Due to all such undesirable effects it is therefore impractical, if not prohibitive, to use excitatory RF trains composed of more than 16 RF pulses (yielding approximately 10 msec-long RF trains). This effectively places a limit on the attainable resolution along the y direction. To increase the attainable resolution we can also segment a longer RF pulse train [115], just as is usually done in segmented fast Fourier imaging methods, such as EPI. This is achieved by interleaving the k-space coverage of the various segments over multiple sequence repetitions.

The main objective is to excite the desired spatial profile in interleaved segments, with each segment excited in a separate repetition of the pulse sequence. Due to linearity, the sum of the responses resulting from signal sampling following the excitation of each individual segment will be equivalent to the response that would be obtained if all RF pulses were excited in a single RF train [115], modulo the undesirable effects. The constraint here is that each hard pulse excited in the shorter RF train of a segmented excitation must undergo precession under the appropriate gradient integral had the RF pulse train not been segmented.

Suppose we wish to obtain the response to an RF train composed of the RF pulses in the rows of the K-by-M matrix P. Also, we wish to perform the acquisitions using Q separate segments, i.e., segment the RF train Q-ways. Q separate repetitions of the experiment are then used, and the response is acquired in Q separate pieces. We proceed by breaking up the matrix P into Q sub-matrices $P^{(q)}$ of size K/Q-by-M, with $q = 1, \dots, Q$, so that

$$P^{(q)}_{r,m} = P_{j,m}, \tag{4.14}$$

where $j = q + (r-1)Q$ for $r = 1, \dots, \lfloor K/Q \rfloor$ and $m = 1, \dots, M$.

In order to force the transverse magnetization excited by each of the Q separate segments to produce the same Fourier modes as if the segments were excited in a single RF train, we must change the y gradient blip appropriately. In particular, since the separation of two consecutive RF pulses (i.e., the separation of two rows of $P^{(q)}$, $\forall q$) is now Q k-space rows of the matrix P, we increase the y gradient blip area to $Q\gamma G_y \Delta t$. This ensures that two consecutive RF pulses in each segment's RF train will be separated by the same amount in k_y as if they were used for excitation in a single RF train. Additionally, the segment described by the matrix $P^{(q)}$ is supposed to produce Fourier modes that begin at an offset of $q-1$ k-space rows from that of the first k-space row of the encoding matrix P. Therefore, at each repetition of the experiment we need to rephase the magnetization excited by the RF train by an additional amount in k_y, corresponding to the offset of $q-1$ rows of the particular segment. This is accomplished by rephasing the segmented train with the final rephasing gradient along y of area $-(1/2K + q)\gamma G_y \Delta t$.

Inserting these gradients in the imaging Eq. (4.13) and adding up the contributions of all segments, we obtain precisely the same response as the composite RF train drawn from the entire matrix P and excited in a single segment, modulo relaxation and off-resonance effects. The signal received from the excitation of segment q is:

$$S^{(q)}_{2D\mathcal{SE}}(t, P^{(q)}) = \sum_{j=1}^{\lfloor K/Q \rfloor} \sum_{m=1}^{M} P^{(q)}_{j,m} \left(\int_z \int_y \int_x \rho(x,y,z) e^{-i2\pi k_z z} e^{-i2\pi k'_y(q) y} e^{-i2\pi k_x x} dx\, dy\, dz \right), \tag{4.15}$$

$$\begin{aligned} k'_y(q) &= \left((K/Q - j)Q - (K/2 + q)\right) \gamma G_y \Delta t \\ &= (K/2 - jQ - q)\gamma G_y \Delta t \end{aligned} \tag{4.16}$$

and the sum of the responses over all q segments then produces the desired response

$$\begin{aligned} S^{\text{comp}}_{2D\mathcal{SE}}(t) &= \sum_{q=1}^{Q} S^{(q)}_{2D\mathcal{SE}}(t, P^{(q)}) \\ &= \sum_{q=1}^{Q} \sum_{j=1}^{\lfloor K/Q \rfloor - 1} \sum_{m=1}^{M} P^{(q)}_{j,m} \left(\int_z \int_y \int_x \rho(x,y,z) e^{-i2\pi k_z z} e^{-i2\pi k'_y(q) y} e^{-i2\pi k_x x} dx\, dy\, dz \right), \\ &= \sum_{g=1}^{K} \sum_{m=1}^{M} P_{g,m} \left(\int_z \int_y \int_x \rho(x,y,z) e^{-i2\pi k_z z} e^{-i2\pi k'_y(\bmod (g,Q)) y} e^{-i2\pi k_x x} dx\, dy\, dz \right), \\ &= S_{2D\mathcal{SE}}(t, P), \end{aligned} \tag{4.17}$$

by letting $g = jQ + q$ and collecting terms. The last equality follows since $\mathrm{mod}\,(g, Q) = g - jQ$ so that by Eq. (4.16), $k_y'(g - jQ) = (K/2 - g)\gamma G_y \Delta t$, resulting in the same modes as those produced in Eq. (4.10).

RF train segmentation allows us to excite 2D spatial profiles with arbitrary resolution [115] while keeping the RF train length manageable in light of the relaxation properties of the imaged sample and the various off-resonance errors, thus making 3D broadband non-Fourier imaging via the sequence of Fig. 4-5.1 practical. Naturally, this flexibility comes at the expense of increasing total imaging time by a factor proportional to the number of ways we segment the excitation of the encoding functions. In Fourier imaging using echo-planar readouts, unless segmentation is used, the excessive signal decay in between the beginning and end of the acquisition and the phase accrual errors caused by the field inhomogeneities and gradient concomitant fields lead to large geometric distortions. Thus, even in current state-of-the-art Fourier EPI imaging, the time expense of segmenting the signal acquisition train is necessary in order to obtain usable images.

4.3.2 2D Echo-Planar Spatial Excitation Spin Echo Pulse Sequence

If the segmented RF train used for each excitation is shorter than the T_2 relaxation time, e.g., of the order of the sampling window, one may readily modify the sequence of Fig. 4-5.1 to obtain a spin echo pulse sequence. This is accomplished by insertion of a 180° refocusing RF pulse in between the center of the RF train and the signal sampling window, similar to the spin echo echo-planar readout Fourier encoded sequences [22]. Using a 16 KHz receive bandwidth, a 256-point readout requires approximately 8 msec. An example is the segmented case mentioned earlier, yielding 10ms RF pulse trains which allow excitation of 16 RF pulses at 128 hard pulse resolution. Accordingly, segmentation makes a spin echo version of the pulse sequence feasible for 3D broadband non-Fourier imaging.

Also, the spin echo RF pulse may be slab-selective, in order to refocus a slab of the desired thickness only. The refocusing can select a slab along either broadband encoded direction (x, y), or along the readout dimension. This can minimize aliasing of magnetization from outside the FOV along the chosen slab-select dimension. Alternatively, if there is no sample outside the extent of the FOV so that aliasing problems are not an issue, a non-selective hard pulse RF refocusing pulse can be used to increase the efficiency of the sequence by minimizing the achievable echo time (a subject we will revisit in Chapter 8).

4.3.3 The Impulse and Broadband Responses of Echo-Planar Spatial Excitation

Suppose we wish to probe the MR system in order to directly produce the Fourier coefficients of the 3D sample, which by 3D DFT produces the MR volume image of the sample. This can be accomplished by repeating the experiment KM times, noting the dependence of Eq. (4.13) on the indexes j and m, each time using for the RF train a K-by-M matrix containing a single unit impulse with zeros elsewhere, such that no two of the KM such matrices (call them $P^{(e)}$), have the impulse at the same index. The set of RF pulse matrices $P^{(e)}$ that will yield a set of RF trains that completely Fourier encode both spatial encoding dimensions, is made up of the matrices $P^{(e)}$ such that each matrix in the set has a single impulse in a unique row and column position (j and m indexes) compared to the other matrices in the set, and zeros elsewhere. This set of RF pulse trains produces samples that are Fourier encoded in all three dimensions. Let the matrix to be used at the lth repetition of the MR experiment have entries

$$P_{j,m}^{(e_l)} = \begin{cases} 1, & \text{if } m = \operatorname{mod}(l, M),\ j = \lfloor l/M \rfloor, \\ 0, & \text{otherwise,} \end{cases} \tag{4.18}$$

where $l = 1, \ldots, KM$, forming the entire family of K-by-M "impulse response" RF input matrices. This set of 2D RF matrix inputs is derived from the set of rows of the KM-by-KM identity matrix by reshaping each row to yield a 2D K-by-M matrix.

The data produced by each repetition of the experiment defines one row of the 3D k-space of the sample. From Eq. (4.8), we have

$$^{(2DS\mathcal{E})}F_{j,m,q}^{3D} = S_{2DS\mathcal{E}}(q\Delta t, P^{(e_l)}), \tag{4.19}$$

where $l = (j-1)M + m$ according to Eq. (4.18). A straightforward 3D DFT of $^{(2DS\mathcal{E})}F^{3D}$ will then yield the volume image of the sample, as shown for example in Fig. 4-5.2.

When an arbitrary 2D RF input matrix is used, the impulses excite a wealth of 2D Fourier modes of the sample which together sum to form a 2D spatial profile. A 2D spatial profile, corresponding to the arbitrary (k-space) RF matrix P that is input in the system, is excited equally throughout the readout direction of the sample. During readout, the active Fourier coefficients of the sample, i.e., that have been excited by the amount corresponding to the entries of P, are projected onto the readout direction and sampled by the system. Thus the impulse response data cube $^{(2DS\mathcal{E})}F^{3D}$ allows us to define the response of the sample to an arbitrary input matrix, again based on superposition.

In order to use the same linear-algebraic language of Section 2.2.2, we reshape the 3D k-space cube as a tall-thin 2D matrix,

$$ {}^{(2DS\mathcal{E})}F^{2D}_{l,q} = S_{2DS\mathcal{E}}(q\Delta t, P^{(e_l)}) \equiv {}^{(2DS\mathcal{E})}F^{3D}_{j,m,q}, \tag{4.20} $$

$$ j = \lfloor l/M \rfloor \tag{4.21} $$

$$ m = \mathrm{mod}(l, M) \tag{4.22} $$

with $l = 1, \ldots, KM$ and $q = 1, \ldots, N$. We can now use the familiar tools of linear algebra to decompose this matrix.

This impulse response matrix produced by the 3D MR experiment is a tall and thin matrix. Each column of F^{2D} has KM entries which, when reshaped into a K-by-M matrix, correspond to one k-space plane of Fourier coefficients of the sample along the readout direction. The entire sample is composed of only N such planes. This has a direct consequence on the subspace spanned by the matrix F^{2D}; its columns belong to $\mathbb{C}^{KM}$ but they span a subspace of dimension $\leq N$, since it only has N columns. Effectively, at most N encoding vectors are needed to obtain the complete matrix, regardless of the properties of the particular sample being imaged and the noise present.

For the arbitrary input RF matrix, P, with entries $P_{j,m}$, the response of the system under the low flip angle constraint, according to Eq. (4.13) is the vector $s = pF$, if the vector p is the similarly reshaped version of P (Eqns. (4.5) and Eq. (4.7)), thus equating manipulation for this 3D echo-planar sequence with that of the 2D example (c.f., Eq. (2.26)). Given a set of L such input RF matrices to be used for repetitions of the sequence, they can be reshaped into such a set of vectors. By placing these vectors in the rows of an L-by-KM matrix (to form an encoding matrix E), then gives the capability to simply rewrite the responses of the system to these 2D excitations as the rows of the matrix $S = EF^{2D}$, in the same fashion as the 2D imaging problem examined at the outset of this work (c.f., Eq. (2.27)).

Returning to the dimensionality of F^{2D}, if a full set of $L = KM$ orthogonal vectors spanning all of $\mathbb{C}^{KM}$ are used to obtain the system response defined by F^{2D}, the (complete) amount of information gathered could have been acquired with a set of just $L = N$ orthogonal vectors. Unfortunately, in order to find the specific N-dimensional subspace of $\mathbb{C}^{KM}$ for which $\|pF^{2D}\|_2 \neq 0$, *a priori* knowledge of F^{2D} is necessary. On the other hand, knowledge of the specific subspace would in effect mean that we can scan the entire object with just those $L = N$ encoding functions, at a speedup of KM/N compared to full Fourier encoding.

If the impulse response matrix F^{2D} is available, then we may obtain the subspace via use of the SVD, just as in 2D imaging. Furthermore, the same methods of Section 3.1 can be used. These are based on employing the noise in the signal to control any additional compression to further compact the signal space and speedup the acquisition. This prospect of lower rank acquisitions that further restrict the subspace of the reconstructed k-space can lead to acquisition efficiency that even Fourier

EPI cannot achieve. Examples of such compressed acquisitions are provided in Section 4.3.4.

Signal acquisition and reconstruction of the linear system obtained by Eqns. (4.20) and (2.27) follows. For the SVD example, if $F^{2D} = U\Sigma V^H$ and the first L columns of the matrix U^H are used as RF inputs, the sampled response will be given by

$$S = U^H_{1:L,:} F^{2D}, \tag{4.23}$$

which can be inverted to yield the k-space estimate of the current FOV contents by the summation of the rank-one matrices equivalent to

$$\tilde{F}^{2D} = U_{1:L,:} S. \tag{4.24}$$

Two examples of truncated 3D SVD imaging using 2D spatial excitations are presented in Figures 4-6 and 4-7.

This approach retains theoretical and numerical implementation correspondence with 2D MRI, but is not limited by the matrix formulation. The left singular vectors of an approximation to F^{2D} (e.g., by its state at an earlier time) that are associated with the (at most) N non-zero singular values, each intrinsically define a 2D profile with maximal (if any) response from the sample. The optimal approximation to the k-space is obtained by using these profiles to excite magnetization in space. The signal acquisition in turn produces the amount of this response to each spatial profile, at each location along the readout direction.

Given one left singular vector $u^{(k)}$ of F^{2D}, of length KM (and using its 2D K-by-M matrix representation, $U^{(k)}$),

$$U^{(k)}_{j,l} = u^{(k)}_{(j-1)M+l}, \tag{4.25}$$

the k-space reconstruction formed by a rank-L SVD-truncated acquisition (Eq. (4.24)) yields the approximation to F^{3D} as

$${}^{(2D\mathcal{S}\mathcal{E})}F^{3D}_{j,l,m} = \sum_{k=1}^{L} \sigma_k U^{(k)}_{j,l} \left\{ v^{(k)}_m \right\}^H , \tag{4.26}$$

with $\{v^{(k)}_m\}^H$ the hermitian conjugate of the corresponding length-N right singular vector of F^{2D}. Equation (4.26) describes the k-space volume reconstructed when the response of a set of 2D broadband encoding functions is acquired along the readout dimension. The reconstructed k-space volume is composed of a sum of rank-one tensors. This enables the prospect of subspace identification via pathways not available in the matrix representation, such as via higher order SVDs [23, 169].

4.3.4 3D Imaging Experiments Employing 2D-Spatial Echo-Planar/1D-Fourier Encoding

The pulse sequence and methods described in this section were used to perform a set of reduced-rank 3D acquisitions of a doped water and an animal tissue phantom using our 1.5T GE Signa LX 8.3 MR scanner. Our interest is initially to examine the prospect of accelerated acquisition by reducing the number of 2D spatial profiles that are excited and their response acquired as exemplified in Eq. (4.23). The reconstructions obtained of the images of the two phantoms are shown in Fig. 4-6 and Fig. 4-7.

The acquisitions using the doped water phantom aimed to acquire a $64 \times 128 \times 256$ resolution 3D image, with 256 frequency encoded readout points along the R/L direction. The other two dimensions were encoded using 64×128 2D spatial encoding profiles. Fourier encoding was used similar to an SPGR acquisition, except that the Fourier modes were acquired by shifting the location of the impulse within the 2D echo-planar excitation as shown in Eq. (4.19). this resulted in different effective TE for each k_x, k_y mode. The excitation of the 2D profiles was 4-way segmented. The dominant 64 of 256 2D profiles (i.e., as determined from the SVD of the impulse response obtained by Fourier acquisition as described) were used to re-acquire the sample. This produced a reconstruction that, as shown in Fig. 4-6, retained imaging quality but that was acquired at a 4x speedup over a 4-way segmented Fourier EPI acquisition. The animal tissue phantom acquisitions were similar, aimed at $32 \times 256 \times 256$ resolution, with the 32×256 2D profiles segmented 8 ways. The fully phase encoded and compressed acquisition results are shown in Fig. 4-7. For both experiments we are able to obtain 32x to 64x acquisition speedup over a GRE or SPGR type Fourier acquisition, and 4x to 8x speedup over a Fourier EPI acquisition without significant loss of resolution.

Dynamic Imaging Results

A more difficult rank-reduced encoding situation arises when there is change in the FOV with profiles designed to encode the MR system response prior to this change, as would be the case in any dynamic experiment. The results in this section were acquired using a version of the "scanner real-time" system that will be presented in Chapter 7, appropriately modified with modules designed for 3D imaging. The experimental results are presented here because of the resulting large latency between acquisition, reconstruction and subspace identification, caused by the lack of sufficient computing resources and the prototype characteristics of the 3D system.

In the experiment, an animal tissue phantom was imaged with a needle partially inserted. The impulse response was first obtained using the identity matrix as previously described. The needle was then partially removed and the next image frame (representing the next time point) was acquired using the 2D SVD profiles that were computed from the system response prior to this dynamic

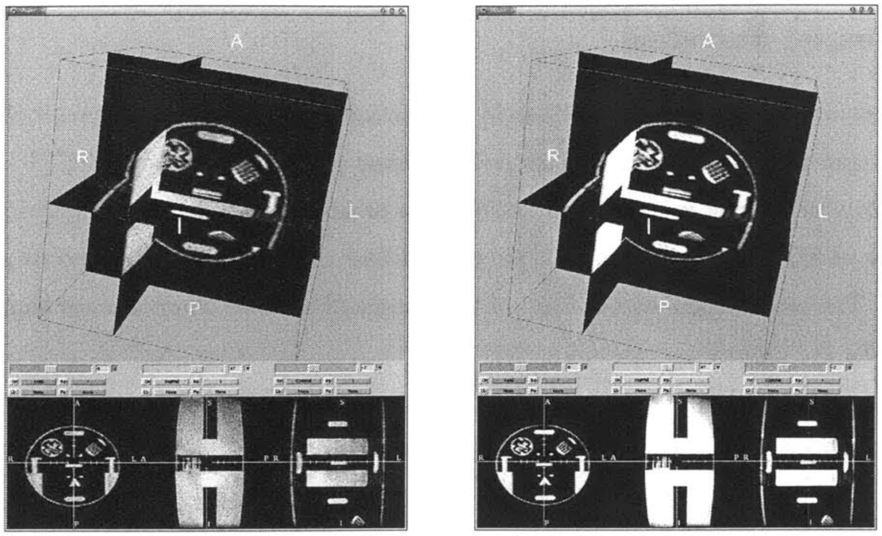
Fourier (64 * 128 Phase encodes, 8192 TRs)

SVD (64 2D profiles, 256 TRs)

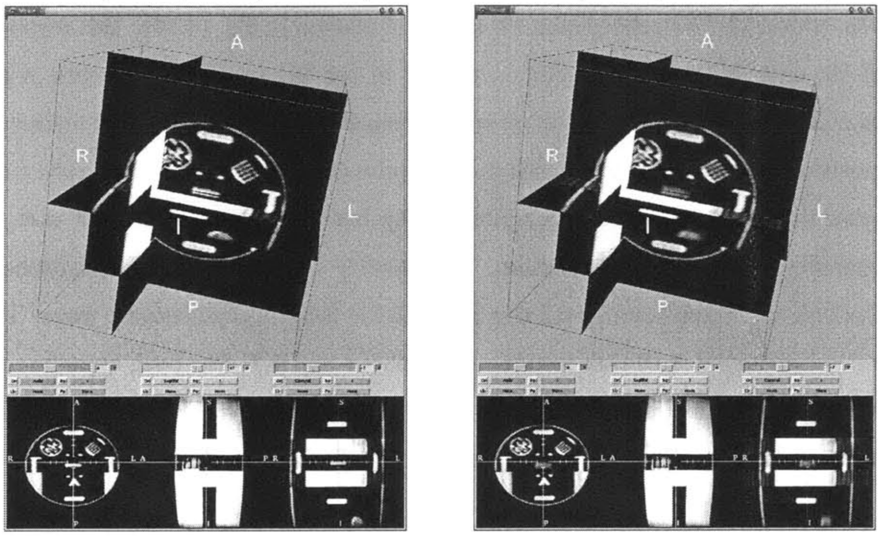
SVD (32 2D profiles, 128 TRs)

SVD (16 2D profiles, 64 TRs)

Figure 4-6: Various levels of compressed acquisition for 3D imaging at 64 × 128 × 256 resolution of a doped-water phantom using the 2D-Spatial Echo-Planar/1D-Fourier sequence of Fig. 4-5.1 and with the 64 × 128 RF train segmented 4-ways. From left to right, top to bottom: The 3D MRI cube acquired with the rows of the $(64 * 128) \times (64 * 128)$ identity matrix (i.e., phase encoding) in 8192 TRs and total imaging time of 27 min. Second, SVD encoded cube using the primary 64 of 256 SVD basis profiles, acquired in 256 TRs and 50 sec imaging time (speedups of 32x over SPGR/GRE and 4x over equivalently segmented EPI). Third, using 32 of the 256 SVD basis profiles in 128 TRs, and 25 sec imaging time (64x over GRE and 8x over EPI). Last, using 16 of the 256 SVD profiles in 64 TRs and 12.5 sec imaging time (128x over GRE and 16x over EPI).

change. For reference, a fully encoded system response, again with the identity matrix, was also obtained after the dynamic change. The imaging parameters for this experiment were 8 ms TE, 190 ms TR, 24 cm FOV, and 64 × 128 × 256 image cube resolution, using 8-way segmentation. As shown in Fig. 4-8, the change is clearly captured, albeit at a loss of resolution, even after truncation of one half the subspace dimensionality leading to 2x speedup over equivalent EPI imaging and 8x

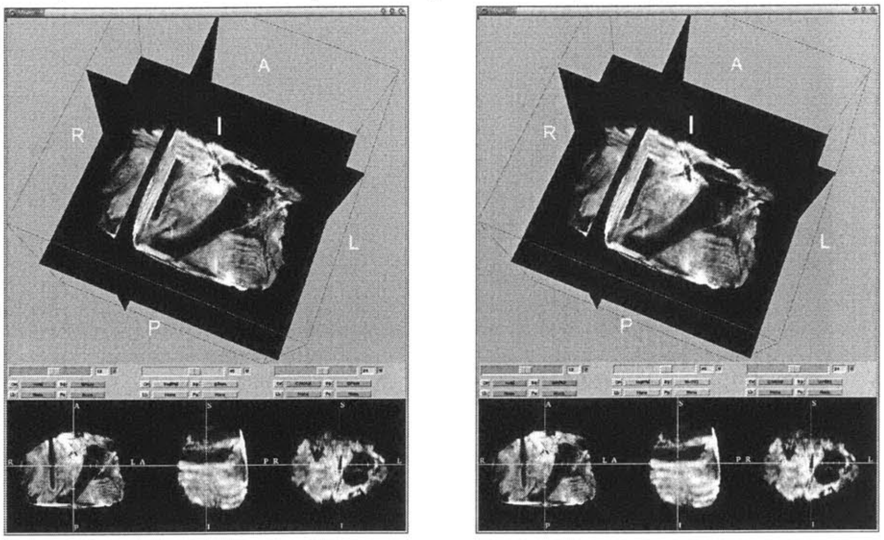
Fourier (64 $*$ 128 Phase encodes, 8192 TRs)

SVD (92 2D profiles, 736 TRs)

SVD (64 2D profiles, 256 TRs)

SVD (32 2D profiles, 256 TRs)

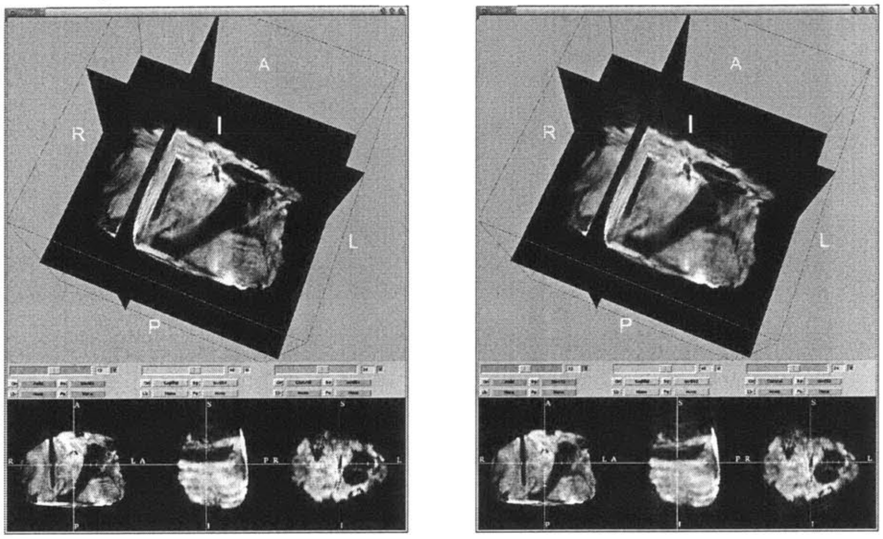

Figure 4-7: Various levels of compressed acquisition for 3D imaging at 32 × 256 × 256 resolution of animal phantom, with biopsy needle inserted, using the 2D-Spatial Echo-Planar/1D-Fourier sequence of Fig. 4-5.1 and with the 32 × 256 RF train segmented 8-ways. Left to right, top to bottom: 3D MRI cube acquired with the rows of the $(32*256) \times (32*256)$ identity matrix in 8192 TRs and total imaging time of 27 min. Second, SVD encoded cube, using the primary 92 SVD basis profiles in 736 TRs and 132 sec imaging time (11x over GRE and 2.7x over equivalently segmented EPI). Third, using 64 SVD basis profiles in 512 TRs, and 90 sec imaging time (16x over GRE and 4x over EPI). Last, using 32 SVD profiles in 256 TRs and 46 sec imaging time (32x over GRE and 8x over EPI).

over a 3D GRE Fourier encoded sequence. Although there is an associated loss of resolving power, the change in the FOV between the fully encoded and SVD encoded cubes was non-trivial, resulting in a large change between the two time frames.

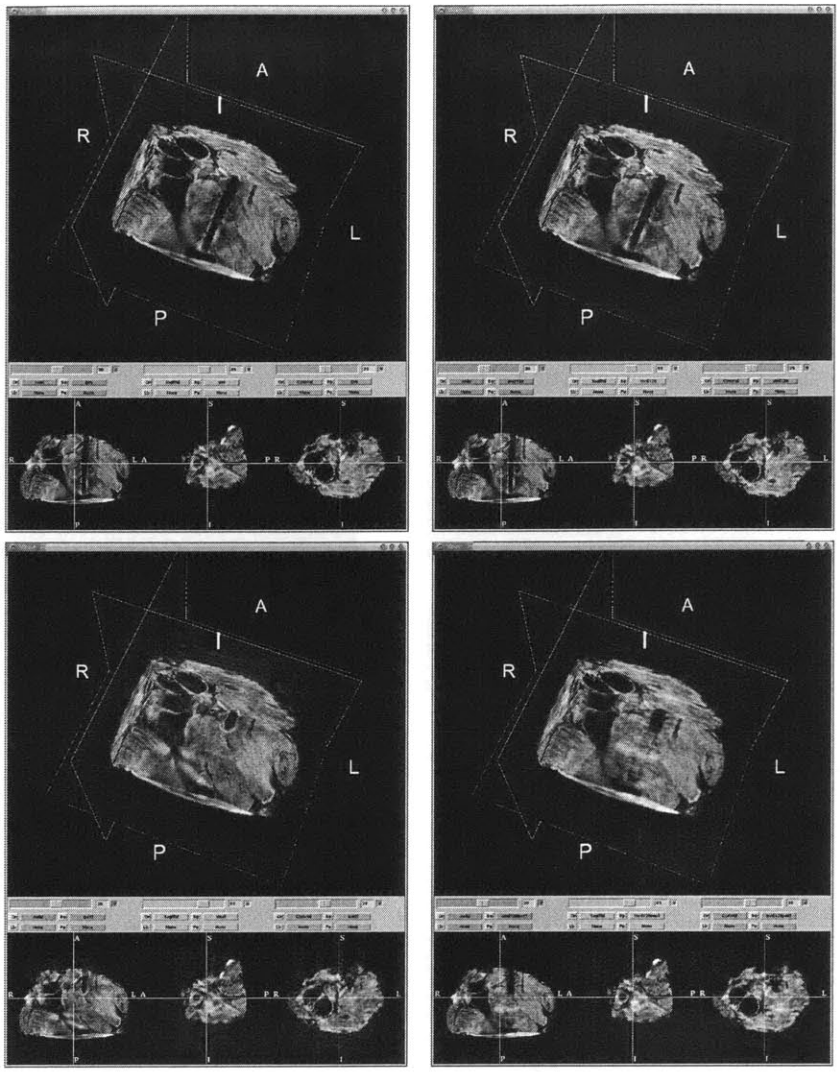

Figure 4-8: Animal tissue phantom 3D dynamic series compressed acquisition, with biopsy needle being removed, using the 2D-Spatial Echo-Planar/1D-Fourier sequence of Fig. 4-5.1. Left column, top row, obtained with the rows of the $(64 * 128) \times (64 * 128)$ identity matrix and the pulse sequence in Fig. 4-5.1, hence producing a fully phase encoded data set. A total of 8192 TRs and total imaging time of 26 min (equivalent to a standard 3D GRE or SPGR pulse sequence) were required. Left column bottom row, same as above, except imaged after the needle was partially removed. Right column, top row, SVD encoded cube using the primary 128 SVD basis profiles of the 256 total, computed from the fully encoded acquisition shown in the right column top row. The 128 profiles were segmented 8 ways, leading to 3 min imaging time (8x over GRE and 2x over an equivalently segmented EPI sequence). Right column, bottom row, using the same 128 SVD basis profiles, were computed to encode the cube prior to needle removal, i.e., same as used to acquire the cube above it, also obtained in 3 min imaging time but after needle was partially removed.

4.4 Pulse Sequences for 3D MRI II: The General Broadband System Response for Arbitrary k-space Trajectories

The general MR imaging problem can be stated as follows: a complete and sufficient set of k-space coefficients needs to be sampled in order to produce the desired FOV MR image. So far we have seen via the non-Fourier encoding principle that these k-space coefficients may be obtained partially via excitation, i.e., when the excitation is used for encoding in conjunction with a spatially selective gradient, and partially post-excitation i.e., via additional gradients used before and during acquisition. In this section we attempt to generalize this principle so that it may be applied to any arbitrary sets of excitation and acquisition k-space coefficients, and not limited to rectilinear trajectories that have so far been successfully used [117].

Spatially selective excitations offer improved MR signal acquisition efficiency by encoding a set of k-space coefficients using encoding bases other than the impulse response that leads to Fourier basis sampling. The information carried by the set of k-space coefficients chosen to be encoded via non-Fourier excitations can be compressed into fewer acquisitions. This is because the useful MR signal content of a given sample may have very small projections onto a subspace of the entire encoding space. Nonetheless, in order to non-Fourier encode these k-space coefficients, we must obviously use a k-space trajectory that visits them. Accordingly, with increasing complexity of excitations, such as the 2D excitations of the previous section, longer RF pulses are necessary which may limit the usefulness of the technique. For the echo-planar trajectories of the previous section we relied on segmentation which enabled us to trade trajectory complexity for increased imaging time. However, even a moderate resolution of 32-by-256 required 8 segments in order to yield acceptable imaging quality, reducing the possible benefit of non-Fourier imaging by a factor of 8. The simple extension of the non-Fourier principle that will be provided here will enable use of arbitrary k-space trajectories with our interest naturally turning to trajectories that can lead to reduced time for the coverage of the excitation or acquisition (or both) k-space coefficient locations.

Acquisition efficiency via maximizing the information carried by each signal acquisition is an optimization handled by non-Fourier encoding. This optimization reduces the number of necessary acquisitions. We now pursue the optimization of the actual acquisition of the signal regardless of the information carried. This will be especially useful for 3D MRI, and will enable further increasing the benefits of non-Fourier MR imaging.

4.4.1 The General Broadband System Response Model

When low flip angle RF excitations are used in conjunction with spatially selective encoding gradients, the RF induces a weighting of the spatial-frequency space. The RF pulse is applied over time, i.e., it is described by the function $p(t)$. The weighting induced by the RF pulse at some time t is implicitly dependent on the applied gradients, since [121]

$$\vec{k}_{exc}(t_{exc}) = \frac{\gamma}{2\pi}\int_{t_{exc}}^{T} \vec{G}_{exc}(t)dt, \tag{4.27}$$

with T the end of excitation gradient application. If this k-space trajectory is not self-intersecting, i.e., $\vec{k}_{exc}(t) = \vec{k}_{exc}(t')$ only if $t = t'$, the applied RF amplitude induces a weighting that is a function of the spatial-frequency trajectory, i.e., $p\left(\vec{k}_{exc}(t)\right) = p(t)$. The transformation from $p(t)$ to a spatial-frequency weighting function $p\left(\vec{k}\right)$ defined throughout k-space is straightforward given the traced k-space trajectory $\vec{k}_{exc}(t)$, [121]

$$p\left(\vec{k}\right) = \int_0^T p\left(\vec{k}_{exc}(t)\right) \vec{\delta}\left(\vec{k}_{exc}(t) - \vec{k}\right) \left(\left|\frac{d\vec{k}(t)}{dt}\right|\right) dt, \tag{4.28}$$

where $\vec{\delta}\left(\vec{k}\right)$ are Dirac delta functions used to represent the actual trajectory via a sampling function defined by their distribution. The derivative of the k-space trajectory, the k-space velocity $|d\vec{k}(t)/dt|$, is the weighting of the delta functions implied when they are not unit-spaced along the trajectory [121, 70].

Application of this spatial-frequency weighting function, describing the low-flip angle RF pulse, results in the excitation of a spatial profile that can then be expressed using Eq. (4.28) as a Fourier transform [121, 41]:

$$\tilde{p}\left(\vec{r}\right) = \alpha \int_K p\left(\vec{k}\right) \lambda\left(\vec{k}\right) e^{-i2\pi\vec{r}\cdot\vec{k}} d\vec{k}. \tag{4.29}$$

α is a weighting factor absorbing physical characteristics of the excitation system which we henceforth drop. $\lambda\left(\vec{k}_{exc}(t)\right)$ is a weighting factor resulting by the coordinate transformation from the traced k-space trajectory to the 3D k-space coordinate system. Alternatively, $\lambda\left(\vec{k}_{exc}(t)\right)$ is the weighting necessary for the sampling (delta) function distribution in the 3D k-space coordinate system [41, 70]. When the trajectory permits (by satisfying certain criteria) [131], the $\lambda\left(\vec{k}_{exc}(t)\right)$ factor is the absolute value of the Jacobian determinant of the transformation from the arbitrary k-space trajectory to the unit-spaced Cartesian grid. For convenience, this factor can also contain the inverse of the k-space trajectory velocity factor of Eq. (4.28). The point spread function implied in the Fourier integral of Eq. (4.29), when the k-space trajectory is discrete and of finite extent, is absorbed within the spatial frequency weighting function $p\left(\vec{k}\right)$, i.e., the delta function distribution of Eq. (4.28).

The analytical strength of the linear system of [117] is the replacement of Eq. (4.29) with a sum of Fourier coefficients, valid in the low-flip angle regime by treating the RF excitation as composed of a set of impulses that instantaneously flip magnetization, thus discretizing time (and hence k-space trajectory). We augment this approach with the k-space weighting factor, $\lambda\left(\vec{k}_{exc}(t)\right)$, so that Eq. (4.29) becomes

$$\tilde{p}\left(\vec{r}\right) = \sum_{k_e \in K_{exc}} p\left(\vec{k}_e\right) \lambda\left(\vec{k}_e\right) e^{-i2\pi\vec{r}\cdot\vec{k}_e}. \tag{4.30}$$

Because this is an approximation sum, there is no Jacobian; rather the factor $\lambda\left(\vec{k}_{exc}(t)\right)$ is a weight that enables Eq. (4.30) to minimize the difference to Eq. (4.29) [51, 123, 127].

As seen from the discretization of Eq. (4.30), the spatial excitation profile that is generated by application of the RF pulse described by Eq. (4.29), intrinsically implies a set of k-space coefficients. These coefficients, which are members of the set K_{exc}, are visited during the excitation trajectory and describe the excitation, i.e.,

$$K_{exc} = \left\{ \vec{k}_{exc}(t_j) \mid t_j = j\Delta t \right\}, \tag{4.31}$$

with time discretized at t_j, $1 \leq t_j \leq T$, $j = 1, \ldots, |K_{exc}|$, and $|K_{exc}|$ the cardinality of the set.

Following the spatially selective RF excitation, application of post-excitation gradients force the excited profile of magnetization to acquire additional encoding. Equivalently, the use of post-excitation gradients force the wavenumbers produced by the excitation to be modified in unison. The additional gradients applied from T until the readout time t_{acq} produce the k-space coefficients

$$\vec{k}_{acq}(t_{acq}) = \frac{\gamma}{2\pi} \int_{T}^{t_{acq}} \vec{G}_{acq}(t) dt. \tag{4.32}$$

We can form another set of traversed k-space locations for the acquisition trajectory,

$$K_{acq} = \left\{ \vec{k}_{acq}(t_n) \mid t_n = n\Delta t' \right\}, \tag{4.33}$$

by discretizing t_{acq} at $t_n = n\Delta t'$, $1 \leq n \leq N$ This is in any case necessary due to A/D conversion.

We now turn to the MR imaging equation. When the excitation is performed by the RF pulse described by $p(\vec{k}_e)$, $\vec{k}_e \in K_{exc}$, and the signal is acquired at the times t_a thus leading to the additional k-space offset $\vec{k}_a \in K_{acq}$, the resulting signal is

$$S\left(p\left(\vec{k}_e\right), \vec{k}_a\right) = \int_R \rho\left(\vec{r}\right) \tilde{p}(\vec{r}) e^{-i2\pi \vec{r}\cdot\vec{k}_a} d\vec{r}, \tag{4.34}$$

for a given spin density $\rho(x, y, z)$. It is the insertion of Eq. (4.30) into the general imaging Eq. (4.34),

$$\begin{aligned} S\left(p\left(\vec{k}_e\right), \vec{k}_a\right) &= \sum_{k_e \in K_{exc}} p\left(\vec{k}_e\right) \lambda\left(\vec{k}_e\right) \int_R \rho(\vec{r}) e^{-i2\pi\vec{r}\cdot\vec{k}_e} e^{-i2\pi\vec{r}\cdot\vec{k}_a} d\vec{r} \\ &= \sum_{k_e \in K_{exc}} p\left(\vec{k}_e\right) \lambda\left(\vec{k}_e\right) \int_R \rho(\vec{r}) e^{-i2\pi\vec{r}\cdot\left(\vec{k}_e + \vec{k}_a\right)} d\vec{r}, \end{aligned} \tag{4.35}$$

that enables us to combine excitation encoding and acquisition (i.e., post-excitation) encoding.

The sampled signal described by Eq. (4.35) is made up of an ensemble of modulations (of the transverse magnetization of the spin density), weighted by the entries in the RF pulse. The wavenumber of each modulation obtained is defined by the combinations of the $\vec{k}_e$ produced by the appropriate manipulation of the excitation, with each of the $\vec{k}_a$. In other words, we can acquire the linear impulse response of the MR system (equivalent to Fourier phase encoding) via special manipulation of the excitations (i.e., using "impulse excitations" for each delay). For example, assume we repeat the arbitrary MR imaging experiment described by Eq. (4.35), a number of times equal to $|K_{exc}|$. In each repetition of the experiment, we select a single spatial-frequency $\vec{k}_e^j$, $j = 1, \ldots, |K_{exc}|$ for which we let the RF excitation $p(\vec{k}_e^j) = 1/\lambda\left(\vec{k}_e^j\right)$, while setting all other RF pulse coefficients to zero. Inserting this resulting RF excitation $p(\vec{k}_e)$ into Eq. (4.35) produces a digitized signal that involves the set of k-space coefficients of the spin density at all spatial frequencies $\vec{k} = \vec{k}_e^j + \vec{k}_a$, $\forall \vec{k}_a \in K_{acq}$. That is, we obtain all the k-space coefficients along the post-excitation trajectory, but, offset by the initial excitation-induced offset $\vec{k}_e^j$ (that in previous sections corresponded simply to the jth impulse of the excitatory RF pulses).

If we gather the set of signals acquired after all such $|K_{exc}|$ sequence repetitions, we form the set of sampled k-space coefficients of the spin density

$$K = \left\{\vec{k}_e + \vec{k}_a \mid \vec{k}_e \in K_{exc}, \vec{k}_a \in K_{acq}\right\}, \tag{4.36}$$

thus forming the complete set of Fourier coefficients of the spin density, of size $|K| = |K_{exc}| \times |K_{acq}|$, and that are presumably necessary and sufficient to reconstruct the MR image of the sample.

For 3D imaging, the complete set of k-space coefficients that suffices to reconstruct the image for the desired FOV typically refers to the Cartesian set

$$K = \left\{(k_x, k_y, k_z)^T \mid k_x \in K_x, k_y \in K_y, k_z \in K_z\right\} \tag{4.37}$$

with

$$K_x = \{-K/2\Delta k_x, \cdots, K/2\Delta k_x\}, \tag{4.38}$$

$$K_y = \{-M/2\Delta k_y, \cdots, M/2\Delta k_y\}, \tag{4.39}$$

$$K_z = \{-N/2\Delta k_z, \cdots, N/2\Delta k_z\}. \tag{4.40}$$

In the previous section we used the sequence of Fig. 4-5.1 to traverse the combinations $\vec{k}_e = (k_x, k_y, 0)^T$, for all $k_x \in K_x$ and $k_y \in K_y$ via the 2D echo-planar trajectory of the spatial RF excitation, while K_z was traversed via the readout samples, thus completing the necessary set of coefficients through Eq. (4.36).

More generally, Eq. (4.35) enables us to use any arbitrary trajectory in excitation, and subsequently acquisition as well, in order to acquire the necessary samples to reconstruct the MR image. This MR imaging equation encompasses any desired separation of the necessary k-space coefficients, via the imaging pulse sequence, into an excitation and an acquisition set. The only requisite assumption made about the excitation trajectory is that it is not self-intersecting. Later in this section we show how this can be applied to the use of spiral trajectories [2, 160].

Before turning to that task, we show how the linear system impulse response described above can be used to perform general non-Fourier imaging. The linear system impulse response matrix can be assembled using Eq. (4.35). Instead of drawing the RF excitations from the rows of an identity matrix, general non-rectilinear trajectories require use of RF pulses drawn from the rows of the $|K_{exc}|$-by-$|K_{exc}|$ identity matrix. In this case the unit impulse of each row j is scaled by the appropriate weighting factor $\lambda\left(\vec{k}_e^j\right)$. Then, the resulting acquired impulse response matrix F is the $|K_{exc}|$-by-$|K_{acq}|$ matrix formed by placing the samples acquired after excitation with the jth row of the weighted identity matrix into the columns of the jth row of the system response matrix F. That is,

$$F_{j,l} = S((0,\cdots,1/\lambda\left(\vec{k}_e^j\right),\cdots,0)^T,\vec{k}_a^l). \tag{4.41}$$

The row index of the matrix F ranges the k-space parameters of the non-Fourier encoded dimensions while the column index ranges readout samples; one row of F is formed from all readout samples that correspond to a particular k-space parameter along the non-Fourier encoded dimension.

Segmentation of the desired excitation trajectory does not affect the generation of this matrix. Each segment produces a different set of rows of the impulse response matrix since each segment produces a different subset of K_{exc}, as we saw in the previous chapter. Similarly, segmenting the acquisition trajectory so that each subset of K_{acq} is acquired at a different sequence repetition does not affect filling the matrix either. Each acquisition segment would produce a different set of $\vec{k}_a$ for a single $\vec{k}_e^j$, and there are more columns of the matrix to fill, with each set of columns representing a different acquisition segment.

Phase encoding, i.e., producing the Fourier modes of the sample, is thus achieved by using the rows of a weighted identity matrix. The resulting system response matrix can then be used to describe the MR signal response to any arbitrary low-flip angle RF pulse. An arbitrary low flip angle RF excitation pulse produces arbitrary combinations of the Fourier modes of the sample, weighted by the values $p(\vec{k}_e)$. Following the linear combination of Fourier modes shown by the summation in Eq. (4.35), we define the arbitrary RF coefficient vector p',

$$p_j{}' = p_j/\lambda\left(\vec{k}_e^j\right) = p\left(\vec{k}_e^j\right)/\lambda\left(\vec{k}_e^j\right). \tag{4.42}$$

This multiplies the system response matrix F, leading to the familiar linear system $s = p'F$, with s the length-$|K_{acq}|$ output response samples, p' the length-$|K_{exc}|$ weighted input RF encoding vector and F the system response matrix defined by Eq. (4.41).

In summary, the weighted RF coefficient vector defined by Eq. (4.42) results in the same linear system representation as the 2D spin warp non-Fourier MR imaging experiment (c.f., Eq. (2.26)), except that it may be used with any arbitrary excitation k-space trajectory. The weighting factors along the trajectory are entirely defined by the density and velocity of the trajectory and can thus be applied to any desired RF encoding vector p to produce the vector p' that leads to the linear system response for any broadband non-Fourier imaging pulse sequence.

Given an encoding matrix P, the weighting may be applied to each of its rows to produce the weighted RF matrix P', whose rows may be used for experiment repetitions, leading to the matrix formulation of broadband non-Fourier MR imaging (c.f., Eqns. (2.27) and (2.28)). Another way to arrive at this result is by turning Eq. (4.35) into a matrix equation, similar to the matrix formulation of Eq. (2.27). We accomplish this by using a diagonal matrix, W in order to apply the weighting factors of Eq. (4.35),

$$W = \begin{bmatrix} \lambda\left(\vec{k}_e^1\right) & 0 & \cdots & 0 \\ 0 & \lambda\left(\vec{k}_e^2\right) & \ddots & \vdots \\ \vdots & \ddots & \ddots & 0 \\ 0 & \cdots & 0 & \lambda\left(\vec{k}_e^{|K_{exc}|}\right) \end{bmatrix} \tag{4.43}$$

so that a new form of Eq. (2.27) is obtained:

$$S = PWF. \tag{4.44}$$

Equation (4.44) describes the general system response of Eq. (4.35). Its practical value is that the linear encoding model of [117], i.e., Eq. (2.27), is no longer limited to rectilinear trajectories.

To return to the simple formulation of Eq. (2.27), the weighting factors are eliminated by using the matrix

$$P' = P\left\{W^{-1}\right\} \tag{4.45}$$

as RF excitations. Substituting the RF encoding matrix P' defined by Eq. (4.45), in place of the encoding matrix P of the general linear system of Eq. (4.44), we see that the subspace spanned by the matrix P must be chosen appropriately to encode the contents of F. That is, matrix factorization techniques [32] can be applied to approximate the generalized system response matrix of the sample, F, given by Eq. (4.41). The resulting encoding vectors must then be weighted according to Eq. (4.45) in order to produce the actual RF excitations.

In order to fully encode a 3D volume when either the excitation or the acquisition encoding k-space coefficient set, i.e., K_{exc} or K_{acq}, is formed by delta functions placed along an arbitrary k-space trajectory, the other set must span the remainder necessary k-space coefficients. This ensures that all k-space locations for the desired FOV and resolution are accounted for. Another way to formulate this is via the point spread function (PSF) of Eq. (4.35). We require that the PSF's aliasing sidelobes are outside the FOV. This means that the ensemble of $\vec{k}_e + \vec{k}_a$ in Eq. (4.36) are sufficiently densely distributed in k-space. In terms of resolution, the requirement is that they extend sufficiently to the edges of the coordinate system to produce the necessary resolution.

In the previous section, the 2D echo-planar trajectory was rectilinear which produced k-space coefficients on a unit spaced grid defined by Eqns. (4.38)–(4.40). This allowed the straightforward application of the discrete Fourier transform to obtain the image. When the set of coefficients is sampled at the non-unit-spaced k-space locations along an arbitrary trajectory, a direct summation of the gathered Fourier coefficients can produce the image (convolved with the inherent PSF of the sampling function, i.e., the distribution of Eq. (4.36)) [131]:

$$\rho(\vec{r}) = \sum_{l=1}^{|K_{acq}|} \sum_{j=1}^{|K_{exc}|} F_{j,l} \frac{1}{\lambda_a\left(\vec{k}_a^l\right)} e^{i2\pi\vec{r}\cdot\left(\vec{k}_e^j+\vec{k}_a^l\right)}, \tag{4.46}$$

where the weighting factor $1/\lambda_a\left(\vec{k}_a^l\right)$ is necessary for arbitrary sampling trajectories, similar to the weighting factor used in Eq. (4.29), although the latter has been absorbed in $F_{j,l}$ (as seen by inserting Eq. (4.35) into Eq. (4.41)). Performing this direct summation for typical trajectories is prohibitive in computational cost. An arbitrary 2D trajectory that can yield a N-by-N resolution will most likely be composed of approximately N^2 samples. If N such 2D trajectories are acquired (to span the orthogonal dimension) to yield a 3D image of N-by-N-by-N resolution, Eq. (4.46) must be evaluated N^3 times (once for each pixel $\vec{r}$). Since each evaluation requires N^3 operations, this yields an $O(N^6)$ reconstruction process.

One popular alternative is to interpolate the non-uniform samples onto a unit-spaced grid, using an intermediate convolution kernel, and then applying the typical FFT on the interpolated coefficients [57, 134]. A commonly used well-behaved convolution function is the Kaiser-Bessel window [134], based on a zeroth order modified Bessel function of the first kind. Newer methods, termed NUFFTs (for non-uniform FFTs) rely on computing an interpolation function for the given trajectory, an error metric, and associated approximation criterion [132, 28]. These methods rely on the fact that the Fourier coefficients of the function on the arbitrary k-space trajectory are non-uniformly spaced, but the coefficients at these non-uniform wavenumber locations may be approximated by interpolating the coefficients of an appropriately weighted function at neighboring uniformly-spaced wavenumbers. This allows the use of the efficient FFT at a finer grid of a weighted (scaled) version of the function [28]. Griding interpolation reconstruction is fast but makes no guarantee about the reconstruction error, which depends on the ad-hoc choice of convolution function. In contrast, NUFFT approaches aim to choose the interpolator in order to bound this error.

Regardless of how the image reconstruction of Eq. (4.46) is performed, the two weighting factors, $\lambda_e\left(\vec{k}_e^j\right)$, $j = 1,\ldots,|K_{exc}|$ and $\lambda_a\left(\vec{k}_a^l\right)$, $l = 1,\ldots,|K_{acq}|$ must be chosen. The former is applied directly onto the excitation, prior to signal acquisition (as shown in Eqns. (4.41) and (4.45)), while the latter needs to be applied prior to griding or NUFFT reconstruction.

As already mentioned, when the corresponding trajectory (i.e., excitation or acquisition) satisfies certain criteria [131], the weighting factors are the Jacobian of the transformation of the corresponding k-space trajectory coordinate system, i.e., the coordinate system in which the trajectory is intrinsically unit-spaced, onto a unit-spaced Cartesian grid. This Jacobian gives the ratio of the elementary 3-dimensional volumes in the two coordinate systems. When either trajectory does not allow this transformation, and analytic weighting factors can not be obtained, the corresponding weighting factor can be estimated by various numerical methods.

The weighting function is ideally chosen so that the approximation sums (of Eqns. (4.30) and (4.46) respectively) yield an image (or excited profile) that is the best approximation to the "true" image (profile). This is equivalent to saying that the PSF (i.e., the reconstruction of Eq. (4.46) when all samples $F_{j,l}$ are 1) must be as close to a delta function as possible. The point spread function of the trajectory is simply the approximation sum of the complex exponentials weighted by the $\lambda_{\{a,e\}}(\cdot)$ factors (i.e., if for an acquisition trajectory the MR sample was a delta function, or, for an excitation trajectory the spatial excitation was a delta function so that in either case the Fourier coefficients are unit everywhere).

Regarding gridding reconstruction, the convolution kernel together with the weight function should produce the desired image, which typically refers to an image with the point spread of the Cartesian grid sampling. This has been exploited in [57] by choosing the weighting function in order to effectively normalize the area of the convolution kernel at each point throughout the sampling function describing the trajectory. This is an attempt to force the convolution of the sampling function with the convolution kernel to be close to an impulse. This choice can be further refined via an iterative procedure [123]. Other methods to obtain the weighting function include directly equating the point spread function of the Cartesian grid with that of the arbitrary trajectory and requiring that the two be the same [127], or, returning to the Jacobian, since it intrinsically defines volume ratios, another approach to estimate the weight is by assigning a volume element to each delta function of the sampling function of the trajectory and using its inverse as the weight. One natural choice of method to separate k-space into volumes surrounding the discrete k-space sampling locations of the trajectory is by using the Voronoi tessellation [124, 129]. In any case, weighting functions are necessary in order to correct for the non-uniform sampling locations of the trajectories, and must be applied in order to ameliorate the effective point spread function of the imaging sequence.

4.4.2 Spiral Echo-Planar Trajectories

In this section we will concentrate on the special cases where either the set of locations K_{exc}, or K_{acq}, are drawn from a 2D spiral trajectory [2, 160], in an attempt to optimize the traversal of the 3D k-space in addition to optimizing the MR signal sampling efficiency via non-Fourier encoding. Spirals minimize the time required to traverse a 2D trajectory by optimizing the gradient subsystem usage. This translates to maximizing either the slew rate (i.e., the rate of change of the gradient) or the gradient magnitude at any one location along the trajectory. Typical slew rates of commercial MRI systems range from 2 Gauss/cm/msec to 15 Gauss/cm/msec. These are the two main gradient hardware limitations, although slew rate is also constrained by physical safety.

An Archimidean spiral k-space trajectory, $k(t) = k_x + ik_y$, is given by [160, 31]

$$k(t) = \frac{N_{int}}{\text{FOV}}\theta(t)e^{i\theta(t)}, \tag{4.47}$$

where N_{int} is the number of spiral arm interleaves, i.e., segments, FOV is the desired field-of-view, and $\theta(t)$ is the azimuthal function of time, whose choice allows the constraints optimization. Given the spiral arm defined by Eq. (4.47), each of the N_{int} segments can be formed as

$$k^{(q)}(t) = k(t)e^{i2\pi q/N_{int}}, \tag{4.48}$$

for $q = 1, \ldots, N_{int}$.

An example spiral trajectory designed for a single spiral arm (i.e., $N_{int} = 1$) is shown in Fig. 4-9.1, while the gradients necessary to produce it, and the resulting slew rates, are shown in Fig. 4-9.2. To a first approximation (i.e., modulo off-resonance and relaxation effects) the same k-space trajectory can be accomplished using a 3-way segmented spiral trajectory: the k-space trajectory traced by each of the 3 spiral arms (shown in Fig. 4-10) is individually designed to maximize the gradient usage, while the ensemble of the 3 arms forms the composite trajectory, shown in Fig. 4-11, which is nearly equivalent to the single-shot trajectory of Fig. 4-9.1.

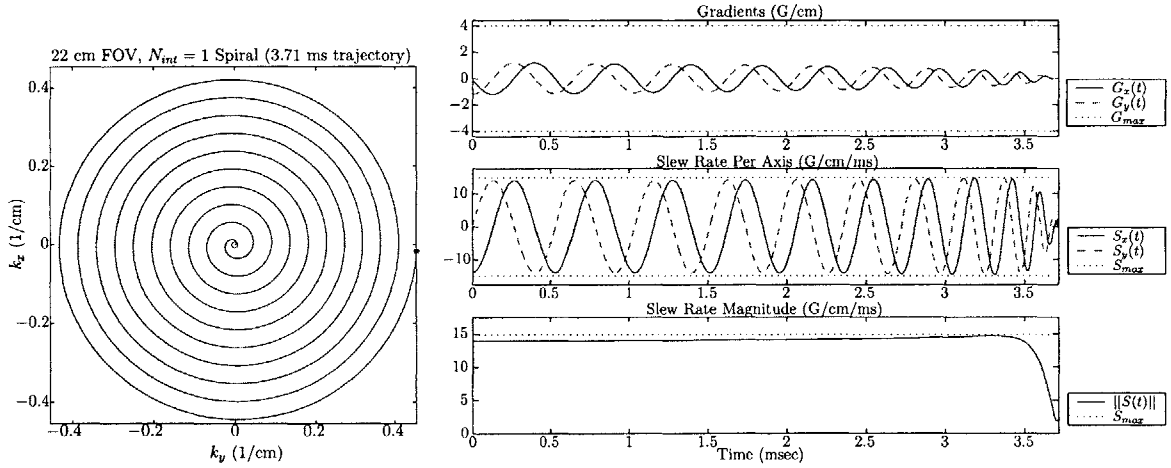

4-9.1: 2D Spiral trajectory

4-9.2: Gradients that produce trajectory and resulting slew rates

Figure 4-9: Left: Single-arm spiral k-space trajectory for 22 cm FOV, $N_{int} = 3$ and $0 \leq \theta(t) \leq 20\pi$. Right: gradient waveforms that generate this trajectory and resulting slew rates. The gradient hardware limits of our system are shown by dashed lines where appropriate. With these limits the trajectory requires 3.71 ms.

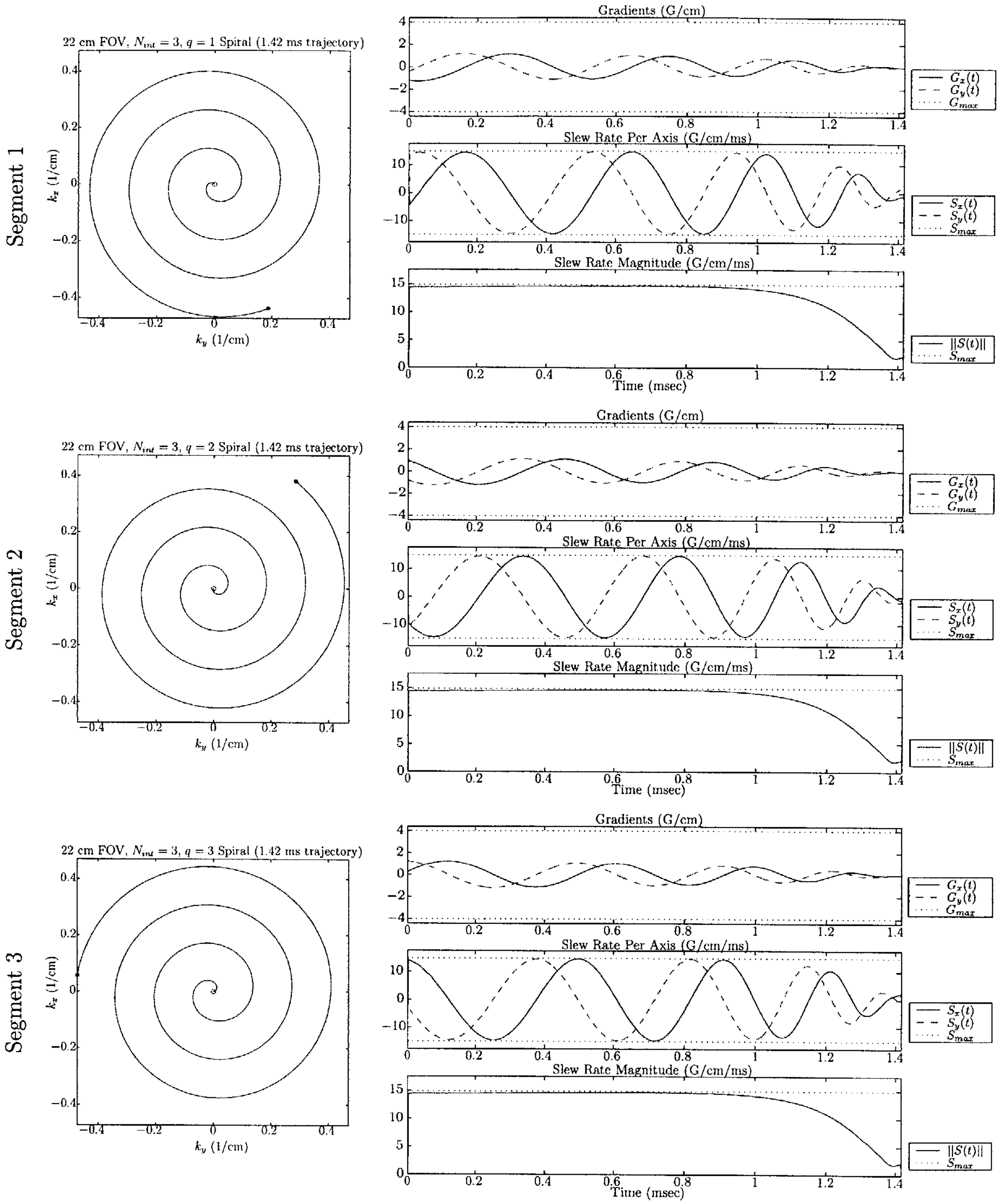

Figure 4-10: Left column: Spiral arm interleaves for a 3-way segmented spiral. 22 cm FOV, $N_{int} = 3$ and $0 \leq \theta(t) \leq 20\pi$. Right column: gradients to generate the respective k-space trajectory and slew rates required by these gradient waveforms. Traversal of each arm requires 1.42 ms to remain within gradient hardware constraints.

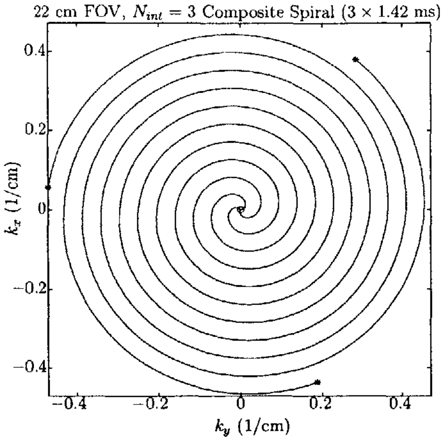

Figure 4-11: Composite k-space trajectory of the 3-arm spiral, formed by combining the trajectories of the 3 arms shown in Fig. 4-10.

In order to minimize the time required to cover a spiral arm, one must maximize either the gradient strength, given by the derivative of the trajectory (c.f., Eq. (4.47)), or the gradient slew rate (that is the rate of change of the gradient strength), given by the derivative of the gradient strength. An analytical solution for the azimuthal function that fulfills these requirements is available everywhere except near the center of the trajectory (i.e., near $t = 0$) where it is only near optimal [31]. This solution was used to generate the trajectories of Figs. 4-9 and 4-11.

The trajectories shown in Figs. 4-9 and 4-11 are examples of reversed spirals [5], obtained by reversing the time parameter of the azimuthal function in Eq. (4.47), i.e., letting $k'(t) = k(T - t)$. These can replace the 2D Cartesian echo-planar trajectory of the previous section (in sequence of Fig. 4-5.1) in order to perform the 2D excitations. This modification is shown in the pulse sequence of Fig. 4-12. With these reversed trajectories, the center of the excitation k-space, which typically carries the bulk power of the Fourier coefficients, is traversed at the end of excitation, just prior to response acquisition, thus enabling shorter echo times in addition to reduced trajectory traversal time as compared to Cartesian echo-planar trajectories.

In Fig. 4-12, the 2D spatially selective RF pulse excites the 2D profile by traversing an x–y spiral trajectory. The resulting spatially selective (that is, spatially varying along the x–y plane) profile of magnetization is equally excited along the third dimension (i.e., z). The response of the profile along z then needs to be acquired, which can be accomplished by Fourier encoding the signal along this third orthogonal dimension during readout. Each impulse in the RF pulse is associated with a corresponding k-space location $\vec{k}_e = (k_x, k_y, 0)^T$, as shown in Figs. 4-9 and 4-11, while frequency encoding traverses the k-space locations along $\vec{k}_a = (0, 0, k_z)^T$, thereby relating the sequence of Fig. 4-12 to the formation of the spin density's Fourier coefficient set according to Eq. (4.36).

4.4.3 1D-Spatial/2D-Fourier Spiral Echo-Planar Sequence

If either the excitation or the acquisition k-space coefficient set is drawn from the spiral, then the other set will have to encode, or, span, the orthogonal dimension. In the example of Fig. 4-12, the

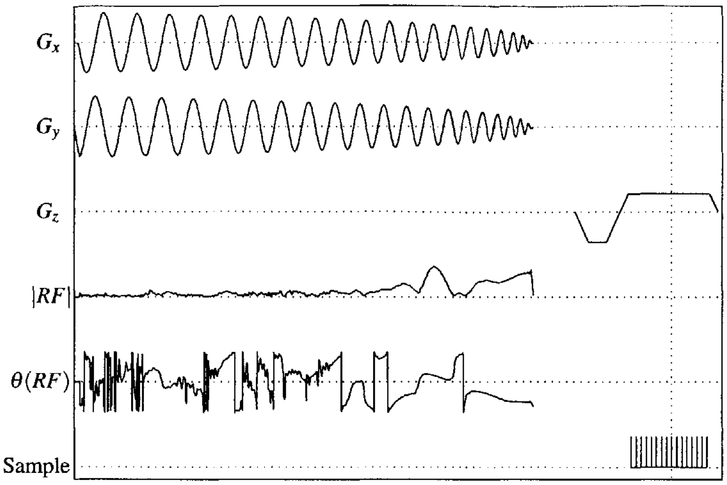

Figure 4-12: The 2D spatial excitation used for 3D imaging in Section 4.3 is performed here along a reversed spiral trajectory thus reducing the necessary time for the excitation compared to the echo-planar trajectory used in Section 4.3.

spiral is used for excitation, with the other dimension Fourier encoded. In the sequence shown in Fig. 4-13, the situation is reversed, with the spiral used in acquisition and a 1D spatial excitation used to encode the orthogonal dimension. We have already examined an example of 2D-Spatial/1D-Fourier imaging in Section 4.3 with the Cartesian echo-planar trajectory. Here, we consider the more immediately useful 1D-Spatial/2D-Fourier encoding example.

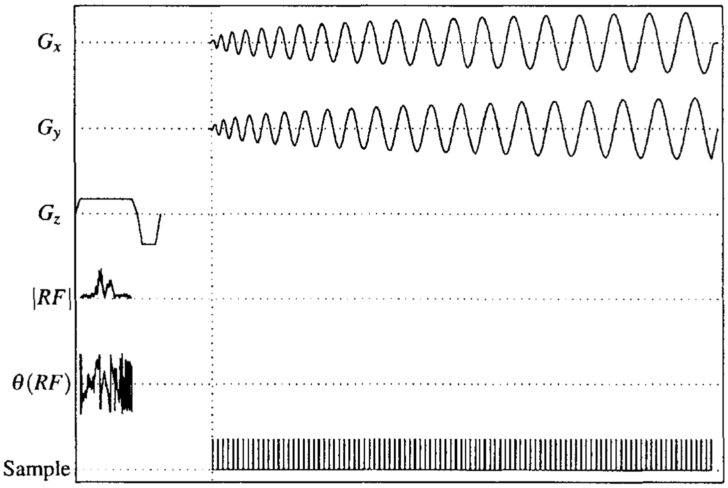

Figure 4-13: This sequence employs a 2D spiral trajectory in acquisition, leaving the remaining dimension to be covered via the excitation trajectory in order to produce the full set of coefficients necessary to reconstruct a 3D MR image.

Compressed broadband non-Fourier encoding with either the sequence of Fig. 4-12 or of Fig. 4-13 follows the same basic principle as emphasized previously, that is, only the spatial profiles that have maximal response need to be excited (and their response acquired) in order to produce a good approximation to the contents of the FOV. However, this principle leads to two very different methods and thus properties for each of the two sequences shown in Figures 4-12 and 4-13.

For the sequence of Fig. 4-12, since there are only N locations along z, at most N 2D spatial excitation profiles $p(x, y)$ are necessary to describe any given MR sample. The system response matrix F is tall and narrow; $|K_{exc}|$ covers two spatial dimensions and is of the order of KM, while $|K_{acq}|$ covers one dimension. More explicitly, each row of F corresponds to a single choice of $(k_x, k_y, 0)^T$, and each column corresponds to each readout sample along $(0, 0, k_z)^T$. The rank of that matrix may be at most N, allowing it to be efficiently encoded with fewer than $N_{int}N$ excitations for an N_{int}-way segmented spiral. The columns of F in this case belong to $\mathbb{C}^{KM}$ so that the N profiles necessary are overly restricted within this large space. To describe any unknown MR sample, KM excitations are needed to fully span the column space. This number of excitations are needed even for an N_{int}-way segmented excitation, since each excitation segment would be of length KM/N_{int}, which means that the sub matrix of F corresponding to each segment only needs KM/N_{int} vectors to be fully encoded, thus leading to the total KM excitations that cover the full KM dimensionality. A simpler way to understand this is that each of the rows of the KM-by-KM weighted identity matrix need not be excited a total of N_{int} times, since the impulse in each row of it would only be included in one of the N_{int} segments!.

In comparison, for the sequence of Fig. 4-13, the non-Fourier dimension spans $\mathbb{C}^N$, since the 2D spiral is traversed during signal acquisition, and z is non-Fourier encoded via a 1D spatial excitation. The system response matrix F now contains a row for each $(0, 0, k_z)^T$, while the columns contain the KM samples along $(k_x, k_y, 0)^T$ that lie on the spiral. This matrix, short and wide can also be very efficiently encoded, with fewer than $N_{int}N$ excitations for an N_{int}-way segmented spiral acquisition. Caution is necessary here since unlike the previous example, each portion of F that corresponds to a readout segment only forms a set of columns of F, not rows. And since each such subset of columns needs to be separately acquired and has columns belonging to $\mathbb{C}^N$, N excitations are needed to encode it, leading to $N_{int}N$ excitations necessary to obtain all the segments! However, in comparison to the previous example, any MR sample can be fully described with N different excitation vectors over $N_{int}N$ repetitions.

4.4.4 3D Dynamic Imaging Experiments: Fourier vs. Prospective Broadband Compression

Armed with the MR system response for arbitrary trajectories, such as spirals, enabled by Eq. (4.44), and the understanding of the encoding and reconstruction procedures necessary, we now turn to applying the sequence of Fig. 4-13 to perform fast, prospectively compressed broadband encoding for 3D MR imaging.

Equipment

All experiments were performed using the 1D spatial/2D Spiral echo-planar gradient recalled echo sequence of Fig. 4-13, operating on a 1.5T GE Signa LX EchoSpeed MR scanner (GE Medical Systems, Milwaukee, WI). For all acquisitions TR was 60 msec and the spiral acquisition was designed to produce a 256-by-256 resolution over the desired FOV, segmented into $N_{int} = 8$ spiral arm interleaves. Traversal of each spiral arm required approximately 26 msec, limited by the 4 G/cm gradients at 14.9 G/cm/msec maximum slew rate of the scanner, and generated approximately 6500 samples. Accordingly, $|K_{acq}| \approx 8 \times 6500$. In both dynamic experiments, the spiral acquisition ranged the A/P and R/L axes, while the S/I axis was non-Fourier encoded at a resolution of $|K_{exc}| = 128$.

Encoding

Acquisition of each time frame involved imaging the sample twice, once using a Fourier encoded "stack of spirals" and once using non-Fourier encoding. A "stack of spirals" refers to a k-space stack of spirals, so that each spiral acquired corresponds to a single k_z mode, i.e., each spiral corresponds to a single Fourier phase encode along z. No information was shared between the two acquisitions; the Fourier sequence was acquired to assess the imaging quality of the non-Fourier encoding method.

The non-Fourier encoding imaging cycle consisted of using a small set of encoding vectors to sample the system response matrix F_i at each time frame t_i, except the first time frame ($i = 0$), which was acquired by using the full $|K_{exc}|$-by-$|K_{exc}|$ Hadamard basis (c.f., Eq. (2.29)). This produced the estimate of the initial system response matrix, F_0, of size $|K_{exc}|$-by-$|K_{acq}|$. For $i > 0$, the encoding basis was formed by taking the SVD of the estimate of the system response matrix formed at the previous time frame, i.e., P_i was formed from the top rows of U^H, with U computed from $P_{i-1}^H \{P_{i-1}F_{i-1}\} := U\Sigma V^H$. Because the contents of the FOV at time t_i are expected to be similar to the contents at the previous time step, F_{i-1}, the basis that is best fit for encoding F_{i-1} is likely close to best fit for F_i. The acquired rank-reduced ($i > 0$) data, $S_i = P_iF_i$, was then used to produce the rank-reduced approximation to F_i, $\tilde{F}_i = P_i^H S_i$ which as described was then used to provide the encoding matrix P_{i+1} to be used for the next acquisition.

Once the encoding matrix P_i for each time frame was computed (a 2–3 sec operation), a change was made to the contents of the FOV. The encoding vectors (computed prior to the change) were then used to acquire the new, changed FOV time frame t_{i+1}. The stack of spirals was also acquired at that time to provide a "ground truth" 3D image of F_{i+1}, before continuing on to the next time frame's non-Fourier imaging cycle.

Noise Estimation From $k_a(0)$ Samples

When using a segmented spiral acquisition, such as the trajectory shown in Fig. 4-11, the center of the 2D k-space trajectory (k_a^0 for which $k_x = k_y = 0$ in this case) is sampled by every interleave. This enables a direct estimation of the noise that can be used for controlling the rank of the approximation of the system response matrix, i.e., to control the number of rows of the encoding matrix P_i, as discussed in Section 3.1. In particular, for each and any arbitrary spatial RF excitation, the resulting transverse magnetization is acquired at k_a^0 by each spiral arm. This results in N_{int} independent samples of the same profile of magnetization at the same k-space location, since the excitation preceding the acquisition of each of the N_{int} arms is the same. Therefore, any difference in the signal observed at that k-space sample over the N_{int} independent acquisitions is principally due to noise (assuming sufficient suppression of stimulated and indirect echoes by spoiling). This allows a direct estimation of its properties, and in particular, the standard deviation. When multiple different spatially selective RF excitations are performed, the deviations computed for each can be averaged to increase the confidence of the estimation.

3D Image Reconstruction

Once the rank-reduced approximation of the system response matrix $\tilde{F}_i$ (or the full phase encoded stack of spiral matrix F_i) for each time frame t_i was available, the 3D image was reconstructed in a number of steps. First, since in this case the set K_{exc} was drawn from a uniformly sampled 1D trajectory, the FFT was applied along the row dimension of $\tilde{F}_i$.

Each row of this resulting matrix then represented the samples gathered by all the arms of the 2D spiral readout trajectory at each location z in physical space. To reconstruct the spiral data for each of these slices along z, the weighting factors $\lambda\left(\vec{k}_a^l\right)$ were computed using the Voronoi tessellation [129] of the composite trajectory formed by the ensemble of spiral arms, as shown in Fig. 4-11. This weighting function was then applied to the spiral samples for each slice. Finally, the NUFFT algorithm [28] was used to produce the image planes of the slices. This final NUFFT step was actually applied a number of times, as we now describe, in order to apply magnetic field inhomogeneity corrections that are central to MR image quality when using time-varying gradients.

Field Map Generation & Multi-Frequency Field Corrections

When using time-varying gradients, such as those necessary for spiral trajectories, off-resonance effects cause blurring of the reconstructed images [108, 81]. By constructing a spatial map of the local resonance, it is possible to perform a reconstruction of the acquired image with reduced blurring. Off-resonance is caused by many factors. These include main magnetic field inhomogeneities, tissue-induced susceptibility differences, chemical shift (i.e., the shift between fat and water), eddy currents [1] and concomitant fields [62].

In general, off-resonance effects appear as an additional location-dependent phase term in the signal equation that evolves in time. Off-resonance effects correction involves first acquiring a local resonance frequency map. This is typically done by acquiring separate images at two different echo times. The difference in phase between the images yields the off-resonance frequency at each location in space. Naturally, only those off-resonance factors that affect the phase with an echo time dependence are detected by this method. Concomitant fields in particular are independent of echo time, as they only depend on the magnitude of the applied gradients. However, their contribution to the magnetic field can be analytically expressed [62] and can be added to the off-resonance frequency map.

Once an off-resonance map has been constructed, conjugate phase reconstruction can be used. Conjugate phase involves reconstructing each pixel separately, as in the example of Eq. (4.46). Because the off-resonance frequency for each pixel is known and since its effect is a phase induced by the off-resonance, which depends on the time of each sample's acquisition multiplied by the off-resonance, each of the samples acquired over the sampling time can be multiplied by a conjugate phase factor.

However, because of the computational cost of pixel-by-pixel reconstruction, other methods have been devised. These methods include approximation of the field map with a linear function. This results only in a redefinition of the k-space trajectory (and a base off-resonance frequency demodulation) [56]. More involved methods perform time [108], or frequency [81] segmented conjugate phase reconstructions.

Here we use multifrequency segmented reconstruction, which involves separating the off-resonance frequencies into bins, and approximating all frequencies in each bin by a single frequency (the central one). Then we reconstruct each plane once for the frequency of each bin, and draw the final pixel values at each location in the plane from the reconstruction pertaining to the bin that the off-resonance for that pixel is nearest.

Results

In the first experiment, a cylindrical doped water phantom was placed with its long axis along S/I. In between each non-Fourier 3D imaging time frame, t_i, the phantom was rotated approximately 3° about the R/L axis, thus maximally changing the axial plane contents. In particular this change of FOV contents enforces the maximal change along the non-Fourier encoded dimension (e.g., consider a purely unit-valued parallelepiped with its long axis parallel to S/I – the rotation about R/L changes the SVD expansion from a single non-zero singular value to a larger dimensionality).

The FOV was 16 cm (R/L) × 16 cm (A/P) × 27 cm (S/I). Each non-Fourier encoded time frame except the first was acquired and reconstructed using 42 encoding vectors. That is, the encoding matrix P_i was 42-by-128. For the desired resolution of 128 along the non-Fourier encoded dimension, the first time frame that was fully encoded with the Hadamard matrix resulted in the 128-by-128 encoding matrix P_0 derived from H_{128} from Eq. (2.29). Each Fourier encoded stack of spirals also required 128 phase encodes. Accordingly, imaging time per time frame was 20 sec for each non-Fourier time frame except the first (8 interleaves per encode, 42 encodes) and 61 sec for the stack of spirals and first non-Fourier encoded time frame.

To put these imaging times in perspective, a 2D or 3D steady state acquisition at equivalent resolution, with the minimum TR of 2.6 msec that is the current limit on our system, would have required 85 sec. Effectively, the SVD encoded time frames were acquired at a speedup of 3 over a fully phase encoded stack of spirals and a speedup of 4.25 over an SSFP sequence.

The reconstructed sequence of 9 3D image frames acquired by each method (non-Fourier and Fourier stack of spirals) is shown in Figures 4-14–4-16. The same image planes are shown in all figures (Axial plane at S 14 mm, Sagittal at L 20 mm and Coronal at A 4 mm). All observed change is due entirely to movement of the sample in the FOV. Three-plane cuts for each reconstructed volume of time frames t_1 and t_4 are shown in Fig. 4-17 for close comparison of the Fourier and adaptive non-Fourier encoding methods. We note the shifting of the doped water to fill empty volumes as indicated by the arrows in Fig. 4-17, as well as the signal void caused in the A–I corner of the phantom due to the air bubble shifting to the top of the phantom. This change is successfully observed in the 3-fold accelerated non-Fourier acquisition as surely as it is observed in the fully encoded Fourier acquisition. If instead we had "accelerated" the Fourier acquisition by using only 42 Fourier phase encodes to acquire the image cube, the resulting 6.4 mm image resolution along S/I would have been insufficient to entirely observe the detail.

The suitability of non-Fourier encoding for this dynamic imaging example task is not surprising; using the noise estimation to separate the subspace spanned by the system response matrix into projections onto a significant and an insignificant subspace, we find that ≈ 20 SVD encoding vectors contain all relevant image information, i.e., more significant than the noise component, yet between 110–80 phase encodes and nearly all 127 Hadamard encodes are necessary to capture the relevant information, as shown by the plots in Fig. 4-18 for the two time frames examined in Fig. 4-17.

In the second experiment, a hand phantom (glove filled with gel) was moved toward an animal tissue phantom and subsequently a 22G biopsy needle was inserted and removed from the tissue. The hand was finally completely removed from the FOV. All parameters were as in the previous experiment, except a 22 cm (A/P) × 22 cm (R/L) × 27 cm (S/I) FOV was used, and the SVD encoded non-Fourier time frames used 64 encoding vectors instead of 42. Accordingly, imaging times were the same as stated for the previous experiment for the Fourier stack of spirals and initial Hadamard non-Fourier encoded frames, but was 30.7 sec for the SVD-compressed time frames.

The imaging series of 15 time frames is shown in Figures 4-19–4-22. Again, the same planes are shown in all figures (Axial plane at S 42 mm , Sagittal at L 12 mm and Coronal at A 8 mm) so that all change observed is entirely due to the changes occurring in the FOV. Detail of this change is shown in three-plane cuts of the reconstructed frames at t_1, t_9 and t_{15} in Fig. 4-24. All change observed in the Fourier encoded frames is also captured rather nicely by the 2x-accelerated non-Fourier acquisition (see e.g., the detail pointed at by the arrows). However, some loss of resolution is observed along the S/I axis of the non-Fourier reconstructions compared to the Fourier encoded stack of spirals.

This loss of resolution is easy to assess by looking at the projections of the system response matrix (acquired by the Fourier phase encoded stack of spiral acquisitions) onto the respective encoding bases, which is presented in Fig. 4-25 for the three time frames of Fig. 4-24. In particular, for the Fourier basis (and even for the Hadamard basis) all 128 basis functions are necessary since their respective response is above the level of noise. In fact, extrapolating the slow fall-off of the tails of the response functions on both ends of the graph, we see that if we were to increase the S/I resolution beyond 128, the response would still be more significant than the noise component for significantly more basis functions.

On the other hand, the SVD basis functions fall below the level of noise past about the 95th SVD basis function. The acquisition subspace was truncated to the first 64 basis functions, compressing the MR signal content beyond the insignificant information in this case. This leads to the loss of resolution. Naturally, the amount of compression that can be applied is intrinsically related to the information of interest. In this case, all the dynamic change is captured with the rank-64 acquisition, and since this is the information of interest, it justifies the additional amount of compression.

Another interesting point evoked by the response functions plotted in Fig. 4-25 is that the (broad) knee of the L-curve of the singular values does indeed occur at the level of noise. However this noise component was calculated independently by the method outlined above, based only on the multiple acquisitions of the center of k-space by the spiral arms. This further suggests the usefulness of using the noise component to guide the otherwise "blind" compression efficiency, as was presented in Section 3.1. In an adaptive acquisition, by estimating the noise statistic via multiple acquisitions of a given k-space location in the acquisition trajectory during sequence repetition, we can automatically stop acquisition of basis functions when the acquired response falls below the noise (assuming of course that we have an ordering of the functions, as is the case with the singular values).

Both of the broadband non-Fourier encoded 3D dynamic MRI experiments that we have presented here demonstrate the properties of adaptively compressed broadband non-Fourier encoding using fast k-space traversal trajectories, thus enabling an additional level of optimization for non-Fourier encoding. These two experiments aimed to simulate MRI monitoring during image guided therapy, and both illustrate the successful depiction of the image dynamics at high spatial resolution and a greater than three-fold temporal acceleration when compared to other fast imaging methods such as stack of spirals or ultra-short TR SSFP steady state imaging.

Dynamic adaptive broadband non-Fourier encoding was used in these experiments to compress the acquisition of the useful MR signal content by relying on the ad-hoc assumption that noise components of the RF excitation/receiving cycle would enable the basis to adapt to the changing FOV over time. This appears to be the case to a large extent, as shown by the small changes of the encoding functions that are shown next to the time frame images of each experiment, shown in Figures 4-14–4-16 and 4-19–4-22. However a truly adaptive experiment is meant to refer to active, and mathematically sound, tracking of the subspace that does not meet the given criteria of significance through time, in the series of changing FOV image frames. This is an area of active research (see e.g., [52]) and it is likely to enable further compression efficiency and higher acceleration factors for adaptive broadband non-Fourier imaging.

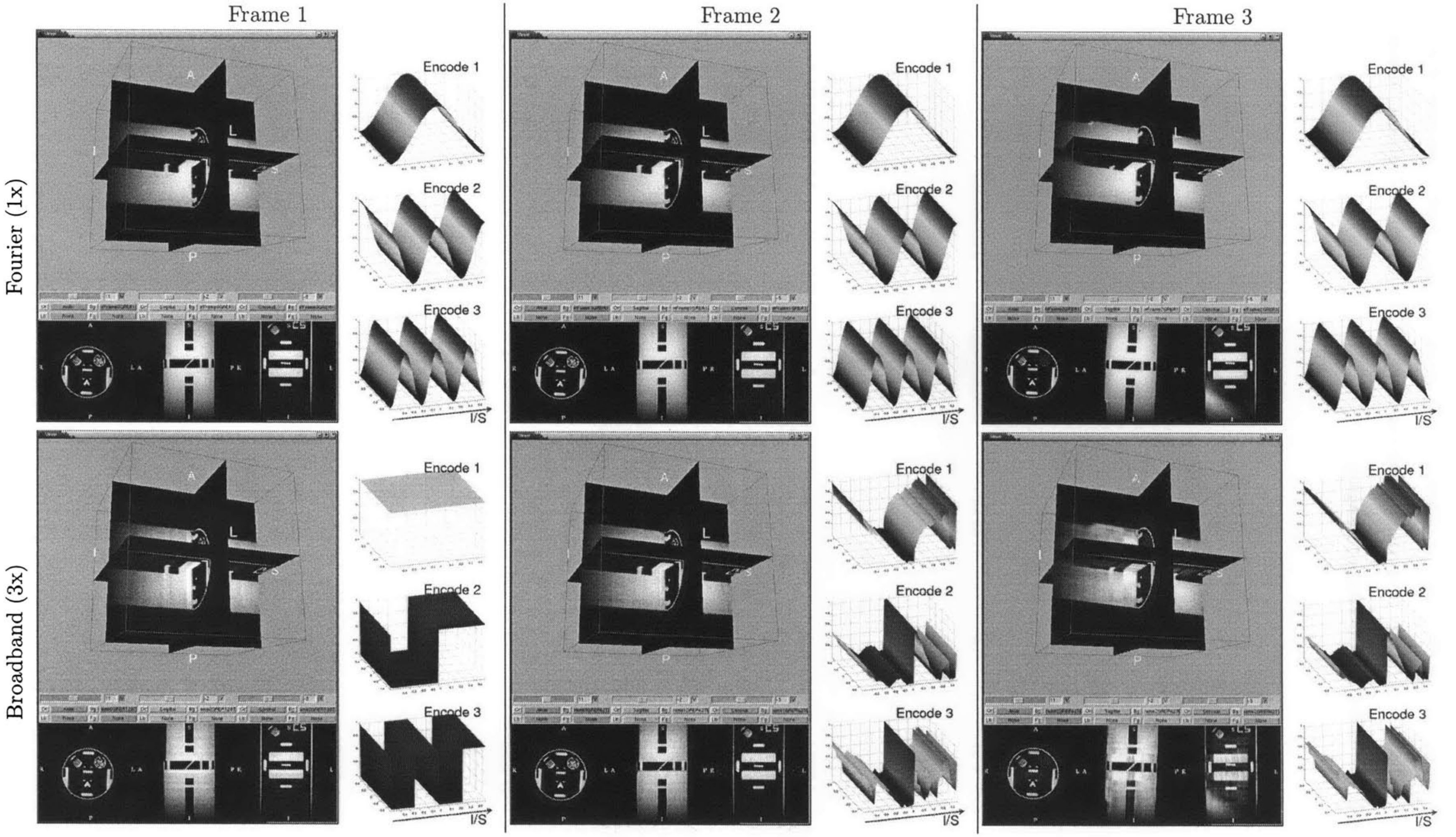

Figure 4-14: Dynamic series of a doped water phantom undergoing rotation. The resolution of 128 along the S/I axis is obtained by Fourier encoding with a stack of 128 spirals (top row, 61 s/frame), and non-Fourier encoded using 42 encoding functions (bottom row, 20 s/frame). The R/L & A/P axes are encoded for 256-by-256 resolution via an 8-interleave spiral. Next to each image are shown three of the encoding functions used to acquire it (complex part of a complex exponential Fourier function, or magnitude for non-Fourier functions). The 42 non-Fourier encoding functions were derived by the SVD of the previous time frame's system response matrix (first frame was Hadamard encoded).

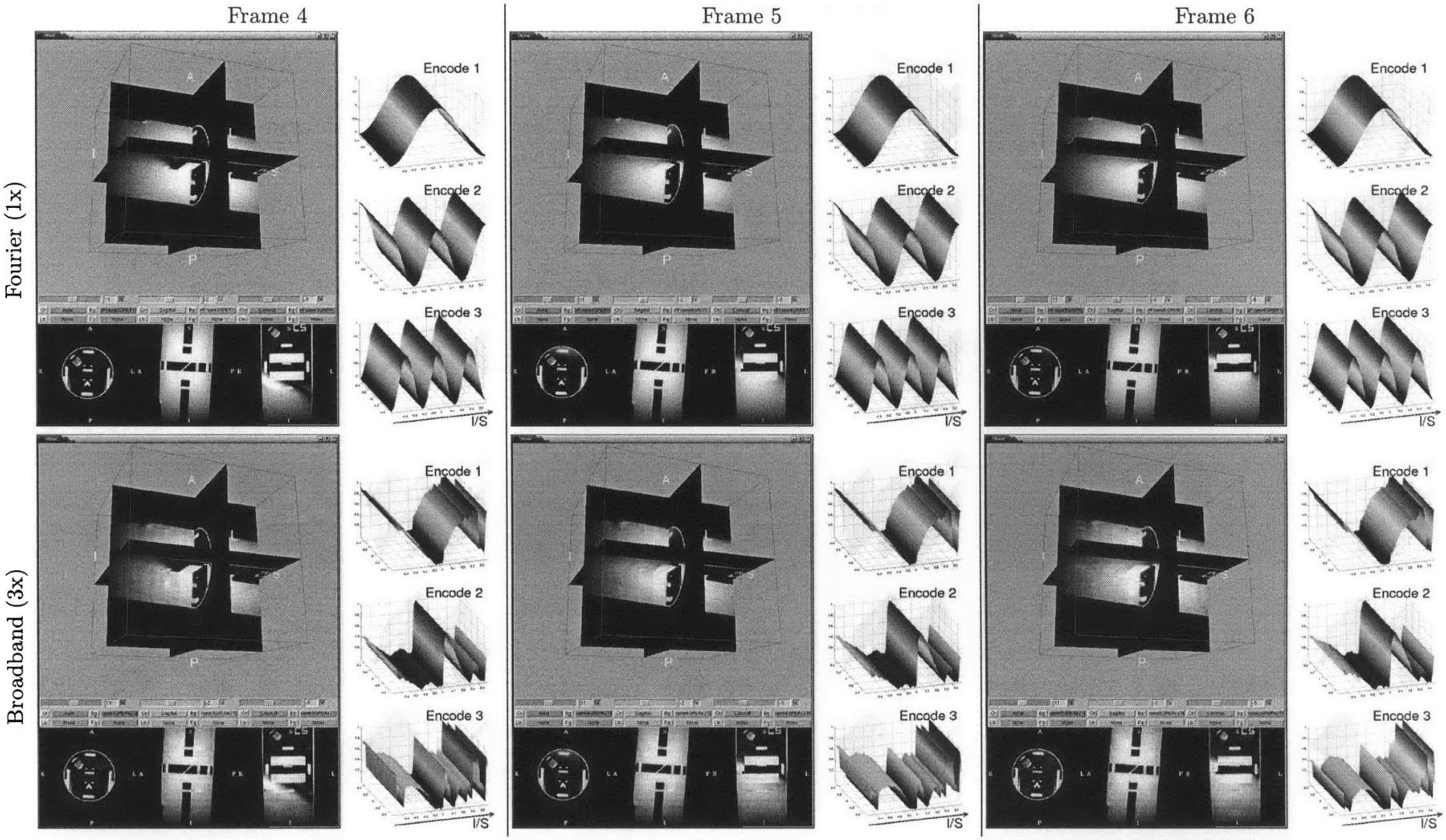

Figure 4-15: Figure 4-14 continued. Note the change of non-Fourier encoding functions as they adapt to the changing FOV contents.

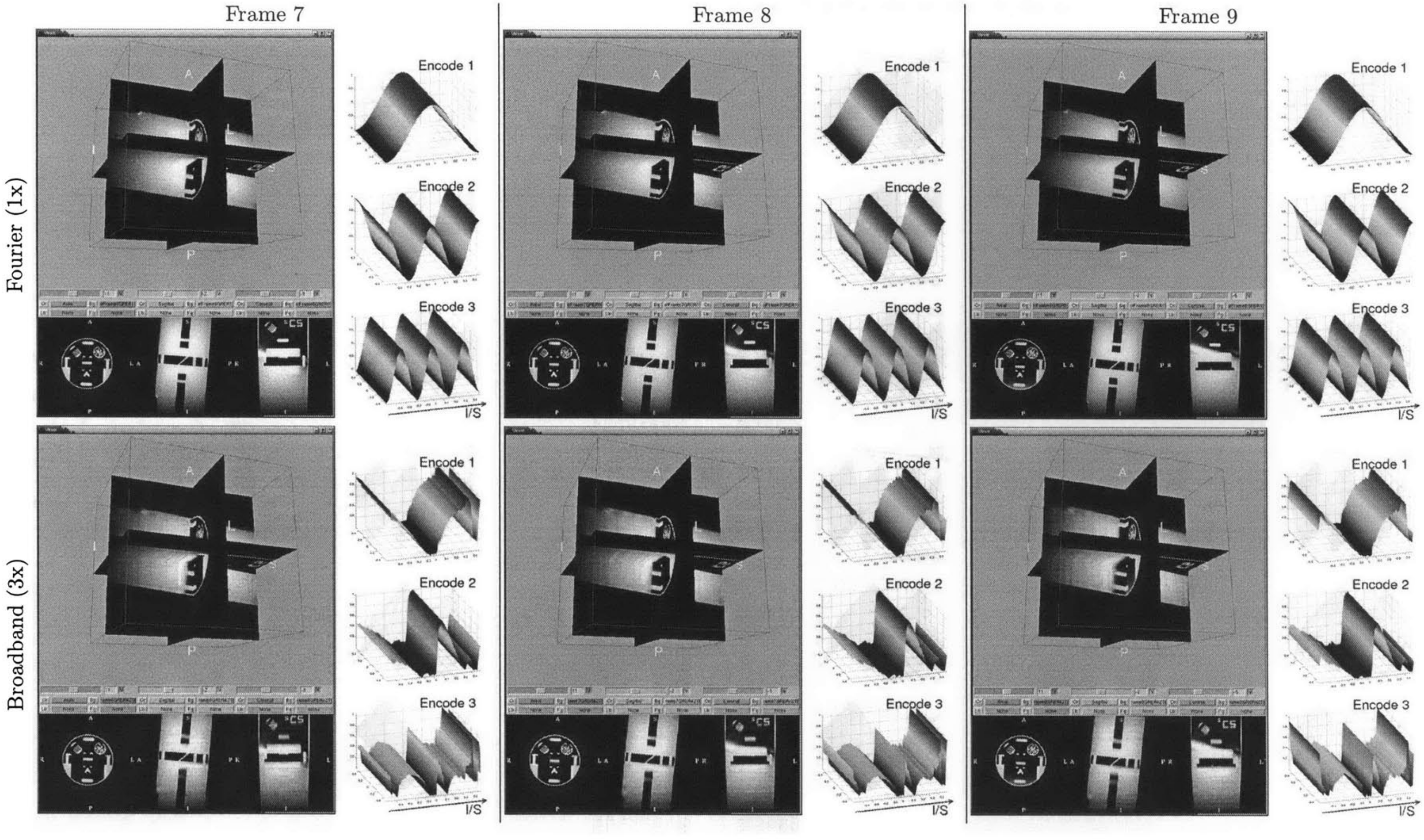

Figure 4-16: Figure 4-14 continued.

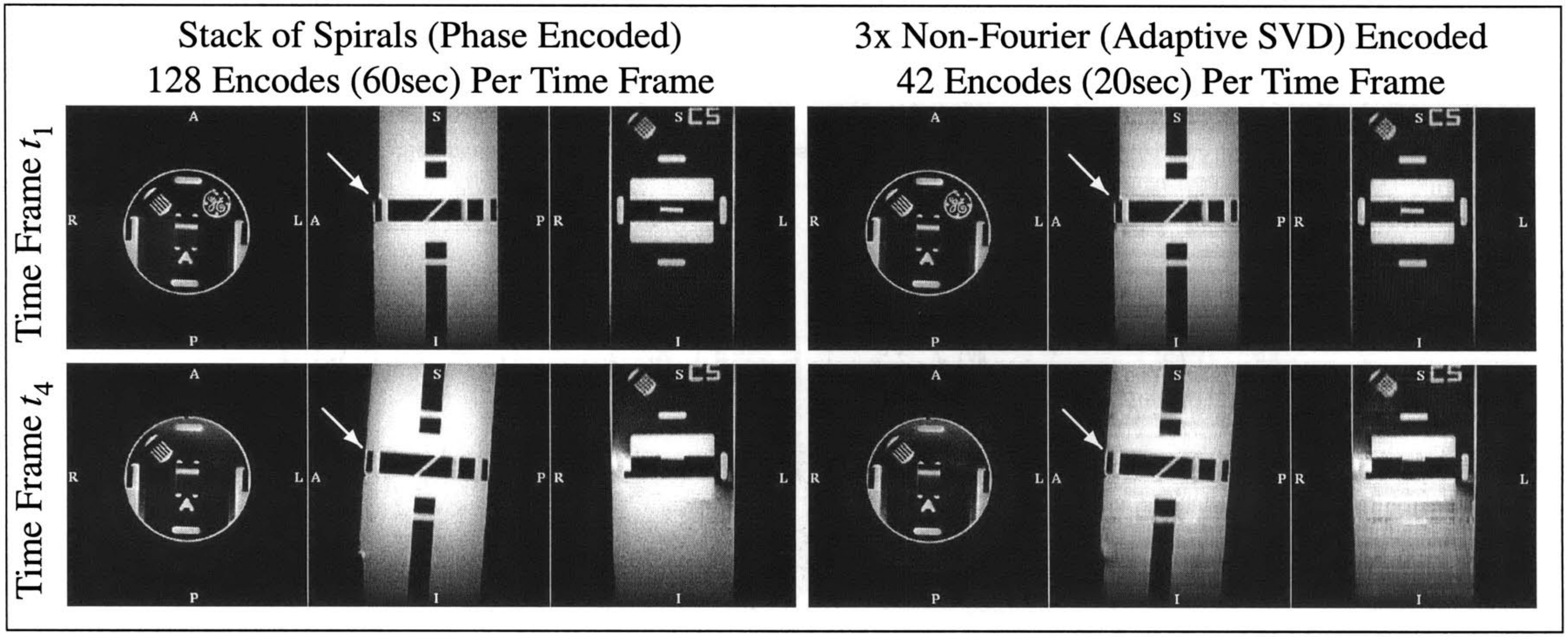

Figure 4-17: Detail of observed change in between selected frames of the dynamic imaging experiment presented in Figs. 4-14–4-16. Fine detail of the changes are observed both when fully encoding the FOV (via Fourier phase encoding thus producing a k-space stack of spirals) as well as in the broadband non-Fourier adaptively encoded at 3x compression factor, such as the shifting of the doped water to fill in a small air bubble in the top of the phantom, as shown by the arrows.

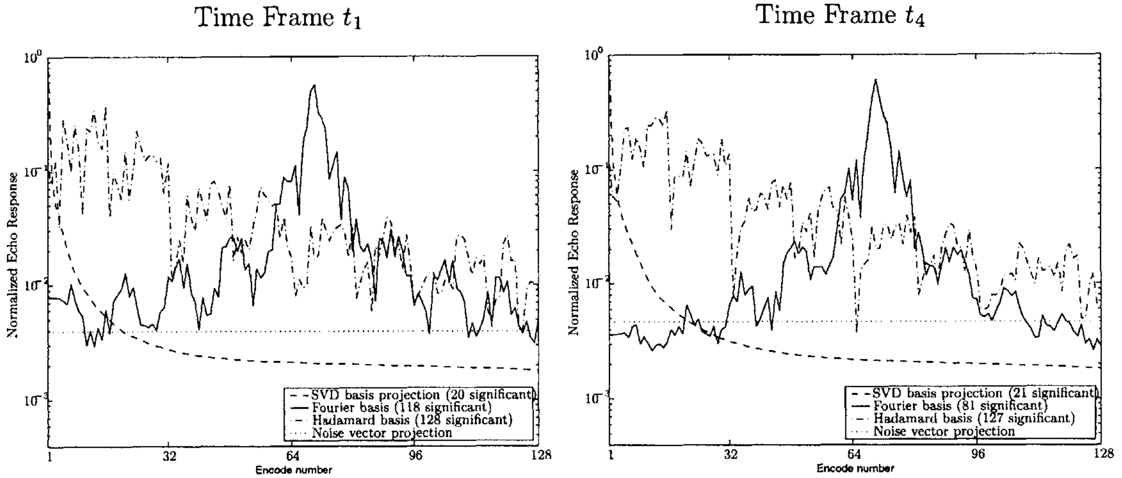
Time Frame t_1

Time Frame t_4

Figure 4-18: Significance of basis function responses for the selected frames presented in Fig. 4-17.

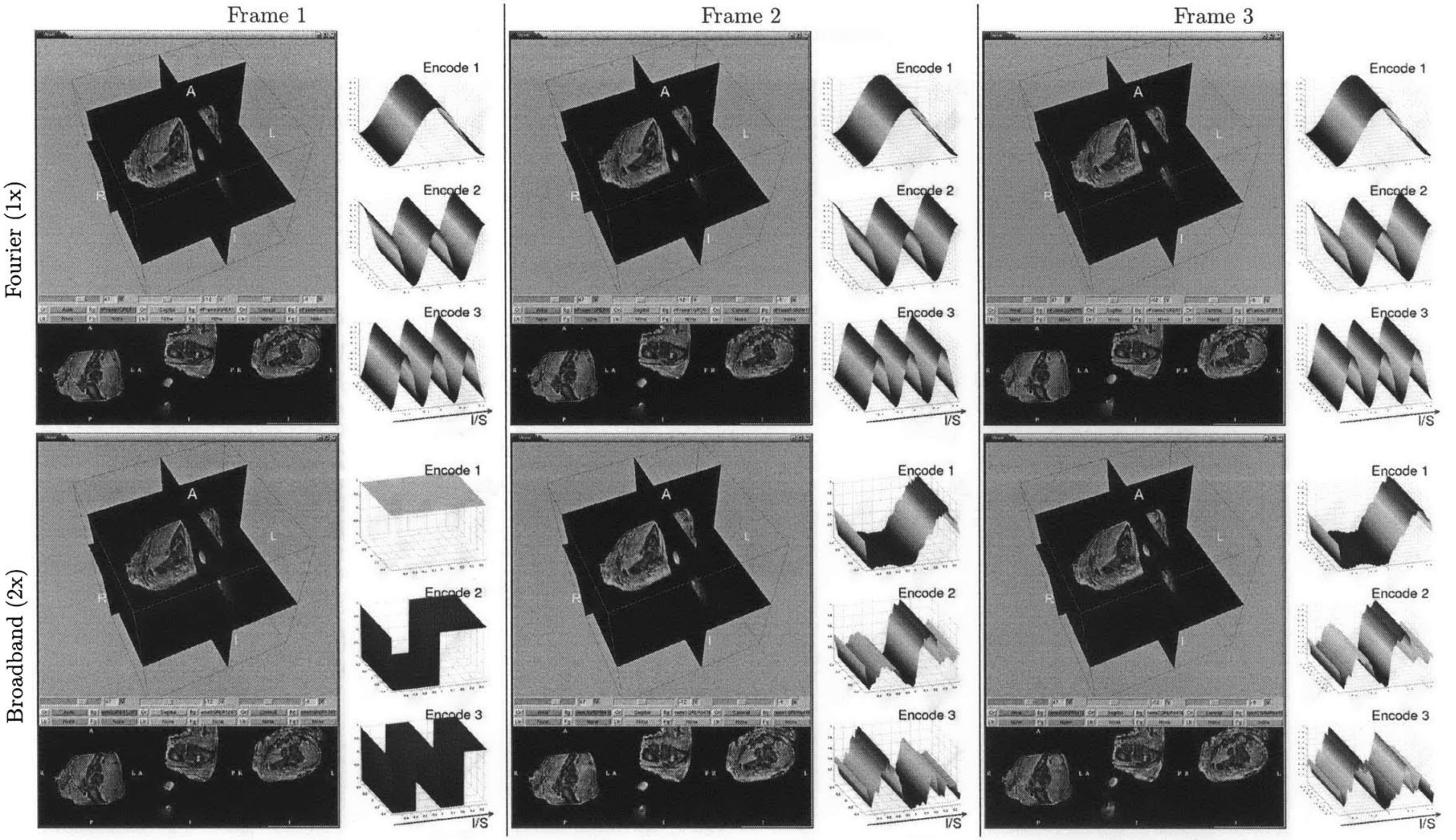

Figure 4-19: Dynamic series of a a hand phantom (glove filled with gel) approaching an animal tissue phantom and subsequently inserting a biopsy needle into it before finally exiting the FOV. Same acquisition parameters as in Fig. 4-14 except using 64 SVD encoding functions for non-Fourier time frames after initial frame and 22 cm FOV along the spiral dimensions.

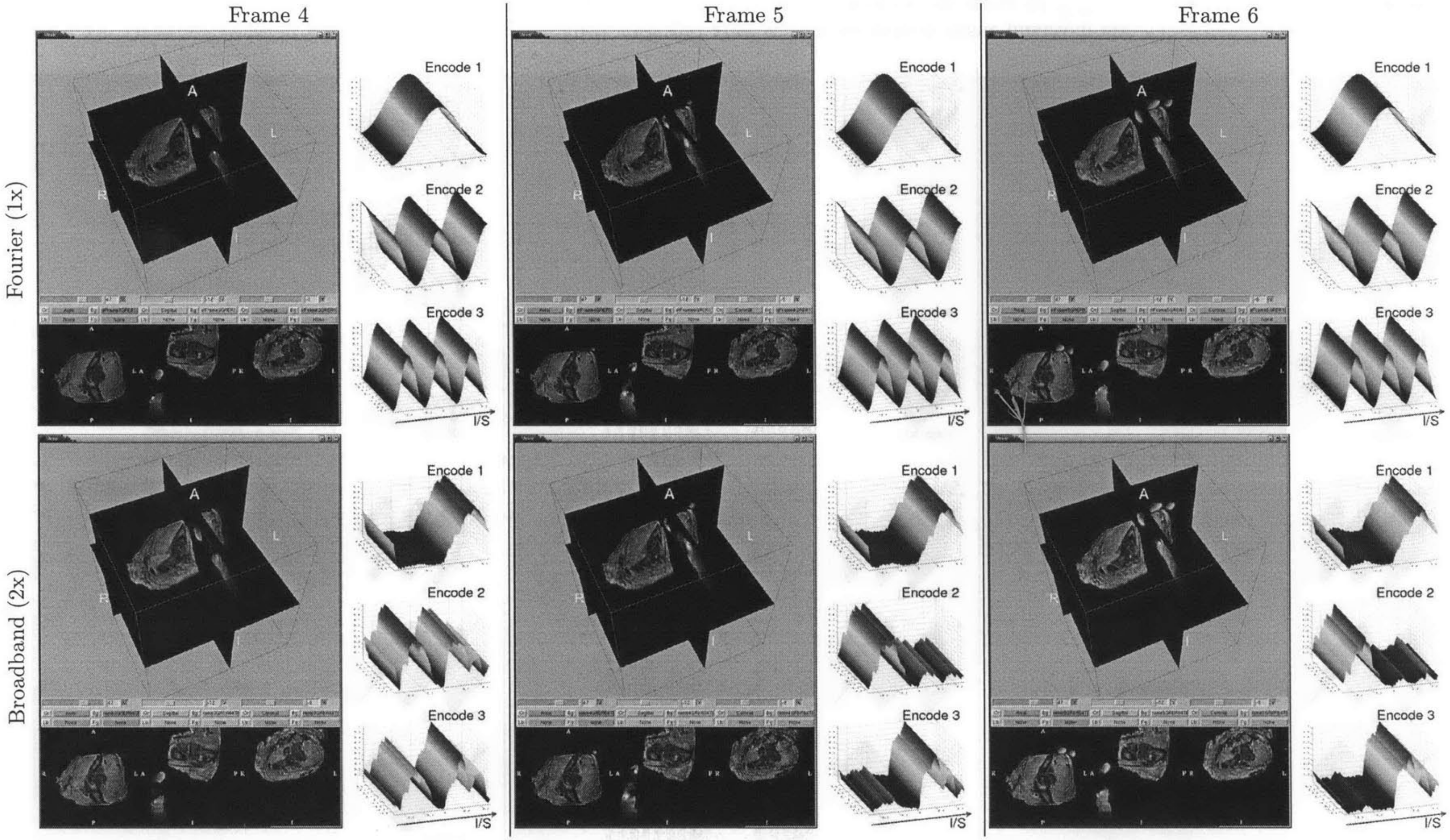

Figure 4-20: Figure 4-19 continued.

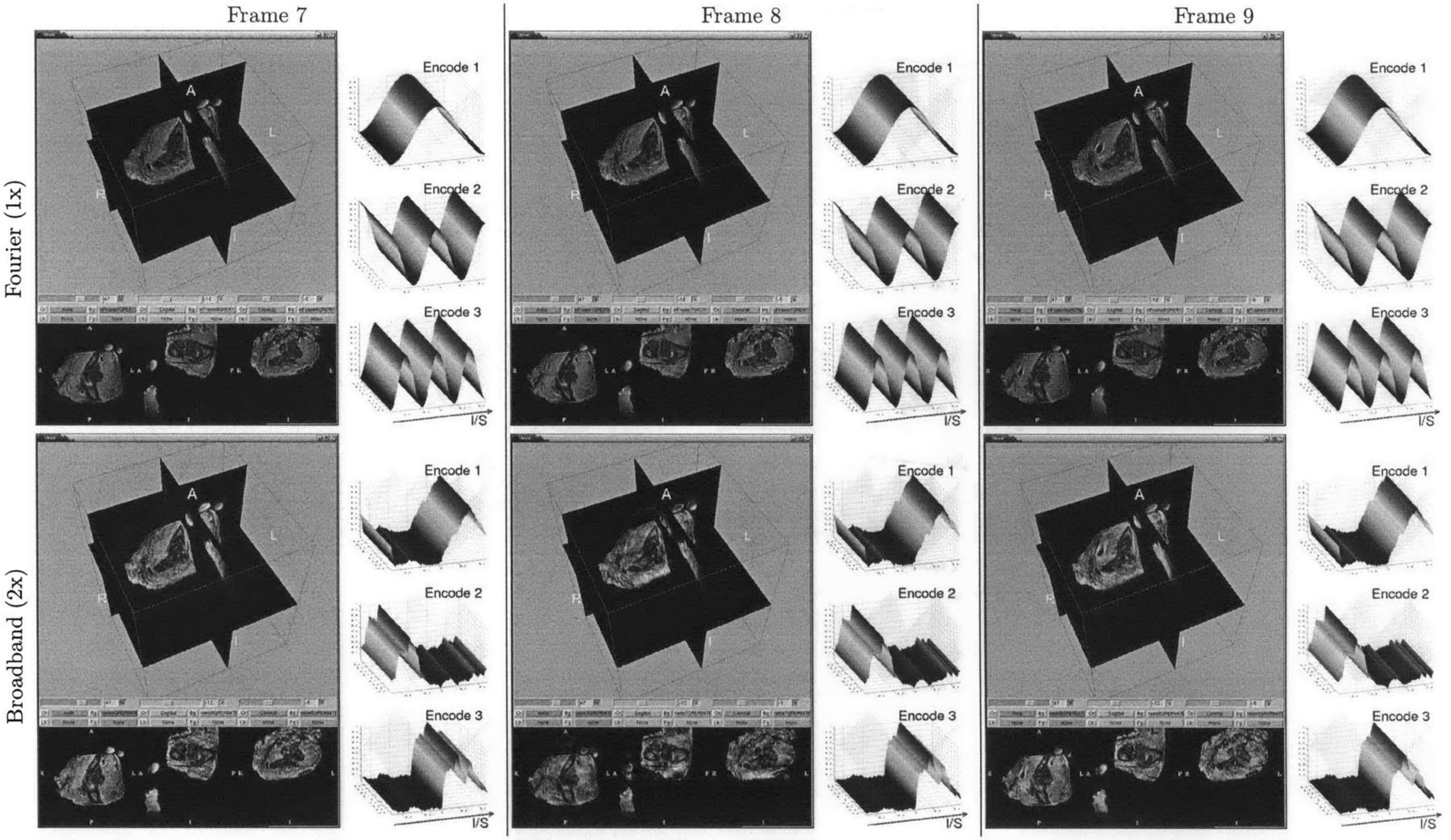

Figure 4-21: Figure 4-19 continued.

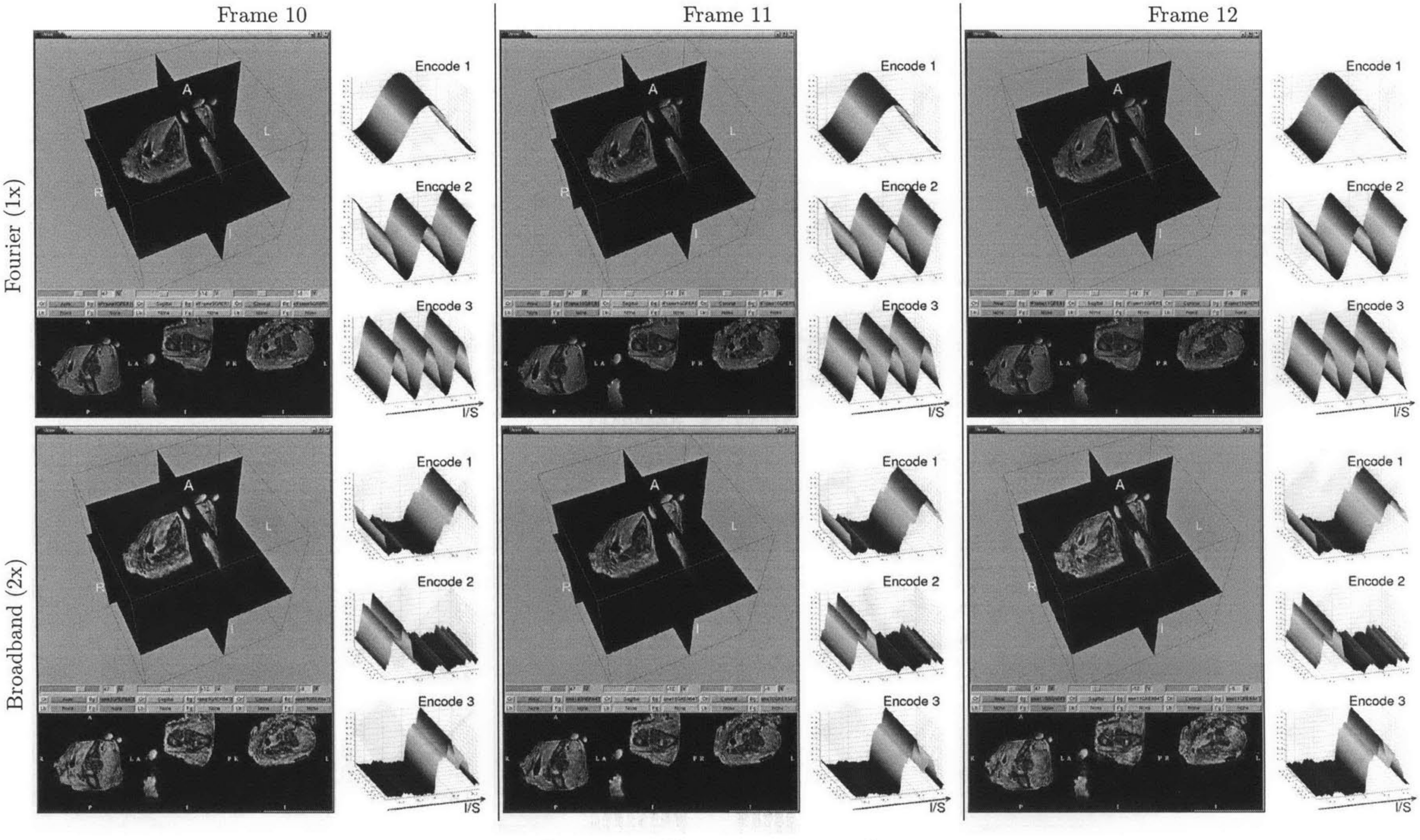

Figure 4-22: Figure 4-19 continued.

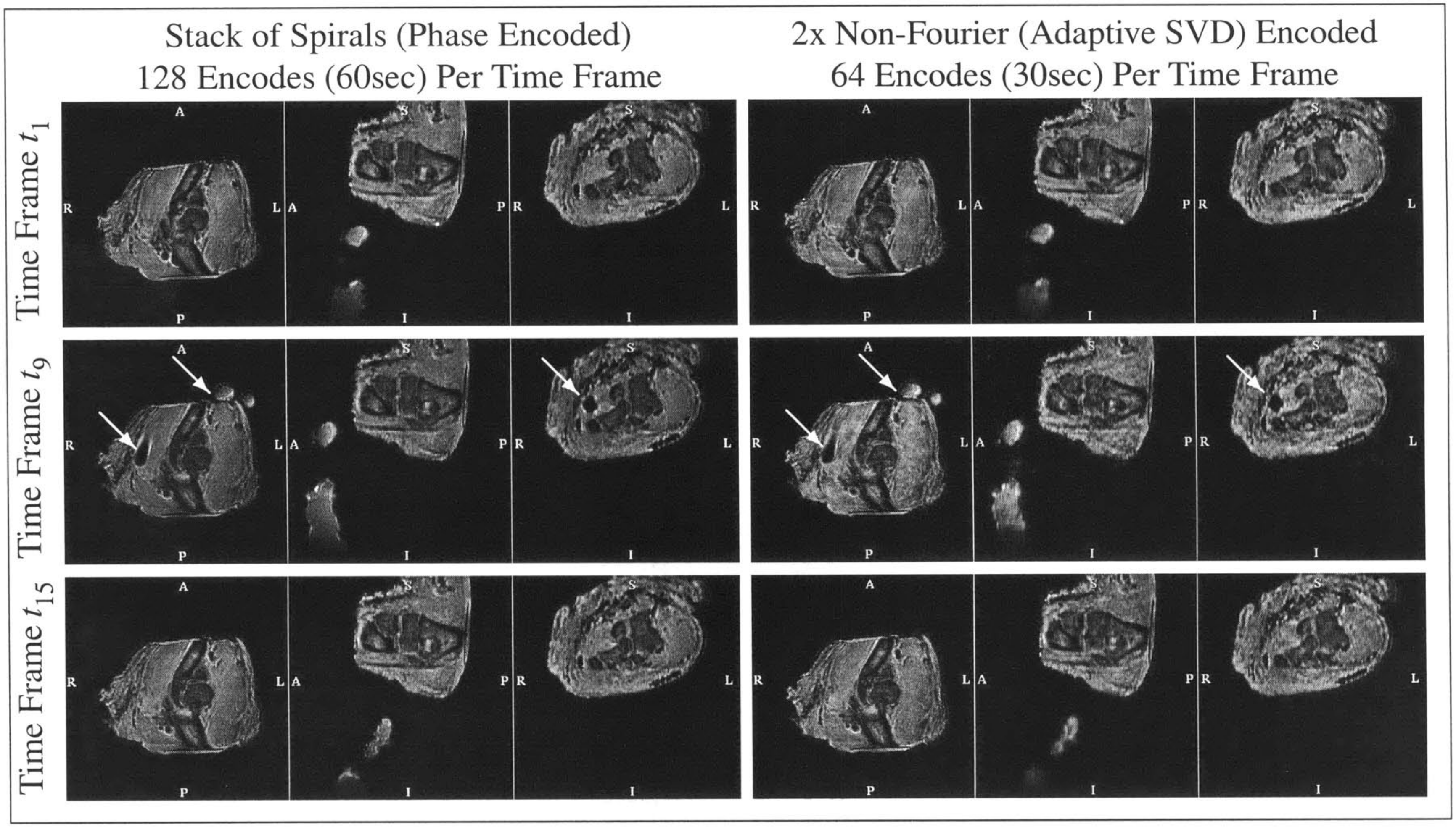

Figure 4-24: Detail of observed change observed in selected frames of the dynamic imaging experiment presented in Figs. 4-19–4-23. All change observed from fully encoding the FOV (via Fourier phase encoding thus producing a k-space stack of spirals) is also observed in the broadband non-Fourier adaptively encoded at 2x compression factor, as pointed by the arrows, such as the movement of the hand shown in the Sagittal plane (middle plane), and the insertion and removal of the biopsy needle seen in the other two planes.

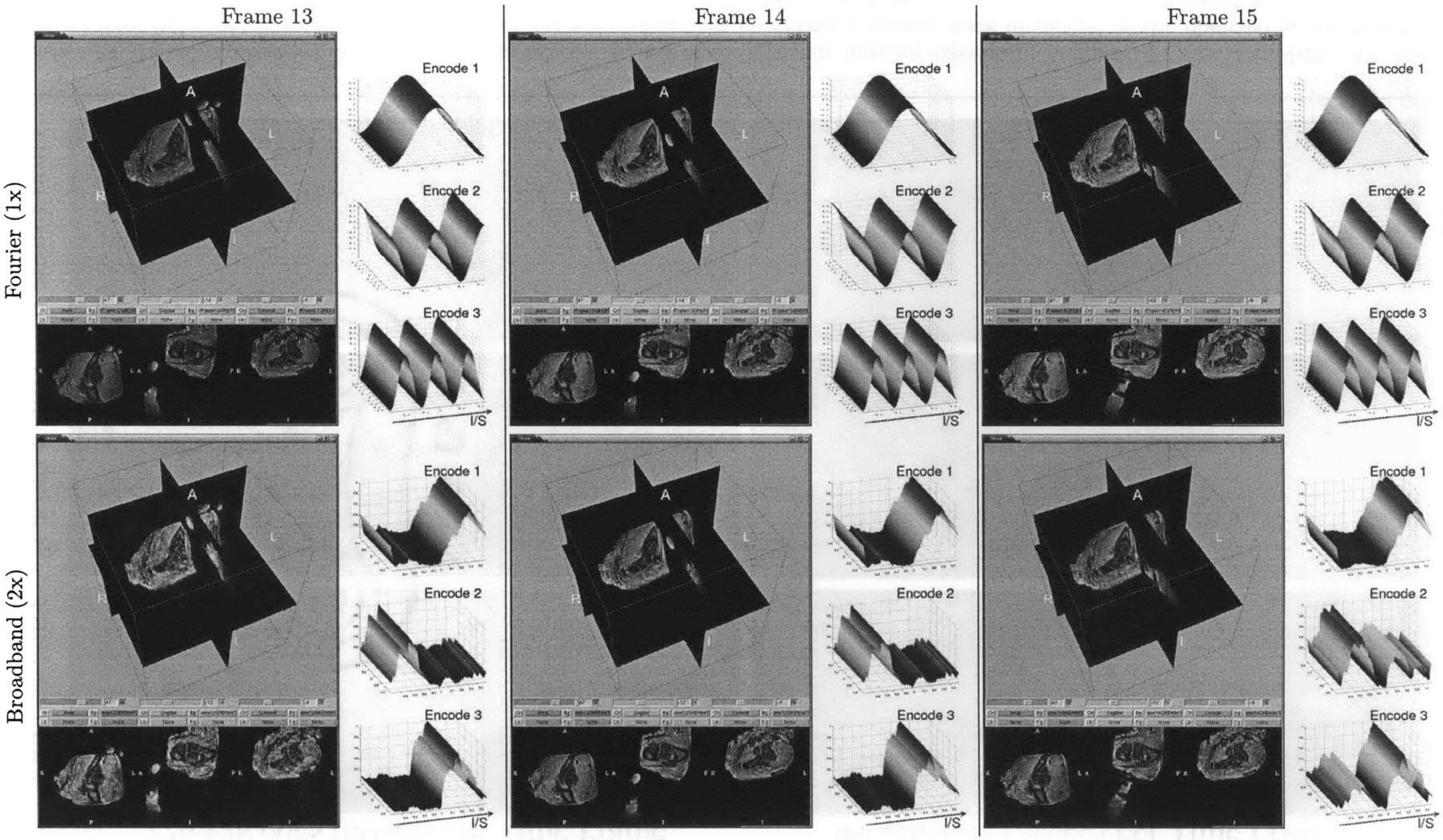

Figure 4-23: Figure 4-19 continued.

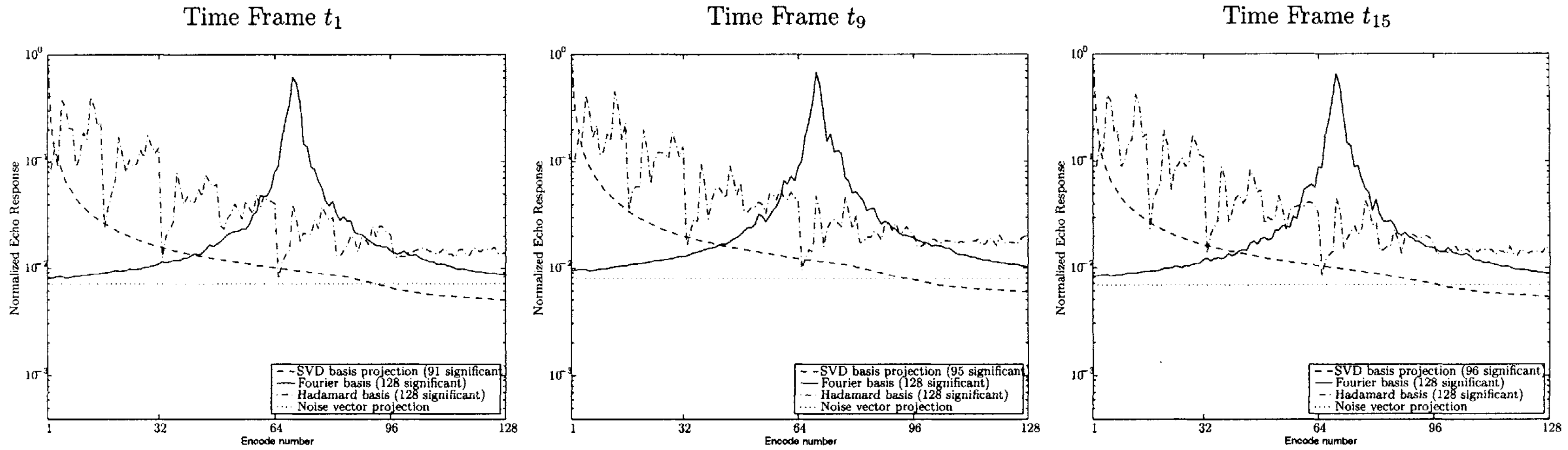

Figure 4-25: Significance of basis function responses for the selected frames presented in Fig. 4-24. Because the goal of the experiment is to capture large-scale change rather than the fine morphological detail of anatomy which leads to a wide subspace, compression beyond the level of noise can be applied, as was performed for the acquisitions of Figs. 4-19–4-23 (by a factor of ~ 1.4).

Chapter 5

NF*P: Broadband Encoding in Parallel in the Presence of Multiple Receiver Coils[1]

A wide variety of MR imaging techniques available today aim to increase Fourier signal acquisition efficiency. A recent addition to the fast imaging methods toolbox are multi-channel parallel data acquisition (P-MRI) methods, characterized by multiple RF receiver coils and associated RF receiver electronics. P-MRI methods such as simultaneous acquisition of spatial harmonics (SMASH) [139], sensitivity encoding (SENSE) [126] and sensitivity profiles from an array of coils for encoding and reconstruction in parallel (Space-RIP) [67] offer improved temporal and/or spatial resolution and are rapidly becoming a prominent focus of research and MR scanner design, motivated primarily by the numerous clinical imaging applications that require both high speed and resolution, such as cardiac imaging. Parallel imaging methods use the intrinsic spatial encoding induced by the weighting of spin density due to the spatial sensitivity of RF receiver coils. By sampling the signal using multiple receiver coils with independent spatial sensitivities, parallel imaging methods achieve partial signal localization that would otherwise require the use of gradients. Each parallel imaging method is differentiated by its use of a unique reconstruction scheme to exploit the independence of the spatial sensitivity profiles of the RF coils.

Parallel imaging methods have been successfully combined with other fast acquisition methods, offering further improvements. For example, the UNFOLD method for increasing temporal resolution was recently applied to parallel coil acquisition [60, 78], and non-Cartesian SENSE [125] renders the use of the SENSE reconstruction technique compatible with the complicated k-space trajectories

---

[1] Portions of this chapter have appeared in [94, 95, 101]

that are typically used for fast MRI (such as spiral trajectories discussed in Chapter 4).

As we have seen, broadband Non-Fourier imaging partially encodes the field-of-view (FOV) by employing arbitrary non-sinusoidal spatial encoding profiles induced via RF excitation. However, the intrinsic sensitivity encoding imposed by RF receiver coils is present regardless of *how* one encodes the MR signal content. In this chapter we describe the analytical separation of the two spatial encoding mechanisms, based on the premise that they are physically separable. This attempt will enable non-Fourier encoding to be expressed as complementary to the inherent encoding imposed by RF receiver coil sensitivities in Section 5.1.2. When the two spatial encoding methods are expressed as complementary, the number of non-Fourier spatial encoding steps necessary to fully encode a FOV is reduced. The complementarity is found from the modus operandi of parallel imaging methods; they are based on a k-space sub-sampling scheme which results in the superposition (aliasing) of multiple regions of the FOV. We exploit this k-space down-sampling by encoding all the aliases simultaneously, in order to reduce the non-Fourier encoding burden. This is performed so that each superimposed portion of the FOV is non-Fourier encoded *identically.*

Armed with that understanding, this chapter will develop a general theoretical framework to combine parallel imaging with non-Fourier spatial encoding methods in a manner that offers advantages in addition to the temporal resolution improvement associated with parallel acquisition. We will see that combination of parallel imaging "decoding" techniques with non-Fourier encoding enables the speedup factors associated with each encoding method to multiply. This leads to greatly reduced image acquisition times. Furthermore, a reduction of the length of each digital non-Fourier spatial excitation may be obtained, up to a factor equal to the speedup factor of the parallel imaging method, by casting the FOV reduction of parallel imaging techniques as a dimensionality reduction of the k-space that is non-Fourier encoded. This is in addition to imaging acceleration; just as aliased images result by skipping acquisition of k-space samples, aliased RF spatial excitations result by skipping excitation k-space samples.

5.1 Broadband Imaging in Parallel using SMASH

5.1.1 The SMASH Parallel Imaging Approach

When the signal emanating from the spin distribution is weighted by the spatial sensitivity $W_l(y)$ of a receiver coil, Eq. (2.6) becomes

$$S_l(k_x, k_y^{(m)}) = \iint \rho(x,y) W_l(y) e^{-i2\pi(k_y^{(m)} y + k_x x)} dx\, dy, \tag{5.1}$$

where we have simplified the spin density to a 2D function for brevity. In a typical SMASH experiment [139] a regular sub-sampling factor along the direction of phase encoding is enforced, yielding insufficient data to reconstruct an alias-free image. Skipping k-space samples reduces the imaged FOV thus causing the reconstructed image to be aliased.

The information necessary to "up-sample" k-space by the same factor as the acquisition down-sampling is generated by linear combinations of the samples obtained by the individual coils. That is, when L coils with independent spatial sensitivities $W_l(y)$, $l = 1, \dots, L$, are used to acquire the MR signal, the skipped k-space samples can be reconstructed by taking linear combinations of the raw coil samples of Eq. (5.1) that mimic the effect of the skipped gradient encoding steps.

Without loss of generality, assume that the y direction is phase encoded and that the coil sensitivities are only variable along y (the former assumption does not pose a limitation since if that is not the case, a 1D DFT of raw data from each coil along the readout direction yields raw data along the physical readout axis which can then be reconstructed on a column by column basis given the y-axis variation of the coil sensitivities at each point x_0 along the readout axis [67, 138]). Given the phase encoding gradient step $\Delta k_y = \gamma G_y^{\text{step}} \tau$ necessary to yield the desired FOV (from Eq. (2.12)), the SMASH method computes a set of scalars $c_l^{(s)}$, for $s = 0, \dots, f-1$, where $f < L$, such that

$$\sum_{l=1}^{L} c_l^{(s)} W_l(y) = e^{i2\pi(s\Delta k_y)y}. \tag{5.2}$$

The sum in Eq. (5.2) is precisely the complex exponential that separates harmonic (i.e., phase encode step) $k_y^{(m)}$ (of Eq. (2.13)) from the harmonic $k_y^{(m+s)}$:

$$\begin{aligned} k_y^{(m)} - s\Delta k_y &= (1/2M - m)\Delta k_y - s\Delta k_y \\ &= (1/2M - (m+s))\Delta k_y \\ &= k_y^{(m+s)}. \end{aligned} \tag{5.3}$$

The number of harmonics we can generate in this manner, f, is the parallel imaging speedup factor. For example, suppose $f = 2$. Via a least squares solution of Eq. (5.2), using the *a priori* measured coil sensitivity functions, we would obtain the linear combinations that yield the harmonics:

$$h^{(1)}(y) = c_1^{(1)} W_1(y) + c_2^{(1)} W_2(y) \simeq 1, \tag{5.4}$$

$$h^{(2)}(y) = c_1^{(2)} W_1(y) + c_2^{(2)} W_2(y) \simeq e^{i2\pi\Delta k_y y}. \tag{5.5}$$

An example of experimentally measured coil sensitivities for a four-element cardiac phased array coil are shown in Fig. 5-1, while a least squares fit of these particular sensitivities, yielding the 0th ($s = 0$) and 1st ($s = 1$) harmonic, are shown in Fig. 5-2.

SMASH imaging is based on the realization that when a set of harmonics $\left\{k_y^{(m)}\right\}$ is induced via gradients, the complex exponentials generated by the linear combinations of the coil sensitivities in

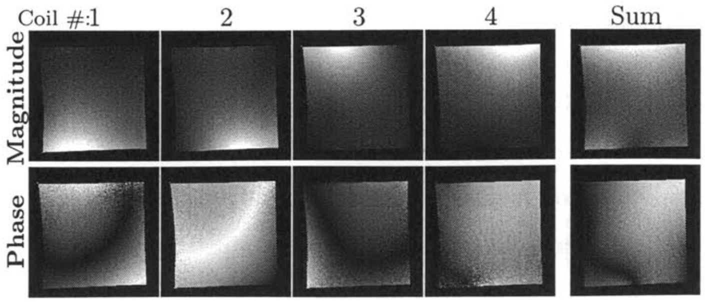

Figure 5-1: Spatial coil sensitivities of the elements of a four-element cardiac phased array. The complex-valued sensitivity profiles were measured by full acquisition of a relatively homogeneous doped water phantom (e.g., $\rho(x,y) \simeq \text{const}$) placed in the FOV.

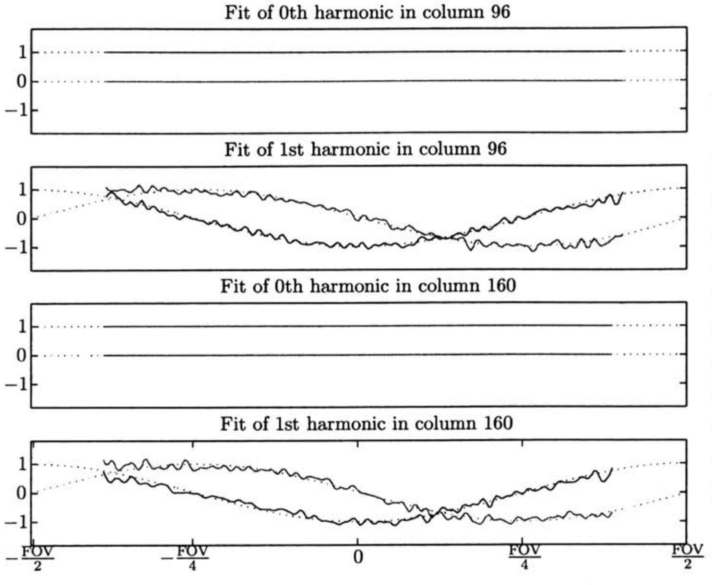

Figure 5-2: SMASH-derived fits of the coil sensitivities in Fig. 5-1 for two harmonics, yielding a speedup factor of 2 in a SMASH-enabled acquisition experiment. The fits shown are those computed for two different columns of the image. True harmonics shown in dotted and least squares fits shown in solid (real components in blue, imaginary components in red). Harmonics were not fitted outside the region of support of the measured sensitivity profiles.

Eq. (5.2) can be used to obtain an additional set of Fourier coefficients of the sample: combining the data acquired from the receiver coils for a gradient-induced k-space location $k_y^{(m)}$ with the $c_l^{(s)}$ yields

$$\begin{aligned}
\sum_{l=1}^{L} c_l^{(s)} S_l(k_x, k_y^{(m)}) &= \sum_{l=1}^{L} c_l^{(s)} \left[\iint \rho(x,y) W_l(y) e^{-i2\pi k_y^{(m)} y} e^{-i2\pi k_x x} dx\, dy\right] \\
&= \iint \rho(x,y) \left[\sum_{l=1}^{L} c_l^{(s)} W_l(y)\right] e^{-i2\pi k_y^{(m)} y} e^{-i2\pi k_x x} dx\, dy \\
&= \iint \rho(x,y) \left[e^{i2\pi(s\Delta k_y)y}\right] e^{-i2\pi k_y^{(m)} y} e^{-i2\pi k_x x} dx\, dy \\
&= \iint \rho(x,y) e^{-i2\pi k_y^{(m+s)} y} e^{-i2\pi k_x x} dx\, dy. \qquad (5.6)
\end{aligned}$$

where the last equality follows from Eq. (5.3).

Accordingly, SMASH experiments perform only M/f experiment repetitions while skipping f phase encode steps in each experiment repetition, i.e., they employ a k-space step of $\Delta k'_y = f\Delta k_y$. That is, in contrast to Eq. (2.13), at each sequence repetition of the SMASH experiment one uses gradients to acquire the coefficient of harmonic

$$k_y^{(f(m'-1)+1)} = \gamma\left(1/2M - (f(m'-1)+1)\right) G_y^{\text{step}}\tau, \tag{5.7}$$

where the parallel imaging experiment repetition m' is drawn from the set $M' = \{1, \ldots, M/f\}$. In effect, the repetition $m' \in M'$ of the SMASH experiment corresponds to the repetition

$$m = f(m'-1)+1, \tag{5.8}$$

of the fully phase encoded experiment (c.f., Eq. (2.11)).

SMASH collects the raw signals sampled by the multiple coils for the gradient-induced harmonic $f(m'_i - 1)+1$, for some $m'_i \in M'$, and combines them with the $c_l^{(s)}$, for each $s \in S = \{0, \cdots, f-1\}$ for which we have computed the linear combinations that satisfy Eq. (5.2). These combinations generate recombined harmonics for each s in addition to the gradient-induced m'_i, so that the ensemble of recombined signals form an entire set of the sample's coefficients for each harmonic in the set $M_i = \{m \mid m = m'_i + s, s \in S\} \equiv \{f(m'_i - 1)+1, \cdots, fm'_i\}$. After all $|M'| = M/f$ sequence repetitions are completed, i.e., $\forall m'_i \in M'$, the recombined signals form the entire set of phase encodes $k_y^{(m)}$, that is necessary to produce the alias-free image of the desired FOV, since

$$\bigcup_{i=1}^{|M'|} M_i = \{1, \cdots, M\}. \tag{5.9}$$

The SMASH image has been acquired at a speedup of f, compared to fully phase encoding it for the desired FOV, since the size of the set of harmonics collected via the repetitions of M' is only M/f.

5.1.2 The Signal Response to Non-Fourier Excitations using SMASH

Now consider an experiment using a broadband non-Fourier excitation with the low flip angle spatial profile $p(y)$ corresponding to the Fourier coefficients p_k that we excite with the RF pulse (c.f., Eq. (2.24)). Each coil produces the signal that includes the spatial weighting it imposes on the spin density,

$$S_l(k_x, p(y)) = \iint \rho(x,y)p(y)W_l(y)e^{-i2\pi k_x x}dx\,dy. \tag{5.10}$$

Combining these signals according to the same $c_l^{(s)}$ as in the Fourier SMASH experiment (Eq. (5.6)) yields

$$\begin{aligned}\sum_{l=1}^{L} c_l^{(s)} S_l(k_x, p(y)) &= \iint \rho(x,y)p(y)\left[e^{i2\pi(s\Delta k_y)y}\right] e^{-i2\pi k_x x} dx\, dy \\ &= \iint \rho(x,y)\left(\sum_m p_m e^{-i2\pi(k_y^{(m)})y}\left[e^{i2\pi(s\Delta k_y)y}\right]\right) e^{-i2\pi k_x x} dx\, dy \\ &= \iint \rho(x,y)\left(\sum_m p_m e^{-i2\pi(k_y^{(m+s)})y}\right) e^{-i2\pi k_x x} dx\, dy,\end{aligned} \tag{5.11}$$

after substitution of the Fourier coefficient formulation of $p(y)$, and where $k_y^{(m)}$ is the harmonic induced by the remainder spatially selective gradient from the location of each p_m in the RF pulse (as in Eq. (2.23)).

From the last equality of Eq. (5.11) it is not immediately obvious how to shape $p(y)$ so as to perform non-Fourier encoding. Certainly, using the combination that yields $s = 0$, i.e.,

$$\sum_{l=1}^{L} c_l^{(0)} S_l(k_x, p(y)) = \iint \rho(x,y)\left(\sum_m p_m e^{-i2\pi(k_y^{(m)})y}\right) e^{-i2\pi k_x x} dx\, dy, \tag{5.12}$$

shows that we may use any non-Fourier encoding method, without any form of down-sampling (i.e., with no associated parallel imaging speedup), to encode the contents of the FOV. That is, the SMASH combination that produces the 0th harmonic may be used to combine the coil samples so as to produce the linear response from each row of k-space for any input RF pulse that one would expect to see from the MR imager (i.e., Eq. (5.12) is the same as Eq. (2.23)).

Let us now scrutinize the combination that yields $s = 1$:

$$\sum_{l=1}^{L} c_l^{(1)} S_l(k_x, p(y)) = \iint \rho(x,y)\left(\sum_m p_m e^{-i2\pi k_y^{(m+1)}y}\right) e^{-i2\pi k_x x} dx\, dy. \tag{5.13}$$

Equation (5.13) reveals that the encoding RF pulse can also produce a signal response wherein the scalar p_m at the mth position in the RF pulse scales not the Fourier mode $k_y^{(m)}$ of the sample, but rather, scales the $k_y^{(m+1)}$ mode, when the samples are combined with the first harmonic combination, $s = 1$. Effectively, the entire input encoding RF pulse produces a signal response that is formed by the familiar inner product of the RF pulse and k-space, but at the not-so-familiar offset of a single line of k-space. That is, the signal response is the inner product of the RF pulse, as if it was shifted by one k-space coefficient, with the k-space matrix of the sample. In general, Eq. (5.11) shows that a single input RF pulse can be used to produce s *separate* signal responses, depending on which SMASH combination of raw signals is used, each one of which is offset to begin the inner product of RF pulse and k-space matrix of Eq. (2.26) at an offset of s rows of k-space.

Nonetheless, Eq. (5.11) does not immediately clarify how to use the 1st and beyond SMASH harmonic reconstructions to speed up the non-Fourier encoding process. Let us return to the basic impulse response of Eq. (2.18), i.e., let us use an RF pulse that is composed of zeros everywhere except for the single coefficient $p_m = 1$. The sampled signals can be recombined to produce s different impulse responses, each of which is delayed by s. That is, the set of impulse responses we can produce from this excitation correspond to the Fourier modes $\left\{k_y^{(m')} \mid m' = m + s,\ s \in S\right\} \equiv \left\{k_y^{(m)}, \cdots, k_y^{(m+(f-1))}\right\}$ of the sample.

Let $f = 2$. The important realization here is that if we skip every even index of k-space in the excitation of the RF pulse, then we can obtain the entire MR system response matrix. This is accomplished by choosing $k_y^{(m)}$ with $m = 2l - 1,\ l = 1, \ldots, M/2$, e.g., by having a 0 in all the even positions of the RF pulse. We imagine the entire RF encoding vector p drawn from the rows of an identity matrix but excited so as to produce only odd-numbered Fourier modes, as multiplying the odd-numbered rows of k-space to produce one linear response that yields the odd-numbered Fourier modes of the sample, when combined according to equation (5.12). We then imagine the same encoding vector (composed of only odd-numbered Fourier modes) as multiplying the even-numbered rows of k-space to produce another response. This response, obtained when signals are combined according to equation (5.13), yields the even-numbered Fourier modes of the sample.

Now, consider the arbitrary RF encoding vector that is made to contain non-zero impulses only at every fth position. Using the appropriate linear combination of acquired signals, the entire RF vector p produces one linear response with the sub-sampled-by-f rows of k-space starting from the top row (when combined with the $c_l^{(0)}$). It also produces another linear response, this time with the sub-sampled-by-f rows of k-space starting from the second row (when combined with the $c_l^{(1)}$), and so on, for each k-space row offset in the set S.

It is therefore sufficient to choose the RF encoding vectors $\vec{p}$ so that they represent an optimal encoding of all the sub-sampled-by-f matrices of k-space *separately and simultaneously.* The physical analogy of these spatial excitations, containing impulses only at every fth position, is that they are in themselves aliased over the extent of the desired FOV, and hence encode each superimposed alias of the SMASH-aliased image identically.

5.1.3 Broadband Encoding in the Presence of SMASH

Matrix Formulation of SMASH

In the previous section we attempted to describe the main idea behind combining SMASH parallel imaging and non-Fourier encoding using the powerful analytical tools afforded by the SMASH signal equations. The raw sample combinations produced by SMASH suggested that a special non-Fourier RF encoding vector p', that only contains impulses that produce every fth Fourier mode, can produce a number of separate responses that can be summarized by the matrix equations

$$s^{(g)} = p' F^{(g)}, \tag{5.14}$$

where the matrices $F^{(g)}$ are each M/f-by-N and are derived from the full FOV k-space matrix F, of dimensions M-by-N, by sub-sampling it by a factor of f, starting from the gth row. That is, $F^{(g)} = F_{g:f:M,:}$ in MATLAB-style notation.

This suggests that the system response matrix of non-Fourier encoding in the presence of SMASH can be written as

$$F^{\mathcal{PSE}} = [F^{(1)}|\cdots|F^{(f)}], \tag{5.15}$$

where the superscript $\mathcal{PSE}$ stands for parallel spatially encoded, and the notation "|" represents matrix concatenation. Although this is a valid system response that can be non-Fourier encoded, there are subtleties that are missed by the analytical forms of the SMASH equations. We thus turn to the matrix formulation of SMASH as this will lead into a general non-Fourier system response in the presence of multiple receiver coils, that we present in Section 5.2.

We assume that we have a set of L coils, $l = 1, \ldots, L$ and that a SMASH speedup factor of $f \leq L$ is employed, relying on the ability of the coils to induce the additional encoding. Our goal is to produce an image of M-by-N resolution. The first step of SMASH is to compute the appropriate combinations of the coil sensitivities, for each column of the image (e.g., for each position x_0 along the readout direction), that produce the first $f-1$ harmonics, so that these can be used to complement the gradient-induced encoding. The 2D spatial sensitivities of the receiver coils are given by the functions $W_l(x,y)$. For each x_i, $i = 1, \ldots, N$, the SMASH linear combination parameters that we seek are $c_l^{(s)}(x_0)$, $s = 0, \ldots, f-1$. The ensemble of these parameters can be obtained by rewriting Eq. (5.2) in matrix form (appropriately discretized)

$$\begin{bmatrix} 1 & e^{-i2\pi\Delta k_y y_1} & \ldots & e^{-i2\pi(f-1)\Delta k_y y_1} \\ 1 & e^{-i2\pi\Delta k_y y_2} & \ldots & e^{-i2\pi(f-1)\Delta k_y y_2} \\ \vdots & \vdots & \ddots & \vdots \\ 1 & e^{-i2\pi\Delta k_y y_M} & \ldots & e^{-i2\pi(f-1)\Delta k_y y_M} \end{bmatrix} = \tag{5.16}$$
$$\begin{bmatrix} W_1(x_0,y_1) & \cdots & W_L(x_0,y_1) \\ W_1(x_0,y_2) & \cdots & W_L(x_0,y_2) \\ \vdots & \ddots & \cdots \\ W_1(x_0,y_M) & \cdots & W_L(x_0,y_M) \end{bmatrix} \begin{bmatrix} c_1^{(0)}(x_0) & \cdots & c_1^{(f-1)}(x_0) \\ c_2^{(0)}(x_0) & \cdots & c_2^{(f-1)}(x_0) \\ \vdots & \ddots & \vdots \\ c_L^{(0)}(x_0) & \ldots & c_L^{(f-1)}(x_0) \end{bmatrix}.$$

Equation (5.16), can be stated as $E(x_0) = W(x_0)C(x_0)$ (with the respective matrix terms). It can easily be solved using the left pseudo-inverse of the matrix containing the coil spatial sensitivities,

$W(x_0)$. Since $W(x_0)$ is of size M-by-L, it has rank at most L, assuming independence of the spatial profiles. This restricts f since $f \leq \text{rank}(W(x_0)) \leq L$ is an intrinsic constraint. In other words, it is not possible to use L coils to induce more encoding steps than there are independent coils in the receiver configuration.

Now let us assume that Eq. (5.16) has been solved for the coefficient matrix $C(x_0)$ that generates the f induced harmonics for each location x_0 along the frequency encoded readout dimension. If we use gradients to produce a specific phase encoding step $k_y^{(m)}$, each coil will produce the signal

$$S_l(k_x, k_y^{(m)}) = \iint \rho(x,y) W_l(x,y) e^{-i2\pi k_y^{(m)} y} e^{-i2\pi k_x x} dx\, dy, \tag{5.17}$$

by augmenting Eq. (5.1) with the 2D spatial coil sensitivity. After Fourier transformation along k_x, Eq. (5.17) yields

$$S_l(x, k_y^{(m)}) = \int \rho(x,y) W_l(x,y) e^{-i2\pi k_y^{(m)} y} dy. \tag{5.18}$$

In the SMASH experiment, the induced steps $k_y^{(m)}$ are drawn according to Eq. (5.7), with the mapping of Eq. (5.8), so that the gathered set of Fourier modes after completing all experiment repetitions is $\left\{k_y^{(1)}, k_y^{(f+1)}, k_y^{(2f+1)} \cdots, k_y^{(M-f+1)}\right\}$. Concentrating on a single column x_0 of our image, we rewrite the signals sampled by the receiver coils for all the induced modes in matrix notation, as:

$$\begin{bmatrix} S_1(x_0, k_y^{(1)}) & S_2(x_0, k_y^{(1)}) & \dots & S_L(x_0, k_y^{(1)}) \\ S_1(x_0, k_y^{(f+1)}) & S_2(x_0, k_y^{(f+1)}) & \dots & S_L(x_0, k_y^{(f+1)}) \\ \vdots & \vdots & \vdots & \vdots \\ S_1(x_0, k_y^{(M-f+1)}) & S_2(x_0, k_y^{(M-f+1)}) & \dots & S_L(x_0, k_y^{(M-f+1)}) \end{bmatrix}. \tag{5.19}$$

By applying the coefficient matrix $C(x_0)$ on the right of Eq. (5.19), we combine the received signals, in effect summarizing SMASH reconstruction as

$$\begin{bmatrix} S_1(x_0, k_y^{(1)}) & \cdots & S_L(x_0, k_y^{(1)}) \\ S_1(x_0, k_y^{(f+1)}) & \cdots & S_L(x_0, k_y^{(f+1)}) \\ \vdots & \ddots & \vdots \\ S_1(x_0, k_y^{(M-f+1)}) & \cdots & S_L(x_0, k_y^{(M-f+1)}) \end{bmatrix} \begin{bmatrix} c_1^{(0)}(x_0) & c_1^{(1)}(x_0) & \cdots & c_1^{(f-1)}(x_0) \\ c_2^{(0)}(x_0) & c_2^{(1)}(x_0) & \cdots & c_2^{(f-1)}(x_0) \\ \vdots & \vdots & \ddots & \vdots \\ c_L^{(0)}(x_0) & c_L^{(1)}(x_0) & \cdots & c_L^{(f-1)}(x_0) \end{bmatrix} =$$

$$\begin{bmatrix} S(x_0, k_y^{(1)}) & S(x_0, k_y^{(2)}) & \cdots & S(x_0, k_y^{(f)}) \\ S(x_0, k_y^{(f+1)}) & S(x_0, k_y^{(f+2)}) & \cdots & S(x_0, k_y^{(2f)}) \\ \vdots & \vdots & \ddots & \vdots \\ S(x_0, k_y^{(M-f+1)}) & S(x_0, k_y^{(M-f+2)}) & \cdots & S(x_0, k_y^{(M)}) \end{bmatrix}. \tag{5.20}$$

The equality of Eq. (5.20) naturally holds according to Eq. (5.6).

The matrix on the right-hand side of Eq. (5.20) contains signal samples that represent modulations of the transverse magnetization of the spin density by phase encoding steps, and that are free of modulations induced by receiver coils (i.e., as if a uniform, unit sensitivity, coil was used to acquire the samples). If we now rearrange the right-hand side of Eq. (5.20) and concatenate the rows of the matrix to form a vector, we obtain the same output signal vector that would result had we fully Fourier phase encoded column x_0 of the MR image. For the required resolution of M, the fully phase encoded signal of column x_0 of the MR image is

$$[S(x_0, k_y^{(1)}), \ldots, S(x_0, k_y^{(f)}), S(x_0, k_y^{(f+1)}), \ldots, S(x_0, k_y^{(2f)}), \ldots, S(x_0, k_y^{(M)})]^T, \tag{5.21}$$

when acquired with a uniform, unit sensitivity coil. This output vector contains all the samples for each of the k-space encoding steps $k_y^{(m)}$ of Eqns. (2.11) and (2.13), and, after Fourier transformation along k_y yields the column x_0 of the full FOV_y image.

Broadband System Response in the Presence of SMASH: NF-SMASH

It was shown in Section 5.1.2 that multiple responses can be obtained from a given spatial excitation. Suppose that the coils are used to individually collect signal responses from the FOV after some non-Fourier excitation $\tilde{p}(y)$, such that

$$\tilde{p}(y) = \sum_{m'=1}^{M/f} \tilde{p}_{m'} e^{-i2\pi k_y^{(m)} y}, \tag{5.22}$$

where the m of the Fourier mode $k_y^{(m)}$ is derived from m' via the mapping of Eq. (5.8). Unlike Eq. (2.24), in Eq. (5.22) we use the Fourier modes in the complex exponentials. Note that the spatial excitation, $\tilde{p}(y)$, described by Eq. (5.22) and resulting from the length-M/f RF vector $\tilde{p}$, describes an f-fold aliased spatial excitation over the extent of the desired FOV_y.

Given this excitation $\tilde{p}(y)$, each coil produces the signal

$$S_l(k_x, \tilde{p}(y)) = \iint \rho(x, y) W_l(x, y) \tilde{p}(y) e^{-i2\pi k_x x} dx\, dy, \tag{5.23}$$

by augmenting Eq. (5.10) with the 2D spatial coil sensitivity. After Fourier transformation along

k_x, and inserting Eqns. (5.22) and (5.18), Eq. (5.23) becomes

$$\begin{aligned} S_l(x, \tilde{p}(y)) &= \int \rho(x,y) W_l(x,y) \tilde{p}(y) dy \\ &= \int \rho(x,y) W_l(x,y) \sum_{m'=1}^{M/f} \tilde{p}_{m'} e^{-i2\pi k_y^{(m)} y} dy \\ &= \sum_{m'=1}^{M/f} \tilde{p}_{m'} \int \rho(x,y) W_l(x,y) e^{-i2\pi k_y^{(m)} y} dy \\ &= \sum_{m'=1}^{M/f} \tilde{p}_{m'} S_l(x, k_y^{(m)}). \end{aligned} \tag{5.24}$$

We can rewrite Eq. (5.24) in matrix form, by combining the signals from all the coils for a single x_0, as

$$\begin{aligned} &\begin{bmatrix} S_1(x_0, \tilde{p}(y)) & S_2(x_0, \tilde{p}(y)) & \cdots & S_L(x_0, \tilde{p}(y)) \end{bmatrix} = \\ &\begin{bmatrix} \tilde{p}_1 & \tilde{p}_2 & \cdots & \tilde{p}_{M/f} \end{bmatrix} \begin{bmatrix} S_1(x_0, k_y^{(1)}) & S_2(x_0, k_y^{(1)}) & \cdots & S_L(x_0, k_y^{(1)}) \\ S_1(x_0, k_y^{(f+1)}) & S_2(x_0, k_y^{(f+1)}) & \cdots & S_L(x_0, k_y^{(f+1)}) \\ \vdots & \vdots & \ddots & \vdots \\ S_1(x_0, k_y^{(M-f+1)}) & S_2(x_0, k_y^{(M-f+1)}) & \cdots & S_L(x_0, k_y^{(M-f+1)}) \end{bmatrix} \end{aligned} \tag{5.25}$$

Equation (5.25) states that if we use a spatial excitation composed of M/f Fourier coefficients spaced at $f\Delta k_y$ steps apart, then the response we receive from each coil, $S_l(x_0, \tilde{p}(y))$ will contain only Fourier modes of the spin density that correspond to the Fourier modes that are present in the spatial excitation, weighted by the entries of the RF encoding vector $\tilde{p}$.

The signals that appear in the vector on the left-hand side of Eq. (5.25) are the samples that we acquire in each coil from the MR system after an f-fold aliased spatial excitation $\tilde{p}(y)$. If we apply the coefficient matrix $C(x_0)$ of Eq. (5.16) to combine these raw sampled signals (applying to the left-hand side of Eq. (5.25) from the right), we obtain

$$\begin{bmatrix} S_1(x_0,\tilde{p}(y)) & S_2(x_0,\tilde{p}(y)) & \cdots & S_L(x_0,\tilde{p}(y)) \end{bmatrix} \begin{bmatrix} c_1^{(0)}(x_0) & c_1^{(1)}(x_0) & \cdots & c_1^{(f-1)}(x_0) \\ c_2^{(0)}(x_0) & c_2^{(1)}(x_0) & \cdots & c_2^{(f-1)}(x_0) \\ \vdots & \vdots & \ddots & \vdots \\ c_L^{(0)}(x_0) & c_L^{(1)}(x_0) & \cdots & c_L^{(f-1)}(x_0) \end{bmatrix} =$$

$$\begin{bmatrix} \tilde{p}_1 \cdots \tilde{p}_{M/f} \end{bmatrix} \begin{bmatrix} S_1(x_0,k_y^{(1)}) & \cdots & S_L(x_0,k_y^{(1)}) \\ S_1(x_0,k_y^{(f+1)}) & \cdots & S_L(x_0,k_y^{(f+1)}) \\ \vdots & \ddots & \vdots \\ S_1(x_0,k_y^{(M-f+1)}) & \cdots & S_L(x_0,k_y^{(M-f+1)}) \end{bmatrix} \begin{bmatrix} c_1^{(0)}(x_0) & \cdots & c_1^{(f-1)}(x_0) \\ c_2^{(0)}(x_0) & \cdots & c_2^{(f-1)}(x_0) \\ \vdots & \ddots & \vdots \\ c_L^{(0)}(x_0) & \cdots & c_L^{(f-1)}(x_0) \end{bmatrix} = \tag{5.26}$$

$$\begin{bmatrix} \tilde{p}_1 \cdots \tilde{p}_{M/f} \end{bmatrix} \begin{bmatrix} S(x_0,k_y^{(1)}) & S(x_0,k_y^{(2)}) & \cdots & S(x_0,k_y^{(f)}) \\ S(x_0,k_y^{(f+1)}) & S(x_0,k_y^{(f+2)}) & \cdots & S(x_0,k_y^{(2f)}) \\ \vdots & \vdots & \ddots & \vdots \\ S(x_0,k_y^{(M-f+1)}) & S(x_0,k_y^{(M-f+2)}) & \cdots & S(x_0,k_y^{(M)}) \end{bmatrix} \tag{5.27}$$

The equality of Eqns. (5.26) and (5.27) directly follows from Eq. (5.20).

Equation (5.27) now leads to the results of Section 5.1.2. Specifically, a separate response for each "s-delayed" and f-sub-sampled matrix of the k-space to the excitation can be synthesized, when the raw coil responses to an arbitrary RF encoding vector $\tilde{p}$, representing an f-fold aliased excitation over the extent of the desired FOV_y, are combined using the SMASH linear combination matrix. That is, we obtain a separate response from each of the f sets of M/f Fourier modes obtained by down-sampling the "s-delayed" (for $s = 0, \ldots, f-1$) k-space matrix of the spin density by f. Of course, Eq. (5.27) shows this only for the single location x_0 along the readout axis, but we can extend it to all N columns of the FOV along the readout direction thus leading to the above statement.

Suppose that a set of K such aliased non-Fourier RF excitations are used to encode the FOV, and we place the acquired signals in the matrix

$$\begin{bmatrix} S_1(x_0,\tilde{p}^{(1)}(y)) & S_2(x_0,\tilde{p}^{(1)}(y)) & \ldots & S_L(x_0,\tilde{p}^{(1)}(y)) \\ S_1(x_0,\tilde{p}^{(2)}(y)) & S_2(x_0,\tilde{p}^{(2)}(y)) & \ldots & S_L(x_0,\tilde{p}^{(2)}(y)) \\ \vdots & \vdots & \vdots & \vdots \\ S_1(x_0,\tilde{p}^{(K)}(y)) & S_2(x_0,\tilde{p}^{(K)}(y)) & \cdots & S_L(x_0,\tilde{p}^{(K)}(y)) \end{bmatrix} =$$

$$\begin{bmatrix} \tilde{p}_1^{(1)} & \cdots & \tilde{p}_{M/f}^{(1)} \\ \tilde{p}_1^{(2)} & \cdots & \tilde{p}_{M/f}^{(2)} \\ \vdots & \ddots & \vdots \\ \tilde{p}_1^{(K)} & \cdots & \tilde{p}_{M/f}^{(K)} \end{bmatrix} \begin{bmatrix} S_1(x_0,k_y^{(1)}) & \cdots & S_L(x_0,k_y^{(1)}) \\ S_1(x_0,k_y^{(f+1)}) & \cdots & S_L(x_0,k_y^{(f+1)}) \\ \vdots & \ddots & \vdots \\ S_1(x_0,k_y^{(M-f+1)}) & \cdots & S_L(x_0,k_y^{(M-f+1)}) \end{bmatrix} \tag{5.28}$$

If we now apply the SMASH coefficient matrix $C(x_0)$ to the left-hand side of Eq. (5.28) from the right, we obtain the synthesized (i.e., recombined) response to each excitation, for the column of the image x_0,

$$\begin{bmatrix} S_1(x_0,\tilde{p}^{(1)}(y)) & S_2(x_0,\tilde{p}^{(1)}(y)) & \dots & S_L(x_0,\tilde{p}^{(1)}(y)) \\ S_1(x_0,\tilde{p}^{(2)}(y)) & S_2(x_0,\tilde{p}^{(2)}(y)) & \dots & S_L(x_0,\tilde{p}^{(2)}(y)) \\ \vdots & \vdots & \vdots & \vdots \\ S_1(x_0,\tilde{p}^{(K)}(y)) & S_2(x_0,\tilde{p}^{(K)}(y)) & \cdots & S_L(x_0,\tilde{p}^{(K)}(y)) \end{bmatrix} \begin{bmatrix} c_1^{(0)}(x_0) & \cdots & c_1^{(f-1)}(x_0) \\ c_2^{(0)}(x_0) & \cdots & c_2^{(f-1)}(x_0) \\ \vdots & \ddots & \vdots \\ c_L^{(0)}(x_0) & \cdots & c_L^{(f-1)}(x_0) \end{bmatrix} =$$

$$\begin{bmatrix} \tilde{p}_1^{(1)} & \cdots & \tilde{p}_{M/f}^{(1)} \\ \tilde{p}_1^{(2)} & \cdots & \tilde{p}_{M/f}^{(2)} \\ \vdots & \ddots & \vdots \\ \tilde{p}_1^{(K)} & \cdots & \tilde{p}_{M/f}^{(K)} \end{bmatrix} \begin{bmatrix} S_1(x_0,k_y^{(1)}) & \cdots & S_L(x_0,k_y^{(1)}) \\ S_1(x_0,k_y^{(f+1)}) & \cdots & S_L(x_0,k_y^{(f+1)}) \\ \vdots & \ddots & \vdots \\ S_1(x_0,k_y^{(M-f+1)}) & \cdots & S_L(x_0,k_y^{(M-f+1)}) \end{bmatrix} \begin{bmatrix} c_1^{(0)}(x_0) & \cdots & c_1^{(f-1)}(x_0) \\ c_2^{(0)}(x_0) & \cdots & c_2^{(f-1)}(x_0) \\ \vdots & \ddots & \vdots \\ c_L^{(0)}(x_0) & \cdots & c_L^{(f-1)}(x_0) \end{bmatrix} = \tag{5.29}$$

$$\begin{bmatrix} \tilde{p}_1^{(1)} & \cdots & \tilde{p}_{M/f}^{(1)} \\ \tilde{p}_1^{(2)} & \cdots & \tilde{p}_{M/f}^{(2)} \\ \vdots & \ddots & \vdots \\ \tilde{p}_1^{(K)} & \cdots & \tilde{p}_{M/f}^{(K)} \end{bmatrix} \begin{bmatrix} S(x_0,k_y^{(1)}) & S(x_0,k_y^{(2)}) & \cdots & S(x_0,k_y^{(f)}) \\ S(x_0,k_y^{(f+1)}) & S(x_0,k_y^{(f+2)}) & \cdots & S(x_0,k_y^{(2f)}) \\ \vdots & \vdots & \ddots & \vdots \\ S(x_0,k_y^{(M-f+1)}) & S(x_0,k_y^{(M-f+2)}) & \cdots & S(x_0,k_y^{(M)}) \end{bmatrix} \tag{5.30}$$

We can rewrite the equality of Eqns. (5.29) and (5.30) in matrix notation as

$$\tilde{P}F_W(x_0)C(x_0) = \tilde{P}F(x_0). \tag{5.31}$$

The matrix $F_W(x_0)$ contains only the Fourier modes of the sample that are induced by the RF encoding vectors, and only involves Fourier modes of the spin density weighted by the sensitivity of each receiver coil. $F(x_0)$ contains the complete set of Fourier modes of the sample for column x_0, as would have been formed by a uniform, unit sensitivity, coil.

The question of how to best encode the FOV given *a priori* knowledge of the FOV contents and spatial sensitivities of the coils can now be addressed. Assuming that the RF encoding matrix $\tilde{P}$ of Eq. (5.31) is square ($K = M/f$) and invertible, we can eliminate it, to note that if the matrix $C(x_0)$ is orthogonal then the left singular vectors of $F_W(x_0)C(x_0)$ are the same as those of $F(x_0)$. Now, if we encode all columns x_i of the image with a single set of encoding vectors, we must look at the concatenated matrices $F'_W = [F_W(x_1)|\cdots|F_W(x_i)|\cdots]$ and $F' = [F(x_1)|\cdots|F(x_i)|\cdots] = [F_W(x_1)C(x_1)|\cdots|F_W(x_i)C(x_i)|\cdots]$. Note that the left singular vectors of F'_W are again undisturbed by the presence of orthogonal $C(x_i)$ compared to those of F'.

To consider the case of encoding in k-space, i.e., with the matrix F' containing columns ranged by k_x rather than x, we note that a Fourier transform of the same numbered columns of all $F(x_i)$

produce the elements along the range of k_x for the mode $k_y^{(m)}$, the latter depending on the row and column number. That is, the elements of every $F(x_i)$ at the same row and column correspond to a single mode $k_y^{(m)}$, so that performing the Fourier transform of the elements $F'_{j,g:f:Nf}$ (with $g \leq f$) by applying the N-by-N discrete Fourier transform matrix, $E^{(N\times N)}$, produces the signal

$$S(k_x, k_y^{(f(j-1)+g)}) = \left[F'_{j,g:f:(Nf)}(x_1), \cdots, F'_{j,g:f:(Nf)}(x_N)\right] E^{(N\times N)}, \tag{5.32}$$

ranged by k_x. A similar approach holds for the matrices $F_W(x_i)$, except that instead of skipping f columns we instead need to skip L columns. Effectively, the matrix F' can be converted into a matrix ranged by k_x by multiplying it from the right with the Kronecker product $I^{(f\times f)} \otimes E^{(N\times N)}$, where $I^{(f\times f)}$ is the f-by-f identity matrix and $E^{(N\times N)}$ is the N-point DFT matrix. In the case F_W, we need to apply the Kronecker product $I^{(L\times L)} \otimes E^{(N\times N)}$. Again, because $I^{(f\times f)} \otimes E^{(N\times N)}$ and $I^{(L\times L)} \otimes E^{(N\times N)}$ are orthogonal matrices, the left singular vectors of F'_W are the same as those of F', giving us the ability to choose to compress either the contents of F' or F'_W in k-space.

To summarize, our main here result is that when the SMASH combinations form orthogonal matrices, the broadband linear system response that we need to encode is given by the concatenation of the sub-sampled-by-f and s-delayed matrices derived from the full k-space matrix of the FOV, as shown in Eq. (5.15) (which is just a rearrangement of the columns of $F' \left[I^{(f\times f)} \otimes E^{(N\times N)}\right]$ in order to range all the k_x before shifting to the s-delay). Missing from Eq. (5.15) is the knowledge that the SMASH linear combination matrices $C(x_i)$ are unlikely to be orthogonal. This subtlety leads to a choice of encoding either F'_W or F'. This is probably best resolved by encoding the contents of F'_W in order to avoid noise amplification.

5.1.4 NF-SMASH Results

NF-SMASH Experimental Verification

In this section we provide experimental verification of the NF-SMASH encoding method. Using a standard cardiac phased array receiver containing four elements, whose sensitivities are shown in Fig. 5-1, we were able to achieve a SMASH speedup of 2, albeit at a significant loss of SNR. Each column of coil sensitivities along the readout axis was individually fitted to pre-conditioned harmonics (the preconditioning included rephasing in order to account for phase differences in between coils e.g., due to differing cable lengths, as well as scaling of the harmonics by the sum of the coil sensitivities [138]) as shown in Fig. 5-2.

The 2-fold accelerated Fourier encoded SMASH experiment produced the reconstructed image shown in the first column of Fig. 5-3. The full FOV target resolution was 256 and since $f = 2$, the 128 Fourier modes acquired by each coil were recombined using Eq. (5.6) for each of the two harmonics. Since the horizontal axis was phase encoded, this combination was individually applied to each row of the image shown (thus corresponding to a given x_i). Since the linear combinations computed for the particular row x_i were fits to pre-conditioned harmonics, the modulation of the preconditioning was removed by dividing the image with it after reconstruction [138].

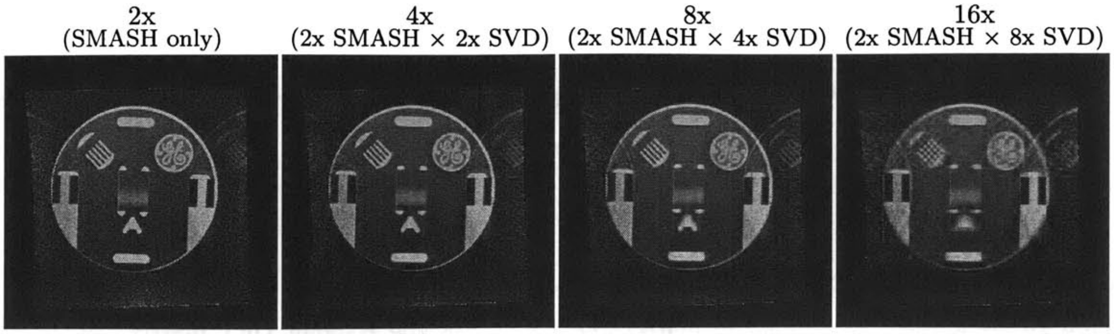

Figure 5-3: Experimental NF-SMASH images of a phantom acquired on a 1.5T scanner using a 4-element receiver array to achieve a 2-fold SMASH parallel acceleration and increasing levels of additional broadband compression. The horizontal dimension is parallel and non-Fourier encoded, and the SMASH harmonic fits used to obtain the parallel reconstruction are shown in Fig. 5-2.

Following the NF-SMASH method described in this section, the raw k-space samples obtained by the coil array elements at the speedup of two (i.e., only even lines of the full FOV k-space) were decomposed via the SVD. Since the target resolution was 256, the system response matrix $F'_W = [\cdots|F_W(x_i)|\cdots]$ was 128-by-1024, yielding a 128-dimensional space. Decomposing this system response via the SVD then produced the set of two-fold aliased spatial excitation profiles, an example of which is shown in Fig. 5-4. In effect, this vector was crafted so as to simultaneously optimally encode each of the two aliases resulting from the SMASH down-sampling of two for the ensemble of coils.

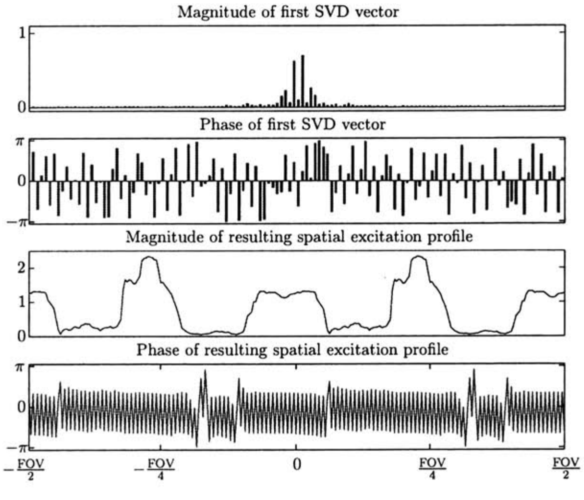

Figure 5-4: Example of an experimental singular encoding vector used to acquire and reconstruct the non-Fourier encoded images of Fig. 5-3. Since a SMASH speedup of 2 was used in the reconstruction, the SVD profile is two-fold aliased over the extent of the full FOV, while the RF encoding vector has zeros in every second sample position.

Reconstruction from various broadband non-Fourier encoding speedup factors, attained by truncating the acquisition basis dimensionality for acquisition, are shown in the last 3 columns of Fig. 5-3. The reconstruction follows trivially from the left-hand side of the equality in Eq. (5.29), by inverting the effect of the encoding matrix prior to applying the SMASH linear combinations.

The shortcomings of SMASH imaging, include the fitting of a small number of arbitrary coil sensitivities to harmonic functions over a large extent of the FOV. This shortcoming is evident in the reconstructions of Fig. 5-3, for both Fourier and non-Fourier acquisitions. These shortcomings can not be remedied unless coils are designed specifically for the task, and their orientation about the imaging plane is carefully chosen.

Additionally, the 1.5T GE Signal LX 8.3 MR scanner that was available to us when we performed these experiments is limited by four receivers, offering little room for parallel imaging applications. The dissemination of parallel imaging has forced most scanner manufacturers to provide upgrades that not only allow a greater number of simultaneous receive channels but that offer parallel imaging reconstruction software as well.

In our institution, both MR scanners that were available for research at the time of these experiments have since been updated to 1.5T GE EXCITE 10.0 systems, that feature 8 to 16-channel receivers. Major incompatibilities in the proprietary scanner system software introduced by the recent change prevented us from acquiring experimental results for higher accelerations. Accordingly, in order to gain some more insight regarding the level of compression attainable between non-Fourier encoding and parallel imaging, we resort to simulation.

NF-SMASH Simulation Results

In a simulated experiment, the original k-space matrix of a phantom was broken into four interleaved matrices $F^{(g)} = F_{g:4:M,:}$, $g = 1, \ldots, 4$ that were placed side by side to form the system response matrix for a SMASH speedup of $f = 4$. The SVD of the $M/4$-by-$4N$ matrix yielded the matrix U of column vectors to be used for RF encoding. Since the simulation does not involve noise, we chose to decompose the k-space matrix of the phantom rather than the down-sampled and weighted k-space matrices obtained by the coils.

Each of the RF encoding vectors obtained from the rows of U^H was length $M/4$. In order to simulate its excitation on the phantom, the spatial profiles corresponding to the RF pulses were derived from $\hat{U}^H E$, where E is the M-point DFT matrix, and the matrix $\hat{U}^H$ contained the up-sampled RF encoding functions, i.e., the rows of U^H with zeros inserted between the Fourier modes that the RF pulses of U^H contained. An example of these encoding functions is shown in Fig. 5-5.3. The acquisition of the signal response of the sample's k-space to each aliased spatial profile was then simulated for each of six coils. The sensitivities of the six simulated coils, shown in Fig. 5-5.1, were chosen as shifted-mean Gaussians which are more amenable to the SMASH harmonic fits.

Four harmonics were fitted to the Gaussian-shaped coil sensitivity profiles, as shown in Fig. 5-5.2. These fits were used to reconstruct the response of each of the k-space interleaves individually to each RF pulse. Figure 5-6 summarizes the results of the NF-SMASH reconstructions. The dimensionality

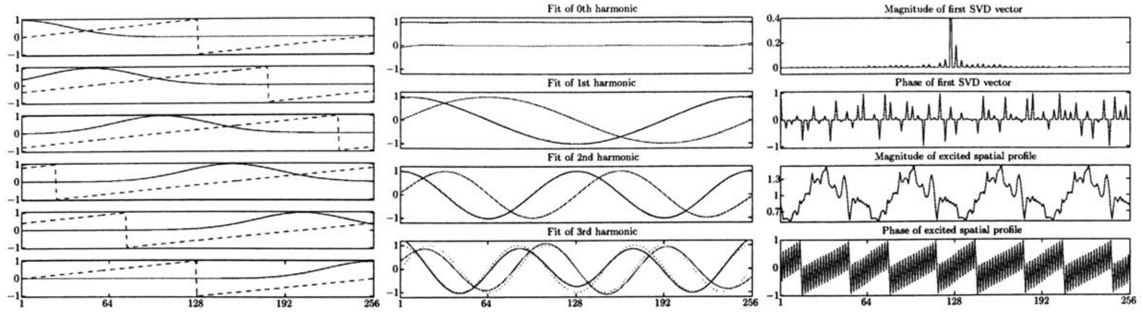

5-5.1: Devised spatial sensitivity profiles of 6 coils. The phase (dotted lines) is plotted in units of radians.. Each profile is a shifted-mean Gaussian with a linear phase profile.

5-5.2: SMASH-fitted harmonics (solid lines) of the 6 coil sensitivities to the first four harmonics (dotted lines).

5-5.3: Example non-Fourier encode produced by SVD of the 64×1024 system response matrix. Because of the 4x SMASH speedup, the spatial profile encodes each of the 4 aliased portions of the image identically.

Figure 5-5: Coil sensitivities and harmonic fits used with the NF-SMASH simulation.

reduction of up to 4x, and even as high as 8x, by non-Fourier encoding, in addition to the 4x speedup obtained by parallel imaging is possible without significant loss of resolution. In particular, the 16x total speedup reconstruction, shown in the fourth column of Fig. 5-6, compares advantageously with the 16x SVD encoded image of Fig. 3-2 where the entire speedup of 16x relied on dimensionality reduction alone.

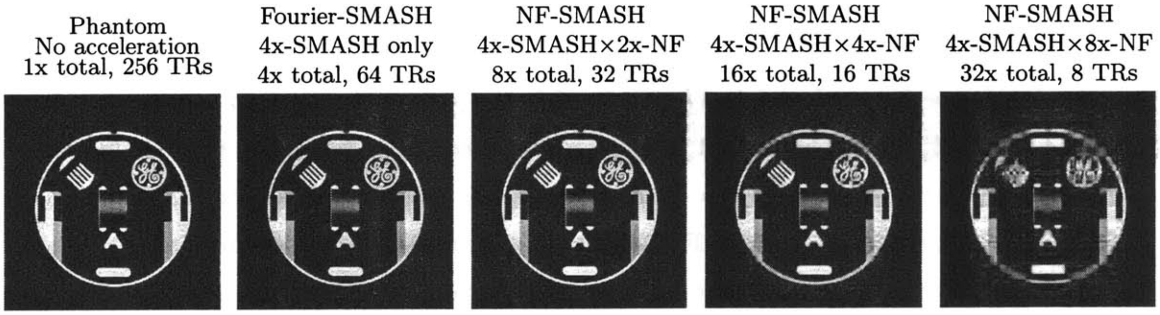

Figure 5-6: Simulation results of combining the SMASH procedure with SVD non-Fourier encoding. Six coils used to achieve a 4x SMASH speedup factor mold the 256×256 original k-space matrix to a 64×1024 system response matrix that can be encoded as described in the text. The spatial encoding profiles used to encode this system response, encode each alias of the k-space matrix simultaneously, thus enabling the SMASH method to unalias the overlapped portions as usual.

5.2 The General NF*P Theory

We are now ready to extend the general digital non-Fourier encoding methodology that was introduced by Panych et. al. [117] in order to include the spatial encoding induced by non-uniform coil sensitivities and use this to construct a composite digital non-Fourier system response that includes signal from multiple RF receiver coils. This composite system response will then be shown to enable non-Fourier spatially encoded parallel MR imaging using any parallel MRI method. In the final sections of this chapter we will present methods that materialize this digital NF*P encoding methodology and provide experimental results that demonstrate the use of the framework.

5.2.1 Revisiting the Non-Fourier Spatial Encoding Model

Because this section will require some additional notation, we first restate the Fourier and non-Fourier encoding models with simplified notation doing away with the nitty-gritty details that were central to Chapter 2. In general Fourier basis imaging, the received MR signal is described by the equation

$$s(k) = \int_V \rho(r) e^{-i2\pi k \cdot r} dr, \tag{5.33}$$

with $\rho(r)$ the excited spin density function throughout the sample volume V and weighted by various imaging factors (e.g., relaxation terms, hardware characteristics etc.), as before.

The simple 2D spin echo experiment of Section 2.2.1, with the readout, phase encode, and slice-select gradients as G_x, G_y and G_z respectively that gave rise to Eq. (2.14) is the representation of Eq. (5.33) as a function of wavenumbers

$$s(k_y, k_x) = \int_{-\alpha}^{\alpha} \left[\iint \rho(x, y, z) e^{-i2\pi(k_x x + k_y y)} dx\, dy \right] dz \tag{5.34}$$

where 2α is the excited slice thickness.

Appropriate manipulation of the readout and phase encoding gradients produces the samples at the wavenumbers k_x and k_y of Eqns. (2.8) and (2.13). As before, the MR system response matrix defined by placing these samples in the M-by-N k-space matrix F, with readout samples placed along the columns, produces the weighted spin density image of the slice as

$$R = \mathcal{F}^{-1}\{F\}, \tag{5.35}$$

with inverse Fourier transformation denoted by $\mathcal{F}^{-1}\{\cdot\}$.

The digital non-Fourier spatial encoding model [117], based on using the shaped RF excitation described by $p(t)$ (Eq. (2.16)) to excite the spatial encoding profile along the phase encode direction while eliminating the phase encode gradient of the Fourier sequence (c.f., Fig. 2-4.1), leads to the superposition of the individual hard pulse contributions, under the assumption of low flip angle excitation, which is then given by (Eq. (2.23)):

$$a(p, k_x) = \int_{-\alpha}^{\alpha} \iint \rho(x, y, z) \left(\sum_{m=1}^{M} p_m e^{-i2\pi k_y^{(m)} y} \right) e^{-i2\pi k_x x} dx\, dy\, dz \tag{5.36}$$

$$= \sum_{m=1}^{M} p_m s(k_y^{(m)}, k_x). \tag{5.37}$$

The row vector $p = (p_1, \cdots, p_M)$ contains the hard pulses p_m corresponding to the RF excitation $p(t)$. Although in Section 2.2.2 we used the 180° refocuser pulse to exclusively perform slice selection, a 2D z-y spatial excitation that induces the spatial profile in the image plane, but additionally selects a slice along z can also be employed. Using the Fourier transform notation of Eq. (5.35), the spatial profile of transverse magnetization generated by the RF pulse is

$$p(y) \approx \mathcal{F}^{-1}\{p\}. \tag{5.38}$$

The counterpart of Eq. (2.26) is now $a = pF$, with the length-M input vector p describing the RF excitation waveform, the length-N output "response" vector a of sampled data, and F the M-by-N system response (k-space) matrix corresponding to the spin distribution. Similarly, the matrix formulation of non-Fourier encoding (c.f., Eq. (2.27), obtained by collecting the sampled responses into the rows of the matrix A is

$$A = PF, \tag{5.39}$$

which yields the k-space matrix by using an appropriate inverse:

$$F_{\text{est}} = P^{\dagger} A. \tag{5.40}$$

5.2.2 Non-Fourier Encoding with Parallel Receiver Coils

To merge non-Fourier encoding with parallel receiver coil signal acquisition, Eq. (5.33) is augmented with an additional term describing the spatial sensitivity weighting $W_l(r)$ of receiver coil l, of a set of L coils. The signal acquired in each coil is then described by [139, 126, 147]:

$$s_l(k) = \int_V W_l(r) \rho(r) e^{-i2\pi k \cdot r} dr. \tag{5.41}$$

Discretization of Eq. (5.41) produces the k-space matrix sampled by each coil as

$$F_l = \mathcal{F}\{W_l \circ R\}, \tag{5.42}$$

where R is the spin density image of the slice from Eq. (5.35), and W_l is the discretized form of the coil sensitivity, $W_l(r)$. Here, the coil's k-space system response matrix F_l is derived from an element-by-element-wise product, (denoted $\circ$), of the discretized spatial sensitivity profile of coil l and the spatial spin distribution.

In Fourier encoded parallel imaging, a reduction in acquisition time is achieved by acquiring only a subset of lines of k-space while sampling the signal using multiple coils with different spatial sensitivities. We will represent this with a sparse matrix D derived from the M-by-M identity matrix, $I^{(M\times M)}$. For Fourier basis imaging, each row of D corresponds to a repetition of the sequence (i.e., phase encode step). For a given sequence repetition (row of D), the column of D that the one appears in represents the particular phase encode step k_y that is sampled at that repetition. The ratio of number of columns to rows in D indicates the parallel imaging speedup factor. The signals sampled by coil l in a parallel imaging experiment can then be compactly expressed using D as

$$S_l^f = D\left(\mathcal{F}\{W_l \circ R\}\right) = DF_l, \tag{5.43}$$

where the superscript f denotes acquisition at a speedup of f. The matrix D then has dimensions M/f-by-M.

Originally, SMASH [139] and SENSE [126] required that D be derived by regular down-sampling of the identity matrix. For example, for a speedup factor of two, D contains only every second row of $I^{(M\times M)}$, corresponding to skipping every second phase encode. Space-RIP [67], and subsequent adaptations of SMASH and SENSE, can reconstruct the image given any arbitrary set of M/f rows of the identity matrix (i.e., given any arbitrary reduced set of phase encode lines).

Regardless of which parallel imaging method is used, once the down-sampling matrix D for a speedup of f is chosen, the weighted k-space matrix S_l^f is obtained from all L coils, with $L \geq f$, each with differing (linearly independent) sensitivity, providing independent information about the sample. Each k-space matrix thus obtained represents the f-fold-aliased and sensitivity-weighted spin density image seen by the respective coil. The ensemble of these matrices are then used with the parallel imaging algorithm of choice to produce the full FOV k-space or image.

The goal of *any* spatial encoding method is then to produce precisely these S_l^f, or accurate estimates thereof, so that parallel reconstruction can be applied to produce the unaliased, full FOV image. To enable the potential of non-Fourier encoding with parallel imaging, we augment Eq. (5.41) with the spatially selective term $p(r)$ that, as before (e.g., Eq. (5.10)), corresponds to the spatial RF excitation p. The equation describing the received signal thus becomes [66]:

$$a_l(k,p) = \int_V W_l(r)\rho(r)p(r)e^{-i2\pi k\cdot r}dr. \tag{5.44}$$

Discretization of this expression, as for the 2D example with the uniform sensitivity coil (c.f., Eq. (5.37)), results in a linear equation relating the signal acquired by coil l and the discrete RF input as

$$a_l = pS_l = p(\mathcal{F}\{W_l \circ R\}). \tag{5.45}$$

We note that the goal of the *parallel* non-Fourier imaging experiment is to produce the matrix S_l^f of Eq. (5.43). Therefore, as we saw in section 5.1.3, the RF pulse only needs to encode those Fourier modes (i.e., those necessary for parallel reconstruction). We may thus craft the spatially selective RF excitation to only encode those modes, which is also accomplished by use of the sub-sampling matrix D. Noting that this matrix operates on the left, it is the vector $p^f = pD^T$ of length M/f, that captures precisely the selected Fourier modes. The signal produced when using this encoding vector only contains those Fourier modes necessary for parallel reconstruction:

$$a_l^f = p^f D(\mathcal{F}\{W_l \circ R\}) = p^f S_l^f. \tag{5.46}$$

Now, the physical analogue of the spatial excitation p^f is revealed by expanding Eq. (5.46) to obtain

$$a_l^f = p\left(D^T D\right)(\mathcal{F}\{W_l \circ R\}). \tag{5.47}$$

In particular, the composite matrix $D^T D$ is simply a projection matrix that, when applied to the full FOV excitation p as the projection $pD^T D$, has the effect of replacing with zeros those elements of p that correspond to Fourier modes of the sample that are not necessary for parallel imaging reconstruction. When D is the regularly down-sampled identity, this projection amounts to replacing with zeros $f-1$ elements following each element of the vector that is retained. The spatial domain analogue of this projection is given by the Fourier transform

$$p^f(y) \approx \mathcal{F}^{-1}\{pD^T D\}, \tag{5.48}$$

which describes a function that is repeated f times over the FOV. That is, the spatial encoding function is an f-fold aliased function.

5.2.3 The non-Fourier Parallel Imaging System Response Matrix

When L coils are used to sample the signal resulting from the application of the spatially selective RF pulse p^f, the individual coil responses of Eq. (5.46) can be combined by concatenation into a single vector as

$$a^f \equiv \left[a_1^f|\cdots|a_L^f\right] = p^f\left[S_1^f|\cdots|S_L^f\right] \equiv p^f S^f, \tag{5.49}$$

where the symbol "|" again denotes matrix or vector concatenation as appropriate. Equation (5.49) effectively reveals a composite k-space system response matrix, S^f, capturing the subsampled output from multiple coils in a concise fashion. This composite response matrix has dimensions M/f-by-LN, given the number of coils L, the size of the desired k-space information (M-by-N), and the parallel imaging speedup factor f. When the input RF encoding vector p^f of length M/f is applied, the ensemble of coils produce the composite response a^f of length LN. Fundamentally then, Eq. (5.49) allows one to apply any non-Fourier encoding method in the same fashion as the single uniform sensitivity coil digital non-Fourier encoding methodology.

The difference of this parallel imaging "enabled" composite system response matrix is that its column space is intrinsically smaller. For example, in order to produce a target resolution of M along the non-Fourier encoded dimension using a parallel imaging speedup of f and full encoding of the k-space, one can use the rows of an arbitrary M/f-by-M/f invertible matrix $\tilde{P}$ for the set of excitations, reflecting the parallel imaging efficiency. For reduced basis adaptive imaging, the encoding matrix $\tilde{P}$ is K-by-M/f, where $K \leq M/f$, reflecting the additional non-Fourier efficiency. In every case, the sampled signals form the matrix

$$A^f = \tilde{P} S^f \tag{5.50}$$

of size K-by-LN, $K \leq M/f$. Inverting the non-Fourier encoding process of Eq. (5.50) yields the individual coil subsampled k-space matrices as

$$S^f_{\text{est}} = \tilde{P}^{\dagger} A^f, \tag{5.51}$$

since they can be separated by reversing the concatenation of the matrix S^f. These constituent matrices can then be used with the parallel imaging algorithm of choice to reconstruct the full M-by-N image of the FOV.

5.3 NF*P Methods & Experiments

5.3.1 Methods

Equipment

All experiments described here were performed using a commercial four-element phased array cardiac receiver (GE Medical Systems, Milwaukee, WI), on a 1.5T GE Signa Horizon LX EchoSpeed MR imager equipped with 4 G/cm gradient coils at 14.9 G/cm/msec maximum slew rate, while maximum B_1 is 250 mG.

The simple non-Fourier encoding spin echo pulse sequence of Fig. 2-4.1 was used to excite the spatial encoding profiles. The RF pulses were not optimized with Variable Rate Selective Excitation (VERSE) [17] as will be described later. Typical low flip ($\theta \simeq 30°$) pulses require Δt in the range of

16 to 20 μsec. RF pulses designed for a resolution of $M = 256$ required $M\Delta t = 4.096$ msec, compared to the standard 3.2 msec 90° slice-select pulse used by commercial sequences on our system. With the parallel imaging speedup of f, the length of the non-Fourier excitation pulses for the regular down-sampling experiments was reduced to $M\Delta t/f$.

Receiver Array Sensitivity Calibration

A simple approach was used to estimate the spatial sensitivities of each array element based on two full Fourier phase encoded acquisitions of a homogeneous NiCl-doped water phantom using the scanner's body coil and the phased array receivers separately [67]. The measured sensitivities were presented in Fig. 5-1. The intended configuration of the cardiac receiver array elements was used, i.e., two coils anterior (coils 3 & 4), two posterior (1 & 2), each set in a left/right configuration.

The same axial plane as measured for the rectangular homogeneous water phantom was used for both sensitivity calibration as well as accelerated imaging experiments. Array geometry was fixed using a simple Plexiglas enclosure also used for fixing the receiver geometry in clinical parallel imaging experiments at our institution. Full phase encoding was achieved using the identity RF encoding matrix [118]. Imaging parameters (TR, TE, BW, etc) were fixed for all experiments, and array element sensitivities were acquired for the entire full FOV of 16 cm along both axes. We note that array self-calibration [58] is readily incorporated in our framework by inclusion of the central rows of k-space in the sub-sampling matrix D.

Parallel Imaging Reconstructions

According to the NF*P framework presented, once the composite k-space system response composed of any set of k-space lines has been non-Fourier reconstructed via Eq. (5.51), any parallel imaging reconstruction method can be used to reconstruct the full FOV image. To demonstrate this ability we use two example methods in addition to the SMASH reconstructions of the previous section:

Cartesian SENSE. A simple Cartesian SENSE [126] implementation with regular integer k-space down-sampling was used. Tikhonov regularization was used to limit receiver noise in the reconstruction [61].

Irregular Space-RIP. Space-RIP [67] was originally designed to enable reconstruction of the image when the set of k-space lines acquired is not a regularly down-sampled subset of the full k-space [67]. The abstraction afforded in the NF*P framework by use of the down-sampling matrix D also allows non-Fourier encoding methods to be applied to any set of lines without changes. A reduced set of lines to acquire (i.e., the down-sampling matrix D) was derived from the *a priori* measured k-space energy distribution of the imaged sample. In particular, the projection of the k-space of the sample onto the readout axis (i.e., norm of each k_y line of k-space) was assumed to describe a probability mass function (PMF). A series of M/f random numbers drawn according to this PMF immediately yields the set of k-space lines used (i.e., the column numbers of D that should contain a 1). Truncated SVD inversion of the Space-RIP system matrix was used to avoid noise amplification.

Spatial Encoding Methods

Two representative non-Fourier encoding methods are used to demonstrate the NF*P framework.

Hadamard Encoding. For M a power of two, the M-by-M Hadamard matrix H_M is defined by Eq. (2.29). In the low flip angle approximation, the RF encoding matrix $\tilde{P}$ was derived by Fourier transformation of each row of H_M, i.e.,

$$\tilde{P} = H_M E^H, \tag{5.52}$$

with E is again the M-point DFT matrix. The rows of $\tilde{P}$ were then used as RF excitations in consecutive experiment repetitions of the sequence. The target resolution of $M = 256$ along the non-Fourier encoded axis required use of H_{128} with the parallel imaging speedup of $f = 2$ that was used, as compared to use of H_{256} when parallel imaging was not applied. Each of the 128 RF pulses derived from H_{128} was naturally composed of 128 hard pulses, while the pulse sequence produced 256 readout samples from each coil.

For the 4-element array, once all repetitions were completed, the samples were arranged in the 128-by-$(256 * 4)$ composite response matrix A^f (c.f., Eq. (5.50)) which then represented the Hadamard spatially encoded FOV contents. Since Hadamard matrices are orthogonal, non-Fourier inversion was achieved by multiplying this acquired composite response matrix by the Hermitian conjugate of the RF encoding matrix, i.e., $\tilde{P}^\dagger = \tilde{P}^H$ in Eq. (5.51). This resulted in the subsampled composite k-space matrix S^f_{est} (c.f., Eq. (5.51)) which was then separated in four pieces, each sized 128-by-256, corresponding to each coil $l = 1, \ldots, 4$. Application of each of the two parallel imaging methods on these reduced FOV k-space matrices directly yielded the complex valued image data. The reconstructed images were 256-by-256, while an acquisition speedup of 2 for the Hadamard encoding method was achieved.

Singular Value Decomposition Encoding. Prior to non-Fourier imaging, the sample was acquired with the coil array using typical parallel imaging phase encoding, yielding four matrices of size 128-by-256. Concatenation of these matrices provided the reference composite system response matrix, S^f (i.e., the *a priori* information). The SVD was then calculated as $S^f := U\Sigma V^H$. Since the matrix S^f was 128-by-$(256 * 4)$, U was 128-by-128, reflecting the parallel imaging dimensionality reduction of M/f.

Accelerated SVD encoding was then achieved by truncating the SVD vector basis to the first $K \leq M/f$ vectors. The amount of subspace truncation, by retaining K basis vectors, represents the SVD encoding speedup $f_{\text{SVD}} = (M/f)/K$. In this example of $M = 256$ and parallel imaging speedup of $f = 2$, the speedups of $f_{\text{SVD}} = 4$ and 8 were obtained by retaining only the first $K = 32$ and 16 columns of U. However, when e.g., $f_{\text{SVD}} = 4$ (i.e., $K = 32$ encoding vectors were used), the total speedup of the NF*P experiment was in fact $f_{\text{tot}} = M/K = 8$, representing a composite speedup due to the combination of the two methods. This is a rather desirable property as we will also see later, since a desired target speedup may be obtained while neither method is used with an individual speedup that is detrimental to imaging quality.

Use of the K SVD basis vectors from U for encoding is straightforward. They were directly placed in the rows of $\tilde{P}$ since, in this case, they were computed from a k-space reference. For $K = 32$, $\tilde{P}$ was 32-by-128 and each row was used as the excitation RF pulse in a sequence repetition. Acquisition and non-Fourier inversion proceeded precisely as with Hadamard encoding: readout samples were concatenated to form A^f, while the rank-K compressed k-space approximation of the FOV contents was then reconstructed using Eq. (5.51): $S^f_{\text{est}} = \tilde{P}^H A^f = \left\{\tilde{P}^H \tilde{P}\right\} S^f$. This k-space estimate was again separated into the respective coil portions and used with the parallel imaging method to reconstruct the image.

RF Excitation of the Parallel-Imaging Enabled Non-Fourier Encoding Functions

In all cases, excitation of the rows of $\tilde{P}$ for regular down-sampling NF*P experiments used the compressed RF form, $p^f = pD^T = \tilde{P}_{j,:}$ for each row j, of length $M/f = 128$ and, for $\Delta t = 20$ μsec, a G_y gradient for 8 cm FOV (c.f., Fig. 2-4.1). Irregular down-sampling experiments made use of the full uncompressed form $pD^T D = \left\{\tilde{P}_{j,:}\right\} D$, and a G_y gradient for 16 cm. As shown in Fig. 5-7, the regular down-sampling parallel imaging case leads to aliasing of the encoding profile over the FOV so that each portion of the image that can be decoded via the parallel imaging method is identically non-Fourier encoded. For the irregular down-sampling case, the omission of Fourier modes from the excitation of the encoding functions according to NF*P leads to a smoother excitation profile which is easier to achieve.

5.3.2 Results

Fourier phase and non-Fourier encoded experiments were performed using a parallel imaging speedup of two, employed along the horizontal direction to reflect coil array element placement (c.f., Fig. 5-1). Target full FOV matrix size was 256-by-256. All acquisitions used 500 msec TR, 20 msec TE, 10 mm slice thickness and 16 cm FOV gradient for 16 KHz BW along readout.

Total imaging time for the phase encoded experiments was 64 sec (2x over non parallel imaging) in order to acquire the 128 phase encodes. The reconstructed images are shown in the first column of Fig. 5-8. Results from Hadamard and SVD encoded acquisitions for each parallel imaging method are shown in the last 3 columns of Fig. 5-8. For the parallel imaging speedup and target resolution, full encoding of k-space also required 128 non-Fourier encoding functions and 64 sec imaging time,

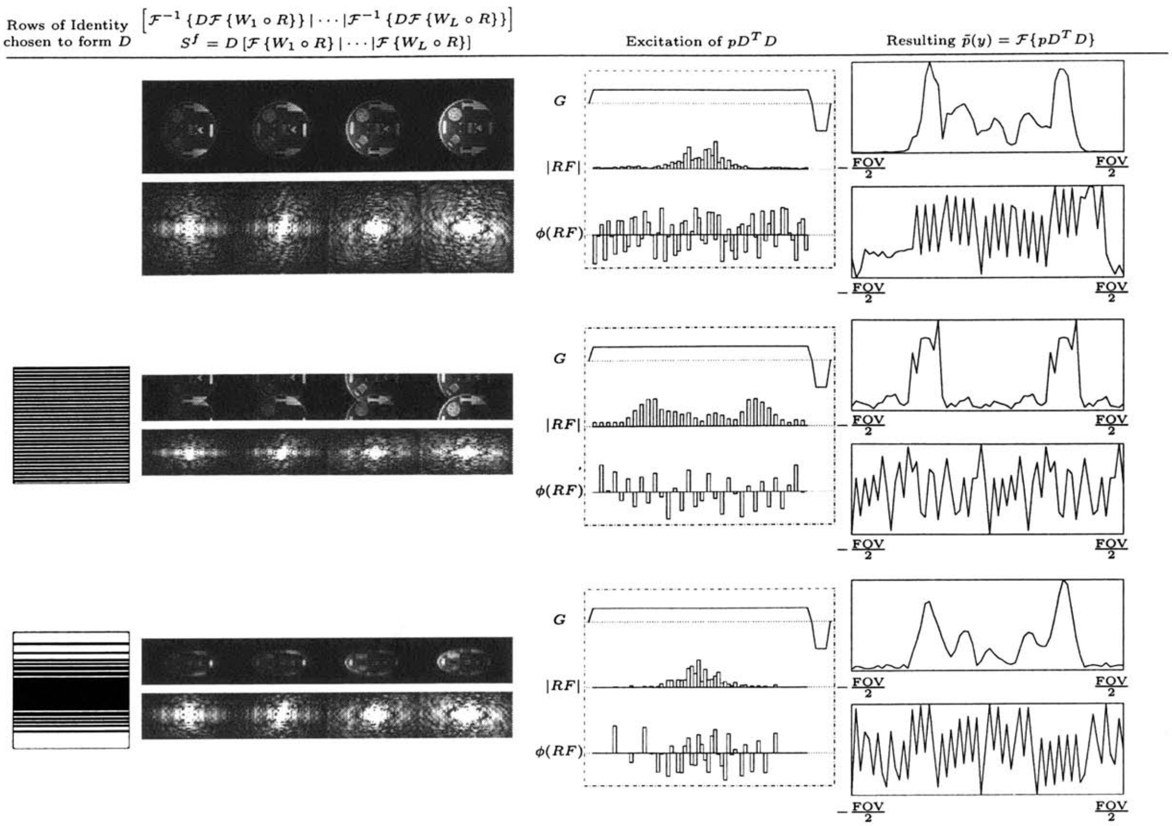

Figure 5-7: Example of non-Fourier encoding functions used in non-Fourier parallel imaging with NF*P. Top row is the typical example of full FOV non-Fourier encoding. The middle row corresponds to encoding for a parallel imaging speedup of two with regular down-sampling. The bottom row corresponds to irregular down-sampling, e.g., for use with Space-RIP. The parallel non-Fourier encoded dimension is the vertical axis of the images as shown. The second column shows the aliased images acquired from each of four coils. The acquired k-spaces are shown underneath the images. The third column shows the excitation of one non-Fourier encoding vector $p^fD = pD^TD$ that is used to encode those k-spaces according to NF*P. For conceptual clarity the excitation of the RF pulses was not compressed, thus revealing the zeros in the RF pulses of the two bottom rows (which correspond to the white rows of the sub-sampling matrix). The final column shows the resulting spatial excitation profile, $\tilde{p}(y)$, induced by the shaped RF excitations (magnitude on top of phase plots). The regularly down-sampled case leads to a two-fold aliased spatial profile within the FOV, while for the irregularly down-sampling case it is seen that the profile is smoother compared to the first row.

e.g., using H_{128} for Hadamard encoding, as shown in the second column of Fig. 5-8. Truncated SVD encoding offered a combined speedup factor of up to 8x in 16 sec imaging time for $K = 32$ encoding functions, with minimal loss of resolution as shown in the third column of Fig. 5-8. Finally, for $K = 16$ (16x total speedup, last column of Fig. 5-8) imaging time was 8 sec.

These results illustrate use of any parallel imaging method with any non-Fourier encoding method and should not be used for comparing the two particular parallel imaging methods. Accordingly, the Fourier phase encoded images and the corresponding non-Fourier encoded images for each P-MRI method, show that image quality is maintained with NF*P across varying speedup factors. The 2x

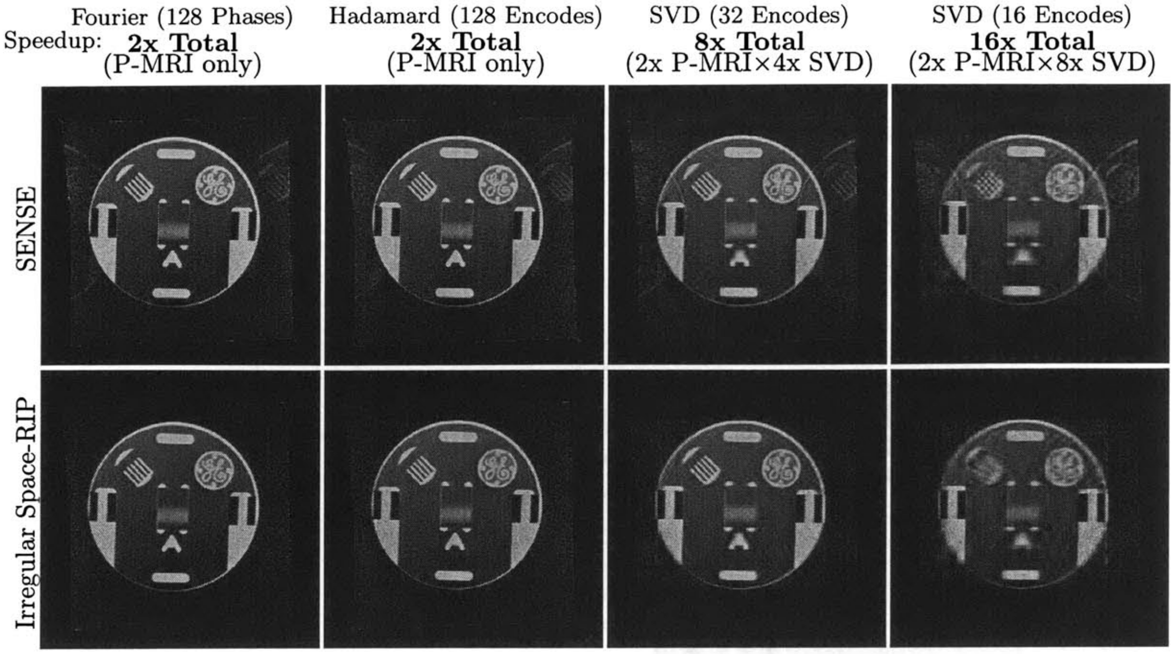

Figure 5-8: Fourier and non-Fourier parallel imaging images acquired using the pulse sequence of Fig. 2-4.1 and the NF*P framework with a 2x parallel imaging speedup combined with Hadamard and SVD encoding. Cartesian SENSE (SENSE) in the top row and irregularly down-sampled Space-RIP reconstructions in bottom row. All images are reconstructed to 16 cm FOV and 256-by-256 matrix size and are identically window/leveled. Fourier or non-Fourier encoding, and subsequent parallel decoding, was applied along the horizontal dimension.

Hadamard and 8x SVD encoded images are similar in quality to their Fourier encoded counterparts.

5.4 NF*P Remarks

NF*P enables parallel image acquisition for non-Fourier encoded MRI. Central to this combination is the proposition of encoding each aliased superimposed portion of the FOV identically. In the language of digital RF encoding, the sub-sampling of k-space employed by parallel imaging acquisitions giving rise to aliasing, is recast as a dimensionality reduction of the digital MR system response matrix that must be encoded. Mathematically then, this dimensionality reduction leads to both fewer as well as shorter RF encoding pulses in the digital RF encoding model.

Resolution along a phase (non-Fourier) encoded dimension is proportional to the number of Fourier (non-Fourier) basis functions used to encode the FOV. In the digital RF encoding model, both statements express the fact that a column of an image (or, equivalently, k-space) matrix with M rows can always be expressed as a combination of precisely M linearly independent basis vectors, whether these vectors are drawn from the Fourier, a Wavelet, or any family of basis functions. Parallel imaging relaxes this sampling requirement by reducing the FOV by a factor of f, while using independent information from multiple receiver coils to achieve image reconstruction. This

FOV reduction is equally a matrix size reduction.

Digital RF encoding derives a direct correspondence of basis vectors to encoding RF pulses, constructing the FOV by sampling the linear combinations of basis functions that compose each of its columns. Accordingly, the matrix size reduction enabled by parallel imaging allows NF*P to reduce the number of RF pulses to M/f, thereby manifesting the imaging acceleration of parallel imaging.

Unfortunately, the direct correspondence between basis vector and RF pulse, that is the strength of digital RF encoding, is also one of its primary limitations; image resolution along the non-Fourier encoded dimension is defined by the resolution of the basis vectors, which is in turn proportional to the length of the RF pulses that are used to excite them. In Section 4.4 we went to great lengths to attempt and surpass this limitation via the use of optimized trajectories. This leads to the second advantage of NF*P: namely, if the basis vectors are only M/f-dimensional, it may be possible to reduce the length of the RF pulses by a factor up to f, as limited by hardware system constraints. In general, NF*P imaging acceleration is affected by hardware system limits just as P-MRI methods are.

The ability to accelerate RF pulse excitations, by removing the zeros from the encoding RF pulses pD^TD which is the intrinsic idea of encoding S^f in Eq. (5.49), is however highly dependent on hardware limits as well as the specific RF pulses. Variable rate selective excitation (VERSE) [17] encapsulates these hardware limitations, while the reduction of the number of hard pulses enabled by NF*P can reduce the RF pulse requirements within VERSE.

5.4.1 NF*P & SNR Considerations

The SNR of parallel imaging can be expressed as [126]:

$$SNR^f(r) = \frac{SNR^{\text{full}}(r)}{g(r)\sqrt{f}}, \tag{5.53}$$

where $SNR^{\text{full}}(r)$ is the SNR attained by full Fourier encoding of the given sample for the given set of acquisition parameters. The factor $1/\sqrt{f}$ is related to the reduction of the FOV by f while maintaining voxel size, while the spatially dependent factor $g(r)$ is related to the conditioning of the numerical inversion problem. The latter is in essence a performance limitation dependent on the ability of the coil ensemble to separate the superimposed aliases at each location in space.

The effective Signal-to-Noise Ratio (SNR) of NF*P depends on the SNR of the parallel acquisition as well as that of the particular non-Fourier encoding method. This SNR of non-Fourier encoding has been studied extensively in e.g., [151, 111, 161] and is affected by a number of factors, viz., similar to the geometry factor $g(r)$ the conditioning of the non-Fourier encoding inversion (i.e., Eq. (5.51)), and, the reduction of acquired signal energy stemming from use of encoding profiles that do not make use of all available magnetization. We revisit this subject in section 9.1.1. For the purpose of this chapter, we note that when non-Fourier encoding replaces phase encoding of equivalent flip angle, $SNR^{\text{full}}(r)$ in Eq. (5.53) is altered to that attained by the particular non-Fourier encoding method.

5.4.2 Acceleration Limits

The immediate benefit of the NF*P framework is to enable P-MRI acceleration for most digital NF encoding MRI modalities, regardless of pulse sequence, k-space trajectory and encoding method specifics. An additional desirable and important property of NF*P is that the total speedup potentially available to it can exceed that achievable by either spatial encoding acceleration method independently.

As discussed in Chapter 3, very large subspace truncation by non-Fourier encoding alone will inadvertently lose pertinent image information, leading to imaging errors. Similarly, large parallel imaging speedups result in badly conditioned reconstructions, that also lead to loss of pertinent image information, as for example shown on the left-hand images of Fig. 5-9. However, by splitting a desired speedup between the two methods, image quality can be maintained, as shown on the right-hand image of Fig. 5-9.

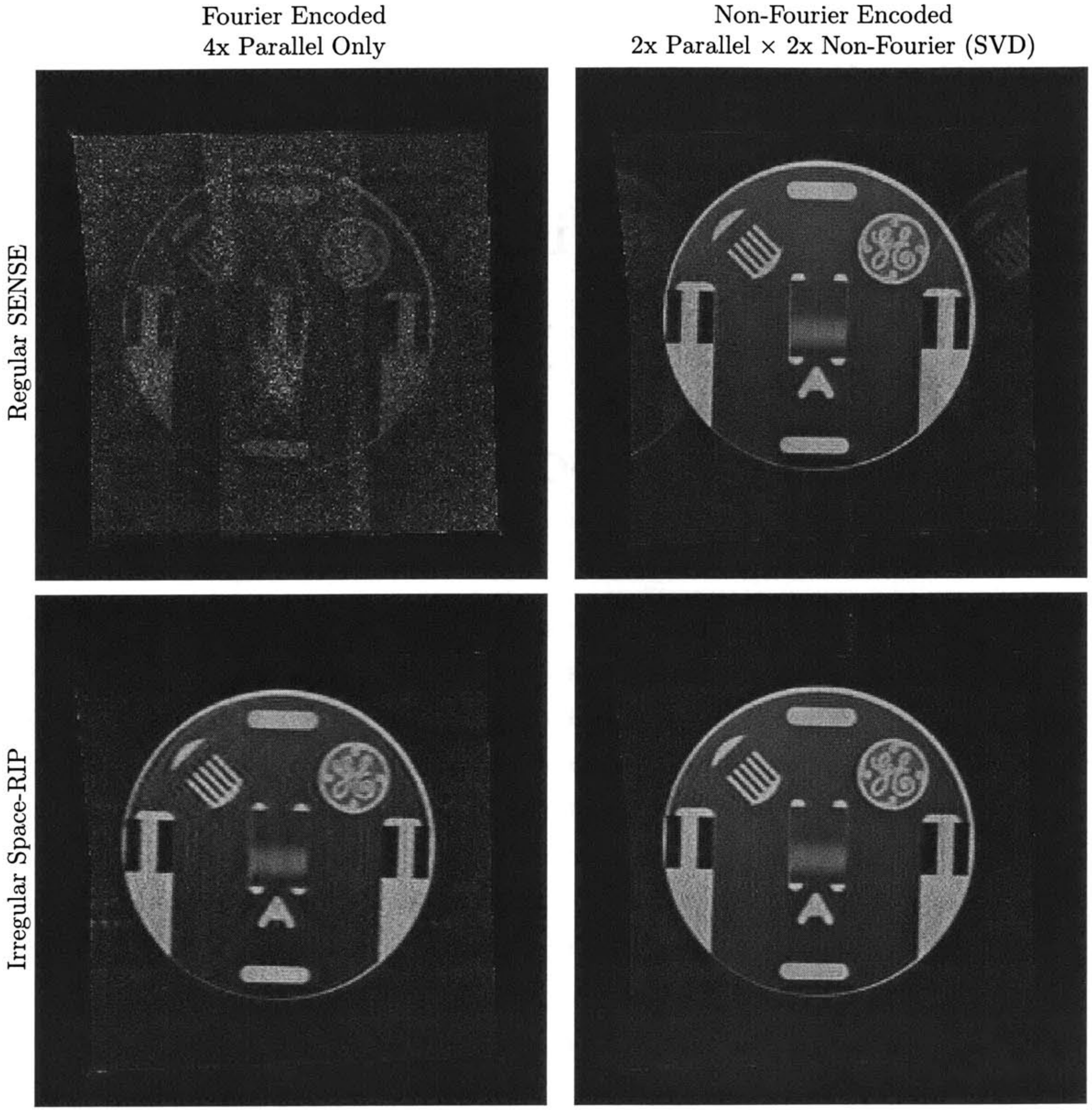

Figure 5-9: By splitting a desired speedup between parallel and non-Fourier acceleration factors, image quality may be maintained since neither method is used with an acceleration that is detrimental to image quality. Notice for example the increased spatial resolution obtained in the irregularly down-sampled images when the 4x speedup is attributable partially to parallel and partially to non-Fourier encoding (bottom row, right-hand image), versus entirely attributable to parallel imaging (bottom row, left-hand image).

Chapter 6

UNFOLD-NF: Time-Axis Compression via FOLDing the Broadband Encoding Functions[1]

UNaliasing by Fourier-encoding the Overlaps using the temporaL Dimension (UNFOLD) [79] is a method which compacts the k-space (i.e., spatial) information by encoding it using otherwise unused portions of the time dimension. The aliasing limitation of Fourier sampling, that requires the sampling FOV to be larger than the extent of the imaged sample in order to avoid aliasing, in most cases necessitates acquisition of images that contain otherwise useless information. That is, effort is expended encoding an FOV that is larger than the region of interest. Central to UNFOLD is the realization that when a dynamic series of images of the same human anatomy are acquired over time, the dynamic range of a single pixel's value does not contain all temporal frequencies.

For example, although a heart in a chest is moving and pixel values within that region undergo significant change over the series, a large portion of the surrounding tissue is quasi-static, requiring very little temporal frequency space. Thus, if one can force the quasi-static and dynamic portions of the FOV to overlap, so that a given pixel of the acquired image contains the information of one dynamic and one quasi-static portion of the FOV, the temporal frequency space will be more tightly packed, making more efficient use of the encoding effort. In this manner, superimposed overlaps of the image are encoded using the time dimension. By superimposing portions of the FOV, fewer encoding steps are required along the spatial dimensions in order to yield the desired resolution. Of course, in order to reconstruct the full image, the encoding of the overlaps induced over the temporal dimension must then be separated.

---

[1] Portions of this chapter have appeared in [96]

In this chapter we will describe a general framework combining the UNFOLD method that encodes some spatial information of a dynamic series using the temporal dimension, with non-Fourier spatial encoding. Largely based on the realization of the previous chapter, we consider that if overlapped portions of the FOV can be unaliased via any method, UNFOLD in this case, then the non-Fourier spatial encoding functions only need to encode the compacted spatial information.

Following the previous chapter, when the compacted k-space at each time frame is encoded via digital non-Fourier spatial excitations, we will see that both fewer RF excitations are necessary to completely encode each time frame, and the length of each digital RF excitation is reduced as well. Finally, using the framework that we develop, we show that the speedup in acquisition time obtained via UNFOLD and that obtained via compressed non-Fourier encoding are multiplied. We will finally demonstrate the method on a typical commercial MR scanner.

The UNFOLD method [79] acquires a sub-sampled k-space at each time frame in a series of images so that portions of the FOV are aliased. The sub-sampled k-space acquisitions result in overlapped portions of the FOV. The overlapped regions of the FOV are resolved by inducing Fourier basis functions over the overlaps in the time dimension (i.e., over the image frames). These Fourier basis functions that modulate the overlaps are induced via appropriately shifting the phase encode sampling function at each k-space acquisition time frame. An example UNFOLD acquisition series is shown in Fig. 6-1.

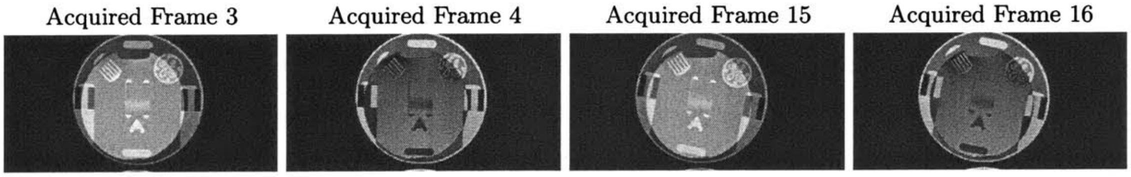

Figure 6-1: Example time frames of phase encoded images acquired using an UNFOLD speedup factor of 2. The phase encode sampling function is down-sampled by the UNFOLD speedup factor so that each pixel in the reconstructed image contains contributions from a pixel in each of the two FOV overlaps. However, in each time frame, the shift of the phase encode sampling function causes the pixel from each overlap to be modulated by a different phase, static for one overlap, while oscillating between consecutive time frames for the other overlap. In this manner, the two contributions are Fourier encoded in time over the time frames.

By cycling through the Fourier basis function modulations in the time domain (i.e., in between image frames) the overlaps are Fourier encoded in the time axis. In the images reconstructed by Fourier transformation of the raw k-space data acquired by the UNFOLD method using two basis functions for the series of Fig. 6-1, this manifests as the ± superposition of the two FOV overlaps. The UNFOLD algorithm subsequently decodes these overlaps by separating the time frequency spectrum of each pixel that contains overlapped portions of the FOV via the use of a simple filtering approach, as shown in Fig. 6-2.

For an UNFOLD speedup factor of 2, one of the overlaps, say the one containing quasi-static

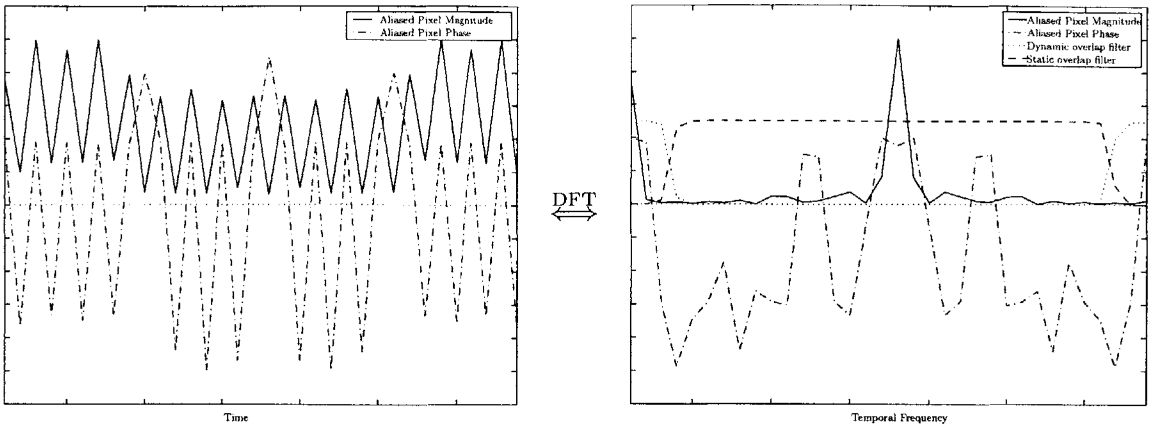

Figure 6-2: The value of an overlapped pixel in time contains the pixel from the static and the oscillating overlap. Fourier transformation of the time-varying value of this overlapped pixel then separates the two contributions in the temporal frequency axis allowing appropriate filters to separate them. The pixel from the static overlap is assumed to be largely dynamic, thus occupying a large frequency bandwidth, while the pixel from the forced oscillating overlap is assumed to be quasi-static, thus allowing appropriate filters to be designed for the separation.

material, flips sign on every frame, thus the small spectrum of temporal frequencies occupied by a pixel within that overlap (due to the intrinsic evolution of the pixel's value over time) will be centered about the Nyquist frequency, as shown in the right-hand plot of Fig. 6-2. Thus allows the use of a high-pass filter to separate its portion of the dynamic range in the temporal frequency domain. The separated temporal frequency spectrum corresponding to this quasi-static pixel can then be Fourier transformed back into the time domain, thus yielding the value of this quasi-static pixel over the dynamic image series, as shown in the reconstructed full FOV images in Fig. 6-3. Similarly, a pixel within the static overlap containing highly dynamic material will occupy a broad range of frequencies, but will be centered about DC, allowing a low-pass filter to separate its contribution to the aliased pixel, and, after Fourier transformation, its value over time. This reconstruction process is repeated over all the overlapped pixels in order to transform the acquired series of Fig. 6-1 to that reconstructed in Fig. 6-3.

6.1 The UNFOLD-NF Framework

The combination of UNFOLD with non-Fourier encoding relies on two facts; first, just as sub-sampling phase encodes in the acquisition of k-space produces aliased overlaps, sub-sampling the k-space excitation samples also produces aliasing sidelobes of the excitation profile. Secondly, just as a shift in the acquisition k-space sampling function induces a Fourier basis function over the FOV overlaps, a shift in the excitation k-space sampling function induces the same basis function over the aliases of the excitation profile.

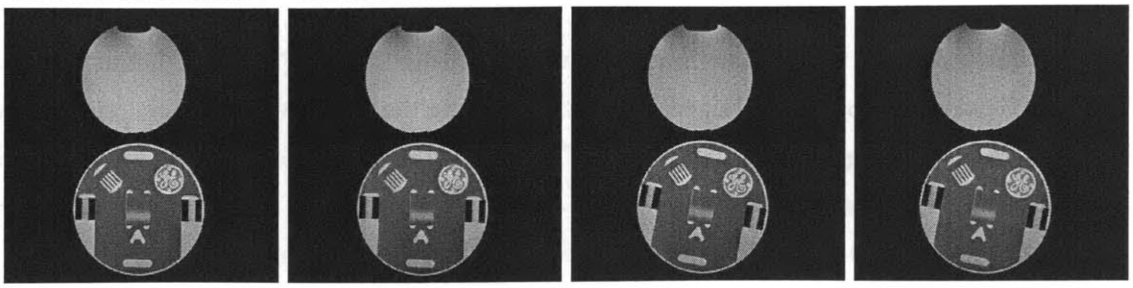
Reconstructed Frame 3 Reconstructed Frame 4 Reconstructed Frame 15 Reconstructed Frame 16

Figure 6-3: With the two FOV overlaps of Fig. 6-1 Fourier encoded in time, each overlap can be resolved by separating the two components in the time frequency domain, since the value of the dynamic pixel from the static overlap occupies the low temporal frequencies while the quasi-static pixel from the oscillating overlap occupies the high temporal frequencies. A simple filtering approach of the temporal spectrum of Fig. 6-2 can separate the value of each superimposed pixel in time.

6.1.1 The UNFOLD Method

UNFOLD achieves a reduction in acquisition time by acquiring a reduced number of rows of the M-by-N k-space matrix F_l at each time frame $l = 1, \ldots L$, while shifting the set of lines that is acquired at each time frame. That is, a shift in the phase encode sampling "function" construct is employed over the time frames, and it is precisely this shift that induces the temporal domain encoding functions.

In the linear response model, we model the reduced acquisition using a sparse sub-sampling matrix D_l derived from the M-by-M identity matrix, similar to that of Chapter 5, except now the down-sampling is necessarily regular. Again, similar to Chapter 5, each row of D_l corresponds to a sequence repetition, i.e., phase encoding step, and contains a single 1 corresponding to the line of k-space that is acquired at that encoding step of the phase encoded experiment. UNFOLD modifies the sub-sampling matrix D_l used to acquire each time frame, in order to induce the temporal dimension encoding functions, by delaying the regular down-sampling by one k-space row at each time step, modulo the UNFOLD speedup factor.

That is, if the UNFOLD speedup factor is f_u, then

$$D_l = I_{(\mathrm{mod}(l-1,f_u)+1):f_u:M,:} \tag{6.1}$$

if the desired resolution along the phase encode dimension is M, and I is the M-by-M identity matrix. The sub-sampling of f_u results in an f_u-fold aliased acquisition. In order to induce the Fourier basis functions on the overlaps over time, the down-sampling of each time frame l is delayed by $l - 1$ lines, modulo the UNFOLD speedup factor. The k-space matrix $F_l^{f_u}$ that is acquired at each FOLDed time frame is then described by

$$F_l^{f_u} = D_l F_l, \tag{6.2}$$

where the superscript f_u denotes the acceleration.

In the image domain, the lth time frame produces the image $R_l^{f_u} = \mathcal{F}^{-1}\{F_l^{f_u}\}$. Let us suppose that $f_u = 2$, and return to the usual signal Eq. (2.6), which, for the full FOV acquisition, requires the wavenumbers given by Eq. (2.8) and Eq. (2.13). The FOLDed acquisition obtains the wavenumbers $k_y^{(2m-1)}$ for the odd l time frames, and $k_y^{(2m)}$ for the even l time frames, in both cases with $m = 1, \ldots, M/2$. These modes correspond to the phase encode steps retained by D_l.

Assume the sample along the phase-encode dimension is entirely supported within 2π, i.e., $y \in [-\pi, \pi]$ and is periodic. An even l time frame acquires the set of signals $S\left(k_x, k_y^{(2m)}, t_l\right)$ which we Fourier transform along the readout dimension, thus yielding the signals as functions of x. The resulting signals are then described by

$$S(x_0, q, t_l) \equiv S\left(x_0, k_y^{(2(q+1/2M))}, t_l\right), \tag{6.3}$$

with t_l the time corresponding to the acquisition of an even l time frame. Reconstruction of the sample $\rho_{unf}(x, y, t_l)$, by summation of the sampled complex exponentials, then amounts to

$$\begin{aligned} \rho_{unf}(x_0, y, t_l) &= \sum_{q\in\text{even}} S\left(x_0, q, t_l\right) e^{iqy} \\ &= \frac{1}{2} \sum_{q\in[\text{even,odd}]} S\left(x_0, q, t_l\right) e^{iqy} + \frac{1}{2} \sum_{q\in[\text{even,odd}]} (-1)^q S\left(x_0, q, t_l\right) e^{iqy}, \end{aligned} \tag{6.4}$$

since $FOV_y = 2\pi$ leading to $\Delta k_y = 1/2\pi$. Using the identity $(-1)^m = e^{i\pi q}$, Eq. (6.4), becomes

$$\begin{aligned} \rho_{unf}(x_0, y, t_l) &= \frac{1}{2} \sum_{q\in[\text{even,odd}]} S\left(x_0, q, t_l\right) e^{iqy} + \frac{1}{2} \sum_{q\in[\text{even,odd}]} S\left(x_0, q, t_l\right) e^{iq(y+\pi)} \\ &= \frac{1}{2}\left(\rho(x_0, y, t_l) + \rho(x_0, y + \pi, t_l)\right). \end{aligned} \tag{6.5}$$

Following the same argument for the odd l time frames,

$$\begin{aligned} \rho_{unf}(x_0, y, t_l) &= \sum_{q\in\text{odd}} S\left(x_0, q, t_l\right) e^{iqy} \\ &= \frac{1}{2} \sum_{q\in[\text{even,odd}]} S\left(x_0, q, t_l\right) e^{iqy} + \frac{1}{2} \sum_{q\in[\text{even,odd}]} (-1)^{(q+1)} S\left(x_0, q, t_l\right) e^{iqy}, \end{aligned} \tag{6.6}$$

which, since $(-1)^{(q+1)} = e^{i(q+1)\pi}$, becomes

$$\begin{aligned} \rho_{unf}(x_0, y, t_l) &= \frac{1}{2} \sum_{q\in[\text{even,odd}]} S\left(x_0, q, t_l\right) e^{iqy} + \frac{e^{i\pi}}{2} \sum_{q\in[\text{even,odd}]} S\left(x_0, q, t_l\right) e^{iq(y+\pi)} \\ &= \frac{1}{2}\left(\rho(x_0, y, t_l) + e^{i\pi}\rho(x_0, y + \pi, t_l)\right). \end{aligned} \tag{6.7}$$

To summarize, the time frames t_l with l odd produce the reconstructed image

$$\rho_{unf}(x_0, y/2, t_l) = \frac{1}{2}\left(\rho(x_0, y/2, t_l) + e^{i\pi}\rho(x_0, y/2 + \pi, t_l)\right), \tag{6.8}$$

(by using the decimation factor of f_u [141]), whereas the time frames t_l with even l produce the reconstructed image

$$\rho_{unf}(x_0, y/2, t_l) = \frac{1}{2}\left(\rho(x_0, y/2, t_l) + \rho(x_0, y/2 + \pi, t_l)\right). \tag{6.9}$$

Thus, using MATLAB notation in order to avoid cluttering subscripts, $R_l^{f_u} = R_l(1 : M/2, :) + R_l(M/2 + 1 : M, :)$ for l even, and $R_l^{f_u} = R_l(1 : M/2, :) + e^{i\pi}R_l(M/2 + 1 : M, :)$ for l odd. The top and bottom halves of the FOV become the Fourier coefficients of a 2-point discrete Fourier transform in time, i.e.,

$$\mathrm{DFT}_2 = \begin{bmatrix} 1 & 1 \\ 1 & e^{i\pi} \end{bmatrix}. \tag{6.10}$$

The UNFOLD algorithm then collects the series of $R_l^{f_u}$ and, via the process described earlier, that we refer to as "UNFOLDing", separates the two contributions for each time frame.

6.1.2 The MR System Response in the Presence of UNFOLD

To enable non-Fourier encoding with UNFOLD, we note that at each time frame l, the UNFOLD algorithm expects the k-space matrix D_lF_l. Thus, at each time frame, non-Fourier encoding needs to encode and reconstruct precisely that matrix. Our non-Fourier response of Eq. (2.26), may then be replaced with

$$s_l^{f_u} = p_l^{f_u}\{D_lF_l\}. \tag{6.11}$$

Following the development of the previous chapter, $p_l^{f_u}$ is now an encoding vector of length M/f_u that, when used at the lth time frame, encodes only the Fourier modes of the sample that are necessary by the UNFOLD algorithm for that time frame. It can be derived, as before, by application of the down-sampling matrix D_l to a digital RF encoding vector that covers the entire full FOV:

$$p_l^{f_u} = pD_l^T. \tag{6.12}$$

Similarly, insertion of Eq. (6.12) into the linear response of Eq. (6.11),

$$s_l^{f_u} = p\{D_l^TD_l\}F_l, \tag{6.13}$$

reveals that the effective spatial encoding function, over the entire FOV, is in fact derived by

$$\tilde{p}_l^{f_u}(y) = \mathcal{F}^{-1}\{pD_l^T D_l\}. \tag{6.14}$$

Scrutinizing the spatial encoding function $\tilde{p}_l^{f_u}(y)$, that is used to encode the down-sampled k-space matrix of the lth time frame in Eq. (6.13), we see that it is an f_u-fold aliased function over the entire FOV. Additionally, according to Eq. (6.14), the choice of Fourier modes excited by the spatial encoding function (itself entirely dependent on the sub-sampling matrix D_l of the time frame it is being applied to), induces the temporal Fourier encoding of the FOV overlaps. That is, the given spatial excitation, operated on by a different projection $D_l^T D_l$ at each time frame, induces copies of the spatial profile that it intrinsically describes (over a FOV of size FOV_y/f_u) over the full FOV, but each copy is modulated by the appropriate factor that UNFOLD would induce over that portion of the FOV for the given time frame. These modulations, as for example those in Eqns. (6.8) and (6.9), are controlled by the projection matrix and hence indirectly on the time frame l.

The system response matrix of each time frame appearing in the linear response of Eq. (6.11), $\{D_l F_l\}$, is sized M/f_u-by-N, given the UNFOLD speedup factor f_u, the non-Fourier encoding dimension resolution of M, and the readout dimension resolution of N. In order to encode it, we need at most M/f_u excitations. If we attempted to encode the first f_u time frames of the system response, we would need at most M sequence repetitions, since each k-space matrix requires M/f_u repetitions to be fully encoded. This effectively means that to encode f_u FOLDed time frames that will yield a resolution of M (after UNFOLDing) requires no more imaging time as is required to encode a single, full FOV, k-space matrix F of size M-by-N. Then, given the periodicity of the sub-sampling matrices D_l (of f_u), and assuming that the FOV contents are nearly static within the time required for encoding a single full FOV k-space, i.e., assuming that $[D_1 F_1|, \cdots |D_{f_u} F_{f_u}] \simeq [D_1 F| \cdots |D_{f_u} F]$, we can imagine using the same set of RF excitations, fixed over the first f_u time frames, to encode all individual system response matrices, $D_l F_l$, for each of the f_u time frames.

Each of these fixed RF encoding vectors, p^{f_u}, is of length M/f_u. When one such encoding vector p^{f_u} is applied to acquire a response from each time frame, the resulting output response at time frame l is,

$$s_l^{f_u} = p^{f_u}\{D_l F_l\}, \tag{6.15}$$

since all $p_l^{f_u}$ of Eq. (6.11) are fixed to p^{f_u}. From the single time frame responses of Eq. (6.15) we can build a composite system response by concatenating them over time, so that

$$s^{f_u} = \left[s_1^{f_u} | \cdots | s_{f_u}^{f_u}\right] = p^{f_u}\left[D_1 F_1 | \cdots | D_{f_u} F_{f_u}\right] = p^{f_u} F^{f_u}. \tag{6.16}$$

Equation (6.16) suggests a composite "FOLDed" system response matrix,

$$F^{f_u} \equiv [D_1 F_1| \cdots |D_{f_u} F_{f_u}], \tag{6.17}$$

that allows a digital RF encoding vector p^{f_u} of length M/f_u to be applied to encode each distinct time frame, thus producing a composite signal output, s^{f_u}, of length Nf_u. The composite system response F^{f_u} contains the sub-sampled k-space matrices with the FOV overlaps temporally encoded over one iteration of temporal modulations (Fourier basis functions). This composite system response matrix can now be non-Fourier encoded as before, using a set of digital RF encoding functions, p^{f_u}, that form the rows of an encoding matrix $\tilde{P}$. This matrix must thus be capable of encoding the modulated sub-sampled system responses simultaneously. Since the composite system response matrix, F^{f_u}, given by Eq. (6.17) is M/f_u-by-Nf_u, the encoding matrix $\tilde{P}$ is at most M/f_u-by-M/f_u, reflecting the efficiency of UNFOLD; at most M/f_u encoding functions are necessary to fully encode the aliased FOV. A truncation of this encoding basis, to $K \leq M/f_u$, for a broadband compressed acquisition, then reflects an additional efficiency.

Each row of this FOLDed broadband encoding matrix $\tilde{P}$, describing the excitation p^{f_u}, that must be used at each consecutive time frame to encode the appropriately sub-sampled k-space matrices $D_l F_l$, contains a number of Fourier modes that are reduced by a factor of f_u compared to an encoding vector necessary for encoding the full FOV k-space matrix. Following Eq. (6.14), the aliased modulated spatial excitations $\tilde{p}_l^{f_u}(y)$ result by using the length-M/f_u encoding vectors p^{f_u}, i.e.,

$$\tilde{p}_l^{f_u}(y) = \mathcal{F}^{-1}\{p^{f_u} D_l\} \tag{6.18}$$

The length-M RF vectors $p^{f_u} D_l$ that must be used to encode each time frame differ depending on the time frame l. If they are excited under a spatially selective gradient designed for a full FOV, FOV_{full}, then in each time frame the hard pulses contained in p^{f_u} must be placed in Fourier modes that are appropriately shifted, as described by the encoding vector $p^{f_u} D_l$. It is this shift that induces the temporal encoding modulations. If we are interested in reducing the length of the excitations as well, the compressed encoding vector p^{f_u}, of length M/f_u, system of Eq. (6.11) may be used. The excitation must occur in conjunction with a spatially selective gradient designed for a FOV of FOV_{full}/f_u. We can simply use the rephasing lobe of the spatially selective gradient to induce the Fourier mode shift required for the excitation corresponding to the specific l (in order to produce the response of Eq. (6.11) implied by D_l^T) at each time frame.

6.2 UNFOLD-NF Experiments

6.2.1 Methods

Equipment

All experiments were performed on our familiar 1.5T GE MR scanner (Signa Horizon LX 8.3 EchoSpeed, GE Medical Systems, Milwaukee, WI) using the simple non-Fourier encoding spin echo pulse sequence of Fig. 2-4.1 and low flip angle ($\theta \simeq 30°$) RF pulses. An UNFOLD speedup factor of $f_u = 2$ was used for all experiments. Accordingly, the half-length ($M/2$) and appropriately shifted, at each time frame, RF encoding pulses were used to excite the sample. The pulse sequence then acquired the resulting system response at each time frame for each encoding pulse.

UNFOLD Reconstruction

UNFOLD reconstruction was applied after applying the non-Fourier reconstruction process to produce the D_lF_l of each time frame from the acquired k-space data $\tilde{P}D_lF_l$. Once the sub-sampled k-space matrices for all time frames were reconstructed, the aliased images were produced via 2D Fourier transformation of each sub-sampled k-space matrix. A Fourier transform of the value of each pixel over the time frames l was then computed, yielding the temporal frequency content of each (overlapped) spatial location in the (aliased) images. Then, a simple UNFOLDing filter was used, as shown in Fig. 6-2, to separate the dynamic component centered about DC from the quasi-static component centered about Nyquist. These two components were then placed in the appropriate pixel location of a full FOV image. Once all pixels were thus separated, an inverse Fourier transform was used to convert the temporal frequency content of each pixel to the time-varying value of the pixel over the time frames.

Spatial Encoding Methods

We again use Hadamard encoding and SVD encoding for the two representative non-Fourier encoding methods.

Hadamard Encoding. We use the Fourier transform of the rows of the matrix H_{M/f_u} (c.f., Eq. (2.29)) to derive our encoding matrix $\tilde{P}$. Each time frame $l = 1, \ldots, L$ is encoded using this RF encoding matrix. The composite system response F^{f_u} is composed of L time frames, rather than f_u time frames as in Eq. (6.16), since the encoding matrix is entirely static. We can thus rewrite the composite response of Eq. (6.16), as

$$S^{f_u} = \tilde{P}\left[D_1F_1|\cdots|D_{\mathrm{mod}(l,f_u)}F_l|\cdots|D_{f_u}F_L\right]. \qquad (6.19)$$

The sub-sampled time frames are reconstructed by applying the inverse of the encoding matrix,

$$[F_1^{\text{est}}|\cdots|F_L^{\text{est}}] = \tilde{P}^H S^{f_u}. \tag{6.20}$$

UNFOLD reconstruction is then applied to these sub-sampled k-space matrices.

SVD Encoding.

For an SVD-based acquisition, the input RF vectors are formed from the dominant left singular vectors of F^{f_u} according to Eq. (6.16). This composite system response matrix includes only f_u time frames, corresponding to the periodicity of the D_l matrices, and intrinsically contains the same k-space information as the full FOV k-space matrix of Section 2.2.2. The rows of the RF encoding matrix $\tilde{P}$ are then drawn directly from the top rows of U^H, where $F^{f_u} := U\Sigma V^H$.

We can use this encoding matrix, computed from the SVD of the first f_u frames, to encode the subsequent f_u time frames, since intrinsically these are designed to encode the same k-space information, in the absence of changes in the FOV. Encoding the composite system response F^{f_u} with the same encoding matrix effectively means that each of the f_u time frames corresponding to one cycle of FOLDing matrices is encoded identically, i.e.,

$$S_j^{f_u} = \tilde{P}_j[D_1F_j|\cdots|D_{f_u}F_{j+f_u}], \tag{6.21}$$

with $\text{mod}(j, f_u) = 1$. All f_u time frames starting from j can then be reconstructed together as

$$[F_j^{\text{est}}|\cdots|F_{j+f_u}^{\text{est}}] = \tilde{P}_j^H S_j^{f_u}, \tag{6.22}$$

in order to yield the sub-sampled k-space matrices for that cycle.

Once $S_j^{f_u}$ is acquired, the RF encoding matrix can then be adapted again, using the completed cycle of time frames included in $S_j^{f_u}$, in order to compute an encoding basis for the next cycle $j' = j + f_u$. Again, this arises naturally if we consider that one cycle of FOLDed frames contains the same amount of k-space information that is contained in a single full FOV k-space matrix. Each set of f_u time frames is non-Fourier reconstructed by inverting the appropriate encoding matrix, $\tilde{P}_j$. For a total of L time frames, once all L/f_u composite system responses have been encoded and reconstructed to yield the L sub-sampled k-space matrices for all time frames, the UNFOLD reconstruction is applied to reconstruct the full FOV images.

Similarly to the parallel non-Fourier framework, the total speedup of a rank-reduced FOLDed acquisition is composed of both the UNFOLD and the prospective compression speedups applied. If we use $K = 32$ RF encoding vectors, i.e., $\tilde{P}_j$ is 32-by-128 for $f_u = 2$ and target resolution along the non-Fourier encoded dimension $M = 256$, the prospective compression speedup is e.g., for SVD $f_{\text{SVD}} = (M/f_u)/K$, but the total speedup is $f_{\text{tot}} = M/K$.

6.2.2 Results

The FOV was populated by two doped water phantoms. A cylinder filled with doped water remained static during the course of the experiment, while a structured phantom, also filled with doped water, was rotated by about 15° clockwise over the course of $L = 18$ time frames. Pulse sequence parameters were 24 cm full FOV, 400 ms TR, 20 ms TE, 16 KHz readout bandwidth. In all acquisitions the vertical axis was either Fourier phase or non-Fourier encoded.

The images acquired using standard phase encoding, with 128 phase encodes over the 2-fold reduced FOV, and the UNFOLD reconstructed full FOV images, are shown in Fig. 6-4. Each time frame required 51 sec acquisition as opposed to 102 sec without using UNFOLD. Each time frame was also Hadamard non-Fourier encoded using 128 Hadamard encodes. The acquired and UNFOLD-reconstructed images for this non-Fourier encoding method are shown in Fig. 6-5. Each time frame also required 51 sec acquisition time.

A compressed acquisition of each time frame was also performed by non-Fourier encoding, using 32 encoding functions derived from the SVD. The encoding functions were adapted to the contents of the FOV at the frequency of the UNFOLD speedup (i.e., every 2 reduced-FOV time frames) according to Eq. (6.21). Acquired and reconstructed images of this adaptive SVD UNFOLD-NF acquisition are shown in Fig. 6-6. Since each frame was acquired in 32 encoding steps, imaging time was 12.8 sec per time frame, i.e., at an overall speedup of 8 over a full FOV acquisition not employing UNFOLD.

Each time frame was also acquired by encoding it with the encoding basis derived by the SVD for the first two time frames, in order to compare the use of adapting the encoding basis at the frequency of UNFOLD. That is, the 32 encoding functions that were computed to optimally encode the first cycle of FOLDed images were also used to acquire every subsequent time frame. As is clearly seen in Fig. 6-7, failure to adapt the encoding basis over the time frames reduces image quality and leads to reconstruction error.

6.3 UNFOLD-NF Remarks

The UNFOLD-NF framework presented in this chapter enables non-Fourier spatial encoding to take advantage of temporal compression techniques. The UNFOLD method relies on reducing the FOV via skipping the acquisition of phase encoding steps in order to acquire aliased images wherein multiple overlaps of an imaged sample are superimposed to form a single pixel in a reduced FOV image. The overlaps of the FOV are resolved by inducing Fourier basis functions on the overlapped pixels over time via a simple shift of the phase encode sampling function. This enables a temporal compression, wherein spatial information is Fourier encoded using the time dimension. To resolve the spatial information, the temporal frequency dimension is separated into components that describe

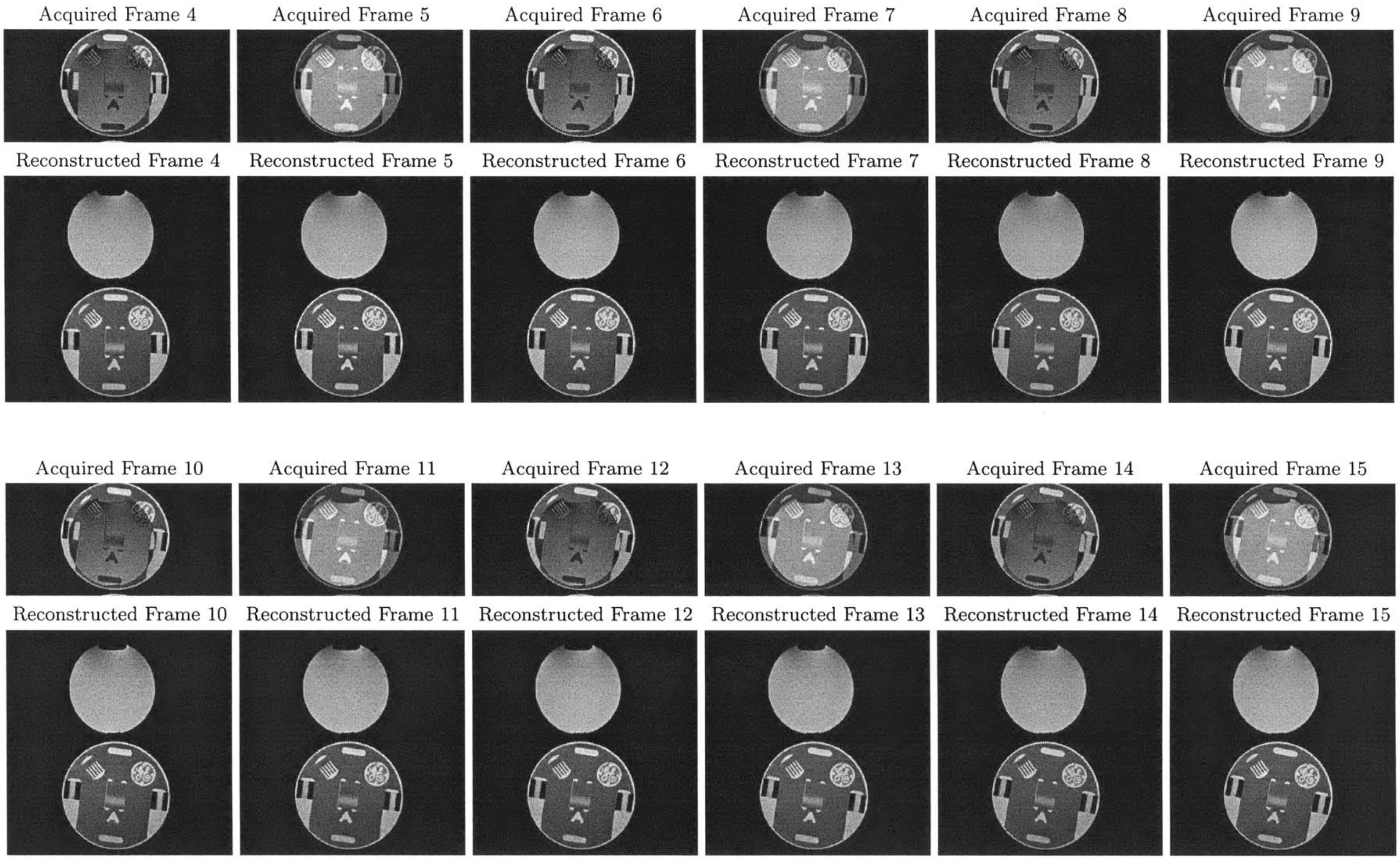

Figure 6-4: A dynamic imaging series acquired with 128 Fourier phase encodes. The UNFOLD-reconstructed images (256-by-256) for each time frame are shown below the actual acquired images.

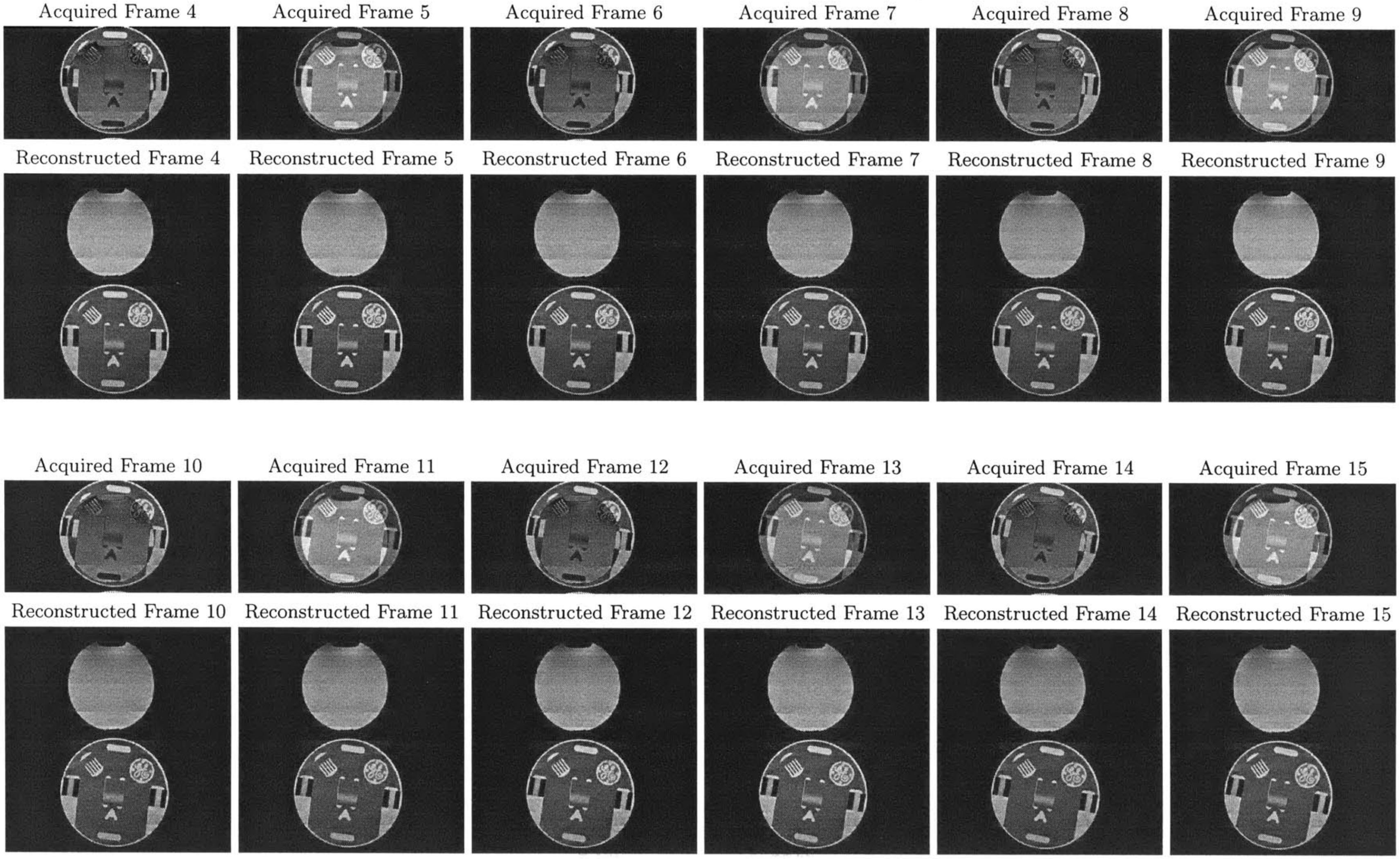

Acquired Frame 4
Acquired Frame 5
Acquired Frame 6
Acquired Frame 7
Acquired Frame 8
Acquired Frame 9

Reconstructed Frame 4
Reconstructed Frame 5
Reconstructed Frame 6
Reconstructed Frame 7
Reconstructed Frame 8
Reconstructed Frame 9

Acquired Frame 10
Acquired Frame 11
Acquired Frame 12
Acquired Frame 13
Acquired Frame 14
Acquired Frame 15

Reconstructed Frame 10
Reconstructed Frame 11
Reconstructed Frame 12
Reconstructed Frame 13
Reconstructed Frame 14
Reconstructed Frame 15

Figure 6-5: A dynamic imaging series acquired with 128 Hadamard encoding functions that completely encode the reduced FOV. The UNFOLD reconstruction applied after Hadamard reconstruction yielded the full FOV reconstructed images (256-by-256) for each time frame that are shown below the actual acquired images.

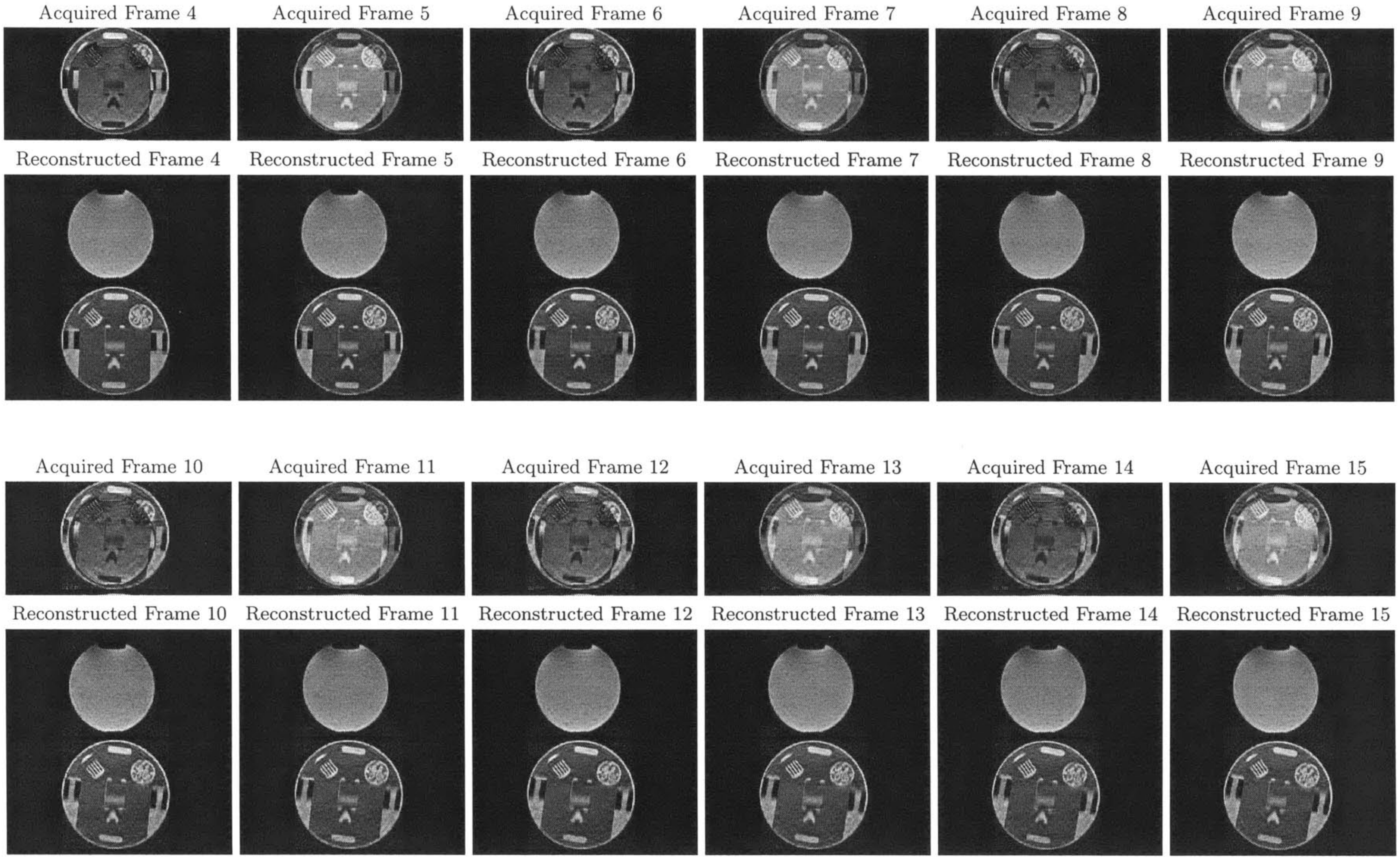

Acquired Frame 4 Acquired Frame 5 Acquired Frame 6 Acquired Frame 7 Acquired Frame 8 Acquired Frame 9

Reconstructed Frame 4 Reconstructed Frame 5 Reconstructed Frame 6 Reconstructed Frame 7 Reconstructed Frame 8 Reconstructed Frame 9

Acquired Frame 10 Acquired Frame 11 Acquired Frame 12 Acquired Frame 13 Acquired Frame 14 Acquired Frame 15

Reconstructed Frame 10 Reconstructed Frame 11 Reconstructed Frame 12 Reconstructed Frame 13 Reconstructed Frame 14 Reconstructed Frame 15

Figure 6-6: A dynamic imaging series of images each acquired with 32 SVD encoding functions that were computed to encode each cycle of FOLDed time frames (i.e., adapted every 2 reduced FOV time frames) according to Eq. (6.21). The UNFOLD reconstruction applied after low-rank SVD reconstruction yielded the full FOV reconstructed images (256-by-256) for each time frame that are shown below the actual acquired images.

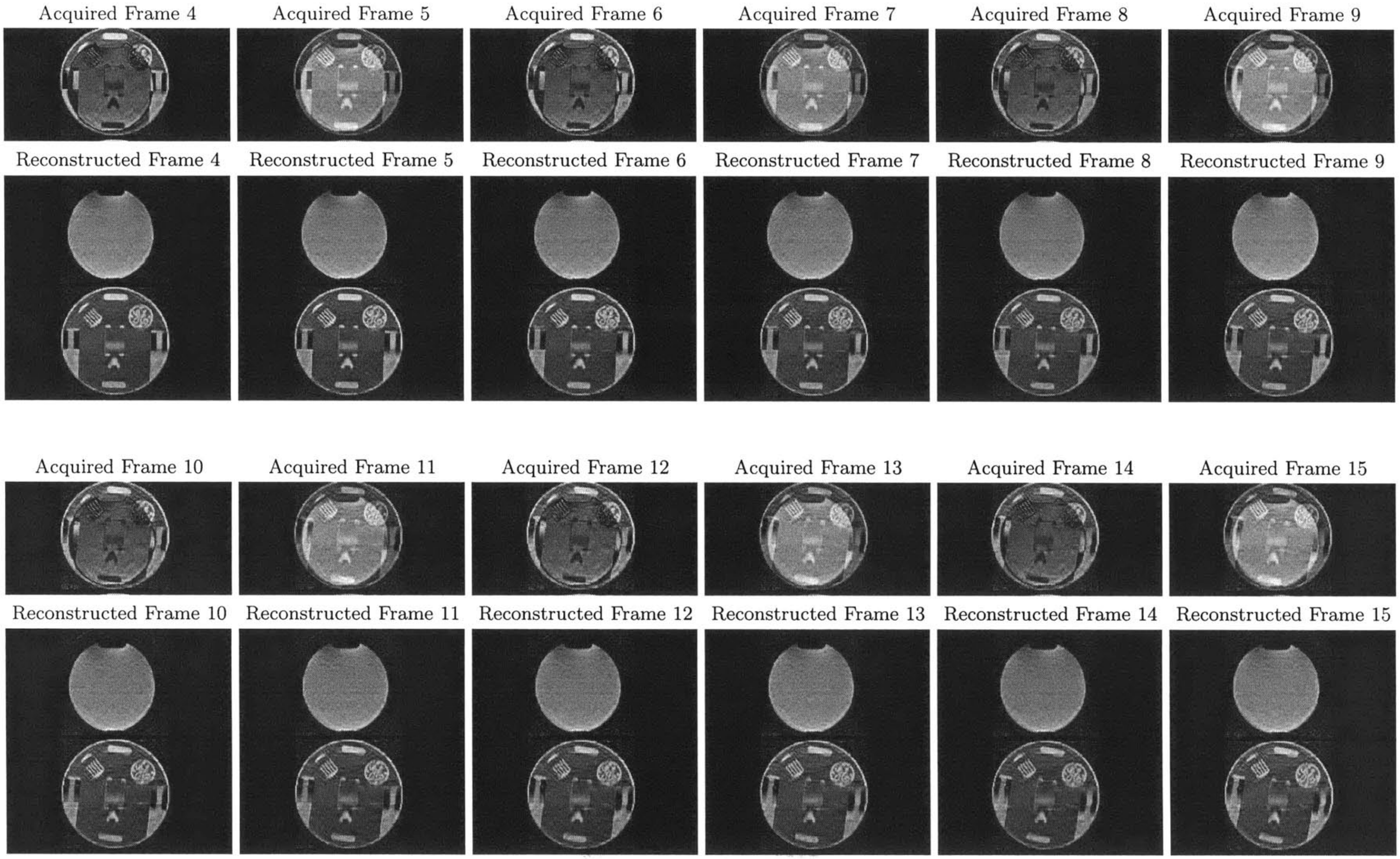
Acquired Frame 4 Acquired Frame 5 Acquired Frame 6 Acquired Frame 7 Acquired Frame 8 Acquired Frame 9
Reconstructed Frame 4 Reconstructed Frame 5 Reconstructed Frame 6 Reconstructed Frame 7 Reconstructed Frame 8 Reconstructed Frame 9
Acquired Frame 10 Acquired Frame 11 Acquired Frame 12 Acquired Frame 13 Acquired Frame 14 Acquired Frame 15
Reconstructed Frame 10 Reconstructed Frame 11 Reconstructed Frame 12 Reconstructed Frame 13 Reconstructed Frame 14 Reconstructed Frame 15

Figure 6-7: A dynamic imaging series of images, each acquired with 32 SVD encoding functions that were computed once to encode the initial cycle of FOLDed time frames (i.e., computed to encode the first 2 reduced FOV time frames). The UNFOLD reconstruction applied after low-rank SVD reconstruction yielded the full FOV reconstructed images (256-by-256) for each time frame that are shown below the actual acquired images. Compared to Fig. 6-6 it is seen that adapting the encoding basis at the frequency of the FOLDing process allows the encoding basis to more accurately encode the changing FOV contents.

each overlapped portion of the FOV.

UNFOLD non-Fourier encoding (UNFOLD-NF) skips excitation k-space samples so that aliases of the spatial encoding profile are produced over the desired FOV. Each overlap of the FOV is therefore encoded simultaneously and identically. The encoding of the aliases in the time dimension is accomplished by modifying the RF encoding scheme (i.e., spatial profiles) at each UNFOLD-NF encoded time frame. In particular, the spatial excitation is changed so that a Fourier basis function is induced over the aliases of the excited spatial profiles, as shown in Fig. 6-8. In parallel to UNFOLD, this is accomplished by appropriately shifting the RF excitation sampling function under the spatially selective gradient. Once all UNFOLD-NF time frames have been non-Fourier encoded, acquired, and reconstructed, the UNFOLD method can be used, as originally proposed, to decode the aliased overlaps.

Accompanying the NF*P framework of the previous chapter, UNFOLD enables a reduction of the k-space matrix necessary at each time frame of a dynamic series of images. This reduction in turn enables non-Fourier encoding to encode a space of smaller dimensionality than in the absence of UNFOLD. This dimensionality reduction again leads to both fewer as well as shorter encoding vectors. The necessity for fewer encoding vectors enables further compacting of the acquisition of the k-space matrix at each time frame via non-Fourier encoding. That is, a speedup is obtained in the acquisition of the sub-sampled k-space matrices that UNFOLD expects, by using fewer spatial encoding functions than the number of phase encodes necessary to achieve the desired spatial resolution. With UNFOLD-NF, as with NF*P, the non-Fourier encoding speedup is in addition to that of UNFOLD, as it is with parallel imaging. The excitation k-space shift of the shorter encoding vectors at each time frame, that is necessary for UNFOLD to operate, is straightforward to accomplish as it only requires a recentering of the Fourier modes produced by the RF encoding vectors. This is typically accomplished by the rephasing gradient. Reducing the length of the RF excitations within hardware limitations is again an issue solved by the VERSE method [17], and again, UNFOLD-NF serves to reduce RF requirements within the VERSE principle.

6.3.1 Toward a Unified Parallel k–t Digital Encoding Framework

The NF*P and UNFOLD-NF digital encoding models that we have presented bear significant resemblance. In this section we will show that they lay the groundwork for a unified digital encoding framework, which suggests that broadband non-Fourier encoding methods can take advantage of both parallel imaging and temporal encoding methods simultaneously.

In the past, combinations of the UNFOLD k-space -temporal method (k–t method), with parallel imaging have been proposed and demonstrated [60, 78]. In the language of the last two chapters, we can define parallel imaging as an operation $\mathcal{P}^{-1}$ which starts with a set of coil sensitivity weighted

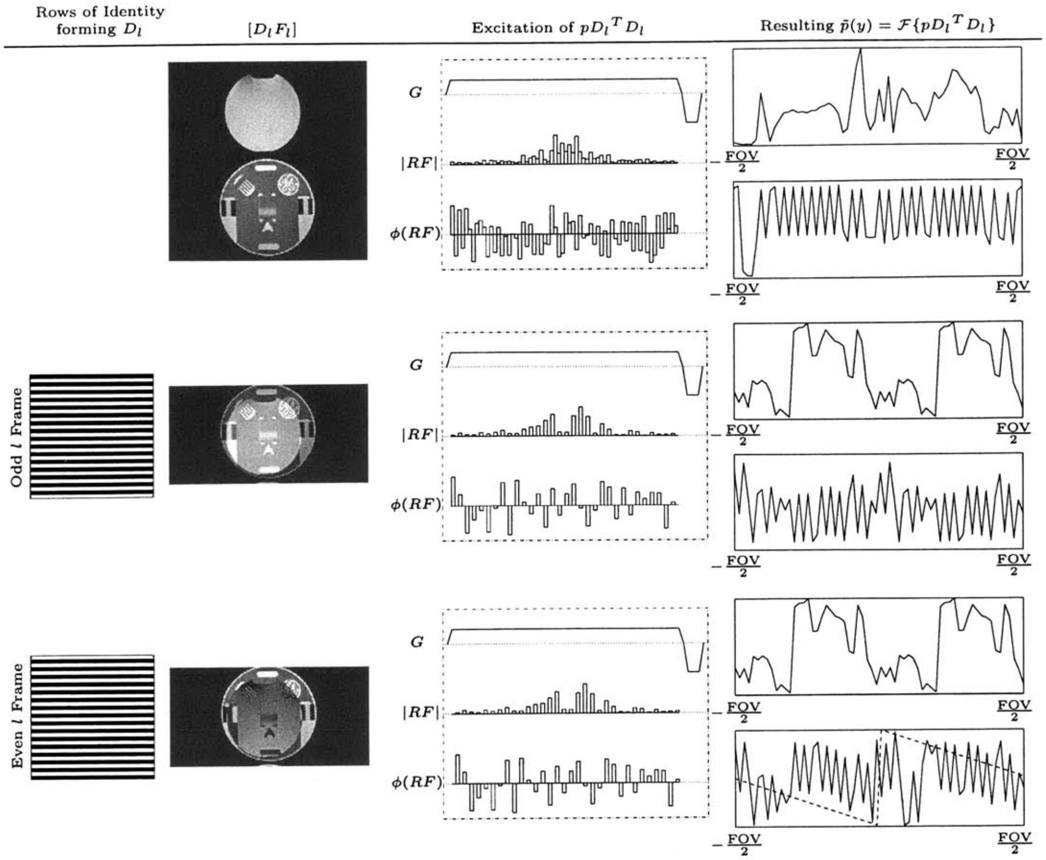

Figure 6-8: Example of non-Fourier encoding functions used for encoding a reduced FOV that will be subsequently unaliased via UNFOLD. The top row gives a typical example of full FOV encoding. Middle row corresponds to encoding an odd frame in a series of 2x FOLDed UNFOLD images. Final row corresponds to encoding an even frame in the 2x FOLDed series. For the FOLDed (accelerated) frames, the non-Fourier spatial excitation is 2-fold aliased over the extent of the full FOV. The shift of the excitation function between odd and even frames causes any two locations in the sample that are separated by FOV/2 to be excited by an equal amount, but with a π degree phase offset, as seen by the dashed line in the phase plot of the even l encoding example in the bottom row. The dashed line represents the phase difference between the spatial excitation induced in the odd frame versus that in the even frame. In the odd frame, both aliases have the same phase, whereas the second alias of the even frame excitation is π degrees offset from that of the first alias.

sub-sampled k-space matrices at a given time frame and recovers the k-space of the unaliased image:

$$F_l = \mathcal{P}^{-1}\left\{D^p\mathcal{F}\left\{W_1 \circ R_l\right\}, D^p\mathcal{F}\left\{W_2 \circ R_l\right\}, \cdots, D^p\mathcal{F}\left\{W_K \circ R_l\right\}\right\} \tag{6.23}$$

where D^p is the k-space sub-sampling matrix used to speedup the parallel image acquisition by a factor of p, W_k is the spatial sensitivity of a receiver coil, R_l is the image of the sample (full FOV) and F_l is the full FOV k-space matrix of the sample at a given time l.

UNFOLD can be similarly defined as an operation $\mathcal{U}^{-1}$ which starts with a series of frames of sub-sampled shifted k-space matrices and also recovers the unaliased images for the frames:

$$\{R_l, \cdots, R_{l+L}\} = \mathcal{U}^{-1}\left\{D_l^{f_u} F_l, D_{l+1}^{f_u} F_{l+1}, \cdots, D_{l+L}^{f_u} F_{l+L}\right\} \tag{6.24}$$

with R_l the image frame at time l, $D^{f_u}_{\mathrm{mod}(l,f_u)}$ the sub-sampling matrices of the time frames, and F_l the full FOV k-space matrix at frame l.

Two main combinations of the parallel and UNFOLD imaging methods have been described. The first relies on performing a parallel imaging accelerated experiment only, while shifting the sampled k-space lines at each time frame [60, 78]. That is, the only acceleration is obtained from the acceleration factor p of the parallel encoding method. However the down-sampling matrix D^p of the parallel accelerated experiment becomes shifted at each time frame. This leads to a down-sampling matrix, D_l^p, of size M/p-by-M, that is necessarily derived by regular down-sampling of the identity matrix, and is the same as the UNFOLD shifted down-sampling matrix of Eq. (6.1), with $f_u = p$. Then, the full FOV M-by-N k-space matrix reconstructed by the parallel imaging experiment becomes

$$F_l = \mathcal{P}^{-1}\left\{D_l^p \mathcal{F}\{W_1 \circ R_l\}, D_l^p \mathcal{F}\{W_2 \circ R_l\}, \cdots, D_l^p \mathcal{F}\{W_K \circ R_l\}\right\}. \tag{6.25}$$

Performing this shift would appear irrelevant until one realizes that if the parallel imaging reconstruction is imperfect, then the residual aliasing remaining in the full FOV k-space matrix F_l is effectively modulated over the time frames l by the UNFOLD modulations for an UNFOLD speedup of $f_u = p$. The UNFOLD method can then be applied not for acceleration but, rather, only to low-pass filter the images $\mathcal{F}^{-1}\{F_l\}$ in the time domain (i.e., only to filter out the residual Nyquist components of the temporal frequency of each pixel), thus further removing residual errors of the parallel reconstruction.

The second combination relies on the fact that the parallel reconstruction is unaware of what a "full FOV" is, allowing the speedups obtained by each of the two methods to be used together. If we use K coil sensitivity estimates that themselves suffer from f_u-fold aliasing, and acquire $f_u \times p$-fold aliased images with our $K \geq p$ coils, we can reconstruct an f_u-fold aliased image estimate. If we do this for a number of time frames, but in each time frame shift the k-space lines that are acquired and reconstructed, the ensemble of time frames can then be further reconstructed using UNFOLD. The result of the UNFOLD reconstruction over the time frames on the parallel reconstructed images then produces the full FOV images for the time series [78]. The parallel imaging method produces $D_l F_l$, if F_l is the full FOV k-space matrix of the time frame. This is accomplished by acquiring the $f_u \times p$-fold accelerated image

$$D^p\{D_l \mathcal{F}\{W_k \circ R_l\}\}, \tag{6.26}$$

where the parallel acceleration down-sampling matrix D^p is derived by a subset of the rows of the M/f_u-by-M/f_u identity matrix and is according of size $M/(f_u \times p)$-by-M/f_u. Using the parallel reconstruction operator of Eq. (6.23) with these sensitivity weighted k-space matrices from the multiple coils yields $D_l F_l$. This allows use of the UNFOLD operator of Eq. (6.24), after all frames have been acquired and parallel reconstructed, in order to reconstruct the full FOV images.

Both cases can be easily derived from the two non-Fourier encoding frameworks we have presented. In the former method, the broadband non-Fourier excitation (instead of Eqns. (5.48) and (6.18)) is p-fold aliased, given by

$$\tilde{p}_l^p(y) = \mathcal{F}^{-1}\left\{p\{D_l^p\}^T D_l^p\right\}, \tag{6.27}$$

based on the M/p-by-M down-sampling matrix derived from the M-by-M identity matrix with the UNFOLD shift. The latter combination is similarly derived by using the $f_u \times p$-fold aliased excitation

$$\tilde{p}_l^{f_u \times p}(y) = \mathcal{F}^{-1}\left\{pD_l^T \{D^p\}^T D^p D_l\right\}, \tag{6.28}$$

derived by the appropriate down-sampling matrices D_l (M/f_u-by-M) and D^p ($M/(f_u \times p)$-by-M/f_u). In this case, a non-Fourier RF encoding matrix necessary to encode the resulting system response would be K-by-$M/(f_u \times p)$ with $K \leq M/(f_u \times p)$.

Chapter 7

SR/TS: A Modular "Scanner Real-Time" Pipeline System for Broadband MRI[1]

In this chapter we will attempt to bring together many of the tools that this work has produced. These tools enable more efficient encoding of the MR signal content of a given sample if one has some *a priori* estimate of it. Linear algebraic tools give us the capability to encode the MR signal content, using a basis other than the Fourier one, with increased efficiency. This can potentially accelerate MR image acquisition by as much as an order of magnitude. This is accomplished by limiting data acquisition only in the significant subspaces of the Fourier coefficient matrix of the sample, e.g., those subspaces whose variation is more significant than noise. This general prospectively compressed encoding methodology allows us to optimize the signal acquisition based on the MR signal content of each specific imaging experiment in order to produce a given resolution over the entire imaged FOV at a reduced imaging time.

Although this encoding efficiency was the impetus to create the tools of the previous chapters, the resulting tools are not limited to this prospective compression application. In general, the interest might be not on such general compression of the signal content, but rather on more precise, application-driven, acquisition of the signal so as to produce e.g., non-uniform resolution across the FOV. The MURPS [116], wavelet encoding [118] and other locally focused [13] approaches aimed precisely to support this need. These methods were designed to break the linear dependence of MR signal acquisition time to MR image resolution. In these methods the basis used to encode the MR signal is adjusted in order to provide resolution *where* and *when* it is necessary, according to the

---

[1] Portions of this chapter have appeared in [88, 91, 92, 101]

specific imaging task at hand. This task might be tracking a biopsy needle or a bolus of contrast agent. It can also be to target imaging resolution on a given portion of the imaged volume that is *a priori* known to be undergoing change, such as laser or RF ablation and cryotherapy.

These are just some additional examples of situations were using some encoding basis other the Fourier one is better suited to encode the MR signal content. Prior to this work, the prospect of additional imaging efficiency via any method other than Fourier basis imaging was only valid when compared to the most simple Fourier acquisition methods. With the introduction of the multiple-echo/multiple-response non-Fourier pulse sequence described in Section 4.1, any 2D imaging method employing non-Fourier encoding can compete with multi-echo Fourier imaging; the speedup factor associated with the truncation of the subspaces is obtained even compared to similar multi-echo Fourier pulse sequences. With the introduction of the 3D pulse sequences employing echo-planar excitations or echo-planar readouts, described in Section 4.2, non-Fourier imaging can compete in the arena of EPI imaging. Chapters 5 and 6 further enable any non-Fourier encoding imaging modality to compete with Fourier basis imaging methods that employ additional encoding such as parallel and k–t imaging approaches.

In this chapter we describe a complete hardware and software platform capable of performing real-time adaptive broadband non-Fourier spatial encoding in concert with a commercial MR imager. The immediate goal is to provide a complete MR imaging system that enables the application of any non-Fourier encoding method using many of the tools created. Additionally, our system should be easily adaptable so that it can be easily extended to encompass those tools that we have created but not yet incorporated, as well as new tools that have not yet been developed. In Section 7.2 we use general (and complex in terms of implementation) non-Fourier imaging methods to demonstrate that this currently operational system can be used in dynamic imaging cases where it is necessary to observe a sample at high temporal as well as spatial resolution over the entire extent of the desired image FOV.

7.1 Designing a Dynamic Adaptive Non-Fourier MRI Platform

The system we have developed [91, 88, 92, 101] operates in a continuous dynamic adaptive imaging cycle. The goal of each iteration of the imaging cycle is to produce a new, high spatial resolution, MR image via the application of non-Fourier encoding methods. At a high level, the steps involved in any non-Fourier imaging method can be summarized by the process shown in Fig. 7-1:

1. An encoding basis is generated.

2. That encoding basis is used to excite spatially selective profiles of the imaged MR sample's

magnetization, the response of which is subsequently acquired.

3. A raw k-space estimate is reconstructed using the encoding basis and the set of acquired responses.

This sequence of events can be repeated to produce additional images in an imaging cycle.

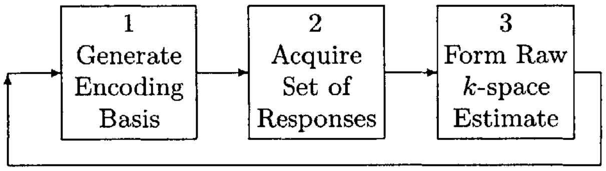

Figure 7-1: High-level view of a dynamic adaptive non-Fourier encoded imaging cycle.

The transformation from encoding basis vector to the spatially shaped profile of excited magnetization is dictated by Eq. (2.24). Regardless of the spatial excitation $p(y)$ that is produced by a corresponding encoding basis vector p, the MR system responses of step 2 in Fig. 7-1 will be a set of vectors containing the discrete samples of the voltage induced on the receiver coils by the excited profile of magnetization. Also, regardless of the spatial excitation profile induced on the sample, the acquired MR system response describes the amount of that spatial profile that is present in the sample throughout the readout axis as in Eq. (2.26). Since $p^H s = p^H pF$, effectively, the acquired response can be used to obtain the projection of the MR system response k-space matrix F onto the subspace spanned by the RF encoding vector p.

7.1.1 System Implementation: Design

Since the simple high level imaging cycle of Fig. 7-1 is capable of capturing most non-Fourier encoding methods, our system is modeled after that cycle and is designed to be easily extensible and/or able to be modified in order to handle any encoding method, whether or not it adapts to the sample over time. To implement the imaging cycle of Fig. 7-1 a modular pipeline platform was designed, arranged as a ring. The pipeline ring is depicted in Fig. 7-2, and is *asynchronous* and *locally timed* (i.e., self-timed). Each logical computation task, or module, performs its task on the input provided to it and, once completed (asynchrony), it distributes the result to all consumer units along with a notification (local timing).

The decision to pipeline our system was was based on taking advantage of all computing resources available. Any MR acquisition is limited by the set of parameters chosen to sample the physical characteristics of a the spin system. In particular, the second stage of Fig. 7-1 will always be limited by the TR and chosen subspace dimensionality. No matter how much computation is added to the MR system, acquisition of the set of responses will be limited by these parameters that are chosen to sample the physical system and dictated by desired image characteristics such as contrast and SNR.

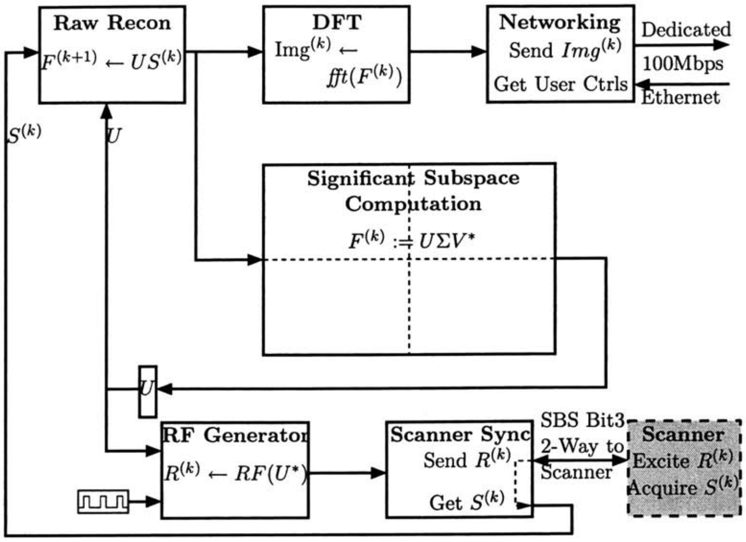

Figure 7-2: The dynamic computation pipeline ring. Each solid rectangle represents a non-Fourier imaging pipeline task and is executed on separate processors. Computation modules encapsulate separate imaging tasks, as indicated in boldface, and may have multiple pipeline stages or execute on multiple processors. The imaging pipeline interfaces via a dedicated Ethernet connection to the display system and via an SBS 413-1 VME bus to VME bus Bit3 adapter to the MR scanner.

In order to use the available computing resources efficiently, we can overlap the stages of execution of different imaging cycles, thus maximizing throughput, since the latency is intrinsically limited by the MR acquisition process. Provided sufficient computing resources, all stages of the pipeline can execute in parallel. For example, while the set of response samples received from one acquisition are being used to form the current k-space estimate, the k-space estimate of the previous acquisition is being Fourier transformed to produce the image, while the image from two acquisitions ago is being sent to the display. Operating simultaneously on all these time steps, via parallel execution of the imaging tasks involved, allows us to maximize throughput for every dynamic experiment. This yields the maximal temporal resolution that can be achieved with the underlying computing hardware or as limited by the operator-prescribed acquisition parameters (e.g., number of excitations per TR, in addition to subspace dimensionality and TR).

The pipeline platform design offers a number of advantages for adaptive spatial encoding, related to extensibility and performance. With the asynchrony and local timing, maximum throughput is maintained regardless of which pipeline stage is the slowest, as shown in Fig. 7-4. Although in some cases this is limited by operator-prescribed scan acquisition parameters, in other cases the slowest stage may be a novel encoding or reconstruction method that requires additional computing, such as spiral acquisitions for 3D imaging or DATUM encoding. In such cases, this pipeline design allows both maximum throughput for a given implementation, as well as easy replacement of existing modules with improved software module implementations or with implementations that use additional computing hardware to reduce their cycle time. Furthermore, new encoding methods that require additional encoding or reconstruction tasks can likewise be accommodated, while replacement modules with additional pipeline depth allow some coarse-grained control of throughput. Finally, new encoding methods that may require additional information, for example receiver coil sensitivity calibration for parallel imaging experiments, can be easily implemented. New pipeline modules that produce and distribute information as needed, can be inserted into the pipeline and the pipeline can be rewired with minimal programmer effort. Our current implementation of the pipeline, shown in Fig. 7-2, is targeted to non-Fourier encoding methods such as Hadamard, SVD and DATUM. To present this implementation, we analyze the steps involved in completing one imaging cycle.

The RF Generator and Scanner Synchronization modules handle the generic tasks of transforming any set of basis vectors to spatial excitations, and acquiring the sample responses from the MR scanner respectively. Given an encoding basis, the RF Generator produces RF pulses of the desired flip angle that conform to the scanner's waveform generators' data format. In the low flip angle regime this requires computing vector magnitude and phase in the k-space domain. Once formed, RF pulses are sent to the scanner's RF waveform generators via the Synchronization module. This module uploads the RF pulses to the scanner and instructs the pulse sequence active on the scanner to apply the shaped RF waveforms in order to produce the spatial profiles of excited magnetization (Eq. (2.24)).

Apart from the MR scanner hardware (e.g., magnet, coils, receivers etc.) the Scanner module encapsulates the non-Fourier pulse sequence. The sequence is responsible for acquiring the sample's response to each RF pulse. Like any sequence provided with the scanner, the non-Fourier sequence enters a real time scanning loop for an appropriate number of repetitions, depending on, for example, whether it is the multi-echo sequence of Section 4.1.

In each repetition of the sequence, the appropriate number of RF pulses are used to excite the magnetization, and the pulse sequence instructs the scanner at the appropriate times to acquire the signal produced under the readout gradients. The scanner performs quadrature detection and A/D conversion of the induced voltage on its receiver coils at the requested times and places the result in its raw data memory. The Scanner Synchronization module then downloads these acquired responses from the scanner's raw data memory directly. The set of responses (currently without any post-processing such as filtering) are combined with the basis vectors (Eq. (2.28)) by the Raw Reconstruction module to produce the current k-space estimate of the FOV contents. Non-Fourier Keyhole [146, 165] reconstructions can also be performed by this module. The raw k-space estimate is subsequently Fourier transformed in the DFT module to produce the image which is then sent to the display and archiver process by the Networking module.

In order to update the encoding basis for adaptive methods, the Raw Reconstruction module also distributes the current k-space estimate to the Significant Subspace Computation module which, via an operator-selected rank-revealing linear algebraic decomposition, produces a new encoding basis. The Significant Subspace module currently executes on up to four processors (as shown by the dashed boxes in Fig. 7-2) in order to minimize adaptivity latency. For non-fixed basis encoding methods, this final step is almost always necessary due to small arbitrary rotations of the most significant subspaces stemming both from noise in the measurements and excited basis profiles as well as new data from changes in the FOV captured by those noise components. The first imaging cycle begins by acquiring a full estimate of the contents of the FOV by encoding with an orthogonal matrix of full rank, such as the identity (i.e., producing phase encoded responses) or Hadamard matrix. The system can also be restarted with a full acquisition, either periodically, or, if the k-space estimate is deemed to no longer accurately represent the contents of the FOV. This decision can be made either manually or automatically, as we describe in Chapter 9.

Let us return to the issue of maximizing throughput. From the point of view of the physical system, the maximum throughput is obtained when one image is generated at a period of

$$T_{\text{scanner}} = K\text{TR}/f + \tau_{\text{sync}}, \tag{7.1}$$

where K is the encoding subspace dimensionality, TR is the repetition time, f is the number of responses acquired by the sequence per TR, and τ_{sync} is the synchronization time necessary for the transfers of sending the excitation profiles to the scanner and downloading the acquired responses. Methods such as NF*P and UNFOLD-NF (described in Chapters 5 and 6) affect Eq. (7.1) by reducing K.

From the point of view of the pipeline, the pipeline must be full. That is, the number of imaging cycles on which computations are being independently performed by separate modules must be equal to the depth of the pipeline. If we separate the ring of the pipeline from the other components as shown in Fig. 7-3, it is easy to see that the condition of maximizing the throughput is equivalent to requiring that each pipeline stage within the critical path (that is the straight path from RF generation to display) must require less time than the scanner acquisition module. When this condition does not hold, additional hardware or further pipelining of the modules should be sought. When it does hold, the Δt of the imaging process becomes precisely $\Delta t_{\text{imaging}} = T_{\text{scanner}}$.

Regardless of whether it is possible for this condition to hold (i.e., as limited by computing resources), the maximal throughput is obtained when one set of response data is available at the frequency of the slowest pipeline stage. Again, this is either limited by Eq. (7.1) or computing resources. Regardless of the source of the slowest stage, this condition is easy to fulfill by beginning acquisition of the next set of responses as soon as the acquisition of the current set of responses is completed.

The RF Generator module therefore differs from other modules in that it starts computations for the next imaging cycle as soon as it has completed the current imaging cycle rather than waiting for notification (represented by the clock wave in Fig. 7-2). The RF Generator module drives the pipeline ring at a period as low as 25-50ms, using the latest encoding basis for multiple acquisitions

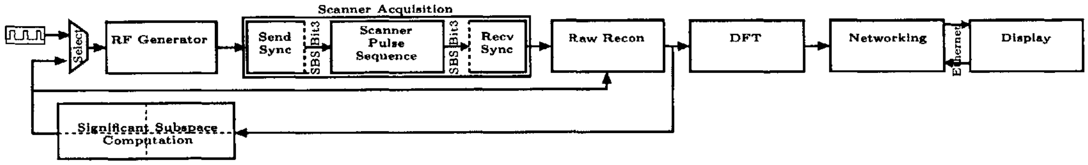

Figure 7-3: Driving the pipeline ring from the RF Generator module at a high frequency, by continually pushing RF pulses computed from the latest encoding basis allows the pipeline to operate at the frequency of the slowest component within the critical path (straight line from RF generation to display).

if that is necessary, as shown in Fig. 7-4.

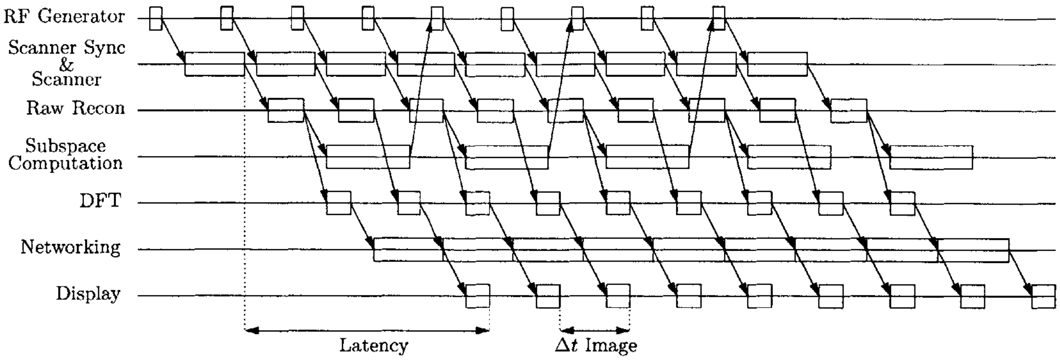

Figure 7-4: By using the RF Generator module to drive the pipeline ring at a period as low as 25-50ms, the pipeline operates at the period of the slowest stage in the critical path (in the depicted case, the Networking module). As shown in Fig. 7-3, the Encoding basis module is removed from the pipeline critical path, allowing the most recently computed encoding basis to be used for multiple acquisitions if that is necessary. The minimum imaging period achievable by the pipeline occurs when the slowest critical path stage is the scanner acquisition module.

7.1.2 System Implementation: Hardware

The pipeline described has been implemented on a Mercury multi-processor computer (Mercury Computer Systems Inc, Chelmsford MA) connected to our 1.5T GE Signa LX EchoSpeed MR scanner (GE Medical Systems, Milwaukee, WI). This three-generation old VME bus based multiprocessor computer contains a number of boards:

- A FORCE dual-slot board (Force Computers Inc, Fremont, CA) based on a μSparc processor (sun4m architecture, 110MHz, 32MB RAM, running the Solaris 2.5 OS, Sun Microsystems Inc., Santa Clara, CA). This board provides a network interface (through a Sun Microsystems 100Mbps fast Ethernet controller), acts as the VME master and also hosts the remainder boards via the embedded MC/OS operating system (Mercury Computer Systems Inc, Chelmsford MA).
- Two Mercury MCH6 boards, each of which holds four PowerPC 750 processors (each 375MHz, 32MB RAM, also called Compute Elements). These boards provide the bulk of the computational power required by our pipeline. In particular, each of the modules in the pipeline shown in Fig. 7-2 executes on one or more of these compute elements, with the exceptions of the Networking module, which operates on the Sparc processor, and the Scanner module, which operates on the MR scanner hardware. Each of the MCH6 boards contains a fast proprietary interconnect (called ILK) which can route data in between the processors on the board at a very high rate. An extra ILK is piggy-backed on the VME bus to allow fast transfers between processors on separate boards.

- An SBS 413-1 (also called a Bit3) adapter board (SBS Technologies Inc., Carlsbad, CA), with DMA capability that we use to interface the multi-processor with the MR scanner. The Bit3 board provides us with access to the raw memory board (called BAM for Bulk Access Memory) of the Transceiver, Processing and Storage cabinet (TPS) of the MR scanner at sustained DMA rates of up to 26MB/sec.

Finally, a Unix-based laptop is used to interface with the multi-processor system in order to control its function and to provide the user with image display. An overview of the elements added to the MR scanner hardware is shown in Fig. 7-5.

The choice of a VME bus architecture for the external system is supported by the VME bus architecture of our GE scanner's data acquisition system. It is possible, if desired, to insert the boards used by our external system directly into the scanner, thereby completely integrating the dynamic system with the scanner. With few exceptions (Scanner Synchronization module, waveform format and pulse sequence implementation), the design is portable to any other MR scanner. The scanner-specific modules may be ported so long as the scanner manufacturer allows access to their hardware and provides sufficient information for programming it.

Finally, in cases where it is desirable to have an external system (e.g. so that it can be used to drive multiple MR scanners via additional Bit3 boards) the choice of the adapter was made since the same type of SBS adapters is used by our scanner manufacturer to interface the TPS with the host workstation and other external options that one may purchase for it (such as a cardiac workstation).

7.1.3 System Implementation: Software

Scanner/Add-on System Communications

The first step of implementing a broadband encoding system begins with the pulse sequence designs (PSDs). A set of programming tools provided by the scanner manufacturer allow us to produce two executables; one running on the scanner host, via which the operator can select pulse sequence parameters such as TE, TR size of desired FOV etc., and a second executable, executing on the Integrated Pulse Sequence Generation Computer (IPG) in the TPS chassis, which is responsible for using the sequence parameters to control the exciter and gradient sequencer boards and the acquisition filters. Any spatially selective pulse sequence can be adapted to work with our add-on system.

Adaptation of a pulse sequence is a two-tier process. First, the part of the pulse sequence executing on the IPG must allocate two memory buffers. One buffer must be allocated from the 256K 16-bit word RF waveform memory of the IPG board. This is where the add-on Mercury system places the RF pulses to be used for excitation in subsequent scan loops of the PSD. The second buffer is a small control buffer that must be allocated from the 4MB DRAM attached to the IPG's 68020

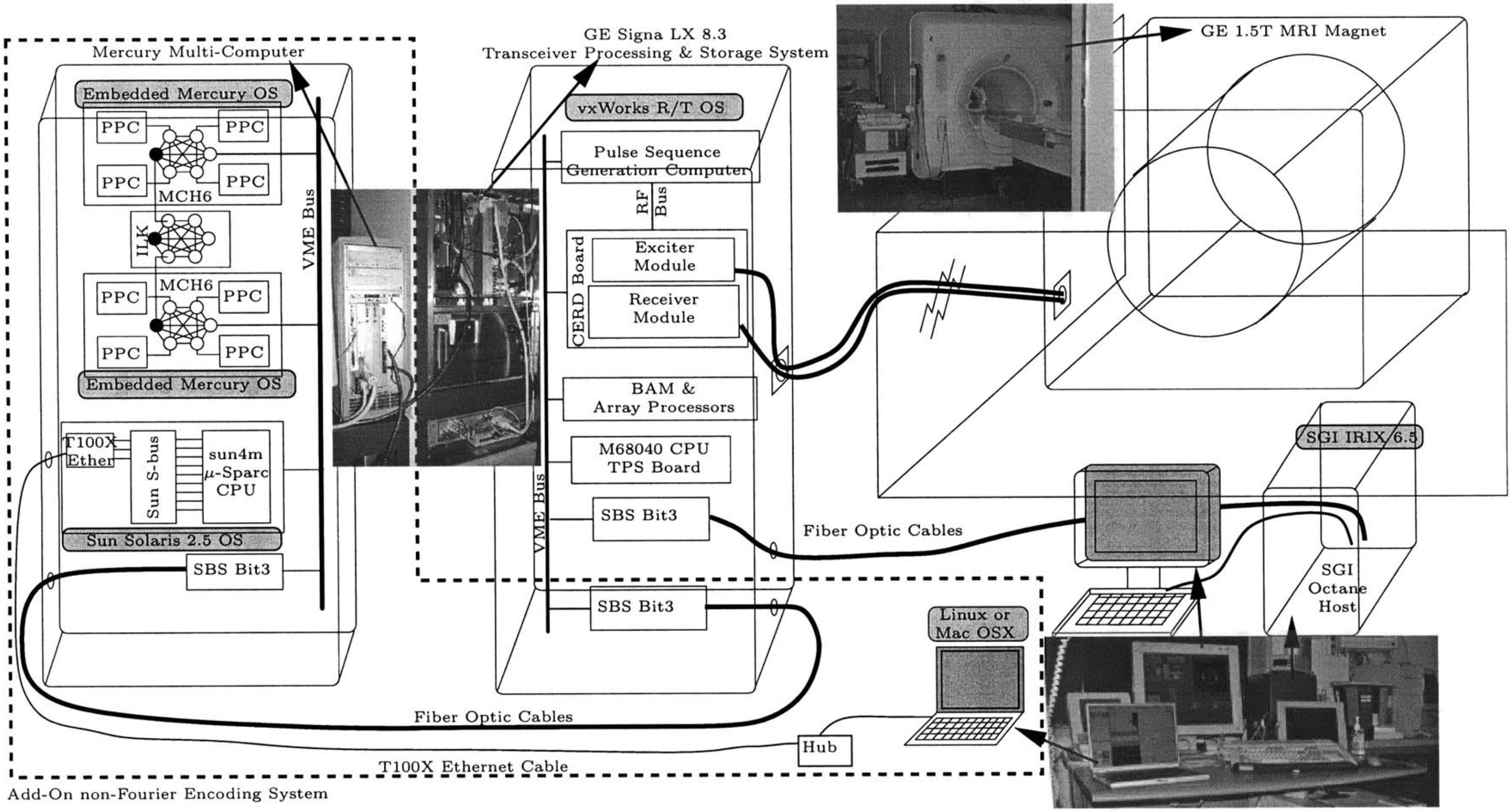

Figure 7-5: Overview of the add-on computation system implementing the pipeline ring of Fig. 7-2, and necessary connections to an MR scanner.

Motorola processor. This small buffer is where the add-on system places the control words that the pulse sequence must recognize and appropriately handle (e.g., the next TR and TE to be used, the number of spatially selective RF waveforms that were uploaded to the IPG waveform memory, and hence how many responses the pulse sequence must generate etc.). Allocating these two buffers is a simple initialization task performed in the source code that produces the IPG executable and an interface has been provided in order to encapsulate and abstract it.

The second step of adapting a pulse sequence involves:

(1.) Adding the ability to read the number of responses required by the add-on system from the control buffer.

(2.) Computing the appropriate number of repetitions to run based on the number of responses that can be acquired per TR (which the sequence is solely aware of).

(3.) Entering the real-time scan loop for that number of repetitions.

(4.) Using the appropriate offset into the RF waveform memory buffer when loading the RF generators in each repetition interval.

(5.) Finally, once the number of repetitions has been completed, setting a flag in the control buffer so that the add-on system can recognize successful completion of response acquisition.

Again, an interface has been produced to encapsulate these tasks and simplify PSD implementation for the dynamic imaging system.

A minor complication of communications stems from providing the addresses of the control and waveform memory buffers to the add-on system, and finding out the BAM address where the TPS's CERD board will place the resulting sampled MR data. The first problem unfortunately still has a manual solution. When the IPG part of the pulse sequence using our interface is initialized, the address of the control memory block is displayed in the scanner host console and must be manually provided to the add-on system. The RF waveform memory address is placed in the control block by the PSD in order to minimize inconvenience.

In order to obtain the BAM address for a specific scan an automated solution is provided by yet another interface. The BAM address range where the results of the next pulse sequence's scan will be placed is selected internally by the TPS CPU board and is available by connecting to a certain IP address port on that computer. However, the TPS is on a reserved IP address, available only through the host. Since the host is on a globally accessible IP address, we provide a small daemon running on the host to query the TPS and return the address. Since the BAM address is only available after a pulse sequence has entered the scan loop, the add-on system must wait for PSD initialization communicated via the control structure, before contacting the daemon.

Most of the spatially selective pulse sequences described in Chapter 4 were modified to use the communication interface provided for communicating with the add-on system as described above. The communications between the add-on system and the scanner utilize the Bit3 VME bus to VME bus adapter board. Part of the communications interface was the design of a specialized device driver, specifically implemented for the needs of our adaptive pipeline, allowing the add-on system to read or write raw memory on the TPS using block memory transfers; the add-on system provides the adapter card an arbitrary address on its local VME bus, an arbitrary address on the remote TPS VME bus, a buffer length, and a direction (to or from the local bus). With this information, the memory transfer is fully specified as far as the Bit3 adapter is concerned.

The Bit3 provides a small 32-byte window on the local VME bus address space that reflects its control registers. Via jumpers located on the adapter board, one selects the starting VME address of this window. Facilities provided by the embedded MC/OS of the add-on system are used to access these registers via the VME bus, since all PPC processors are capable of read/write access to any raw VME address. In this manner, another portion of the interface was provided, on the add-on system side, so that every PPC processor may initiate a transfer through the Bit3 board. The interface encapsulates the tasks of writing the relevant addresses and sizes to the registers of the Bit3, and relying on the latter to perform the DMA transfer to, or from, the remote bus, in the background.

Local Add-on System Communications

DMA transfers are also utilized by the PPC processors for inter-process communications in order to achieve maximal efficiency and minimum latency. An interface was designed to encapsulate the tasks of allocating memory buffers on the individual processors and arranging the data transfers between them. The interface follows the pipeline abstraction, i.e., offering simplifications that enable the pipeline to be easily rewired. Whenever a module is instantiated it can allocate any number of local input "sink" and output "source" buffers. The input buffers are where the module collects the input that it performs its function on. These input buffers of the module are "sink" buffers for the modules that generate the data that the module needs to operate on. Similarly, the output buffers of the module are where the results of the module's computation will be placed.

A module is solely responsible for requesting that each of its output buffers be attached to the input buffer of all modules that require its output to operate. That is, a module requests that a transfer path is generated at startup from each of its output buffers to the source buffers of all modules that require its result as input. The input buffers of these consumer modules are then the sink endpoints of a transfer from the output buffer of each module. In this manner, the producer portion of each module attaches its output buffer to the corresponding input endpoint that has been allocated by each module that needs to consume its output. It is this portion of the interface that arranges for the routing of the block transfers via the ILKs.

During the imaging cycle, when a module completes processing of its input data, it places the data into its output endpoint and begins the block transfer which is routed from that endpoint to the input endpoint of any module that needs to process the data next. Broadcasts are used to multiple input endpoints, such as the *k*-space output buffer of the Raw Reconstruction module which is broadcast to the input buffers of both the DFT module as well as the Subspace Computation module (c.f., Fig. 7-2). Test and set locks, provided by MC/OS, are used by the transfer abstractions in order to guarantee atomic access to endpoints where necessary, i.e., when requested by the modules. After a transfer is complete, the source module typically notifies the sink module via a counting semaphore, also provided by MC/OS. Figure 7-6 presents the complete data path of the current implementation of the pipeline ring.

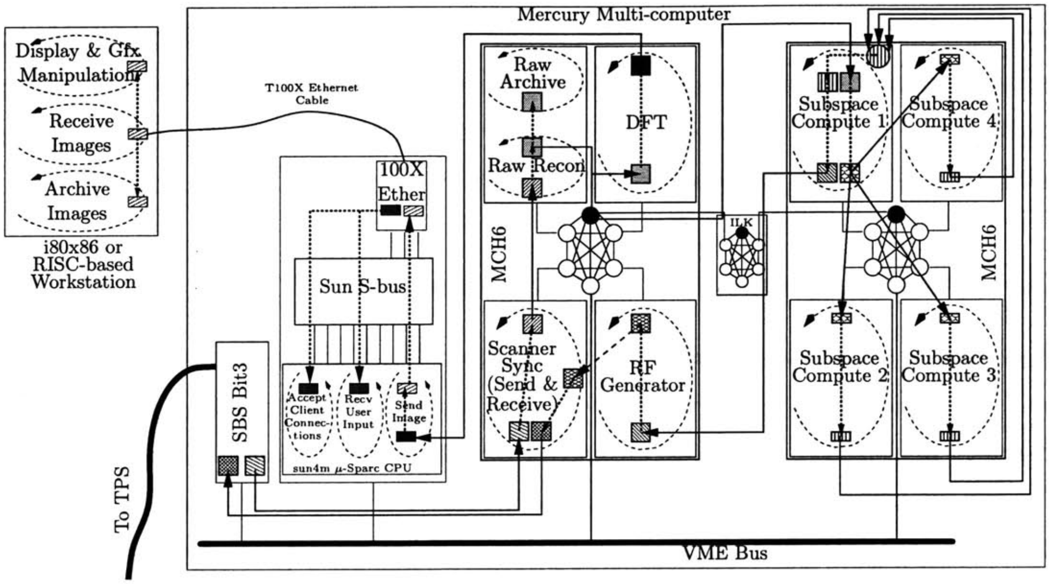

Figure 7-6: Data movements between pipeline computation modules. Rectangles denote processors. A filled box denotes a transfer endpoint (boxes are color or pattern-coded when crossing processor boundaries for easier identification). Solid lines denote block transfers in between processors which are always routed via the ILKs. Dotted lines inside processors denote data processing and/or copying. Arrowheads specify the direction of the transfer. POSIX execution threads are depicted by oval-shaped dashed arrows inside processor rectangles.

System Display & Control

As mentioned previously, a laptop (or workstation) is connected via a dedicated 100Mbps Ethernet to the add-on system in order to provide display and additional archiving functions. This front-end system also provides basic image processing (e.g., window and level). For 3D imaging, we have implemented a module that is used with the Slicer tool [30]. Since Slicer is intrinsically a 3D viewing tool, a purpose-built 2D front end was implemented for the case of 2D imaging.

Raw Recon	DFT	Network	Rank-32 Subspace Computation						RF Generate	Scanner Sync
			L	R	C	CW	CP	F		
50ms	25ms	55ms	600ms	225ms	3s	1.2s	600ms	13.6s	25ms	75ms

Table 7.1: Module times for one imaging cycle. Subspace methods are: Lanczos (L), Randomized SVD (R), Conjugate Gradient SVD (C), Conjugate Gradient SVD with warm restarts (CW), CW parallelized on 4 processors (CP) and Full SVD (F).

Both front ends allow the operator to control imaging parameters in real time. These parameters fall into one of two categories; those which affect the pulse sequence execution on the scanner, and those which affect the computation pipeline. The former set of parameters are familiar to clinicians accustomed to a Fourier imaging system, and are in fact just patched via the add-on system through the Bit3 to the pulse sequence. These include TE and TR, number of excitation/echo pairs (e.g., echo train length) etc. The latter set of parameters allows control of the non-Fourier components of the system. Through these, the operator can choose the particular linear-algebraic method for the subspace truncation as well as the dimensionality of the subspace to be used. They also enable controlling the reconstruction process, to e.g. perform keyhole imaging, wherein newly acquired data replaces the old data in the acquisition subspace.

7.1.4 System Implementation: Performance

Most modules in the pipeline are optimized to a moderate degree in order to reduce latency. Typical module execution times are given in Table 7.1. A number of methods for subspace truncation are currently implemented in order to accommodate different adaptive time-resolution requirements and to provide some versatility in encoding choice. Although many different algorithms may be used to identify the encoding subspace, our method of choice is a gradient descent (CG) algorithm that searches for the vector associated with the highest singular value by maximizing the Rayleigh quotient [36]. The matrix is iteratively deflated before searching for the next largest singular vector. Computing time is reduced using warm restarts to speed up subsequent decompositions. That is, singular vectors computed for the previous cycle are used to re-initiate calls to the algorithm. The parallel implementation of the algorithm uses 4 processors to achieve a moderate speedup of 2, partially due to the small size of the matrix in 2D imaging (typically 256-by-256) which makes communications overhead a significant portion of running time.

Other subspace identification methods currently offered include a randomized approximate version of the SVD [29] and a spatial-frequency ordered Krylov subspace method [166]. These methods represent trade-offs between subspace accuracy and computational cost. The main trade-off for MR imaging purposes is the number of signal responses, or TRs, necessary to encode all important image information. We have found that when using such methods one needs to retain a much larger subspace to keep the imaging error small relative to noise (e.g., typically about 80 encoding vectors are needed in comparison to 32 of the singular vectors). Reducing the approximation error of these methods, e.g., using more columns of the matrix in the approximate SVD computation or using more iterations of Lanczos tridiagonalization, the computational expense reaches that of CG SVD, making their use impractical at this time.

7.2 Dynamic 2D Imaging Results

In this section we present some MR imaging results obtained with the dynamic system we have described. Using doped water and animal tissue phantoms, our experiments cover a range of cases that may be encountered in a dynamic MR imaging session. In all images presented, the direction of the spatially selective excitation is the horizontal, while the vertical is frequency encoded. The warm restart CG SVD algorithm was used for subspace identification.

7.2.1 First Experiment: Bolus Tracking

A small syringe filled with contrast agent is continuously moved around a large static bottle filled with doped water. This imaging experiment allows us to assess adaptation of encoding to the movement of a bolus in the FOV. Imaging parameters for this sequence were 56 ms Eff.TE, 115 ms TR, 256-by-256 image matrix and 24 cm FOV. The multi-echo spin echo pulse sequence described in Section 4.1 was used, with 4 RF excitation/echo pairs. The 256-dimensional subspace was truncated to the 40 primary SVD vectors, leading to a total acquisition time of 1.15 sec per image, compared to 29.4 sec for a single echo and 7.4 sec for a four echo Fourier encoded pulse sequence.

Two small continuous portions of this series are shown in Figs. 7-7 and 7-8. We note that the syringe is in constant motion. That is, while responses that will be used to form a single image are being acquired the syringe changes location. This "inter-view motion" leads to large artifact in Fourier basis imaging. However, in this compressed non-Fourier encoding method, the ability to image this motion properly is inherent. This is related to both the imaging time of a single time frame, which requires only 10 TRs to be formed, but also related to the properties of SVD encoding. In particular, the first few SVD encodes carry more energy than any individual Fourier mode of the sample, thus encoding more signal with a single acquisition. Additionally, the largest signal components that are captured by the first few encodes correspond to the lowest spatial frequencies, which in turn determine salient image features [168].

7.2.2 Second Experiment: Needle Tacking

In an experiment to assess the ability to capture changes occurring within an object during dynamic imaging, a 22G biopsy needle was continuously inserted into, and subsequently removed from, an animal tissue phantom. The final portion of the insertion and the removal portion of the series are

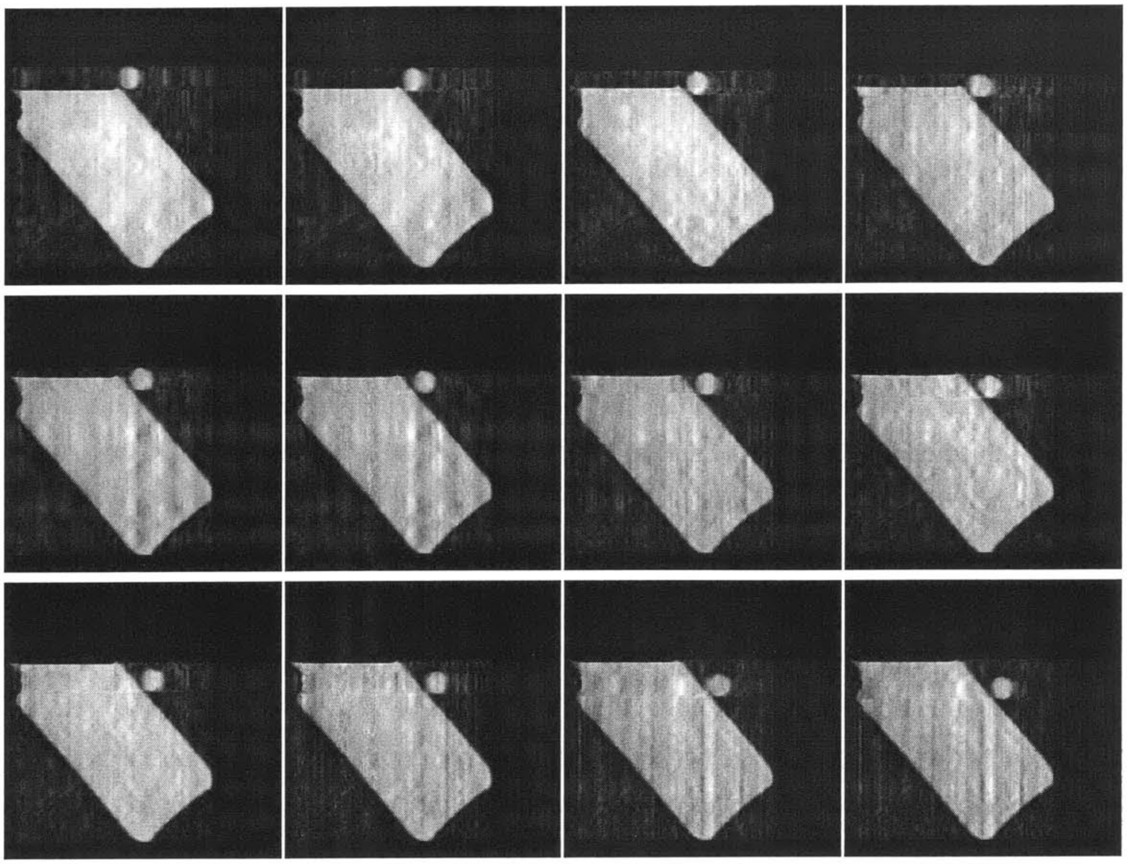

Figure 7-7: Syringe filled with contrast agent, moving around a bottle filled with doped water. Time flows from left to right, top to bottom. Images were acquired at a rate of 1.2 sec per image, a speedup of 6.4 over an equivalent 4 echo train length Fourier encoded acquisition, and 25.6 speedup over a single echo Fourier encoded acquisition. Note that the syringe was moving constantly throughout the experiment, therefore contaminating the acquired responses with inter-response motion artifact, as in any Fourier encoded image.

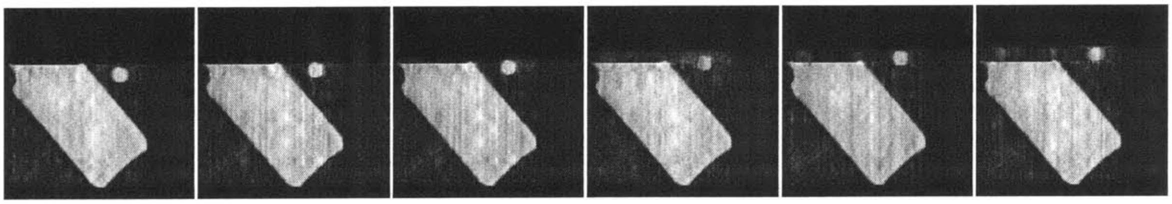

Figure 7-8: Syringe filled with contrast agent, moving around a bottle filled with doped water. Time flows from left to right. Images were acquired at a rate of 1.2 sec per image, a speedup of 6.4 over an equivalent 4 echo train length Fourier encoded acquisition, and 25.6 speedup over a single echo Fourier encoded acquisition. Note that the syringe was moving constantly throughout the experiment, therefore contaminating the acquired responses with inter-response motion artifact, as in any Fourier encoded image.

presented in Fig. 7-9. Imaging parameters were 20 ms TE, 180 ms TR, 256-by-256 matrix, 24 cm FOV, and rank-32 acquisition, resulting in 5.8 sec per image, a speedup of 8 over the equivalent single-echo Fourier acquisition.

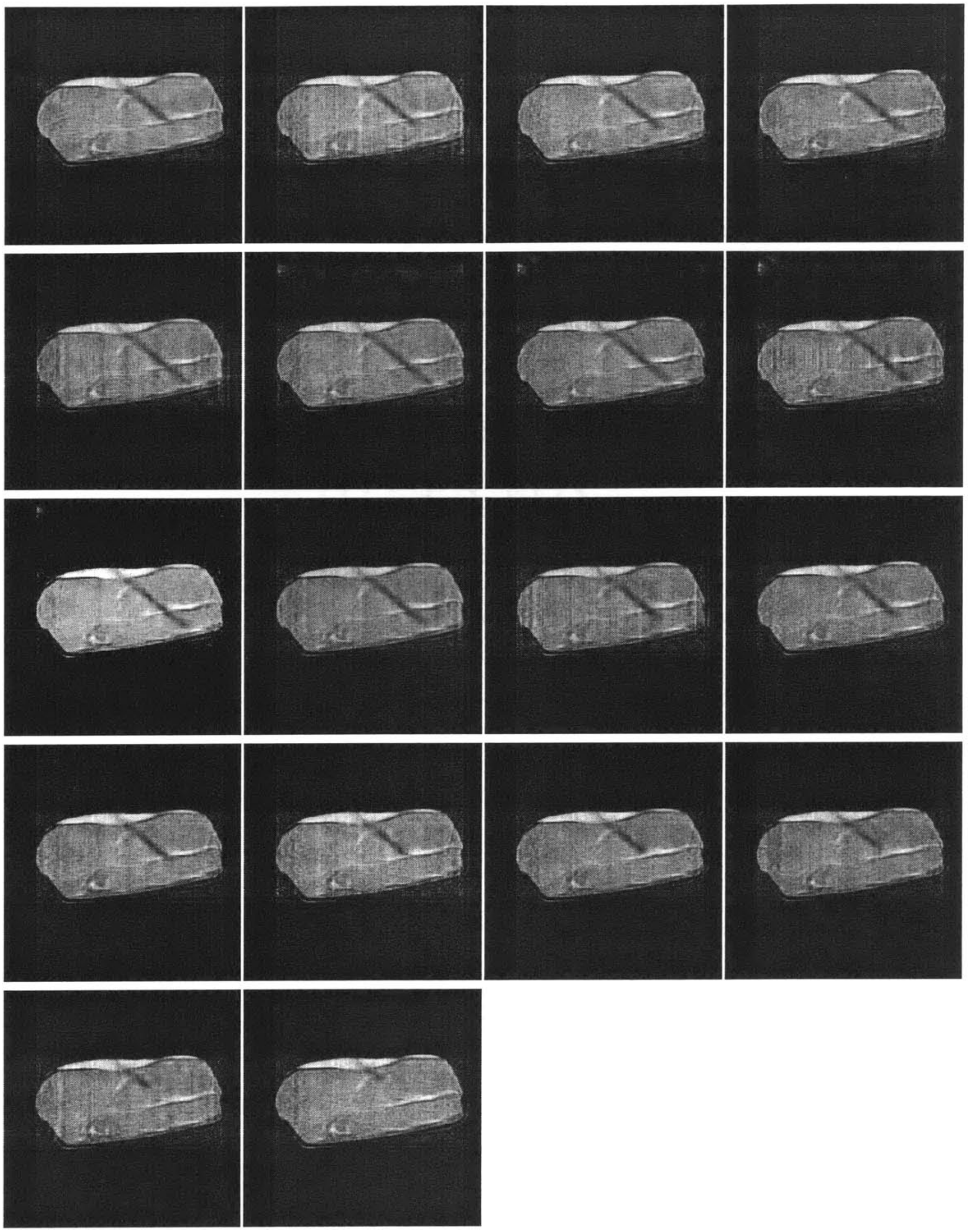

Figure 7-9: A 22G biopsy needle inserted and subsequently removed from animal tissue phantom. Imaging at a speedup of 8 over equivalent single-echo Fourier encoded imaging.

Closer examination of another needle removal experiment, shown in Fig. 7-10, shows the surface of the tissue being pulled upward and to the right as the needle is being removed. This surface tension detail, that ranges 3 out of 256 pixels, or 3 mm, is captured even at speedup of 8 over

Fourier imaging. The equivalent 32-coefficient Fourier acquisition would possess a 7.5mm pixel size, versus 0.9375mm in this non-Fourier acquisition, which would have undoubtedly caused loss of this detail. This is an intrinsic difference between rank-reduced (i.e., compressed) non-Fourier imaging and low-order Fourier imaging; spatial resolution may not always be sacrificed to the same degree by subspace truncation.

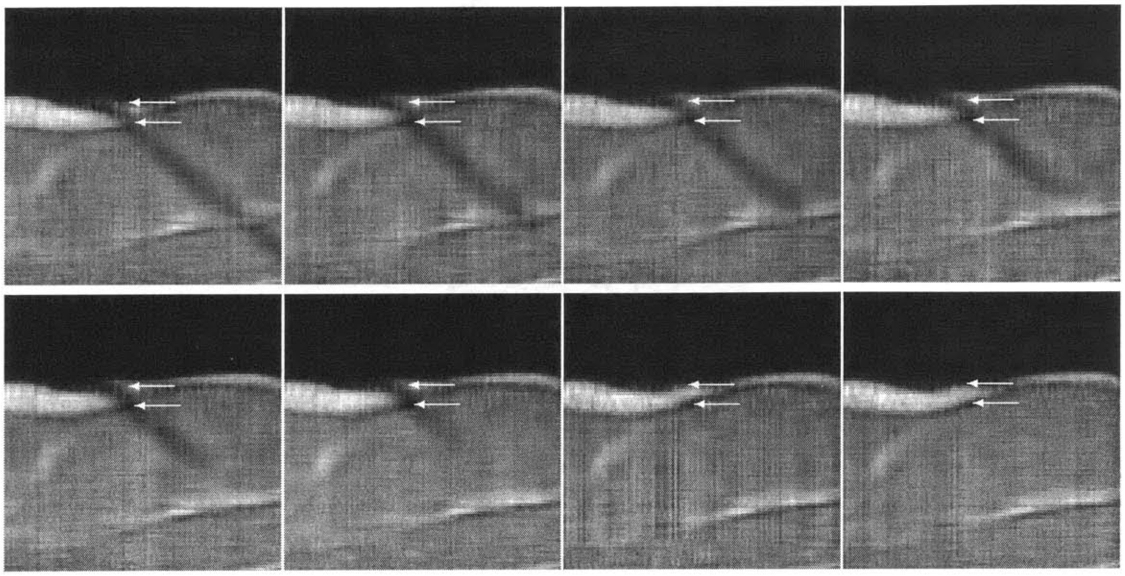

Figure 7-10: Animal tissue phantom detail captured by SVD encoding. Close inspection shows the tissue moving upward at the exit point of the needle. All white arrows are placed in the same location in each image.

7.2.3 Third Experiment: Object Deformation

Rank-reduced non-Fourier imaging becomes more problematic when large changes occur in the contents of the FOV. These result in large changes in the encoding basis vectors, to the extent that the spatial excitations may no longer excite locations within the FOV where the spin density resides. Adaptivity to one such case is demonstrated in Fig. 7-11, where the animal tissue phantom was deformed. A human hand entered the FOV and applied pressure to the phantom. Imaging parameters were the same as used in the last experiment. The 32-dimensional subspace contains most of the useful information in the image and manages to capture those changes in the FOV, as demonstrated by the results. Although the individual maximal response basis vectors may change significantly between two acquisitions, the subspace they form may remain fairly similar.

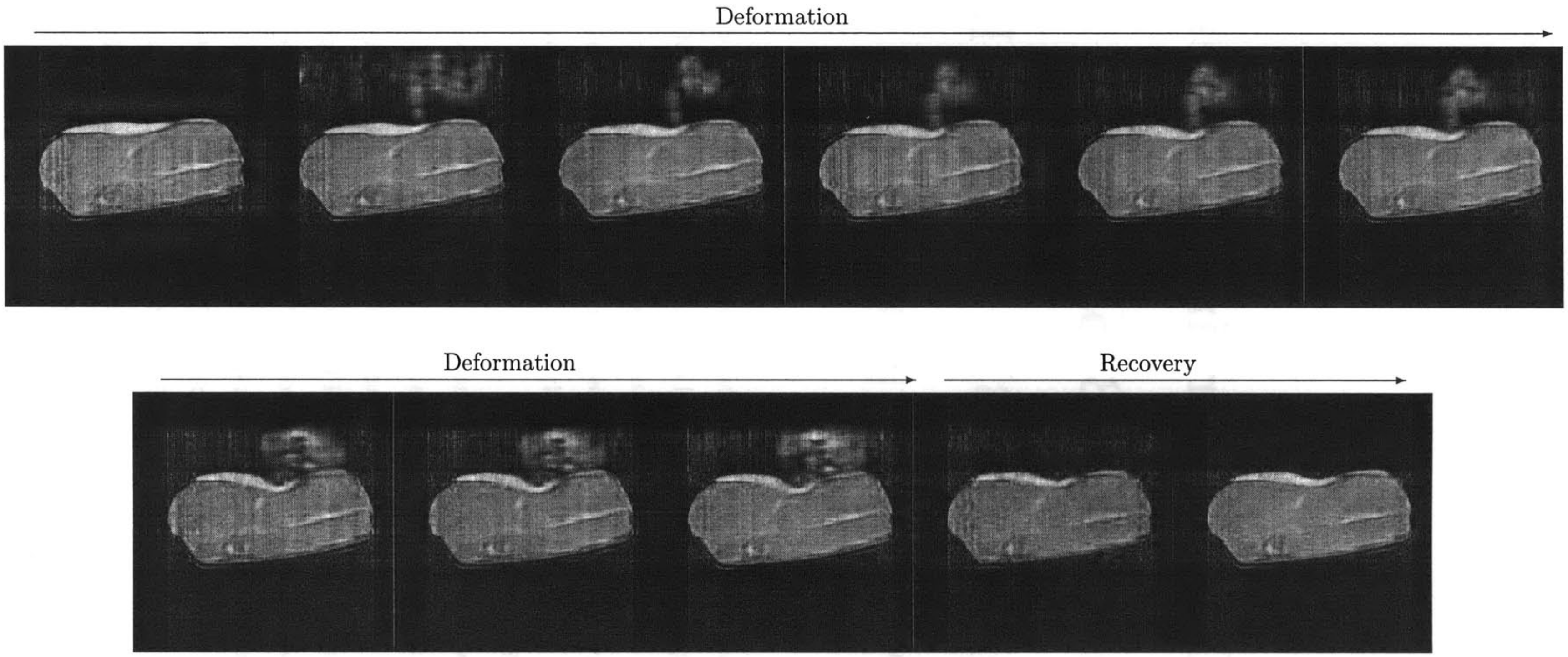

Figure 7-11: Animal tissue phantom being deformed. Same imaging parameters as in Fig. 7-9

Chapter 8

3DIVUFSE: Merging Fourier Encoding with Broadband Excitations for 3D Inner Volume Ultra-Fast Spin Echo MRI[1]

So far this dissertation has concentrated on the use of non-Fourier broadband encoding methods in order to prospectively compress the MR signal content, and therefore achieve MR imaging efficiency that is not available to fixed basis encoding methods, such as Fourier basis imaging. Nonetheless, in most MRI applications scan time is expended acquiring high resolution data from portions of the field of view that are outside the diagnostic volume of interest (VOI), in order to avoid aliasing while achieving the desired spatial resolution.

In this chapter we aim to achieve increased efficiency not by modification of the encoding of the MR signal but, rather, by limiting the radiated signal to emanate only from within the VOI. Methods that focus imaging time at resolving the VOI are becoming central to efficient MRI, as witnessed by the number of reduced FOV (rFOV) methods that have been proposed to-date and that are currently being installed in commercial MRI equipment. The limitation of Fourier basis imaging to uniform resolution over the extent of the transverse magnetization, in conjunction with the simplistic slab-selective excitation approach used for sample excitation in MRI, leaves little room to improve efficiency. In effect, efficiency in Fourier imaging is most often equivalent to sacrificing spatial resolution, or resorting to specialized limited sensitivity receiver coils. Ergo, to increase VOI imaging efficiency in general imaging cases, one must either supplement gradient-induced Fourier

---

[1] Portions of this chapter have appeared in [100, 97, 98, 99]

basis imaging, or, completely replace it with non-Fourier or Fourier-like methods.

Fourier rFOV methods use additional information to reduce encoding burden, such as that provided by multiple independent receivers, as discussed in Chapter 5, or, by making simplifying assumptions about the imaged sample [54, 79, 10], with one such example examined in Chapter 6. Although widely applicable, the use of intrinsically inaccurate additional information, e.g., due to noise or the nature of living tissue, involves error minimization to achieve image reconstruction. Error minimization (e.g., via matrix regularization [138]) inadvertently leaves unresolved image subspaces, wherein diagnostically significant information might exist. Often, these methods are applied in situations wherein reconstruction errors do not adversely affect use of the reconstructed images and can be tolerated, such as in continuous dynamic imaging for the MRI monitoring of therapies. In fact, this tolerance is central to most such methods, as witnessed by their intricate interconnection with additional information that is obtained from the time axis.

Non-Fourier encoding methods, that have been at the spotlight of this thesis, enable rFOV imaging while avoiding the sampling limitations to some degree [116, 20]. This is enabled by relying on more intricate direct use of radio frequency (RF) excitation of spatially shaped profiles, such as wavelet-shaped functions [112] or SVD-derived profiles [164], for encoding. Apart from the typically reduced SNR and specialized imaging sequences required, one main drawback of these methods is the shift from acquisition to excitation sampling requirements.

Because image resolution is intrinsically defined by the resolution limits of the spatial excitations, large excitation k-space coverage is required, often leading to lengthy pulses. This is especially the case when multiple dimensions are encoded (see e.g., the discussion in Section 4.3.1). Section 4.2 was devoted to an attempt to circumvent this limitation. Another problematic case, that was mentioned in Section 5.2, is when additional FOV reduction is required by the RF excitations, such as when using an RF pulse to select a slice and perform non-Fourier encoding within that slice, as would be necessary e.g., for 2D GRE broadband non-Fourier MRI. Lengthy pulses limit the use of broadband non-Fourier encoding primarily due to motion, off-resonance, and flow effects. Methods that employ non-Fourier analyses but that approximate the acquisition via Fourier basis sampling [12, 72, 13, 38] in order to avoid these limitations, unfortunately suffer data extrapolation errors often in addition to reconstruction error minimization issues.

One approach for efficient VOI imaging is the class of Inner Volume (IV) imaging methods, which employ multi-dimensional spin selection to limit the extent of the coherent transverse magnetization along the slice and phase encoded dimensions, e.g., via 2D spatially selective RF excitation. Then, Fourier basis sampling of the emanating signal requires fewer phase encoding steps to yield the desired resolution over the VOI, while enabling reconstruction of all significant (w.r.t. SNR) diagnostic information. IV imaging sequences are often derived from standard Fourier encoding sequences with well-understood (and necessary) imaging qualities, usually by replacement of the simple slice-selective RF pulse. Additionally, IV methods can be used in conjunction with many other rFOV methods to achieve additional efficiency, thus making them widely applicable. Many of the prior chapters of this thesis attempted to provide precisely this applicability to non-Fourier imaging as well.

In IV methods, image resolution is independent of the resolution limits of the inner volume selection. Nonetheless, 2D spatially selective RF excitations [8, 7] still require relatively lengthy RF pulses to achieve acceptable frequency cutoffs [40]. Accordingly, to-date, very few applications of IV imaging have been successful. Examples include cases such as when the length of the RF pulse has little effect on sequence timing [6], when additional measures are taken to account for shorter RF pulses [158, 78], or, when the imaging task necessitates optimization of only specific aspects of the RF excitation [75].

Alternatively, for IV imaging, lengthy multi-dimensional RF pulses can be avoided by capitalizing on the efficacy and ubiquitousness of simple 1D-selective RF excitations in conjunction with the wide usage base of spin echo (SE) imaging. This is done by selectively refocusing magnetization only within the intersection of two orthogonal RF excitation slabs [27]. This is essentially the method we used of the non-Fourier 2D SE sequences we have examined so far. Although this method readily applies to fast SE (FSE) sequences [19], the lengthy refocusing pulses necessary to avoid slab profile degradation [75] elongate the FSE inter-echo spacing, thus greatly amplifying dephasing artifacts [105, 86, 18].

The shortest attainable echo spacing is achieved by using non-selective refocusing pulses, resulting in non-selective (termed single-slab) UFSE imaging [104]. In this chapter we couple an initial, strongly selective, 2D spin selection method that selectively excites magnetization along the two phase encoded dimensions, with data acquisition filtering along the readout dimension in order to produce 3D IV imaging of the VOI via a UFSE echo train. In Fourier basis imaging this is the one case where it is most necessary to provide sampling efficiency: 3D imaging requires $O(N^2)$ sequence repetitions, while SE imaging requires very long relaxation times resulting in very long TR.

Strong 2D selection requires efficient use of both gradient and RF subsystems. Although gradient optimization techniques are fairly mature [42], attempts to achieve excitation efficiency [17, 41, 107, 135] are still at infancy compared to methods available for the closely related problem of finite impulse response (FIR) filter design [84, 120, 11]. In the following section we introduce the combination of each of the two IV selection methods, i.e., 2D spatial excitation and selective refocusing, with UFSE echo trains. We will merge various techniques to ameliorate their selection properties to increase outer volume signal suppression, and conclude by analyzing the resulting combinations.

8.1 The 2D RF Method (2DRF-UFSE)

Multi-dimensional selective RF excitation [8] was popularized with the Fourier transform (F.T.) design paradigm for low flip angle RF pulses [121], i.e., $\theta \leq 30°$ [53, 50], summarized by Eqns. (4.29) and (4.34) (assuming that the entirety of k-space locations are visited in the set K_{acq} in the language of those sections). In the general case, the RF pulse and spatial profile generated are effectively related via the weighted Fourier transform relation of Eq. (4.29), with expansion coefficients drawn from the RF pulse and wave functions from the spatial-frequency space (k-space) traced by the gradients applied during RF excitation. Some k-space trajectories and RF pulses retain this Fourier transform linearity at large flip angles [122], making this principle central in selective excitation.

8.1.1 2D RF Design principles

Starting with equilibrium magnetization $M_0(\vec{r})$ in each voxel centered at $\vec{r}$ and a desired low flip angle profile $P_{des}(\vec{r})$, with Fourier transform $\hat{P}_{des}(\vec{k})$, application of the RF pulse

$$B_1(t) = \frac{-i||\gamma\vec{G}(t)||}{\lambda\left(\vec{k}(t)\right)}\hat{P}_{des}\left(\vec{k}(t)\right), \tag{8.1}$$

produces the transverse magnetization [121, 41]

$$M_{xy}(\vec{r}) = M_0(\vec{r})(P_{des}(\vec{r}) \otimes S(\vec{r})) \equiv M_0(\vec{r})P_{obs}(\vec{r}), \tag{8.2}$$

where $\otimes$ denotes convolution. Here, the point spread function (PSF) (from Eq. (4.28)) will be the item of interest. It is denoted by $S(\vec{r})$ and is the Fourier transform of the spatial frequency sampling function, $\hat{S}(\vec{k}) = \int_0^{T_{end}} \delta(\vec{k}(t) - \vec{k})|\dot{\vec{k}}(t)|dt$ [121], intrinsic to the applied gradients

$$\vec{k}(t) = -\gamma \int_t^{T_{end}} \vec{G}(\tau)d\tau, \tag{8.3}$$

where T_{end} is the end of the RF and gradient application including rewinders. Again, since the interest here is the PSF, the implicit weighting induced by non-unit-spaced sampling locations [70, 131] is explicitly absorbed in the RF excitation, as shown in Eq. (8.1), and absorbs both the k-space velocity compensation factor, $-||\gamma\vec{G}(t)||$ [121], and the k-space density compensation factor, $\lambda\left(\vec{k}(t)\right)$ [41].

8.1.2 Choice of 2D RF Excitation Profile and Trajectory

Salient features of the PSF are determined by the discreteness and finite extent of the k-space trajectory. Discrete coverage gives rise to spatial periodicity of the PSF (aliasing), resulting in excited magnetization “sidelobes” at periodic intervals. The limited extent of the coverage gives rise to oscillations (ripples) extending throughout the periodic interval of the PSF, resulting in excited magnetization throughout it.

Spiral trajectories have been widely used for 2D selective excitation [121, 40, 107] due to their optimality with respect to gradient usage, and their symmetric coverage of 2D k-space. Accordingly, they are well-suited for excitations that require similar properties (i.e., pass/stop-band) along the two phase encoded dimensions, as necessary for 3D rFOV imaging. The principal polar PSF [9] of a N-loop spiral trajectory has approximately N ripples in between the aliasing ring sidelobes [9, 143, 70]. These are located at $j/\Delta k_r \equiv jD$, for $j \in \mathbb{Z}^+$, the positive integers, when Δk_r is the radial discretization of the spiral [70].

Ripple minimization, both at the plateau of the pass-band as well as the stop-band, is of paramount importance to 2D-selective excitation for rFOV imaging. The former in order to obtain uniform intensity images and the latter in order to avoid residual excited magnetization outside the VOI as that will alias into it at rFOV sampling. This has stipulated use of profiles with smooth transitions that reduce rippling for a given k-space coverage, such as the Fermi function, [41]

$$P_{des}(\vec{r}) = \frac{1}{1 + e^{(||\vec{r}|| - r_0)/r_w}}, \tag{8.4}$$

were r_0 is the radius of the pass-band and r_w the transition width. Rather than exclusively focusing on choice of the excitation profile, and similarly to windows used in FIR filter design, convolution of the principal polar PSF with a narrow disk [107] effectively averages out ripples, at the expense of further widening the main lobe of the PSF, i.e., increasing the transition width. Such windowing is accomplished by multiplying the RF with a jinc function, $J_1(||\vec{k}||r_d)/||\vec{k}||$, where J_1 is a Bessel function of the first kind, and r_d is the radius of the central lobe of the PSF, $r_d = 3.83/N\Delta k_r$ [107]. In our experience, a jinc window for the spiral trajectory slightly outperforms e.g., the Hamming window that is typically used in 1D designs.

This simple windowing procedure greatly reduces rippling at the plateau, as can be seen in Fig. 8-2, where we plot the profiles produced by excitation of nearly homogeneous phantom of doped water (shown in Fig. 8-1) using a Fermi disk (r_0 = 2 cm, r_w = .1 cm) and a given spiral trajectory. Nonetheless, the choice of desired profile still remains significant. If instead of the Fermi disk a true disk had been used ($P_{des}(\vec{r}) = \Pi\left(||\vec{r}||/r_0\right)$, where $\Pi(r)$ given by Eq. (2.17)), the ripples in the plateau would be increased by a factor of 3, even with application of the jinc window, as shown in Fig. 8-3.

Also shown in Fig. 8-2 are the resulting aliasing sidelobes when choice of D (i.e., $1/\Delta k_r$) in the k-space excitation trajectory design is insufficient to place them beyond the sample's extent. The trajectory used in Fig. 8-2, designed with D = 12 cm, was used to excite a sample of appx. 36 cm

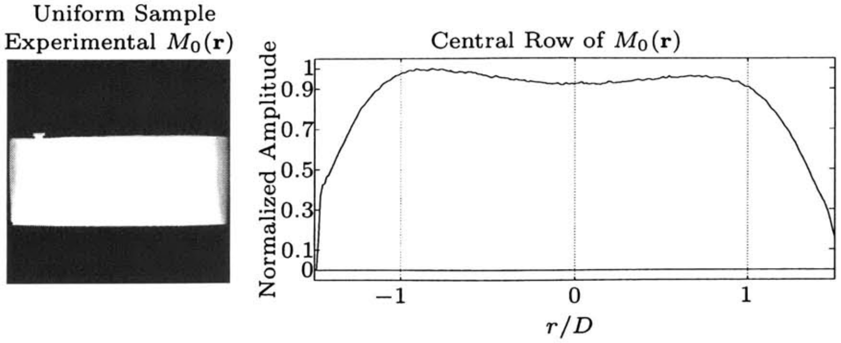

Figure 8-1: Nearly homogeneous doped water phantom used to obtain the results in Fig. 8-2, acquired with a standard 2D FSE sequence using the same imaging parameters.

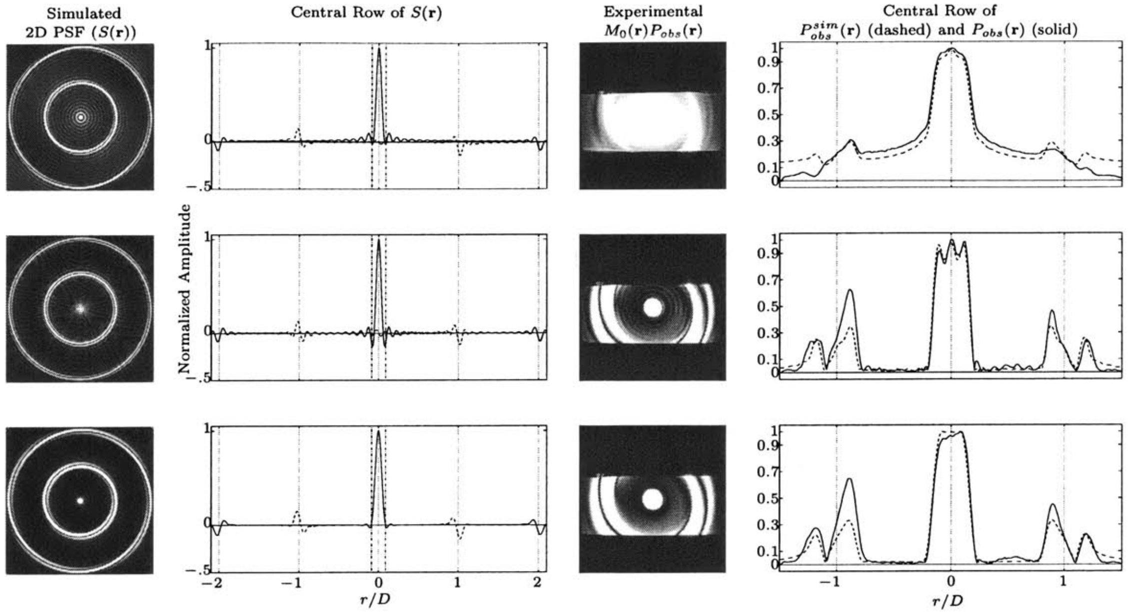

Figure 8-2: Measured excitation profile for a given spiral k-space excitation trajectory, designed with $T_{end} = 5.1$ ms, $D = 12$ cm, and $N = 10.5$ loops. Experimental images (third column) were acquired with a 2D Fourier encoded FSE (1 sec TR, 16 ms Eff.TE, 32 KHz BW, 2 ETL, 10 mm refocuser Sl. Thk., 256 matrix size) covering a 36 cm acquisition FOV. The π refocusers were applied orthogonal to the excited disk so as to produce a slice of the excitation profile. The doped water phantom used for the image acquisitions is shown in Fig. 8-1. In the last column, plots of the central row of each image (solid line), show good agreement with the linear design result (dashed line). Top row: RF derived from a Fermi disk ($r_0 = 2$ cm, $r_w = .1$ cm) without density compensation (i.e., without $1/\lambda\left(\vec{k}(t)\right)$. Middle row: RF derived from a Fermi disk ($r_0 = 2$ cm, $r_w = .1$ cm) with density compensation. Bottom row: RF as above row, but further windowed with a jinc, smoothing out ripples in the PSF at the expense of a broader PSF main lobe. The first and second columns show the simulated effective PSF resulting for each RF excitation.

extent along the horizontal axis, leading to large amounts of excited magnetization at the edges. Finally, for the pass-band to stop-band ratios useful in rFOV VOI imaging, say in the range $D/5 \leq r_0 \leq D/10$ cm, we found that short spiral trajectories can yield acceptable selection profiles; the $D = 12$ cm trajectory with and $N = 10.5$ loops, required 5.1 ms, limited by the 14.9 G/cm/msec slew rate of our system.

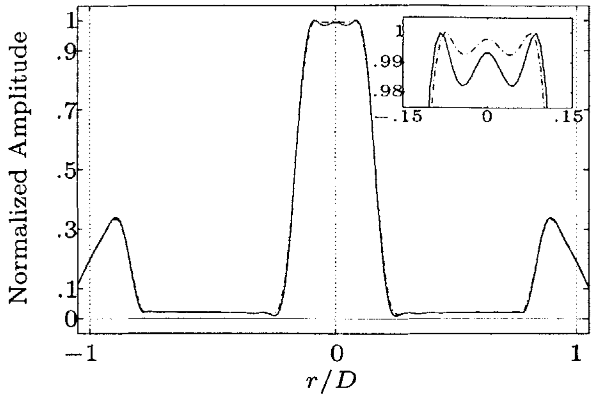

Figure 8-3: Use of a Fermi function for P_{des} reduces Gibbs ringing at the plateau of excited spin density (inset plot). In the depicted situation the desired excitation is a disk of radius $r_0 =$ 2cm. Ringing at the plateau is reduced from 1.8% when using a true disk for the desired profile P_{des}, i.e., $P_{des}(y, z) = 1$ when $\sqrt{y^2 + z^2} \leq r_0$ and zero otherwise (solid line) to 0.6% when using a Fermi function (dash-dot line) with $r_w = .1$cm. The remaining features (i.e., frequency cutoff) are equivalent.

8.1.3 On-line RF Generation

To produce a 2D spatially selective RF excitation, one must:

(1.) Calculate the gradients to produce the k-space trajectory.

(2.) Calculate the Fourier coefficient expansion of the desired profile for chosen the trajectory.

(3.) Calculate the density compensation weighting function for the chosen trajectory.

(4.) Finally, calculate the desired windowing function for the desired trajectory.

For the purposes of IV imaging, these steps must be performed during sequence setup and with minimal user input, in order to offer wide applicability. Additionally, versatility in the way each step is performed is sought, in order to enable extensions, such as support for rectangular rFOVs that require different trajectories and desired profiles.

By default, a Fermi disk profile with $r_w = r_0/20$ is generated over an analytic spiral trajectory [31] with N chosen to extend to the fourth lobe of the Fourier transform of the profile. The Fourier transform of the profile is computed via a non-uniform fast Fourier transform algorithm (NUFFT) [28] by sampling the (any) desired profile onto a dense Cartesian grid and applying the NUFFT to obtain the Fourier coefficients along the (any) k-space sampling trajectory. Density compensation [41] for the (any non self-intersecting) trajectory is computed via the non-iterative Voronoi tessellation [124, 129]. The jinc window is then multiplied into Eq. (8.1) to form the final RF field $B_1(t)$. The gradients, k-space trajectory, weighting factors and final RF field components of the 2D RF design used in much of the remainder of this chapter are shown in Fig. 8-4. Positioning of the profile to an off iso-center location $\vec{r}_d$ is applied directly onto $B_1(t)$ as a a phase offset [39],

$$B_1^{\vec{r}_d}(t) = B_1(t)e^{i\vec{k}^T(t)\cdot\vec{r}_d}. \tag{8.5}$$

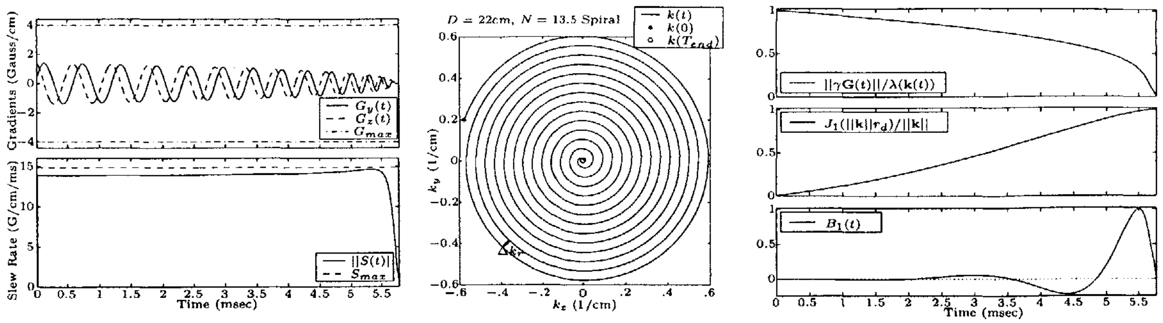

Figure 8-4: Gradients (left) used to produce a $D = 22$ cm, $N = 13.5$-loop spiral excitation trajectory (center). Weighting factors applied to produce the RF field (right) for excitation of a $r_0 = 3.5$, $r_w = .25$ cm Fermi disk along this trajectory.

Assuming correct sequence implementation, and timing of the RF pulse with respect to the gradients, inconsistencies in the quality of the observed spatial profile stem from off-resonance effects that cause blurring [121], and eddy currents that warp the excitation k-space trajectory [142]. With RF durations of 5 to 6 ms used here, the former is minimal. The latter is not accounted for, but, if desired, correction methods exist, such as measuring the trajectory directly and computing the RF based on the warped trajectory [142], or by pre-warping the gradients when the gradient system response function can be sufficiently approximated [107].

8.1.4 Combining 2D RF & UFSE: The 2DRF-UFSE Pulse Sequence

The 2D disk-shaped excitation produces a cylinder of transverse magnetization which can be imaged using the UFSE echo train with frequency encoding applied along the cylinder axis, as shown in Fig. 8-5. This 2DRF-UFSE sequence merely replaces the $\pi/2$ pulse of the fully hard pulse non-selective (HP-UFSE) sequence [104] with the 2D RF pulse. The FID crushers around the hard pulse refocusers are fused into the readout gradient by equally elongating it along both ends [104] in order to reduce gradient ramps. This achieves shorter echo spacings. On our 1.5 T scanner (see

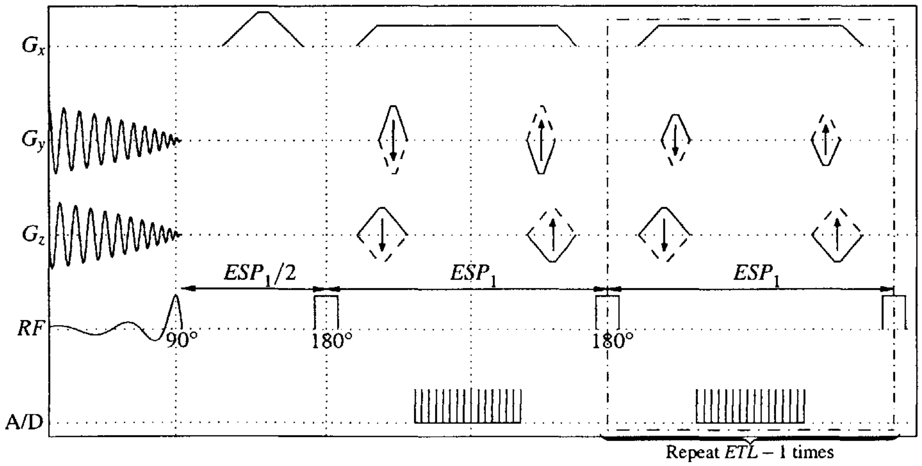

Figure 8-5: 2DRF-UFSE sequence employing a 2D RF spatial excitation coupled with UFSE. FID crushers are built into the readout gradient wings.

Experiments section below), hard π pulses require 500 μsec, while the spiral trajectory shown in Fig. 8-4 and used in the remainder of this chapter, unless otherwise noted, requires 5.7 ms. This trajectory covers $N = 13.5$ loops for $D = 22$ cm and was found appropriate for the Fermi disk with $r_0 = 3.5$ cm and $r_w = 25$ mm.

The 2D RF pulse derived from the Fermi window on the spiral trajectory is inherently refocused [122], thus behaving near-linearly at high flip angles [122], as is verified in Fig. 8-6. We chose to scale the RF pulse to impart a 60° nutation rather than $\pi/2$ typically used in FSE imaging, in order to avoid extraneous excitation profile degradation that is unavoidable at the higher flip angles [142]. Bloch equation simulation of the aforementioned RF pulse on-resonance produces stop-band excitation of 1%, 2% and 3% at flip angles 30°, 60° and 90° respectively, which are slightly higher than the linear design approximation. Additionally, profiles of a homogeneous doped water phantom at these flip angles, measured with the 2DRF-UFSE (shown in the plot of Fig. 8-7), deviate between two and three times these percentages, stipulating the 60° choice so as to limit extraneous magnetization to under 5% excitation.

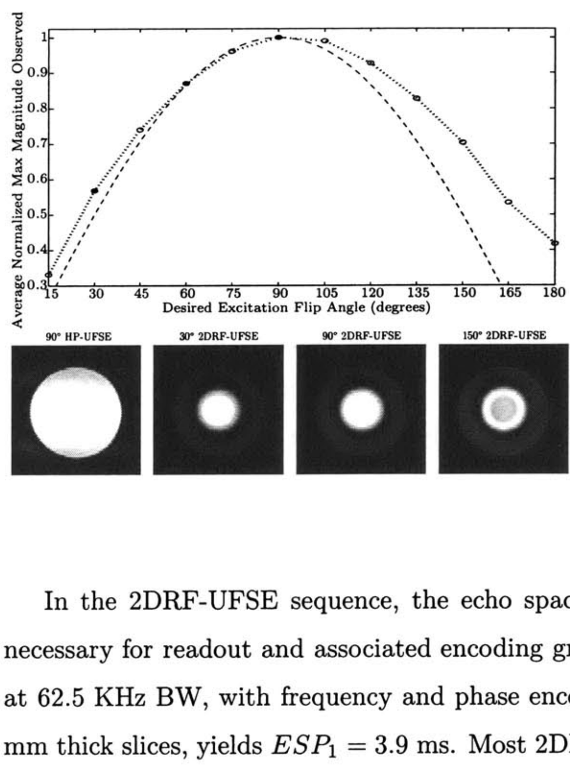

Figure 8-6: Top: the average normalized transverse magnetization (M_{xy}/M_0) produced at the plateau of the spatial profile when the default 2D RF pulse is scaled to produce a gamut of flip angles ranging from well within the linear solution regime to well outside it. Good agreement with a sinusoidal curve (dashed curve) is observed. The pulse was 5.7ms long, with $D = 22$cm and $N = 13.5$ loops and a Fermi function with $r_0 = 3.5$cm and $r_w = 0.25$cm. Bottom: first image shows a slice of the doped water phantom, imaged via the non-selective HP-UFSE sequence. Remaining images are of the same slice of the phantom imaged via the 2DRF-UFSE at the flip angles shown by filled circles in the graph. The "average" signal was obtained by a small volume at the center of the acquired phantom images.

In the 2DRF-UFSE sequence, the echo spacing (ESP_1) is determined by the minimum time necessary for readout and associated encoding gradients. For example, a typical 256-point readout at 62.5 KHz BW, with frequency and phase encoding gradients for 10 cm in-plane FOV and 50, 2 mm thick slices, yields $ESP_1 = 3.9$ ms. Most 2DRF-UFSE acquisitions we have performed required ESP_1 between 3.2 and 4.2 ms. The calculation of ESP_1 is performed independent of the 2D spatial RF excitation. This is based on the assumption that the moment of zero phase precession of the produced transverse magnetization occurs at the very end of the spiral trajectory. Furthermore, the bulk of magnetization is excited near the end of the trajectory, since spatial profiles useful for IV imaging (low-pass filters) have most energy concentrated in the lowest spatial frequencies.

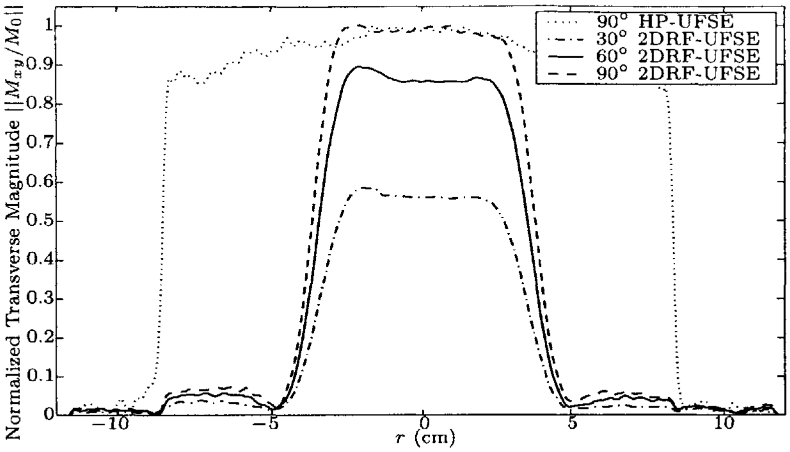

Figure 8-7: Magnetization profiles of homogeneous water phantom, measured with the 2DRF-UFSE by application of the 2D RF pulse used throughout this work (see text) at various flip angles. For reference, the profile of the phantom measured by a 90° hard pulse UFSE (HP-UFSE), is shown. Excitation in desired stop-band is 1–3 times higher than expected by Bloch equation simulation on-resonance.

Nonetheless, RF energy deposited in the higher spatial frequencies, visited early in the excitation trajectory, produces at least some transverse magnetization. This complicates use of echo spacings of the order of the RF pulse's duration. Accordingly, we must turn to the characterization of the magnetization rephasing that is achieved within this echo spacing.

8.1.5 2D RF Outer Volume Suppression Analysis

The 2DRF-UFSE and standard HP-UFSE sequences were modified to obtain Carr-Purcell-Meiboom-Gill (CPMG) sequences [16, 85], wherein an image is constructed from each echo (2DRF-CPMG and HP-CPMG respectively). This enables the determination of the extent of rephasing of transverse magnetization inside the excitation profile's plateau, as well as the amount of coherent transverse magnetization forming outside the VOI throughout the echo train.

These two sequences were used to image a homogeneous spherical doped water phantom ($T1 \simeq T2 \simeq 100$ ms) at each of 16 CPMG echoes, spaced $ESP_1 = 3.4$ ms apart. The acquisition FOV was chosen to fully encompass the phantom for both experiments. Due to limited scanner raw signal sample memory, the acquisition was limited to a 16 echo CPMG train, thus producing 16 3D image volumes for each scan. The volumes obtained by each sequence in the first eight echoes are shown in Fig. 8-8. The signals measured with each sequence in small sub-volumes within the VOI and the outer volume (OVOI) are plotted in Fig. 8-9, revealing no inconsistencies over the echo train. The signals measured in a $4 \times 2 \times 3$ cm volume within the VOI deviate on average between 1.5–4%. Signal measured within the outer volume by the 2DRF-CPMG was greatly suppressed to 4% of its nominal amount which was measured with the HP-CPMG, as shown in the plot of Fig. 8-10.

8.1.6 2D RF Excitation and Imaging Quality Experiments

The incomplete ($\sim$ 96%) outer volume suppression, in addition to off-center excitation errors and off-resonance and motion effects during excitation can potentially limit imaging quality of the 2DRF-

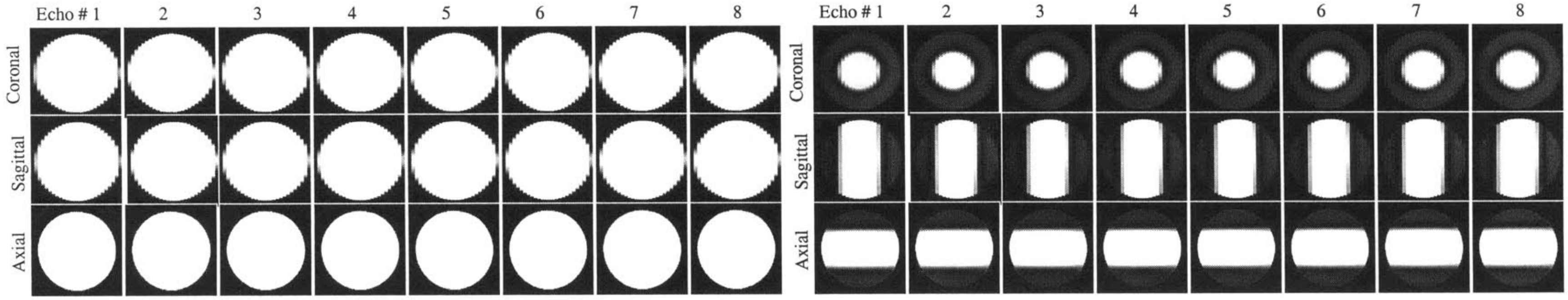

Figure 8-8: Volume images of doped water phantom obtained at each of the first eight CPMG echoes of a fully HP train (HP-CPMG, left) and of a 2D RF followed by HP train (2DRF-CPMG, right). All images are identically window/leveled to show transverse magnetization outside the VOI. Scan parameters were 600 ms TR, 20 cm cubic FOV, 256-by-128 in-plane resolution, 26 slices, and $ESP_1 = 3.488$ ms.

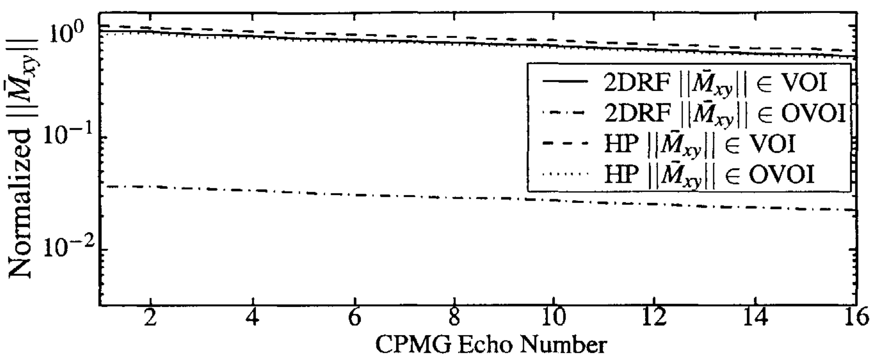

Figure 8-9: Average signal observed at each (individually encoded) echo of HP-CPMG and 2DRF-CPMG sequences, in small volumes located in the inner volume (VOI) plateau of the 2D RF excitation and the outer volume (OVOI).

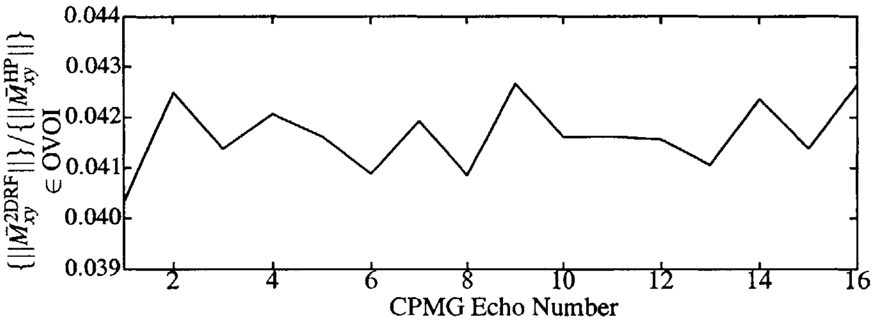

Figure 8-10: Signal observed in the outer volume of the 2DRF-CPMG over the corresponding volume measured with the hard pulse non-selective HP-CPMG, both normalized to account for differing flip angles.

UFSE method. In order to assess these limitations, a number of experiments were performed.

2D RF Excitation Quality

Off-resonance and motion during RF excitation can degrade the quality of the excited 2D profile, regardless of the imaging portion of the sequence. By applying the 2D RF excitation to cardiac imaging we are able to assess robustness in the presence of cardiac motion and chemical shift from chest wall fat. Also, in the cardiac imaging case, chest wall fat is the strongest contributor of signal. Two scans, a coronal and a sagittal, were performed using a standard black blood gated 2D FSE sequence with the $\pi/2$ pulse replaced by the 2D RF pulse and excited orthogonal to the refocusing π pulses of the sequence. A commercial 4-element receive-only cardiac phased array and standard cardiac protocol parameters (32 KHz BW, 20 ETL, 256 matrix size, 20 ms Eff.TE, breath hold acquisition) were used.

The 2D RF pulses used in the two scans differed from the default 2D RF that was used throughout the rest of this chapter. Specifically, the coronal scan used a 4.4 ms spiral with $D = 28$ cm and $N = 12$ loops, while the profile was a Fermi disk with $r_0 = 5$ cm and $r_w = .5$ cm. The sagittal scan used a 6.9 ms spiral with $D = 26$ cm, $N = 16$, and a $r_0 = 2.5$ cm, $r_w = .25$ cm Fermi disk excitation. These excitations were not specifically optimized for these experiments. Rather, they were initial tests performed to assess 2D RF excitations. Nonetheless, we found them sufficient for this assessment since they cover a wide range of parameters.

IV selection in the heart, by use of the 2D-selective RF excitations shown in Fig. 8-11, emphasized that off-resonance and motion effects are not detrimental to rFOV imaging with RF durations of the order of 4–7 ms. Given the suppression of the fat signal to the level of noise, stop-band suppression is adequate to allow rFOV sampling. In the case of the coronal scan, an 8.5 cm rFOV image was successfully acquired without aliasing.

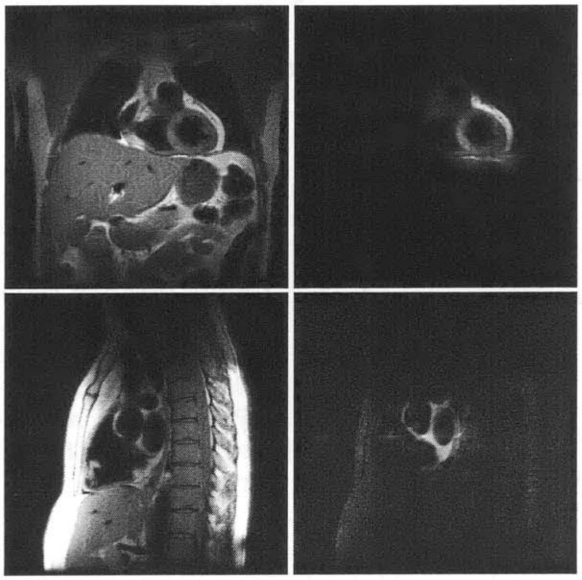

Figure 8-11: Left column: Standard black-blood 2D FSE. Right column: Black-blood 2D FSE with $\pi/2$ pulse replaced by a 60° 2D RF excitation orthogonal to the π refocusers. All scans were cardiac gated with breath hold. Top row: 36 cm FOV coronal scan, 2D RF was 4.4 ms (details in text). Bottom row: 32 cm FOV sagittal, with 6.9 ms 2D RF (details in text).

2DRF-UFSE Imaging Quality

Our aim was to assess the effect of the incomplete outer volume suppression, as well as off-center excitation errors, on our ability to perform rFOV imaging with the 2DRF-UFSE method. A structured NiCl doped water phantom of approximate dimensions 12 × 12 × 22 cm was imaged at a fixed high spatial resolution (appx. 0.35 × .7 × 1.5 mm) using a commercial transmit/receive head quadrature coil with both the HP-UFSE and 2DRF-UFSE sequences.

The phantom was first imaged with both sequences at an FOV fully encompassing it, and subsequently with a rFOV surrounding only the VOI, using the 2DRF-UFSE sequence. The 2D RF pulse of the 2DRF-UFSE scans was excited at L19 mm and S15 mm off-center, with table S/I centering disabled. Imaging parameters were kept constant for the three acquisitions, and were 800 ms TR, 30 ms Eff.TE, 62.5 KHz BW and 32 ETL. Only readout/phase/slice encode matrix resolution was varied for the rFOV scan, in order to produce the fixed voxel resolution. To offset the large reduction of imaging time w.r.t. SNR, the rFOV scan used 2 NEX in contrast to the 1 NEX of the full FOV scans.

The fixed resolution of 0.35 × 0.70 × 1.5 mm was obtained by performing the two full 18 × 18 × 26 cm FOV acquisitions with 512 A/P readout, 256 R/L phase and 174 S/I slice encode resolution, requiring 18 min 33 sec. A representative slice of each plane is shown in the top two rows of Fig. 8-12 while 3D views centered at magnet iso-center are shown in Fig. 8-13. The reduced $9 \times 9 \times 9$ cm FOV 2DRF-UFSE acquisition was obtained with $256 \times 128 \times 60$ along the respective axes, requiring 6 min 24 sec with 2 NEX. The representative slices of this scan are shown in the bottom row of Fig. 8-12. Although the imaged volume was reduced by a factor of 11.5 and the imaging time was reduced by a factor of 2.9, the results of Fig. 8-12 clearly demonstrate that use of the 2D RF pulse for FOV reduction with the 2DRF-UFSE method does not introduce imaging errors and allows all image detail to be discerned.

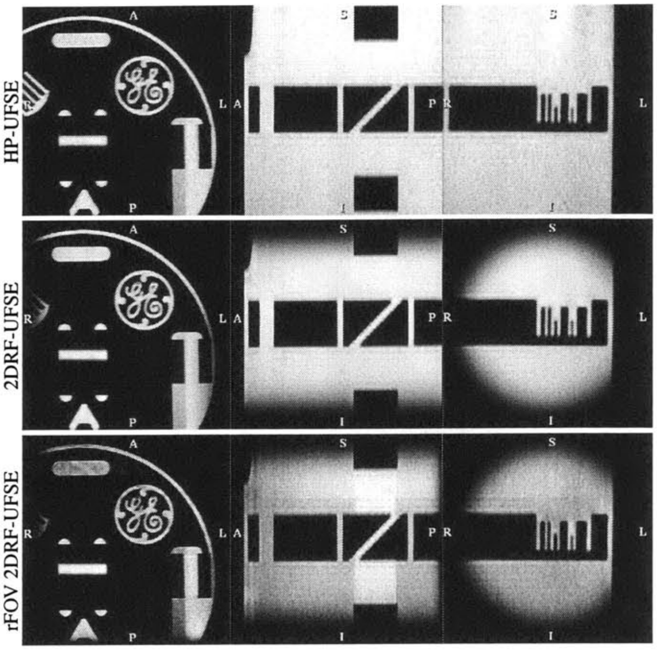

Figure 8-12: Large structured water phantom ($12 \times 12 \times 22$ cm) imaged with HP-UFSE and 2DRF-UFSE at fixed spatial resolution ($0.35 \times 0.7 \times 1.5$ mm) with a FOV fully encompassing the entire object (top two rows, 18 min 33 sec scan time) and reduced FOV with the 2DRF-UFSE (bottom row, 6 min 24 sec). The 2D RF excitation was centered at L19 mm and S15 mm relative to magnet iso-center.

8.2 The Dual-Soft UFSE Method (DS-UFSE)

IV selection can instead be performed by applying two "soft" (i.e., selective) RF pulses that are slab-selective in orthogonal directions [27]. A spin echo is produced from the intersection of the slabs (volume labeled "A" in Fig. 8-14). Transverse magnetization produced by the $\pi/2$ slab but that is outside the refocusing π slab (volume labeled "C") is assumed dephased at the echo time. To simplify our task compared to the 2D-selective RF pulse design, we used the default slice-selective $\pi/2$ and π spin echo pulses provided by our scanner manufacturer in their FSE sequence. The two pulses are a 2.748 KHz 3.2 ms, and a 905 Hz 4 ms, respectively, and both are designed using the Shinnar-Le Roux [120] method. Using these pulses FSE echo spacings exceed 12 ms.

8.2.1 Combining Dual-Soft & UFSE: The DS-UFSE Pulse Sequence

Once the spin echo from the intersecting slabs forms, we may use tightly packed non-selective refocusing pulses in order to produce subsequent spin echoes, as shown in the DS-UFSE pulse

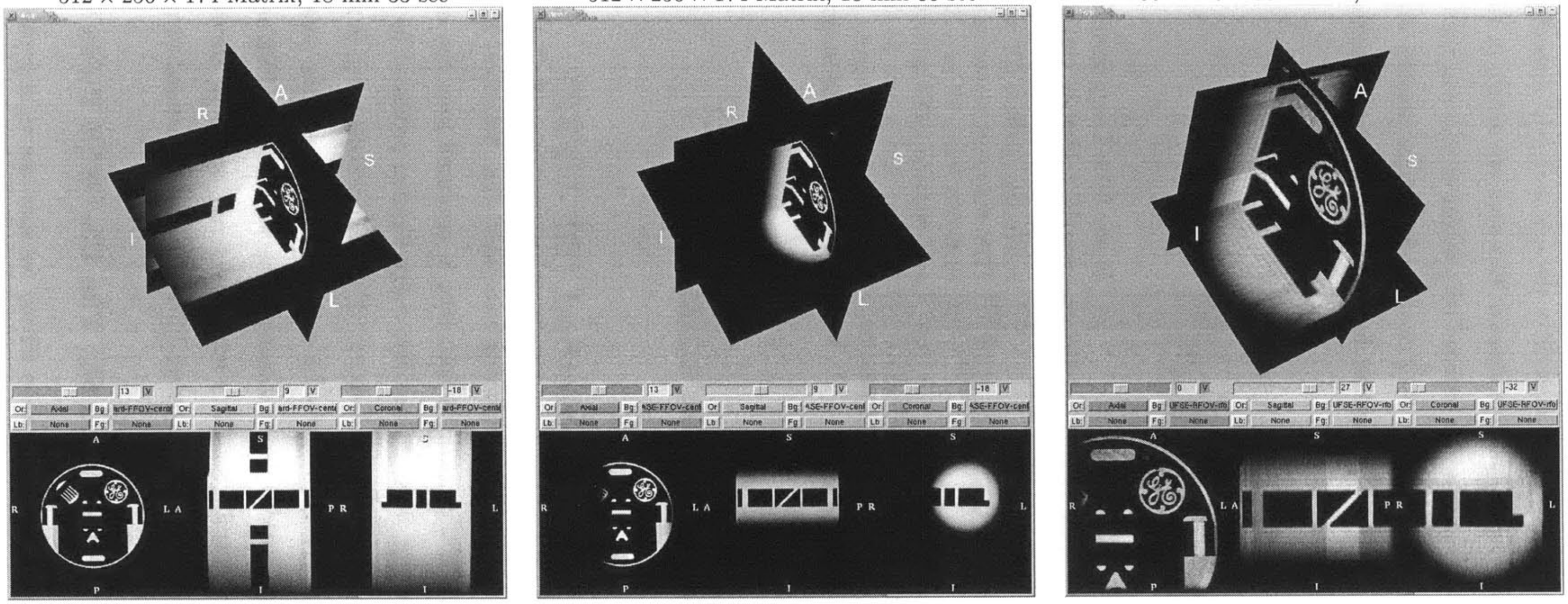
Full FOV HP-UFSE
512 × 256 × 174 Matrix, 18 min 33 sec

Full FOV 2DRF-UFSE
512 × 256 × 174 Matrix, 18 min 33 sec

Reduced FOV 2DRF-UFSE
256 × 128 × 60 Matrix, 6 min 24 sec

Figure 8-13: Water phantom results displayed at scale comparable to that of the respective acquisition FOV (18 cm shown in first two figures, 9 cm shown in last figure). Scan Parameters: 800 ms TR, 30 ms Eff.TE, 62.5 KHz BW and 32 ETL. Voxel resolution for all three scans was $0.35 \times 0.70 \times 1.5$ mm. The default 2D RF pulse was used (5.7 ms duration producing a Fermi function of $r_0 = 3.5$ cm and $r_w = 0.25$ cm). The echo spacing ESP_1 was 6.684 ms for the two full FOV scans and 4.636 ms for the reduced FOV scan. The full FOV scans were acquired at 18 cm (R/L) by 18 cm (A/P) by 26 cm (S/I) and the reduced FOV at 9cm (R/L) by 9cm (A/P) by 9cm (S/I).

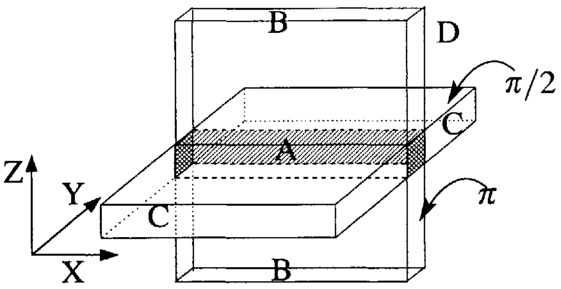

Figure 8-14: Labels for volumes used in DS-UFSE outer volume effects analysis.

sequence in Fig. 8-15. The sequence of Fig. 8-15 is the first instance we are aware of wherein two different echo spacings are used in an FSE train. Typically, this is avoided because whenever three or more RF pulses are applied to magnetization that is initially at thermal equilibrium, stimulated and indirect echoes occur.

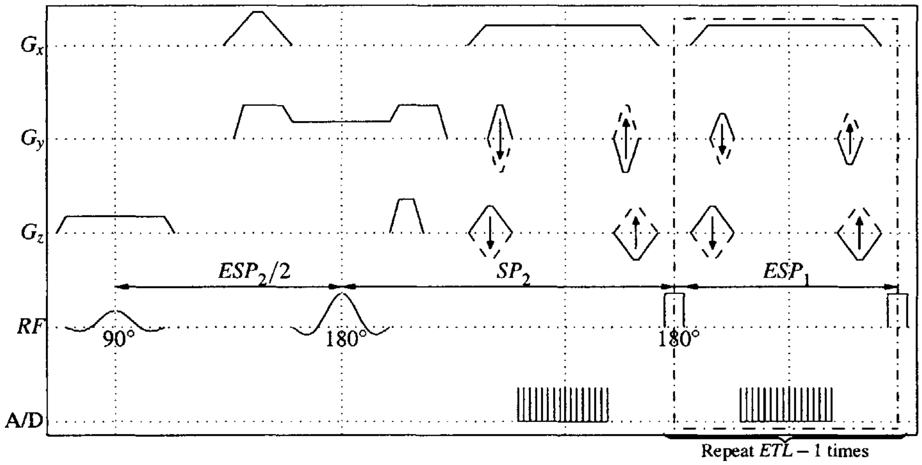

Figure 8-15: The DS-UFSE sequence employs a dual 1D-selective orthogonal excitation/refocusing pair followed by the UFSE train. An additional set of crushers along the soft slab-selective refocuser suppresses transverse magnetization outside the slab intersection.

The discussion of magnetization pathways that lead to such echoes is lengthy [49, 46, 48, 47] and outside the scope of this work. We summarize, noting that transverse magnetization dephases while longitudinal magnetization does not. When some transverse magnetization that has undergone a duration of dephasing is converted into longitudinal magnetization, its phase history is stored, and that memory may lead to stimulated echoes. Transverse magnetization may be converted to longitudinal magnetization e.g., when the refocusing RF pulse in a spin echo sequence is not a precise uniform 180° RF pulse. This is unattainable in a system bounded by physical properties such as limited excitation time. The mechanism by which stimulated echoes occur requires another subsequent RF pulse to convert this longitudinal magnetization, with the prior phase history, back into transverse magnetization. Any new phase evolution of this transverse magnetization will be added to the phase history. At the moment the new phase evolution cancels the original phase history, the coherence of the magnetization vector will lead to a spin echo.

Returning to the DS-UFSE sequence, when the echo spacing of refocusing RF pulses is not held constant, the number of magnetization phase histories increases [48] and can lead to both destructive interference, which reduced the desired signal, as well as undesired (in the case of VOI imaging) constructive interference. In the remainder of this section we will describe how one might retain useful echoes while avoiding the undesired ones. The resulting method, using two distinct echo spacings in the course of the FSE train [100], appears to have been well-received [103], leading to more efficient approaches over the original the original HP-UFSE sequence [104].

If the delays defined in Fig. 8-15 satisfy the equation

$$SP_2 - ESP_2/2 = ESP_1/2, \tag{8.6}$$

then all direct, stimulated, and indirect echoes [46] originating from magnetization that was in fact inverted by the soft π pulse (i.e., the desired region within the intersection of the slabs), will form precisely at the center of each subsequent readout. That is, all echoes from the desired slab intersection will form at $ESP_2 + kESP_1$, for $k \in \mathbb{Z}^+$. Unfortunately, transverse magnetization generated by the $\pi/2$ pulse in the outer volume ("C", c.f., Fig. 8-14) will also be affected by the non-selective spin echo π hard pulses, causing it to generate stimulated and indirect echoes in subsequent readouts. Furthermore, any transverse magnetization produced by the imperfect slab-selective spin echo π pulse (volume "B", c.f., Fig. 8-14) will also produce stimulated and indirect echoes when disturbed by the non-selective spin echo pulses.

The timing of the sequence suggests that selecting

$$ESP_2 = \left(n + \frac{1}{2}\right) ESP_1, \tag{8.7}$$

with n the smallest positive integer that does not violate gradient timings within ESP_2, then all echoes from magnetization in volumes "C" and "B" will recover the recoverable portion of T_2^* at $ESP_2 + (k + (n/2 \pm 1/4))ESP_1$ and $ESP_2 + (k + (n + 1/2))ESP_1$ ($k \in \mathbb{Z}^+$, see Appendix A.2). That is, the undesired echoes will form at either one quarter ESP_1 off the center of the readout windows between the hard pulses, or at the times of hard pulse application. However, the amount of dephasing of the undesired echoes at the center of each readout within the hard pulse train which will then be proportional to 1/4 or 1/2 ESP_1, is rather negligible considering the short 3–4 ms ESP_1. Accordingly it may still cause artifact, unless sufficient gradient-induced dephasing is applied.

8.2.2 DS Outer Volume Suppression Analysis

Since all FSE encoding gradients must be balanced to avoid signal cancellation from stimulated and indirect echos stemming from within the VOI ("A"), a single set of additional crusher gradients is employed along the selective dimension of the soft refocusing π pulse in order to permanently dephase magnetization within "C". This dephasing will remain unbalanced throughout the remainder of the echo train and will suppress all spurious echoes originating from within "C".

This simple addition of dephasing gradients reduces spurious echo formation from volume "C" from approximately 25% to less than 1% of the region's signal, as shown in Fig. 8-16. This was measured using the CPMG version of the DS-UFSE sequence, DS-CPMG, and the same spherical doped water phantom that was imaged with the 2DRF-CPMG and HP-CPMG sequences (c.f., Fig. 8-8). The suppression is so effective that we find most outer volume signal emanating from magnetization within the slab-selective π refocuser (volume "B"), which remains at approximately 2% of its maximum, as shown in Fig. 8-17. This indicates the soft π pulse produces a flip angle of approximately 178°, which is well within the expected variability of MRI hardware.

Gradient crusher effectiveness is naturally dependent on the location of the VOI, since gradients impart zero phase at magnet iso-center. However, by choosing the logical y axis of the DS-UFSE sequence to coincide with the direction of scanner table movement, we can rely on its default placement to ensure that the VOI is always centered at magnet iso-center along that dimension, ensuring the effectiveness of the dephasing gradients to crush magnetization outside the desired VOI.

8.3 IV Pulse Sequences and *in vivo* Imaging Experiments

All sequences described in this chapter were implemented on a 1.5 T GE Signa CNV3 scanner (GE Medical Systems, Milwaukee, WI) as opposed to the Signa LX 8.3 EchoSpeed scanner that experiments in previous chapters were conducted on. Although the scanner hardware is similar, equipped with 4 G/cm gradients at 14.9 G/cm/msec maximum slew rate and 250 mG maximum B_1 strength, the scanner software is later revision. Additionally, the magnet itself is somewhat different, with a smaller bore. The main magnetic field is homogeneous to within 5–10 Hz within a 12 cm radius from iso-center. The sequences developed in the analyses presented above and the results presented below are summarized in Table 8.1. The column labeled "Observed T_2 of a phantom" refers to the least-squares fitted constant of an exponential decay to the signal decay measured by the HP-/2DRF-/DS-CPMG acquisitions of the spherical doped water phantom measurements shown in Figs. 8-8 and 8-16. For comparison, a series of single echo SE sequence acquisitions at different TEs was acquired which, as shown in Fig. 8-18, leads to a similar T_2 fit.

8.3.1 2DRF-/DS-UFSE Neuroimaging Applications

The final validation of the two 3D IVUFSE methods that were developed in this chapter was based on assessing their utility in human imaging. A set of imaging experiments used each of the two 3D IVUFSE sequences to image the spine and the brain of a healthy human volunteer.

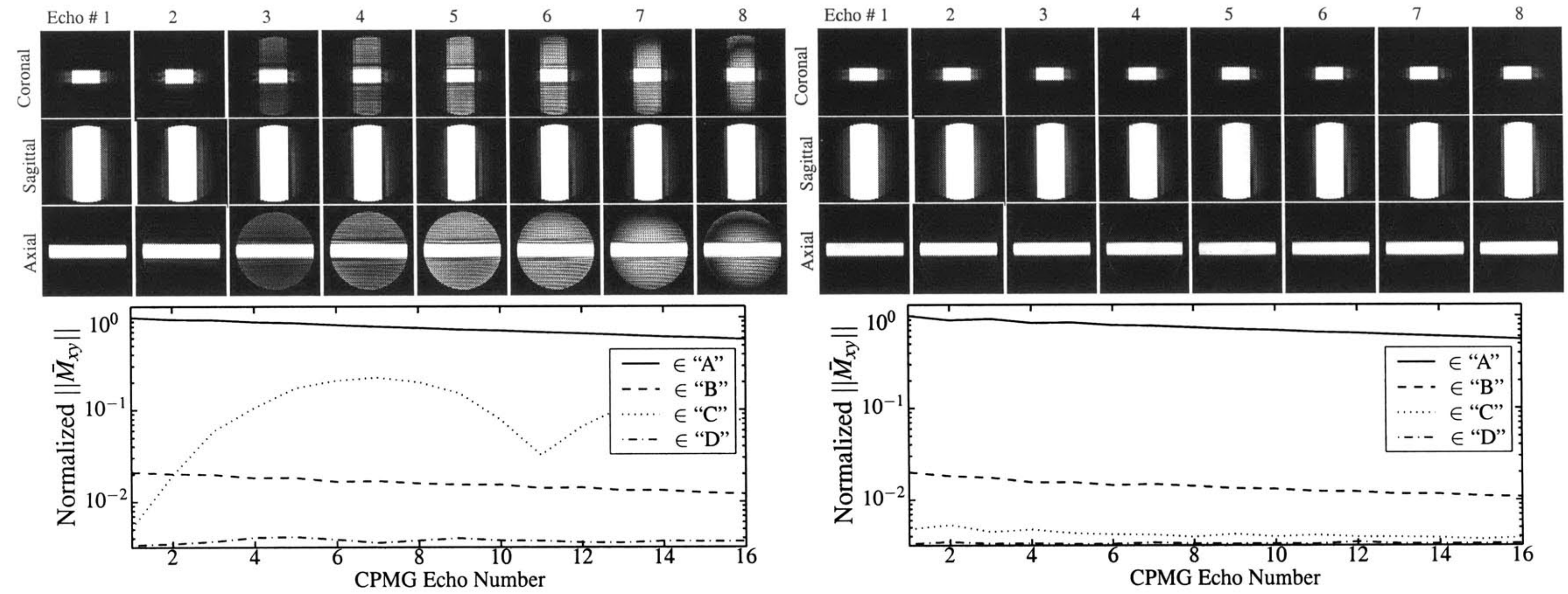

Figure 8-16: Volume images of same doped water phantom imaged with HP-/2DRF-CPMG sequences (c.f., Fig. 8-8), at each of the first eight echoes of the DS-CPMG sequence with (right-hand) and without (left-hand) additional crushers about the slab-selective π pulse. Images are identically window/leveled. A 5 cm R/L slab-selective $\pi/2$ excitation and a 3 cm A/P slab-selective π spin echo pulses were used. All other scan parameters were as in Fig. 8-8 except, additionally, $ESP_2 = 12.208$ ms in order to math the $ESP_1 = 3.488$ ms according to Eq. (8.7). The graphs beneath each set of images show average signals observed in small ($4 \times 1.5 \times 2$ cm) volumes within the representative volume divisions.

Sequence Name	Explanation	Purpose	Typical ESP	Observed T2 of a phantom
SE	Standard slice-selective 90 followed by single slice-selective π pulse	Measuring T2	N/A	100.26 ms
2D RF FSE	2D spatial RF excitation followed by orthogonal dimension slice-selective π pulses	Measuring 2D RF excitation slice profiles	12 ms	N/A
HP-UFSE	Non-selective hard pulse $\pi/2$ followed by non-selective π hard pulses	Full sample UFSE imaging	3.4 ms	100.44 ms
2DRF-UFSE	2D RF excitation followed by non-selective π hard pulses	Cylindrical VOI 3D IVUFSE imaging	3.4 ms	N/A
2DRF-CPMG	Same as 2DRF-UFSE but each echo independently encoded	Measuring 2D RF IV imaging quality	3.4 ms	98.7 ms
DS-UFSE	Orthogonally slab-selective $\pi/2$ and first π pulses, followed by π hard pulses	Rectangular VOI 3D IVUFSE imaging	12 ms (first) / 3.4 ms (subsequent)	N/A
DS-CPMG	Same as DS-UFSE but each echo independently encoded	Measuring DS IV imaging quality	12 ms (first) / 3.4 ms (subsequent)	97.98 ms

Table 8.1: Inner Volume Pulse Sequences developed & used

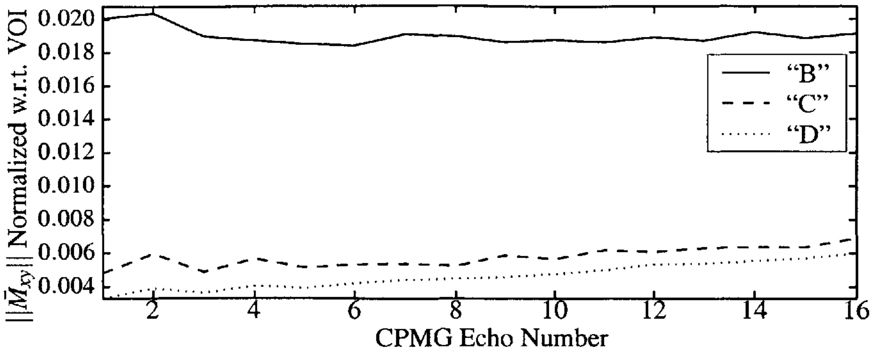

Figure 8-17: Amount of coherent transverse magnetization in the representative outer volume divisions of the DS selection, normalized by average magnetization measured within the VOI (sub-volume "A").

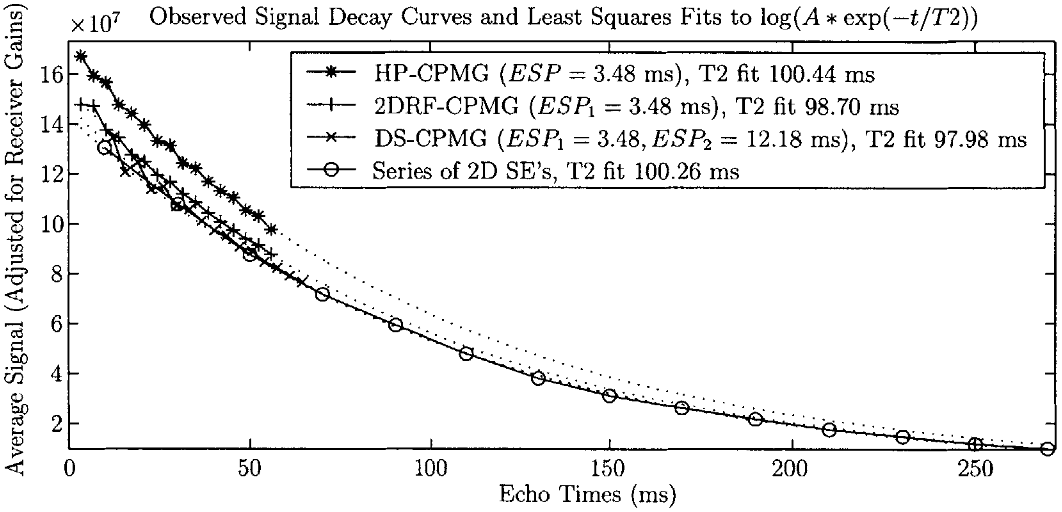

Figure 8-18: Comparison of T_2 fits computed from acquisition of a phantom with each of the two IV CPMG sequences, the non-selective HP-CPMG and a set of SE acquisitions at different TEs. These results are in excellent agreement with the gold-standard T_2 decay observation performed using a standard spin echo sequence.

Spine Imaging

Scans were performed using a commercial receive-only 4-element spine phased array. The two 3D IVUFSE methods were used to acquire a 8 cm S/I by 8 cm A/P by 8.4 cm R/L FOV, encompassing the 2nd and 3rd thoracic vertebrae and inter-vertebral disks. Voxel size was .625 × .8 × 2 mm, achieved with 128 S/I readout, 100 A/P phase encode, and 42 R/L slice encode resolution. Sequence parameters were 4 sec TR, 50 ETL, 32 KHz BW, and 2 NEX. Effective TE was 100 ms for the 2DRF-UFSE and 102 ms for the DS-UFSE. ESP_1 was 4.8 ms, limited by the BW which was chosen to reflect that of a standard spine protocol scan. ESP_2 for the DS-UFSE was 12 ms. Total imaging time for each scan was 672 s.

For comparison, a 2D FSE T2-weighted acquisition from a standard clinical spine protocol was also acquired, consisting of seven 4 mm-thick slices, spaced 1 mm apart. Each slice was acquired with 40 cm in-plane FOV at .781 × 1.042 × 4 mm voxel size, achieved using 512 S/I readout and 384 A/P phase encode resolution. Imaging parameters were 4 sec TR, 102 ms Eff.TE, 16 ETL, 12.8

ms echo spacing, 32 KHz BW and 4 NEX, requiring 392 s total imaging time. Compared to the standard scan, imaging time of the two 3D IVUFSE scans was increased by a factor of 1.7, but voxel size was reduced by a factor of more than 3.2 (1 mm^3 vs. 3.26 mm^3). With the increased overall imaging efficiency, a lesion in the spine is visible with more clarity in the IVUFSE scans, appearing in 4 consecutive sagittal planes (L5 mm – R1 mm planes shown in Fig. 8-19) rather than just a single plane of the 2D FSE scan. The lesion is clearly visible in the axial slices (see e.g., slice S12 mm in Fig. 8-19) as well, whereas it is not visible in the reformatted axial slice of the 2D FSE scan.

Brain Imaging

Brain scans used a quadrature head coil to image the region of the sella turcica. The two 3D IVUFSE scans were performed with a 7 cm S/I, 7 cm R/L and 7.6 cm A/P FOV. Voxel size was .547 × .7 × 2 mm using 128 S/I readout, 100 R/L phase encode and 38 A/P slice encode resolution. All sequence parameters were the same as for the spine scan, except 3 sec TR and 456 s total imaging time. The VOI was centered at A37 mm and was R/L centered.

A single echo SE T1 weighted sagittal acquisition from a clinical brain protocol was also acquired, although not presented due to the difference in contrast weighting. The scan consisted of 24 slices, each 3 mm thick with 26 cm in-plane FOV and voxel size 1.016 × 1.354 × 3 mm, which was achieved with 256 A/P readout and 192 S/I phase encode resolution. Sequence parameters were 500 ms TR, 14 ms TE, 16 KHz BW and 1 NEX, requiring 208 s total imaging time. In comparison to this standard protocol scan, 3D IVUFSE imaging time was increased by a factor of 2.2, while voxel size was reduced by a factor of almost 5.4 (0.77 mm^3 versus 4.13 mm^3). Imaging the region of the sella turcica is especially problematic due to susceptibility in air-tissue interfaces. The combination of short yet sufficient IV selection with the short echo spacings, afforded by hard pulse refocusers, minimizes the resulting potential limitation of distortions as seen in Fig. 8-20 in addition to the additional efficiency of the IVUFSE scans.

The results from the spine and brain of a human volunteer that are summarized in Fig. 8-19 and Fig. 8-20 respectively show that although the 3D IVUFSE imaging time was longer compared to typical clinical imaging, in both cases imaging efficiency was increased, yielding superior results than standard clinical protocol scans. If we measure efficiency as resolution obtained per unit time, and *even* setting aside the increase in efficiency of 2D multi-slice imaging, compared to the TR dead time of 3D imaging, the 3D IVUFSE scans yielded a 1.9-fold increase in efficiency for the spine, and an almost 2.5-fold increase for the brain.

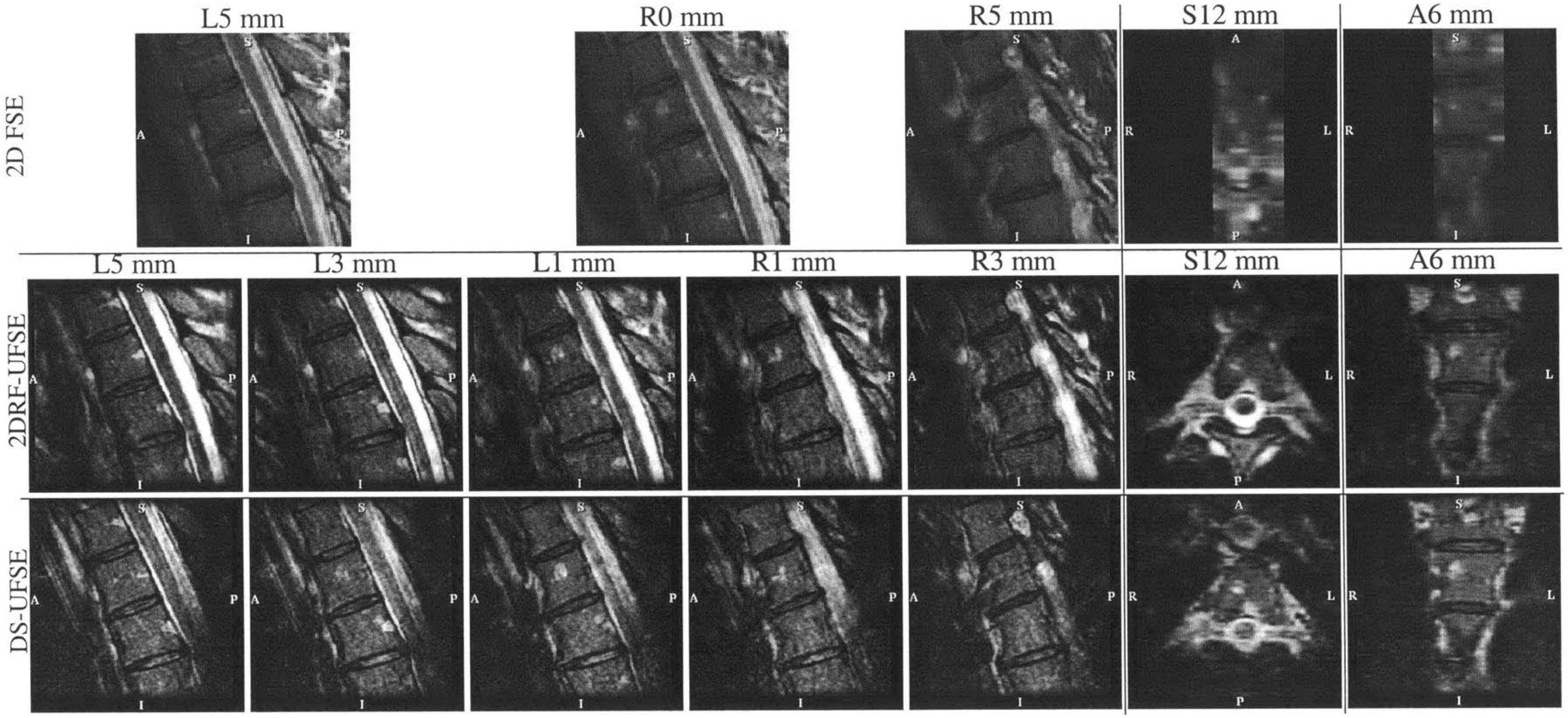

Figure 8-19: Imaging of the mid-thoracic spine of a healthy volunteer. T2W scans using a standard 2D FSE (top row), 2DRF-UFSE (middle) and DS-UFSE (bottom row). Parameters described in the text.

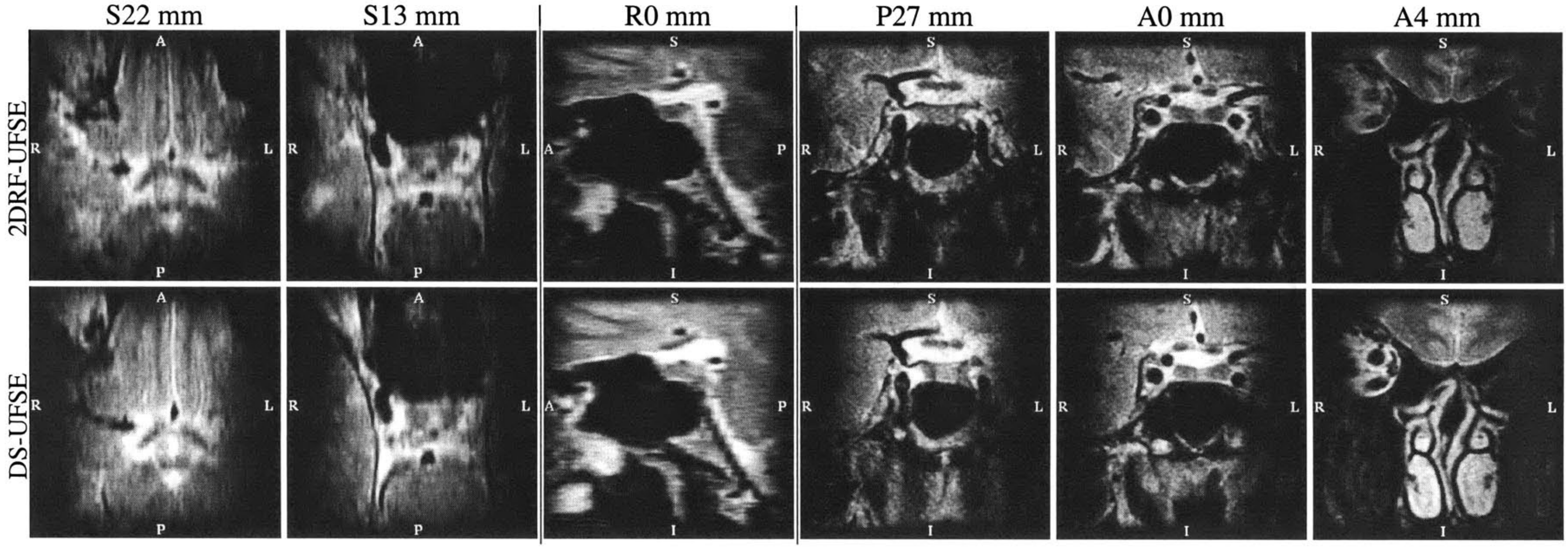

Figure 8-20: Imaging of the region of the sella turcica of a healthy volunteer. T2W 2DRF-UFSE and DS-UFSE (top and bottom rows respectively). Parameters described in the text. Imaging this region of the brain is typically especially problematic due to magnetic susceptibility in air-tissue interfaces leading to distortions. As seen in the images, both the 2DRF- and DS-UFSE methods achieve excellent image quality by minimizing the potential limitation of such distortions.

8.4 2DRF-/DS-UFSE Remarks

Central to MRI is the trade off between imaging time and the constraints imposed by the physical system being sampled, e.g., relaxation, physiological motion, volume of interest versus resolution, among many others. Balancing them is a difficult task and in general not yet fully resolved. 2D multi-slice imaging produces very low resolution along the slice select dimension, in order to attain adequate SNR for clinical imaging. Full 3D encoding requires prohibitively long imaging times. 3D multi-slab imaging [110] either requires thick slabs that are difficult to reorder in a way that the TR dead time can be filled while sufficient distance between the slab profiles can be maintained, or, thin slabs that greatly suffer from partial volume effects (Gibbs ringing) because of the reduced number of phase encode steps in the slice direction.

Prior to this chapter, this dissertation attempted to increase MR imaging efficiency largely via broadband non-Fourier encoding, enabling the use of prospective signal compression to speed up image acquisition. Although this is useful in many imaging cases, such as dynamic imaging, there are cases, such as structural (also called morphological) imaging, wherein the existence of a pathological condition is not known in advance and compression methods can not be employed. For diagnostic imaging, one typically desires the highest possible spatial resolution at the maximum SNR possible, usually together with some specialized tissue contrast.

In this respect, 3D IVUFSE methods offer many advantages over conventional techniques. The short echo spacing allows the echo train duration to be used more efficiently, e.g., by acquiring more phase encoding steps per TR, or, reducing FSE artifact. The latter enables an increase of the effective spatial resolution (less blurring). A combination of the two is also possible. Furthermore, because the FOV is reduced along both phase encoded dimensions, the total number of readouts available with a fixed ETL and number of TRs can be more equally distributed between the "phase" and "slice" encoded dimensions. This offers greatly reduced partial volume effects. Additionally, the overall reduction of the number of phase encoding steps necessary to produce the desired resolution over the VOI allows a reduction of imaging time. Finally, the increase in SNR associated with the simultaneous imaging of the entire 3D VOI allows reduction of the voxel size and/or imaging time while still attaining adequate SNR.

3D IVUFSE can ease some of the trade offs of routine MRI and thus has potential for routine clinical use for many targeted imaging applications that require both high SNR and high spatial resolution. The two 3D IVUFSE methods we have presented in this chapter, termed 2DRF-UFSE and DS-UFSE, require minimal operator effort and achieve high quality reduced FOV 3D imaging with ultra short FSE echo spacing. Imaging results obtained with both methods were shown to successfully reduce the FOV by a factor of more than 2 along each of the two phase encode dimensions.

Moreover, each method was shown to produce 3 to 4 times as many phase encode lines in the same echo train duration as the 2D and 3D FSE sequences provided by our scanner manufacturer, which are typically limited to a 12.8 ms echo spacing. Their achieved efficiency is evident in the two neuroimaging applications presented; the time-wise efficiency of 2D multi-slice imaging was easily surpassed by both methods. If imaging time was fixed to that of the 2D multi-slice experiments, both 3D IVUFSE methods would have produced a 1.8 to 2.5 resolution improvement over the VOI. The 2DRF-UFSE and DS-UFSE methods differ significantly, giving each distinct advantages and limitations, some of which can be overcome.

Compared to DS-UFSE, the current implementation of 2DRF-UFSE does not provide as high suppression of magnetization in the outer volume. Also, the imaged rFOV is inefficiently used because of long transition regions from pass-band to stop-band. Although both limitations are intrinsic to constraints of RF excitations, related to well known properties of FIR filter design [120], our interest turns to the trade offs in the context of 2D excitations used in rFOV imaging. The difference here is that the number of samples is severely limited because of the 2D k-space coverage required, and that no efficient algorithms are known to design 2D FIR filters. For our purposes, we found that stop-band suppression is primarily limited by the simple analytic density compensated 2D RF design used, rather than k-space coverage, and can be increased via better density weighting. Coverage is however the major limiting factor for transition width, although an increase in rippling over that achieved by our design can be traded to shorten the transition for a fixed k-space coverage.

These observations are based on an on-resonance Bloch equation simulation of various 60° 2D RF designs that were used to derive their relevant characteristics which are provided in Table 8.2. In terms of window function, the jinc window is compared to the Hamming window popular in FIR filter design, i.e.,

$$H(\vec{k}(t)) = 0.54 + 0.46\cos\left(\pi||\vec{k}(t)||/(N\Delta k_r)\right), \tag{8.8}$$

as well as to the use of no window. In terms of desired profile, the Fermi disk with $r_0 = 3.5$, $r_w = .25$ cm, is compared to the Disk profile, referring to the function $\Pi(r/r_0)$, where

$$\Pi(r) = \begin{cases} 1, & 0 \leq r < 1 \\ 0, & \text{otherwise} \end{cases}. \tag{8.9}$$

In terms of design, the density weighted design via use of Eq. (8.1), is compared to a Least Squares design, referring to L_2 error minimization by least-squares solution of the system $Ab = p$, where

$$A_{lj} = \exp\left(-2\pi i(\vec{r}_l \cdot \vec{k}(t_j))\right), \tag{8.10}$$

RF Design	Window	Profile	N	Total RF duration	Pass-band Diameter	Total Stop-band Width	Max Deviation from Avg.		Average Stop-band Excitation	Transition Width
							Pass-band	Stop-band		
Density Weighted	Jinc	Fermi	11.0	4.24 ms	3.74 cm	11.86 cm	0.10%	1.30%	2.14%	3.18 cm
			13.5	5.76 ms	4.08 cm	12.20 cm	0.06%	1.39%	2.12%	2.84 cm
			20.0	10.40 ms	4.51 cm	12.55 cm	0.04%	1.36%	2.09%	2.45 cm
			27.0	16.31 ms	4.68 cm	12.72 cm	0.02%	1.44%	2.08%	2.28 cm
		Disk	13.5	5.76 ms	4.94 cm	12.98 cm	0.71%	1.58%	1.98%	2.02 cm
	Hamming	Fermi	13.5	5.76 ms	3.91 cm	11.95 cm	0.16%	1.28%	2.13%	3.05 cm
	None		13.5	5.76 ms	5.46 cm	13.23 cm	3.15%	1.64%	2.06%	1.63 cm
Least Squares (L_2)	Jinc		13.5	5.76 ms	4.00 cm	12.20 cm	0.08%	1.74%	0.52%	2.88 cm
	None		13.5	5.76 ms	5.46 cm	13.15 cm	3.15%	1.42%	0.50%	1.68 cm

Table 8.2: 2D RF pulse design characteristics

b is the unknown RF field with elements

$$b_j = B_1(t_j), \tag{8.11}$$

and p is the column vector representation of the 2D Fermi disk, with

$$p_l = P_{des}(\vec{r}_l), \tag{8.12}$$

sampled on a discrete Cartesian grid at locations $\vec{r}_l$. Pass-band and stop-band characteristics were derived by examining the derivative of the profile and looking for the last occurrence of a specified tangent. Nominal stop-band was derived by a similar procedure.

According to Table 8.2, and as shown in Fig. 8-21, when restricting the design to that obtained via Eq. (8.1) and windowed with the jinc function, the $N = 13.5$ trajectory maximizes the benefits with respect to RF pulse duration. Compared to $N = 11$, the 1.5 ms additional RF duration achieves a .68 cm reduction of transition region, counting both sides. Interpolating the reduction achieved by higher N from Table 8.2, suggests that to obtain another .68 cm reduction over that achieved by $N = 13.5$, would require a nearly 70% increase in RF duration. In terms of pass-band ripple, the .1% ripple achieved even with $N = 11$ is practically unobservable for attainable SNRs. For the $N = 13.5$ trajectory used throughout this chapter, the 0.06% pass-band ripple allows sufficient room, up to an order of magnitude, to both account for actual RF excitation errors as well as to obtain a shorter transition width. As shown in Table 8.2, stop-band suppression is also nearly independent of N.

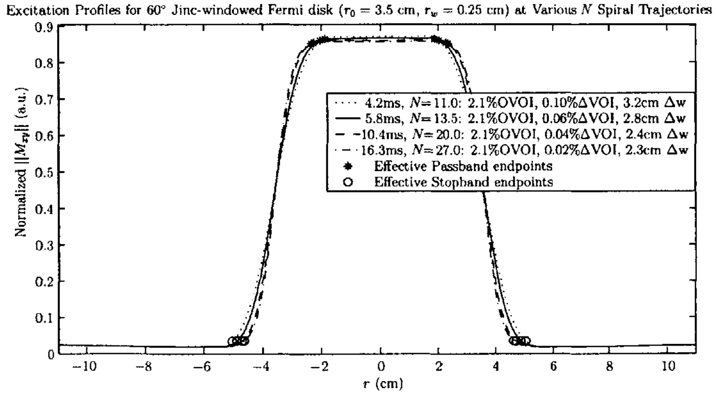

Figure 8-21: Simulated excitation profiles for a jinc-windowed density weighted Fermi disk profile at various spiral trajectory lengths. For all N, stop-band suppression (pct. of OVOI magnetization) is approximately 2.1% while pass-band rippling (ΔVOI) is minimal, ranging from .1% to .02%. As N increases, only the transition width, Δw, is appreciably reduced.

The stop-band suppression was approximately 2% for all density weighted designs based on Eq. (8.1). However, comparison of the excitation profiles obtained by density weighted Fermi disk designs and those produced by a least-squares solution, demonstrates that the low suppression is a direct consequence of inadequate k-space density compensation. The least-squares designs essentially produce the RF field $B_1(t_j)$ that minimizes the L_2 norm of the difference between the Fourier series summation of $B_1(t_j)$ and the desired profile. As shown in Fig. 8-22, the least-squares design produces 4 times lower stop-band (outer volume) excitation, while producing similar characteristics in all other aspects (c.f., Table 8.2). Nonetheless, the Voronoi density weighting design was chosen due to its computational efficiency that is unmatched by more accurate methods [123]. The least-squares design is outright computationally intractable in a scan sequence preparation setting but serves to show in Fig. 8-22 that the 4–5% outer volume suppression achieved by the current implementation of the 2DRF-UFSE can be potentially readily reduced to under 1.5%.

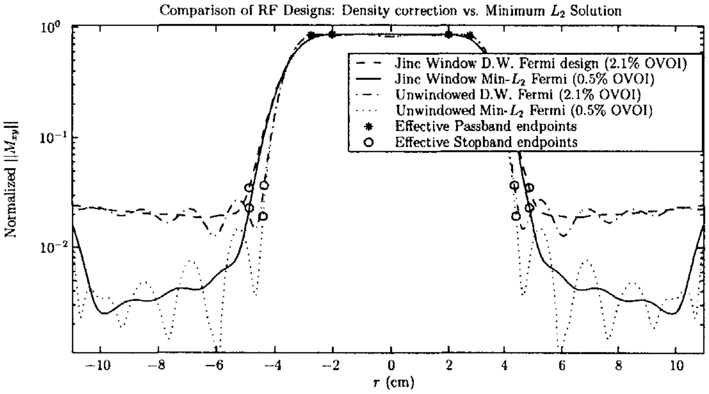

Figure 8-22: Simulated excitation profiles for Density Weighted RF designs computed by application of Voronoi density correction onto the Fourier transform of the desired profile, and, for minimum L_2 designs computed by least-squares solution of the system $Ab = p_{des}$, with b the RF pulse, A the matrix representation of the Fourier transform, and p_{des} the column vector representation of the desired profile. Profiles plotted were generated with the $N = 13.5$ trajectory simulations.

The plots of Fig. 8-22 further emphasize the relation of rippling to transition width, in particular with respect to window choice. The large transition width of the 2D spatial RF excitations is the main intrinsic limitation of the 2DRF-UFSE method. The jinc-windowed Fermi disk design used throughout this work produced a 2.84 cm transition width from nominal pass-band to nominal stop-band. Although the non-diagnostic value of the transition region enables us to allow its latter half to alias into its first half, this still requires that a 1.42 cm wide annulus surrounding the pass-band be resolved via phase encoding at the same resolution as the VOI, in order to avoid transition region signal aliasing into the pass-band. Considering that the 4.08 cm nominal pass-band must be acquired at an rFOV elongated by 1.42 cm on each side of the two phase encoded dimensions, only about 35% of the total phase encode steps are then actually used for resolving the VOI. This immense inefficiency is of course offset by the large overall FOV reduction that more than accounts for it.

This inefficiency can be somewhat offset without impacting increased RF duration by designing better excitation profiles. The transition width is at least as large as the diameter of the lobe of the trajectory's PSF, which intrinsically depends on k-space coverage [107], and is limited by RF duration for 2D trajectories. The use of window functions effectively molds the trajectory's PSF, and will thus intrinsically further increase this diameter, making transition width strongly dependent on window choice rather than choice of profile's r_w. The radii to the first zero crossing of each "effective" PSF for the $N = 13.5$ trajectory and different window choices, shown in Fig. 8-23, closely correspond to the transition widths of the respective simulated RF designs shown in Fig. 8-24. Unfortunately, with short 2D RF pulses leading to small 2D k-space coverage, and lacking explicit

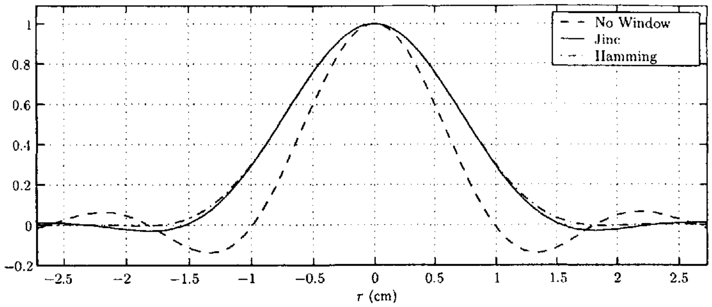

Figure 8-23: Main lobe of the point spread functions resulting from the $N = 13.5$, $D = 22$ cm excitation k-space sampling trajectory using different window functions.

numerical optimization methods, at least some window is necessary to reduce rippling regardless of profile choice, as can be deduced by comparing the Fermi disk profiles in Table 8.2 and Fig. 8-24. Even when the k-space trajectory covers the first four lobes of the Fourier transform of the desired profile, the resulting ripples are unacceptably high. Beyond the fourth lobe, the Fourier coefficients of the desired profile of the Fermi disk are less than 1% of the maximum.

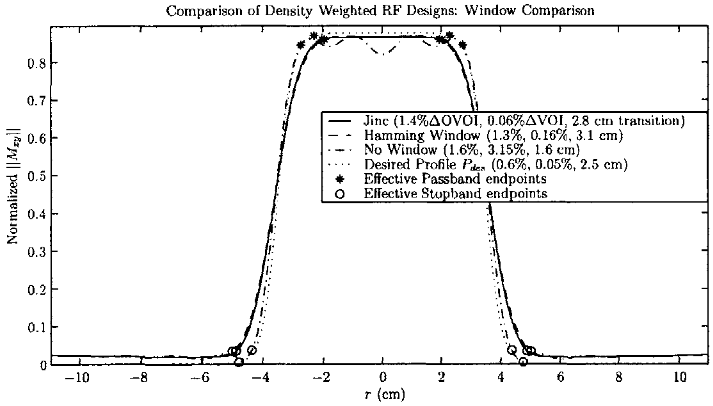

Figure 8-24: Simulated excitation profiles for the density weighted design with the $N = 13.5$ trajectory, by application of different windows. Windowing increases the transition region but reduces rippling, as seen by the %ΔVOI. Rippling in the stop-band is also reduced, but the 2% overall outer volume excitation of D.W. designs is too large to be affected.

The analytic 2D RF design used here was optimized to the best of our ability, yet it still resulted in lower than necessary rippling, effectively not optimizing the transition width for the excitation k-space coverage. In practice, acceptable ripple limits must be defined first. The transition bandwidth must then be optimized within those limits, as is possible with 1D RF pulse designs [120]. The unrestricted choice of 2D k-space sampling functions available to multi-dimensional RF excitation and the inherent computational complexity of designing 2D filters has led to a lack of efficient methods to solve this problem. Algorithms are necessary that enable fine control of the error tolerance in the pass- and stop-bands, similar to those available for FIR filter design [11], but that are efficient for the MR excitation problem. Particularly L_∞ (min-max, also known as Chebysev or equirriple) designs will be useful for the 2D spatial RF excitation problem as they are for 1D excitations.

In contrast to the 2DRF-UFSE method, the DS-UFSE method enables the efficiency available to 1D-selective RF pulse designs to be used. This provides better outer volume suppression, minimal transitions from pass-bands to stop-bands, and the ability to produce a rectangular rFOV, with RF pulses of the order of a few milliseconds [120]. Its potential drawback is that maximal transverse magnetization is produced by the $\pi/2$ slab in the desired outer volume to be suppressed. Although measures are taken by the DS-UFSE method to account and silence this magnetization, stimulated and indirect echoes may potentially limit its use.

However, an important aspect of the DS-UFSE method can be used to avoid this limitation. Namely, all but the first echo spacings are very tightly packed and independent of the duration of the first. Accordingly, a longer first echo spacing can be afforded, without detrimentally affecting echo train duration. The longer first echo spacing can then be used to accommodate 2-dimensional selective $\pi/2$ and first π pulses to achieve well defined VOI selection [80], even using non-self-refocused excitation trajectories, such as echo-planar trajectories that are particularly well-suited for rectangular profile excitation. Furthermore, rectangular profiles that are separable along the two dimensions can be designed more efficiently with well known methods [120].

In every case, the achieved suppression of the outer volume should be considered in relation to the achievable SNR. Since

$$\text{SNR} = \text{Signal Energy}/\sigma_{\text{noise}}, \tag{8.13}$$

if the coherent transverse magnetization in the outer volume produces a signal proportional to σ_{noise} then it has effectively been suppressed. With most morphological MR imaging performed at SNRs of 20 – 50, the suppression achieved by the two methods is already sufficient for many MRI applications. This is evident from the brain and spine results of the previous section. Furthermore it is clear that RF excitation profile improvements to increase suppression are well within reach. In terms of the attainable SNR of the two methods, although use of IV selection reduces the signal volume while not affecting the noise volume which depends solely on coil sensitivity, as pointed out in [27], SNR per unit time is not sacrificed, relatively depending only on voxel size and number of encoding steps. The 2DRF-UFSE method currently incurs an additional small loss of SNR due to use of a 60° flip angle, although methods to obtain non-linear designs by correcting linear ones [65] can be readily applied.

Chapter 9

Discussion, Conclusions, and Further Work

9.1 Concluding Remarks

Non-Fourier encoding of the MR signal has been previously presented [109, 150, 168], analyzed [43, 151, 111, 167, 161], and compared to reduced encoding Fourier imaging [52] (such as RIGR [72] and Keyhole [146]).

Non-Fourier spatial encoding can be derived from well-known fixed mathematical basis sets, such as Hadamard [109] and wavelet [45] bases that are popular in signal processing. In MRI such encoding methods have enabled effective inter-view motion compensation [45], volume imaging of the heart [20], increasing the effective relaxation times [45], or, imaging with multiple resolutions along the phase-encode and slice-select dimensions (MURPS) [116].

Spatial encoding methods can also be derived dynamically to adapt to the changing contents of the FOV [164, 114, 168, 52]. Such dynamic adaptive *near-optimal* non-Fourier encoding can exploit *a priori* information about the imaged sample in order to further reduce image acquisition times, for example via wavelet or Singular Value Decomposition (SVD) encoding [118, 164, 114]. In MRI adaptive methods enable compacting the acquired signal space while maximizing the amount of pertinent image information that is acquired during each broadband non-Fourier signal readout.

The application of non-Fourier encoding to MRI imaging relies on the ability of MR physics to treat spatial profiles of excited spins as vectors in a vector space. In such a framework one is free to ignore the acquisition of those vector subspaces that are deemed unimportant. The term unimportant can have wide-ranging meaning, and may be application-dependent. Subspaces can be deemed unimportant based on the diagnostic value of the regions of the image that they encode. This is one premise of wavelet encoded MRI [118]. Alternatively, they can be deemed unimportant based on a given allotted imaging time, thus limiting the number of basis functions that can be sampled. This is effectively a limit on the subspace dimensionality, becoming the premise of maximizing image information captured by rank-revealing decompositions of the signal matrix [168]. Our own definition, presented in Section 3.1, relies on a precursor to the Rose model [148], defining unimportant subspaces with respect to noise in the imaging system [87, 93]. This enables general signal compression over the entire image without necessarily compromising diagnostic information. In every case, a good approximation to the FOV contents (for the desired task) can be acquired and reconstructed in typically a fraction of the normal acquisition time.

However, despite its many potential advantages, non-Fourier encoding has not come to routine use in MRI. The premise of this dissertation was that this is in part attributed to the lack of non-Fourier MR imaging technologies that can compete with present-day Fourier MRI methods. Thus, this dissertation has first and foremost attempted to produce some of the technologies that are necessary to enable fast non-Fourier MRI.

Before we summarize these technologies and attempt to suggest directions for future research, we note that non-Fourier MR imaging is not without disadvantages. Its benefits are paid for in, firstly, the large computational complexity of the imaging system necessary compared to standard Fourier MRI techniques. Secondly, there is an associated loss of applicability to a certain degree. This loss stems from the facts that reduced signal-to-noise ratio may be incurred [43, 151, 111, 161], as well as the fact that a subspace truncation may cause certain changes in the FOV to be inadvertently lost. It is these disadvantages, to a large degree, that we must consider and that must suggest directions for further work.

9.1.1 SNR Considerations

When non-Fourier encoding replaces phase encoding of equivalent flip angle and imaging parameters, the signal to noise ratio of Fourier encoding, $SNR^{\mathrm{full}}(\vec{r})$, is altered to that attained by the particular non-Fourier encoding method. This SNR has been studied extensively in e.g., [43, 151, 111, 161]. It is affected by a number of factors, viz., the conditioning of the non-Fourier encoding inversion (i.e., Eq. (2.28), similar to the geometry factor $g(r)$ of parallel imaging [126]), and, the reduced acquired signal energy stemming from use of encoding profiles that do not make use of all available magnetization.

The Hadamard and SVD encoding examples that we used throughout this dissertation incur no inversion SNR loss since the encoding matrices are orthogonal. Furthermore, like phase encoding, Hadamard encoding only uses the phase of magnetization for encoding and thus maintains SNR for equivalent flip angle imaging. However, SVD encoding, and probably most encoding methods that will prove useful for accelerated compressed MR imaging, employs encoding functions that produce variable flip angles throughout space, hence not all imaged magnetization contributes to each signal acquisition.

An intuitive understanding of this SNR loss can be obtained by considering the case of Line Scan encoding which, in the low flip angle approximation, is achieved by deriving the RF encoding matrix P of Eq. (2.27) from the Fourier transform of each row of the identity matrix. It is well known that the SNR of Line Scan techniques is reduced by a factor of $1/\sqrt{M}$, when M lines are scanned [130].

Typical SVD encoding profiles lie somewhere between the Hadamard and Line Scan examples. However, the SNR loss of truncated SVD encoding may be reduced compared to Fourier imaging, similarly to SVD denoising used in signal processing [63], when the Rose model [148] is used to control the subspace truncation as we suggest in Section 3.1. Although our motivation there was imaging acceleration, truncation of the encoding vector basis at the point that signal energy falls below the k-space noise threshold adds no new information but only noise.

9.1.2 A Comment on the Use of High Flip Angle RF Pulses

A major contributing factor to SNR is the signal energy. For a given sample, magnetic field, and imaging parameters, and assuming adequate relaxation or steady state formation, the single most determining factor of signal energy is the excitation flip angle. The larger the flip angle, the larger the induced signal.

The non-Fourier encoding framework and all derivatives we have presented, such as NF*P and UNFOLD-NF, use the low flip angle approximation to set up the linear equations enabling "digital" RF encoding, i.e., Eq. (2.26). Transition to high flip angle excitations follows by deducing these equations (i.e., the encoding vectors p) directly from the Fourier transform of the desired spatial encoding profiles $p(y)$. The Fourier coefficients of $p(y)$ replace the specific RF waveforms. Once a spatial encoding profile is chosen, the actual RF excitation that produces the profile at any desired flip angle may be computed (e.g., numerically [136, 137, 65]). Once that RF pulse is used for sample excitation to produce the desired spatial profile, multiplication of the spatial domain spin density $\rho(r)$ and profile $p(y)$, as in Eq. (2.23), is equivalent to writing the Fourier transform of the profile within the signal equation. It is then the Fourier coefficients of this direct transform of the spatial profile that lead to the linear system and enable use of the matrix equations and digital encoding model in every situation we have presented.

9.2 Directions of Further Research

Although this dissertation has been concerned with a number of subjects in the development of fast non-Fourier MRI, many questions remain unanswered regarding the applicability of compressed MR imaging. Even setting applicability aside, many more technologies must be developed and implemented before non-Fourier imaging can competitively challenge Fourier basis MRI. In this section, we wish to gather certain ideas, both our own as well as some based on well-known aspects of MRI, that may be useful in augmenting the image quality and control aspects of non-Fourier encoding systems. Some of these represent cutting edge technology which can be readily applied to, or modified for, the needs of non-Fourier MRI. We also attempt to go a step further and summarize some of the issues we believe are central to the future of broadband compressed MR imaging.

9.2.1 Further Implementation and Integration of Technologies Developed

Most of the technologies we have presented are, to a large extent, prototypes. These prototypes can and must be consolidated into a single, modularized platform. This platform can then serve as a black-box add-on system to commercial MR imagers that is capable of taking advantage of any subset of modules for a given desired MRI acquisition. This platform should also be able to serve as an extensible platform capable of taking advantage of new methods and techniques by module extension, reimplementation, or addition, as appropriate. In particular, the goal should be similar to what was attempted in Chapter 7. That is, a simple collection of abstractions that allows encoding, reconstruction and any other signal-dependent computation modules to be implemented uniformly, i.e., based on standardized components. The resulting system must allow any collection of such modules to be hot-wired on a need-basis to the system, in order to provide a pipeline instantiation that is seamlessly capable of acquiring and reconstructing the images for for any MR imaging experiment that we desire to perform.

Most technologies we have developed in Chapters 3, 4, 5, 6 and 8 are fairly easy to wrap into the abstractions we already provide with the scanner real-time system presented in Chapter 7. For example, automated subspace dimensionality control can be accomplished by inserting a module between the raw k-space reconstruction and spatial image reconstruction modules to compute the SNR of acquisitions. The result of this module can be input to the given subspace encoding module. Such a noise estimation module should be instantiated into the pipeline when the pulse sequence used in the given experiment does not provide the functionality to estimate noise nor is that information readily available from the results produced by the sequence. This was the case in Section 4.4.4. If, on the other hand, the sequence is capable of a noise estimation mode, then a different module, that operates near the scanner synchronization module, should instead be instantiated in order to drive the sequence in this noise estimation mode so as to acquire the necessary data and use them to perform the estimation. What is suggested is that the pipeline should offer a method of instantiating different modules, as well as the wiring between them, without having to change the source code nor recompile. It would then be straightforward to have either kind of module provide the noise estimate to the prospective compression or subspace truncation modules which can then use this information to select the encoding basis to be used.

Similarly, seamless integration of the NF*P parallel imaging technique of Chapter 5 requires the addition and modification of modules. The scanner synchronization module must be able to to pull data from multiple receiver coils. A new module must also be inserted to require the RF generation module to produce additional excitations that will yield receiver coil array auto-calibration [58]. In fact, with the appropriate design in place, a simple polymorphic method could enable the reconstruction module loaded at each instantiation of the pipeline for each acquisition to be selected to perform one of the many different parallel reconstruction methods as desired. The UNFOLD k–t method for non-Fourier encoding of Chapter 6 can similarly be implemented by yet another module that would cache reconstructed images past the Fourier transform module in the pipeline into a FIFO buffer and perform the UNFOLDing step on those images in order to estimate the most recently acquired image.

In both these cases, the raw k-space reconstruction, subspace generation, and RF generator modules would all need to encapsulate implementations that make use of the knowledge that such parallel or k–t modules are in place in the pipeline. For example, the RF generator module would need to make use of Eqns. (5.48) and (6.14) as appropriate, while the subspace computation module would also have to keep a short FIFO in the case of UNFOLD-NF.

Such a list of modules and data pathways will only grow with every new method and technique that is devised. It is therefore in the best interest of the researchers studying non-Fourier imaging to preemptively design a system that is capable of encapsulating any new acquisition, reconstruction, encoding, or general data processing method. The modular platform provided in Chapter 7 lays the groundwork of enabling this via a system that only requires the extension of well-defined application abstractions and the description of a wiring diagram.

9.2.2 Further Pulse Sequence Development

As we have shown throughout this dissertation, at the heart of any MRI experiment are pulse sequences. They are the circuit diagrams of MRI. Fast, optimal pulse sequences must be further developed, specifically aimed at optimizing tasks that Fourier basis imaging is not well suited for. In Chapter 4 we attempted to provide a number of general, and hopefully useful, examples of non-Fourier encoding. The aim was to optimize signal encoding in many different imaging scenarios, i.e., 2D multi-echo imaging or 3D spiral and EPI imaging. The description of broadband encoding with arbitrary trajectories that we defined in Section 4.4 further enables the use of non-Fourier encoding in any imaging sequence we can devise. The implementation of fast spoiled sequences for broadband encoding must now continue not in the general fashion but, rather, by attempting to design sequences that are aimed at optimally solving specific problems, such as magnetic resonance angiography (MRA) or black-blood (blood-suppressed) cardiac imaging.

As an aside, we note that stimulated and indirect echoes [119, 48] used in fast steady-state Fourier imaging do not immediately appear to be useful in non-Fourier encoding. The echoes being sampled in these methods contain encoding information that can not be easily removed, as is accomplished via gradient reversal in Fourier MRI. Although such echoes may prove to be useful for yet to be discovered non-Fourier encoding methods, for the time being, magnetization from previous encoding steps must be spoiled. Nonetheless, we have shown that implementation of fast gradient recalled echo and low flip angle short-TR spin echo sequences is well within reach and a subject that must be more extensively explored. When this task nears completion, attention can return to stimulated and indirect echo encoding, just as occurred in the Fourier imaging world.

9.2.3 Adaptivity of Compression Methods

The issue of prospective MR signal compression must be more closely studied in the context of adaptivity to a changing FOV. The implementation and immediate application of useful fixed basis imaging is now immediately possible with the pipeline system we developed in Chapter 7. This includes wavelet encoding, e.g., in order to obtain a sequence of images with high resolution in a given region of interest. This region can be adapted to the changing sample, by tracking the location of the desired high resolution region. For example, this would require changing the subspace computation module with one that e.g., tracks the location of a needle (or some other tracking method).

However, all signal compression methods that adapt the encoding basis over time pose the risk of improperly encoding important changes in the FOV. In particular, there may be changes of diagnostic interest that have a small or no projection onto the basis set used for the compressed acquisition. We can quantify this based on equation (3.7) as the situation

$$\left\|U(t_0)U^H(t_0)\Delta F(t)\right\|_F \approx 0, \text{ and} \tag{9.1}$$

$$\left\|\Delta F(t)\right\|_F \gg 0. \tag{9.2}$$

On this subject, we note that it is possible to obtain an estimate of the component of $\Delta F(t)$ that lies in the subspace complementary to that acquired, by switching the readout and non-Fourier encoded directions. One can obtain $F(t)e$, with e a column of the identity matrix. The complementary subspace projection for that column of $F(t)$ then provides an estimate of $\Delta F(t)$. This estimate can be used to either restart with a full k-space acquisition, or to update the acquisition subspace.

On the subject of updating the acquisition subspace, navigator acquisitions can be used much like in Fourier imaging in order to assess and correct for sample movement in the spatial encoding profiles, as we will discuss shortly. Finally, on the subject of adaptivity, new methods must be devised that are aimed by design to adapt the input RF vectors to track dynamic changes in the FOV. One such example is the DATUM approach [52], while optical flow methods may provide another approach. Such methods hold promise in making non-Fourier encoding a useful imaging modality for dynamic MRI.

9.2.4 Correcting Spatial Encoding Profiles

Just as in the case of Fourier imaging, non-Fourier imaging suffers from motion artifact during imaging. Unlike Fourier encoding however, rigid body motion on a large scale may become much more limiting, since the spatial excitations may no longer correspond to the actual location of spin density. In practice, rigid body motion of the bulk of the spin density is the major problem we have encountered with SVD imaging. Automated restarts, discussed above, can help ameliorate the situation by restarting the imaging pipeline. However, this approach is very costly in the setting of a dynamic experiment, since full acquisitions are time-consuming. Until encoding methods that are guaranteed to adapt to such changes are available, a simple approach is to correct the spatial encoding profiles directly, once the current position of the sample is assessed via use of "navigator" echoes.

Navigator echoes are based on the realization that translations of a sample lead to linear phase shifts in k-space while rotations of a sample lead to rotations of the k-space. In 2D MRI, a circle of the Fourier coefficients in the k-space plane may be used to assess the rigid motion by two separate least squares fits (one after removing phase information in order to assess the rotation and another after correcting for rotation to assess the translation). In 3D MRI, a spherical shell of coefficients within the k-space volume is sufficient [153]. Such acquisitions are used in Fourier imaging in order to correct Fourier encoded results.

For non-Fourier spatial encoding, navigator acquisitions that trace the prescribed navigator trajectory can be employed prior to the non-Fourier excitations. The assessed motion can then be corrected directly on the spatial encoding profiles. Trivially, translations require that the phase shifts be applied to the non-Fourier excitations, a process that can be performed in real-time. Depending on the encoding method, rotations may require more involved correction. For example, in SVD encoding they unfortunately appear to require that the SVD be recomputed, although this may also be performed much faster than a full acquisition of k-space using warm restarts. Such navigator approaches would enable the dynamic pipeline a much lower latency than a full re-acquisition and would also enable consistent imaging quality in the dynamic experiments.

9.2.5 Parallel Excitation of Spatial Encoding Profiles

Parallel imaging has succeeded in shortening acquisition times by scanning k-space less densely than required for the prescribed FOV, instead using the encoding enforced by the differing spatial weightings of multiple acquisition coils in order to generate the k-space data lost in down-sampling.

Similarly to signal acquisition acceleration via the use of multiple receiver coils with differing independent sensitivities that we analyzed in Chapter 5, it has recently been shown that multiple RF excitation coils with differing spatial weightings may be used to excite a k-space less densely, while still achieving the desired spatial resolution of the excitation profile [162, 59]. The direct effect of using such methods for the excitation of 2D spatial profiles used for 3D non-Fourier encoding in Sections 4.3 and 4.4, or for the 2DRF-UFSE inner-volume technique of Chapter 8 is trivially evident. That is, the length of the excitatory RF pulse length required to achieve the excitation profile will be reduced proportionally to the number of coils used. By coupling parallel excitation with parallel acquisition, it is prudent to speculate that within a single TR we will be able to acquire the response to a single high resolution 2D encoding profile with future MR imagers, considering that 16 to 32 receiver channel systems are already appearing. In light of this, it is certainly expected that 1–2 sec, high resolution 3D imaging will certainly be well within reach in the near future.

9.2.6 Optimal Parallel and k–t Imaging

Parallel imaging allows one to speedup MRI up to a factor of K when K receiver coils with different spatial sensitivities are used to acquire the signal. In general, one can think of the coils acting as filters through which the MR signal passes prior to detection (with the coil sensitivities being the filter coefficients). Since there are multiple such filters, the goal is to use them in the form of a filter bank, down-sample the signal, i.e. acquire fewer encoding steps than normally required, and invert the filter bank in order to reconstruct the signal. Non-Fourier encoding is perhaps best-suited to this MR imaging modality. A typical goal in filter bank design is to generate orthogonal filters that are guaranteed to exactly reproduce the signal. In parallel MRI, non-Fourier excitations can aid precisely in this sense; one should be able to use them in order to "orthogonalize" the filtering incurred by the fixed sensitivities of the coils, (which depend on physical factors alone e.g., electronics characteristics, placement, size etc). This is complementary to the problem solved in Chapter 5. Instead of ignoring the existence of the parallel reconstruction, and only being aware of the existence of parallel acquisition, non-Fourier encoding could aid both in the acquisition as well as enabling a better parallel reconstruction. Also, rather than using the fact that a k–t compression is present and will be used to reconstruct the MR images, it may be possible for the non-Fourier excitations to aid in concentrating the spectra to be overlapped. This would then aid their demodulation by the k–t decompression method. Such aspects should be explored to assess the use of non-Fourier encoding in providing better parallel and k–t imaging.

9.2.7 Tighter MR Scanner Integration

Last, but not least, non-Fourier encoding research is necessarily intimately linked to the low level details of MR scanners. These details, concerning RF subsystems, acquisition and reconstruction technologies among others, are known to scanner manufacturers, and can greatly enhance or hinder non-Fourier imaging quality. In this sense, our experimental results were in essence "worst-case" imaging, due to the very limited knowledge of the implementation of proprietary MR scanners available to us, and whose complexity is indeed monumental and not to be underestimated. Further increase in imaging quality by multiples and perhaps orders of magnitude can possibly be obtained. This opinion is based on quality improvements we obtained haphazardly in our limited trial-and-error attempts to reverse engineer certain aspects of the proprietary MR scanner hardware and software.

9.3 Conclusions

Despite the many open problems remaining, this dissertation is only the natural progression of a new MRI encoding approach, similar to the progression that has been underway for many years in Fourier basis MR imaging.

There are two main conclusions of this work. Firstly, accelerated fast MRI via broadband non-Fourier encoding of the MR signal content is a viable solution for dynamic MR imaging applications. Secondly, non-Fourier imaging is capable of offering many of the advantages that are used, and are necessary, in the fast Fourier encoding arena, thus allowing non-Fourier imaging to compete on equal grounds.

The multi-linear response pulse sequence developed in Section 4.1 shows that non-Fourier encoding can achieve efficiency even when compared to fast multi-echo Fourier imaging. The 3D broadband sequences developed in Sections 4.3 and 4.4 enable application of non-Fourier encoding in an area that has traditionally been problematic for Fourier imaging methods, due to the long scanning times required to fully sample a 3D k-space. The general broadband response model of Section 4.4 is further capable of encapsulating any method that partially encodes the MR signal in the excitation step, regardless of trajectory and k-space coverage. This model removes all restrictions on the latter, enabling it to not even need to have a physical meaning such as "1D" or "2D" spatial excitation.

The theory of non-Fourier parallel imaging developed in Chapter 5 shows that additional imaging efficiency can be obtained by combining the MR signal compression available to non-Fourier encoding with the additional spatial encoding provided by multiple coils in parallel imaging methods. The UNFOLD-NF framework of Chapter 6 further shows that other additional encoding, such as via use of the temporal axis, can also be incorporated into the non-Fourier encoding principle.

Perhaps of most interest, the immediate benefit of the NF*P and UNFOLD-NF methodologies is that of enabling parallel and k–t acceleration for most existing digital non-Fourier encoding MRI modalities, regardless of pulse sequence and encoding method specifics. For example, application of NF*P to volume imaging [20] can increase the number of slices without increasing imaging time and possibly RF pulse length. Alternatively, it can be used to reduce imaging time for a given number of slices.

These two frameworks enable us to combine the static analysis of parallel and k–t encoding with the dynamic analysis offered by near-optimal adaptive non-Fourier encoding methods in order to further reduce acquisition times. Additionally, the total speedup potentially available to NF*P and UNFOLD-NF can exceed that achievable by either encoding method independently. It is also noteworthy that combination of these techniques may be of further benefit for non-Fourier imaging, for example the possibly reduced excitation time that can extend the suitability of non-Fourier encoding that is typically hampered by long excitation times.

Finally, as far as the general broadband non-Fourier MRI methodology is concerned, the implementation of a complete, currently operational, non-Fourier MR imaging system was described in Chapter 7. This system brings together many of the components and technologies we have developed and enables non-Fourier encoding to become an alternative to a dynamic imaging session in a commercial clinical MR scanner. This development should greatly enhance the ability of further research to attain prototype status within a short time. As an example, following the independent development of the DATUM approach [52], its implementation within this system required a day's worth of work, most of which was related in implementing that algorithm, and enabling the graphical user interface to select it.

Lastly, in Chapter 8, we described, developed, and analyzed two methods that rely on the combination of broadband excitations and Fourier basis sampling, in order to achieve 3D inner volume ultra fast spin echo imaging. The strengths of each method are combined to produce an imaging sequence that minimizes echo spacing while avoiding aliasing from regions outside the selected volume of interest. Both methods developed achieve large increases in VOI imaging efficiency without sacrificing SNR per unit time nor introducing errors from truncated encoding. Coupled with the alleviation of long echo spacings that typically limit FSE imaging, our results already suggest that both methods maintain or increase image quality for 3D neuroimaging applications which only require a limited diagnostic field of view. Due to the small voxel sizes achievable with adequate SNR, 3D IVUFSE methods may prove superior for clinical implementation.

In closing, we hope that the results of this research serve two purposes: firstly, to re-introduce the ideas and theory of non-Fourier encoding, while at the same time extending it to compete with present-day fast MRI techniques. Secondly, to instigate further research on this exciting and promising subject.

Appendix A

Appendices

A.1 Effect of Gradients on Magnetization Precession

Some excellent reviews of MRI physics relevant to this work may be found in the many articles referenced in this work, such as [50, 130, 155], as well as the myriad of books written on the subject. Here we summarize a few results that we extensively use in the main text and wish to include for the purpose of self-containment.

The Bloch equations [3] which describe the motion of the magnetization vector under the influence of arbitrary magnetic fields can be written, disregarding relaxation, as [50]:

$$\frac{d\vec{M}}{dt} = \gamma\vec{M} \times \vec{B}, \tag{A.1}$$

where $\vec{M}$ is the magnetization, $\vec{B}$ is the applied magnetic field strength and $\times$ in this context denotes outer product. We refer to the individual components along the three spatial axes by using a subscript defining the axis. The magnetic field in the absence of an excitatory RF pulse, is aligned with the z (i.e., $\hat{\mathrm{k}}$) axis and is typically composed of two components. First, its static component, B_0, which is responsible for sustaining the magnetization vector by the excess protons in the sample that are forced to align with it. The second component, the gradient fields, modify the strength B_0, linearly along the axis they are said to be applied along. For example an x-axis gradient imposes $\frac{\partial B_z}{\partial x} = \text{const} = G_x$, therefore modifying B_0 to

$$\vec{B} = (0, 0, B_0 + (G_x x)). \tag{A.2}$$

We can then rewrite Eq. (A.1) using Eq. (A.2) as

$$dM_x/dt = M_y\omega, \tag{A.3}$$

$$dM_y/dt = -M_x\omega, \tag{A.4}$$

$$dM_z/dt = 0, \tag{A.5}$$

where we have let $\omega = \omega_0 + 2\pi\gamma G_x x$ and $\omega_0 = 2\pi\gamma B_0$. The solution of equation (A.5), in the absence of relaxation terms, dictates that the longitudinal component of the magnetization remains constant. To solve Eqns. (A.3) and (A.4), we first switch to a complex plane representation, wherein the transverse magnetization can be conveniently described as $M_{xy}(t) = M_x(t) + iM_y(t)$. We then have

$$\frac{dM_{xy}}{dt} = \frac{dM_x}{dt} + i\frac{dM_y}{dt} = \omega(M_y - iM_x) = i\omega M_{xy}(t). \tag{A.6}$$

This equation has the trivial solution

$$M_{xy}(t,x) = M_{xy}^0 e^{i\omega t} = M_{xy}^0 e^{i(\omega_0 + 2\pi\gamma G_x x)t}. \tag{A.7}$$

In the absence of a gradient, $M_{xy}(t)$ rotates at a fixed angular velocity ω_0. When a gradient is applied along any axis, e.g., the x axis, then depending on the magnetization's position along that axis, the base Larmor frequency is increased by $\gamma G_x x$. This is where the frequency dependence of the acquired signal to the applied gradient magnetic field, that we have used throughout e.g., for the readout pulses, originates from. If the gradient pulse is applied for a fixed amount of time τ, then the magnetization advances or slows down with respect to other positions in the sample, by $2\pi\gamma G_x x\tau$. In the main text we also absorb a factor -1 into γ. Finally, the raw voltages induced on the receiver coil, emanating from the magnetization vector [50], are always demodulated by the base frequency corresponding to ω_0, producing the phase factors that were used throughout.

A.2 The Stimulated and Indirect Echoes of DS-UFSE

In the description of the DS-UFSE sequence of Section 8.2 it was stated that, disregarding encoding and dephasing gradients, undesired echoes from volumes "C" and "B" (c.f., Fig. 8-14) generated in the course of the echo train will occur at $ESP_2 + (k + (n/2 \pm 1/4))ESP_1$ and $ESP_2 + (k + (n + 1/2))ESP_1$, for $k \in \mathbb{Z}^+$ and with n fixed (c.f., Eq. (8.7)). These were empirically derived by examining the extended-phase graph [46] of the sequence, shown in Fig. A-1. Because of the two different RF pulse spacings, there are multiple magnetization pathways and here we consider the main contributors to these empirically derived equations.

Consider a 3-pulse DS-UFSE sequence, i.e., composed of a soft $\pi/2$, soft π, hard π RF pulse

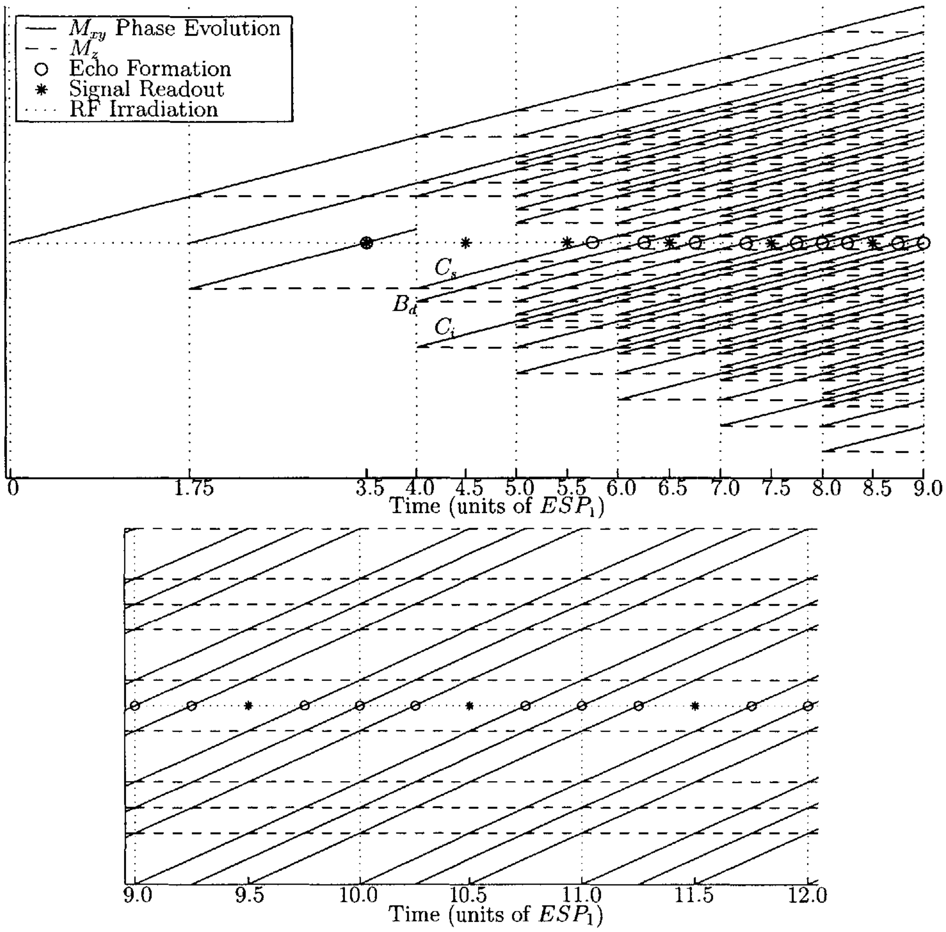

Figure A-1: Top: Extended-phase graph of undesired magnetization pathways of the DS-UFSE echo train. For clarity, the desired pathway is not shown beyond the occurrence of the first hard-pulse. Bottom: periodicity arrived at later in the echo train.

train, and concentrate on the dephasing of a specific T_2 species. Assuming that the echo spacing delays defined in Fig. 8-15 satisfy Eqns. (8.6) and (8.7) for a given n, and referring to the volume labels in Fig. 8-14, the following cases are descriptive of the echo pathways labeled in Fig. A-1:

C_i: An indirect echo from volume "C" is formed at

$$2(ESP_2/2 + SP_2) = ESP_2 + \left(1 + \left(n + \frac{1}{2}\right)\right) ESP_1, \tag{A.8}$$

by transverse magnetization resulting from the soft $\pi/2$ pulse and that remains unaffected by the soft π pulse but is inverted by the hard π pulse.

C_s: A stimulated echo from volume "C" is formed at

$$\begin{aligned} 2\left(\frac{ESP_2}{2}\right) + SP_2 &= ESP_2 + \left(\frac{1}{2} + \frac{n}{2} + \frac{1}{4}\right) ESP_1 \\ &\equiv ESP_2 + \left(1 + \left(\frac{n}{2} - \frac{1}{4}\right)\right) ESP_1, \end{aligned} \tag{A.9}$$

by transverse magnetization in "C" resulting from the soft $\pi/2$ pulse and that is converted to longitudinal magnetization by the soft π pulse and back to transverse by the hard π pulse.

B_d: A direct echo from volume "B" is formed at

$$\frac{ESP_2}{2} + 2SP_2 = ESP_2 + \left(1 + \left(\frac{n}{2} + \frac{1}{4}\right)\right) ESP_1, \tag{A.10}$$

by transverse magnetization produced in "B" by the soft π pulse and inverted by the hard π pulse.

To complete the empirical echo time equations, we note that in DS-UFSE the hard π pulses are located at $ESP_2 + (k + 1/2)ESP_1$, for $k \in \mathbb{Z}^+$. Now, if we follow the evolution of echo C_s, which occurs at $ESP_2 + (1 + (n/2 - 1/4))ESP_1$, it will freely dephase until the next hard π pulse. Since by constraints, $n \geq 1$, if n is odd we can write that echo C_s occurs at $ESP_2 + (1 + \lfloor (n/2) \rfloor + 1/2 - 1/4)ESP_1 = ESP_2 + (g + 1/4)ESP_1$ with $g \geq 1$. If n is even then we can instead write $ESP_2 + (g - 1/4)ESP_1$, with $g \geq 2$. It is now evident that for odd n the echo C_s occurs at $1/4ESP_1$ before an additional (i.e., a second, third etc.) hard π pulse, or, for even n, at $3/4ESP_1$ before it. For n odd, if the hard π pulse that irradiates the sample at $1/4ESP_1$ after C_s (i.e., the hard pulse with $k = g$) inverts some of that echo's transverse magnetization, then it will again rephase, at $1/4ESP_1$ *after* the hard π pulse, thus completing the $\pm 1/4ESP_1$. A similar argument follows for C_s in the even n case, and the entire argument follows for the B_d echo. Since the C_i echo occurs at the location of a hard pulse, any subsequent echo originating from its magnetization will also necessarily occur at the time of a hard pulse as well.

References

[1] C. B. Ahn and Z. H. Cho. Analysis of the eddy-current induced artifacts and the temporal compensation in nuclear magnetic resonance imaging. *IEEE Trans Med Imaging*, 10:47–52, 1991.

[2] C. B. Ahn, J. H. Kim, and Z. H. Cho. High-speed spiral-scan echo planar NMR imaging - i. *IEEE Trans Med Imaging*, 5:2–7, 1986.

[3] F. Bloch. Nuclear induction. *Phys Rev*, 70:460–474, 1946.

[4] F. Bloch, W. W. Hansen, and M. Packard. The nuclear induction experiment. *Phys Rev*, 70:474–485, 1946.

[5] P. Börnert, B. Aldefeld, and H. Eggers. Reversed spiral MR imaging. *Magn Reson Med*, 44:479–484, 2000.

[6] R. M. Botnar, W. Y. Kim, P. Börnert, M. Stuber, E. Spuentrup, and W. J. Manning. 3D coronary vessel wall imaging utilizing a local inversion technique with spiral image acquisition. *Magn Reson Med*, 46:848–854, 2001.

[7] P. A. Bottomley and C. J. Hardy. Progress in efficient three-dimensional spatially localized in vivo 31P NMR spectroscopy using multi-dimensional spatially-selective pulses. *J Magn Reson*, 74:550–556, 1987.

[8] P. A. Bottomley and C. J. Hardy. Two-dimensional spatially selective spin inversion and spin-echo refocusing with a single nuclear magnetic resonance pulse. *J Appl Phys*, 62:4284–4290, 1987.

[9] R. N. Bracewell and A. R. Thompson. The main beam and ringlobes of an east-west rotation-synthesis array. *Astrophysical Journal*, 182:77–94, 1973.

[10] M. E. Brummer, D. Moratal-Pérez, C.-Y. Hong, R. I. Pettigrew, J. Millet-Roig, and W. T. Dixon. Noquist: Reduced field-of-view imaging by direct Fourier inversion. *Magn Reson Med*, 51:331–342, 2004.

[11] C. S. Burrus, J. A. Barreto, and I. W. Selesnick. Iterative reweighted least-squares design of FIR filters. *IEEE Trans Signal Processing*, 42:2926–2936, 1994.

[12] Y. Cao and D. N. Levin. Feature-recognizing MRI. *Magn Reson Med*, 30:305–317, 1993.

[13] Y. Cao, D. N. Levin, and L. Yao. Locally focused MRI. *Magn Reson Med*, 34:858–867, 1995.

[14] J. W. Carlson. MRI data acquisition and image reconstruction from multiple, non-interacting receiver coils. In *IEEE Conference in Engineering in Medicine and Biology Society*, volume 2, pages 607–608, 1989.

[15] J. W. Carlson and T. Minemura. Imaging time reduction through multiple receiver coil data acquisition and image reconstruction. *Magn Reson Med*, 29:681–688, 1993.

[16] H. Y. Carr and E. M. Purcell. Effects of diffusion on free precession in nuclear magnetic resonance experiments. *Phys Rev*, 94:630–638, 1954.

[17] S. Conolly, D. Nishimura, A. Macovski, and G. Glover. Variable-rate selective excitation. *J Magn Reson*, 78:440–458, 1988.

[18] R. T. Constable and J. C. Gore. The loss of small objects in variable TE imaging: Implications for FSE, RARE, and EPI. *Magn Reson Med*, 28:9–24, 1992.

[19] L. A. Crowe, P. Gatehouse, G. Z. Yang, R. H. Mohiaddin, A. Varghese, C. Charrier, J. Keegan, and D. N. Firmin. Volume-selective 3D turbo spin echo imaging for vascular wall imaging and distensibility measurement. *J Magn Reson Imaging*, 17:572–580, 2003.

[20] C. H. Cunningham, G. A. Wright, and M. L. Wood. High-order multiband encoding in the heart. *Magn Reson Med*, 48:689–698, 2002.

[21] R. Damadian, K. Zaner, D. Hor, T. DiMaio, L. Minkoff, and M. Goldsmith. Nuclear magnetic resonance as a new tool in cancer research: Human tumors by NMR. *Ann N Y Acad Sci*, 31(222):1048–1076, December 1973.

[22] C. P. Davis, G. C. McKinnon, J. F. Debatin, D. Wetter, A. C. Eichenberger, S. Duewell, and G. K. von Schulthess. Normal heart: evaluation with echo-planar MR imaging. *Radiology*, 191:691–696, 1994.

[23] L. De Lathauwer, B. De Moor, and J. Vandewalle. A multilinear singular value decomposition. *SIAM J Matrix Anal Appl*, 21(4):1253–1278, 1999.

[24] J. L. Duerk, D. H. Wu, Y. C. Chung, Z.-P. Liang, and J. S. Lewin. A simulation study to assess SVD encoding for interventional MRI: Effect of object rotation and needle rotation. *J Magn Reson Imaging*, 6:957–960, 1996.

[25] R. R. Edelman, P Wielopolski, and F. Schmitt. Echo-planar MR imaging. *Radiology*, 192:600–612, 1994.

[26] R. R. Ernst, G Bodenhausen, and A. Wokaun. *Principles of nuclear magnetic resonance in one and two dimensions.* Oxford University press, Oxford, 1987.

[27] D. A. Feinberg, J. C. Hoenninger, L. E. Crooks, L. Kaufman, J. C. Watts, and M. Arakawa. Inner volume MR imaging: technical concepts and their application. *Radiology*, 156(3):743–747, 1985.

[28] J. A. Fessler and B. P. Sutton. Nonuniform fast Fourier transforms using min-max interpolation. *IEEE Trans Signal Processing*, 51:560–574, 2003.

[29] A. Frieze, R. Kannan, and S. Vempala. Fast Monte-Carlo algorithms for finding low-rank approximations. In *Proceedings of the 39th Annual Symposium on Foundations of Computer Science*, 1998.

[30] D. Gering, A. Nabavi, R. Kikinis, W. Eric L. Grimson, N. Hata, P. Everett, F. Jolesz, and W. Wells III. An integrated visualization system for surgical planning and guidance using image fusion and interventional imaging. In *Medical Image Computing and Computer-Assisted Intervention (MICCAI)*, 1999.

[31] G. H. Glover. Simple analytic spiral k-space algorithm. *Magn Reson Med*, 42:412–415, 1999.

[32] G. H. Golub and C. F. Van Loan. *Matrix Computations.* The Johns Hopkins University Press, Baltimore, Maryland, third edition, 1996.

[33] M. A. Griswold, P. M. Jakob, M. Nittka, J. W. Goldfarb, and A. Haase. Partially parallel imaging with localized sensitivities (PILS). *Magn Reson Med*, 44:602–609, 2000.

[34] E. M. Haacke and J. A. Tkach. Fast MR imaging: Techniques and clinical applications. *Am J Roentgenol*, 155:951–964, 1990.

[35] E. L. Hahn. Spin echoes. *Phys Rev*, 80:580–594, 1950.

[36] R. Haimi-Cohen and A. Cohen. Gradient-type algorithms for partial singular value decomposition. *IEEE Trans Pattern Anal and Machine Intelligence*, 9:137–142, 1987.

[37] J. M. Hanson, Z.-P. Liang, R. L. Magin, J. L. Duerk, and P. C. Lauterbur. A comparison of RIGR and SVD dynamic imaging methods. *Magn Reson Med*, 8:155–161, 1997.

[38] J. M. Hanson, Z.-P. Liang, E. C. Wiener, and P. C. Lauterbur. Fast dynamic imaging using two reference images. *Magn Reson Med*, 36:172–175, 1996.

[39] C. J. Hardy, P. A. Bottomley, and P. Roemer. Off-axis spatial localization with frequency modulated nuclear magnetic resonance rotating (ρ) pulses. *J Appl Phys*, 63(9):4741–4743, 1988.

[40] C. J. Hardy and H. E. Cline. Broadband nuclear magnetic resonance pulses with two-dimensional spatial selectivity. *J Appl Phys*, 66(4):1513–1516, 1989.

[41] C. J. Hardy, H. E. Cline, and P. A. Bottomley. Correcting for nonuniform k-space sampling in two-dimensional NMR selective excitation. *J Magn Reson*, 87:639–645, 1990.

[42] B. A. Hargraves, D. G. Nishimura, and S. M. Conolly. Time-optimal multidimensional gradient waveform design for rapid imaging. *Magn Reson Med*, 51:81–92, 2004.

[43] D. M. Healy and J. B. Weaver. Adapted waveform encoding for magnetic resonance imaging. *IEEE Engineering in Medicine and Biology Magazine*, 14:621–638, 1995.

[44] D. M. Healy and J. B. Weaver. Joint best basis for fast encoding in magnetic resonance imaging. *ICASSP-95, International Conference on Acoustics, Speech, and Signal Processing*, 5:2923–2926, 1995.

[45] D. M. Healy Jr and J. B. Weaver. Two applications of wavelet transforms in magnetic resonance imaging. *IEEE Trans Information Tech*, 38(2):840–860, 1992.

[46] J. Hennig. Multiecho imaging sequences with low refocusing flip angles. *J Magn Reson*, 78:397–407, 1988.

[47] J. Hennig. Echoes – how to generate, recognize, use or avoid them in MR-imaging sequences part II: Echoes in imaging sequences. *Concepts in Mag Reson*, 3:179–192, 1991.

[48] J. Hennig. Echoes – how to generate, recognize, use or avoid them in MR-imaging sequences part I: Fundamental and not so fundamental properties of spin echoes. *Concepts in Magn Reson*, 3:125–143, 1991.

[49] J. Hennig, A. Naureth, and H. Friedburg. RARE imaging: A fast imaging method for clinical MR. *Magn Reson Med*, 3:823–833, 1986.

[50] W. S. Hinshaw and A. H. Lent. An introduction to NMR imaging: From the Bloch equation to the imaging equation. In *Proc IEEE*, volume 71, pages 338–350, March 1983.

[51] R. D. Hoge, R. K. S. Kwan, and G. B. Pike. Density compensation functions for spiral MRI. *Magn Reson Med*, 38:117–118, 1997.

[52] W. S. Hoge, E. L. Miller, H. Lev-Ari, D. H. Brooks, and L. P. Panych. A doubly adaptive approach to dynamic MRI sequence estimation. *IEEE Trans Image Processing*, 11(11):1168–1178, October 2002.

[53] D. I. Hoult. The solution of the Bloch equations in the presence of a varying B_1 field – an approach to selective pulse analysis. *J Magn Reson*, 35:69–86, 1979.

[54] X. Hu and T. Parrish. Reduction of the field-of-view for dynamic imaging. *Magn Reson Med*, 31:691–694, 1994.

[55] M. Hutchinson and U. Raff. Fast MRI data acquisition using multiple detectors. *Magn Reson Med*, 6:87–91, 1988.

[56] P. Irarrazabal, C. H. Meyer, D. G. Nishimura, and A. Macovski. Inhomogeneity correction using an estimated linear field map. *Magn Reson Med*, 35:278–282, 1996.

[57] J. I. Jackson, C. H. Meyer, A. Macovski, and D. G. Nishimura. Selection of a convolution function for Fourier inversion using gridding. *IEEE Trans Med Imaging*, 10:473–478, 1991.

[58] P. M. Jakob, M. A. Griswold, R. R. Edelman, and D. K. Sodickson. AUTO-SMASH: a self calibrating technique for SMASH imaging. *MAGMA*, 7:42–54, 1998.

[59] U. Katscher, P. Börnert, C. Leussler, and J Van den Brink. Theory and experimental verification of transmit SENSE. In *Proc* 10*th ISMRM*, page 189, Hawaii, USA, May 2002.

[60] P. Kellman, F. H. Epstein, and E. R. McVeigh. Adaptive sensitivity encoding incorporating temporal filtering (TSENSE). *Magn Reson Med*, 45:846–852, 2001.

[61] K. King. Sense image quality improvement using matrix regularization. In *in Proc* 9*th ISMRM*, page 1771, Glasgow, Scotland, April 2001.

[62] K. F. King, A. Ganin, X. J. Zhou, and M. A. Bernstein. Concomitant gradient field effects in spiral scans. *Magn Reson Med*, 41:103–112, 1999.

[63] K. Konstantinides, B. Natarajan, and G. S. Yovanof. Noise estimation and filtering using block-based singular value decomposition. *IEEE Trans Image Processing*, 6:479–483, 1997.

[64] A. Kumar, D. Welti, and R. R. Ernst. NMR Fourier zeugmatography. *J Magn Reson*, 18:69–83, 1975.

[65] W. E. Kyriakos and L. P. Panych. Implementation of wavelet encoded MRI with large flip angle pulses. In *Proc* 5*th ISMRM*, page 1990, Vancouver, Canada, 1997.

[66] W. E. Kyriakos and L. P. Panych. Optimization of SPACE RIP imaging by use of RF selective excitation. In *Proc ISMRM Workshop on Minimum Data Acquisition Methods*, pages 76–80, Florida, USA, October 2001.

[67] W. E. Kyriakos, L. P. Panych, S. F. Kacher, C.-F. Westin, S. M. Bao, R. V. Mulkern, and F. A. Jolesz. Sensitivity profiles from and array of coils for encoding and reconstruction in parallel (SPACERIP). *Magn Reson Med*, 44:301–308, 2000.

[68] W. E. Kyriakos, L. P. Panych, G. P. Zientara, and F. A. Jolesz. Implementation of a reduced field-of-view method for dynamic MR imaging using navigator echoes. *J Magn Reson Imaging*, 7:376–381, 1997.

[69] P. C. Lauterbur. Image formation by induced local interactions: Examples employing nuclear magnetic resonance. *Nature*, 242:190–191, 1973.

[70] M. L. Lauzon and B. K. Rutt. Effects of polar sampling in k-space. *Magn Reson Med*, 36:940–949, 1996.

[71] Z.-P. Liang, H. Jiang, C. P. Hess, and P. C. Lauterbur. Dynamic imaging by model estimation. *Int J Imaging Syst and Technol*, 8:551–557, 1997.

[72] Z.-P. Liang and P. C. Lauterbur. An efficient method for dynamic magnetic resonance imaging. *IEEE Trans Med Imaging*, 13:677–686, 1994.

[73] Z.-P. Liang and P. C. Lauterbur. *Principles of Magnetic Resonance Imaging: A Signal Processing Perspective.* IEEE Press, New York, NY, first edition, 2000.

[74] S. Ljunggren. A simple graphical representation of Fourier-based imaging methods. *J Magn Reson*, 54:338–343, 1983.

[75] G. T. Luk-Pat, G. E. Gold, E. W. Olcott, B. S. Hu, and D. G. Nishimura. High-resolution three-dimensional in vivo imaging of atherosclerotic plaque. *Magn Reson Med*, 42:762–771, 1999.

[76] G. T. Luk Pat, A. B. Kerr, and D. G. Nishimura. Inhomogeneity correction for echo-planar imaging with a polynomial estimate of the field map. In *Proc 3rd SMR*, page 617, Nice, France, August 1995.

[77] A. Macovski. Noise in MRI. *Magn Reson Med*, 36(3):494–497, 1996.

[78] B. Madore. Using UNFOLD to remove artifacts in parallel imaging and in partial-Fourier imaging. *Magn Reson Med*, 48(3):493–501, 2002.

[79] B. Madore, G. H. Glover, and N. J. Pelc. Unaliasing by Fourier-encoding the overlaps using the temporal dimension (UNFOLD), applied to cardiac imaging and fMRI. *Magn Reson Med*, 42:813–828, 1999.

[80] S. E. Maier. Slab scan diffusion imaging. *Magn Reson Med*, 46:1136–1143, 2001.

[81] L.-C. Man, J. M. Pauly, and A. Macovski. Multifrequency interpolation for fast off-resonance correction. *Magn Reson Med*, 37:785–792, 1997.

[82] P. Mansfield. Multi-planar image formation using NMR spin echoes. *J Phys C: Solid State Phys*, 10:55–58, 1977.

[83] P. Mansfield. Real-time echo-planar imaging by NMR. *British Medical Bulletin*, 40(2):187–190, 1984.

[84] J. H. McClellan and T. W. Parks. A unified approach to the design of optimum fir linear-phase digital filters. *IEEE Trans Circuit Theory*, CT-20:697–701, 1973.

[85] S. Meiboom and D. Gill. Modified spin-echo method for measuring nuclear relaxation times. *Rev Sci Instrum*, 29:688–691, 1958.

[86] P. S. Melki, F. A. Jolesz, and R. V. Mulkern. Partial RF echo planar imaging with the FAISE method. I. experimental and theoretical assessment of artifact. *Magn Reson Med*, 26:328–341, 1992.

[87] D. Mitsouras. Near real-time 2D non-Fourier basis MRI. Master's thesis, Massachusetts Institute of Technology, 2000.

[88] D. Mitsouras. Near real-time 2D dynamic adaptive MRI using near-optimal spatial encoding. In *Proc ISMRM Workshop on Minimum Data Acquisition Methods*, pages 71–75, Florida, USA, October 2001.

[89] D. Mitsouras, A. Edelman, L. P. Panych, F. A. Jolesz, and G. P. Zientara. Echo planar pulse sequence for 3D dynamic adaptive MRI. In *Proc 9th ISMRM*, page 1807, Glasgow, Scotland, April 2001.

[90] D. Mitsouras, A. Edelman, L. P. Panych, F. A. Jolesz, and G. P. Zientara. Fast multiple-excitation multiple-echo spin-echo pulse sequence for non-Fourier spatial encoding. In *Proc 9th ISMRM*, page 1808, Glasgow, Scotland, April 2001.

[91] D. Mitsouras, A. Edelman, L. P. Panych, F. A. Jolesz, and G. P. Zientara. Sub-second continuous 2D non-Fourier dynamic adaptive MRI using near-optimal spatial encoding. In *Proc 9th ISMRM*, page 1779, Glasgow, Scotland, April 2001.

[92] D. Mitsouras, A. Edelman, L. P. Panych, F. A. Jolesz, and G. P. Zientara. 3D non-Fourier dynamic adaptive MRI via near-optimal spatial encoding: Toward real-time imaging. In *Proc 10th ISMRM*, page 2379, Hawaii, USA, May 2002.

[93] D. Mitsouras, A. Edelman, L. P. Panych, F. A. Jolesz, and G. P. Zientara. Spiral echo-planar trajectories for 3D non-fourier encoded MRI. In *Proc 11th ISMRM*, page 1009, Toronto, Ontario, Canada, May 2003.

[94] D. Mitsouras, W. S. Hoge, A. Edelman, and G. P. Zientara. MR imaging via non-Fourier encoding and multiple receiver coils. In *Proc 11th ISMRM*, page 16, Toronto, Ontario, Canada, May 2003.

[95] D. Mitsouras, W. S. Hoge, F. J. Rybicki, W. Kyriakos, A. Edelman, and G. P. Zientara. Non-Fourier encoded MRI using multiple receiver coils. *Magn Reson Med*, 52:321–328, 2004.

[96] D. Mitsouras, B. Madore, F. J. Rybicki, A. Edelman, and G. P. Zientara. Accelerated MR imaging via FOLDing the non-Fourier encoded dimensions. In *Proc 12th ISMRM*, page 2092, Kyoto, Japan, May 2004.

[97] D. Mitsouras, R. V. Mulkern, A. Edelman, G. P. Zientara, and F. J. Rybicki. 3D ultra-fast spin echo inner volume MRI: Neuroimaging applications. In *Proc 12th ISMRM*, page 2105, Kyoto, Japan, May 2004.

[98] D. Mitsouras, R. V. Mulkern, A. Edelman, G. P. Zientara, and F. J. Rybicki. Neuroimaging applications of two reduced field-of-view 3D fast spin echo magnetic resonance imaging methods with ultrashort, nonselective, hard-pulse refocusing radiofrequency pulses. In *90th Scientific Assembly and Annual Meeting of the Radiological Society of North America*, pages SSG19–02, Chicago, IL, USA, November 2004.

[99] D. Mitsouras, R. V. Mulkern, A. Edelman, G. P. Zientara, and F. J. Rybicki. Strategies for inner volume 3D ultra-fast spin echo MRI. *in preparation*, April 2004.

[100] D. Mitsouras, R. V. Mulkern, L. P. Panych, A. Edelman, G. P. Zientara, and F. J. Rybicki. Strategies for inner volume 3D fast spin echo MRI. In *Proc 11th ISMRM*, page 987, Toronto, Ontario, Canada, May 2003.

[101] D. Mitsouras, F. J. Rybicki, A. Edelman, and G. P. Zientara. Fast magnetic resonance imaging via adaptive broadband encoding of the MR signal content. *IEEE Trans Med Imaging*, May 2004. *invited for revised submission.*

[102] D. Mitsouras, F. J. Rybicki, A. Edelman, and G. P. Zientara. Ultra high spatio-temporal resolution 3D dynamic MRI via adaptive non-Fourier encoding: Experimental results. In *Proc 12th ISMRM*, page 2667, Kyoto, Japan, May 2004.

[103] J. P. Mugler and J. R. Brookeman. Efficient spatially-selective single-slab 3d turbo-spin-echo imaging. In *Proc 12th ISMRM*, page 695, Kyoto, Japan, May 2004.

[104] J. P. Mugler III, S. Bao, R. V. Mulkern, C. R. Guttman, R. L. Robertson, F. A. Jolesz, and J. R. Brookeman. Optimized single-slab 3D spin-echo MR imaging of the brain. *Radiology*, 216(3):891–899, 2000.

[105] R. V. Mulkern, P. S. Melki, P. Jakab, N. Higuchi, and F. A. Jolsez. Phase-encode order and its effect on contrast and artifact in single-shot RARE sequences. *Med Phys*, 18(5):1032–1037, 1991.

[106] K. S. Nayak, C.-M. Tsai, C. H. Meyer, and D. G. Nishimura. Efficient off-resonance correction for spiral imaging. *Magn Reson Med*, 45:521–524, 2001.

[107] K. Nehrke, P. Börnert, J. Groen, J. Smink, and J. C. Böck. On the performance and accuracy of 2D navigator pulses. *Magn Reson Imaging*, 17(8):1173–1181, 1999.

[108] D. C. Noll, C. H. Meyer, J. M. Pauly, D. G. Nishimura, and A. Macovski. A homogeneity correction method for magnetic resonance imaging with time-varying gradients. *IEEE Trans Med Imaging*, 10:629–637, 1991.

[109] C. Oh, H. W. Park, and Z. H. Cho. Line-integral projection reconstruction (LPR) with slice encoding techniques: Multislice regional imaging in NMR tomography. *IEEE Trans Med Imaging*, MI-3:170–178, 1984.

[110] K. Oshio, F. A. Jolesz, P. S. Melki, and R. V. Mulkern. T2-weighted thin-section imaging with the multislab three-dimensional RARE technique. *J Magn Reson Imaging*, 1:695–700, 1991.

[111] L. P. Panych. Theoretical comparison of Fourier and wavelet encoding in magnetic resonance imaging. *IEEE Trans Med Imaging*, 15(2):141–153, 1996.

[112] L. P. Panych, P. D. Jakab, and F. A. Jolesz. An implementation of wavelet encoded magnetic resonance imaging. *J Magn Reson Imaging*, 3:649–655, 1993.

[113] L. P. Panych, R. V. Mulkern, P. Saiviroonporn, G. P. Zientara, and F. A. Jolesz. Non-Fourier encoding with multiple spin echoes. *Magn Reson Med*, 38:964–973, 1997.

[114] L. P. Panych, C. Oesterle, G. P. Zientara, and J. Hennig. Implementation of a fast gradient-echo SVD encoding technique for dynamic imaging. *Magn Reson Med*, 35:554–562, 1996.

[115] L. P. Panych and K. Oshio. Selection of high-definition 2D virtual profiles with multiple RF pulse excitations along interleaved echo-planar k-space trajectories. *Magn Reson Med*, 41:224–229, 1999.

[116] L. P. Panych, L Zhao, F. A. Jolesz, and R. V. Mulkern. Dynamic imaging with multiple resolutions along phase-encode and slice-select dimensions. *Magn Reson Med*, 45:940–947, 2001.

[117] L. P. Panych, G. P. Zientara, and F. A. Jolesz. MR image encoding by spatially selective RF excitation: An analysis using linear response models. *Int J Imaging Syst and Technol*, 10:143–150, 1999.

[118] L. P. Panych, G. P. Zientara, P. Saiviroonporn, S.-S. Yoo, and F. A. Jolesz. Digital wavelet-encoded MRI: a new wavelet-encoding methodology. *J Magn Reson Imaging*, 8(5):1135–1144, 1998.

[119] S. Patz and R. C. Hawkes. Rapid Fourier imaging using steady-state free precession. *Magn Reson Med*, 4:9–23, 1987.

[120] J. Pauly, P. Le Roux, D. Nishimura, and A. Macovski. Parameter relations for the Shinnar-Le Roux selective excitation pulse design algorithm. *IEEE Trans Med Imaging*, 10(1):53–65, 1991.

[121] J. Pauly, D. Nishimura, and A. Macovski. A *k*-space analysis of small tip angle excitation. *J Magn Reson*, 81:43–56, 1989.

[122] J. Pauly, D. Nishimura, and A. Macovski. A linear class of large-tip-angle selective excitation pulses. *J Magn Reson*, 82:571–587, 1989.

[123] J. G. Pipe and P. Menon. Sampling density compensation in MRI: Rationale and an iterative numerical solution. *Magn Reson Med*, 41:179–186, 1999.

[124] F. P. Preparata and M. I. Shamos. *Computational Geometry*, chapter 5.5–5.7, pages 198–217. Texts and Monographs in Computer Science. Springer-Verlag, New York, New York, 1985.

[125] K. P. Pruessmann, M. Weiger, P. Börnert, and P. Boesiger. Advances in sensitivity encoding with arbitrary k-space trajectories. *Magn Reson Med*, 46:638–651, 2001.

[126] K. P. Pruessmann, M. Weiger, M. B. Scheidegger, and P. Boesiger. SENSE: Sensitivity encoding for fast MRI. *Magn Reson Med*, 42:952–962, 1999.

[127] Y. Qian, J. Lin, and D. Jin. Reconstruction of MR images from data acquired on an arbitrary k-space trajectory using the same-image weight. *Magn Reson Med*, 48:306–311, 2002.

[128] J. B. Ra and C. Y. Rim. Fast imaging using subencoding data sets from multiple detectors. *Magn Reson Med*, 30:142–145, 1993.

[129] V. Rasche, R. Proska, R. Sinkus, P. Börnert, and H. Eggers. Resampling of data between arbitrary grids using convolution interpolation. *IEEE Trans Med Imaging*, 18(5):385–392, 1999.

[130] W. P. Rothwell. Nuclear magnetic resonance imaging. *Applied Optics*, 24(23):3958–3967, 1985.

[131] G. E. Sarty. Natural k-plane coordinate reconstruction method for magnetic resonance imaging: Mathematical foundations. *Int J Imaging Syst and Technol*, 8:519–528, 1997.

[132] G. E. Sarty, R. Bennet, and R. W. Cox. Direct reconstruction of non-Cartesian k-space data using a nonuniform fast Fourier transform. *Magn Reson Med*, 45(5):908–915, 2001.

[133] F. Schmitt. Gradient systems. In *Syllabus, Weekend Educational Courses of the Proc 10th ISMRM*, pages 477–486, Hawaii, USA, May 2002.

[134] H. Schomberg and J Timmer. The gridding method for image reconstruction by Fourier transformation. *IEEE Trans Med Imaging*, 14:596–607, 1995.

[135] C. Schröder, P. Börnert, and B. Aldefeld. Spatial excitation using variable-density spiral trajectories. *J Magn Reson Imaging*, 18:136–141, 2003.

[136] M. Shinnar, S. Eleff, H. Subramanian, and J. S. Leigh. The synthesis of pulse sequences yielding arbitrary magnetization vectors. *Magn Reson Med*, 12:74–80, 1989.

[137] M. Shinnar and J. S. Leigh. The application of spinors to pulse synthesis and analysis. *Magn Reson Med*, 12:93–98, 1989.

[138] D. K. Sodickson. Tailored SMASH image reconstructions for robust in vivo parallel MR imaging. *Magn Reson Med*, 44:243–251, 2000.

[139] D. K. Sodickson and W. J. Manning. Simultaneous acquisition of spatial harmonics (SMASH): Fast imaging with radiofrequency coil arrays. *Magn Reson Med*, 38:591–603, 1997.

[140] G. Strang. *Introduction to Applied Mathematics*, chapter 4, pages 269–272. Wellesley-Cambridge Press, Wellesley, Massachusetts, 1986.

[141] G. Strang and T. Nguyen. *Wavelets and Filter Banks*, chapter 1.6, pages 24,32–33. Wellesley-Cambridge Press, Wellesley, Massachusetts, 1997.

[142] A. Takahashi and T. Peters. Compensation of multi-dimensional selective excitation pulses using measured k-space trajectories. *Magn Reson Med*, 34:446–456, 1995.

[143] A. R. Thompson and R. N. Bracewell. Interpolation and Fourier transformation of fringe visibilities. *Astronomical Journal*, 79:11–24, 1974.

[144] J. A. Tkach and E. M. Haacke. A comparison of fast spin echo and gradient field echo sequences. *Magn Reson Imaging*, 6:373–389, 1988.

[145] D. B. Twieg. The k-trajectory formulation of the NMR imaging process with applications in analysis and synthesis of imaging methods. *Medical Physics*, 10:610–621, 1983.

[146] J. J. van Vaals, M. E. Brummer, W. T. Dixon, H. H. Tuithof, H. Engels, R. C. Nelson, B. M. Gerety, J. L. Chezmar, and J. A. den Boer. Keyhole method for accelerating imaging of contrast agent uptake. *J Magn Reson Imaging*, 3:671–675, 1993.

[147] Y. Wang. Description of parallel imaging in MRI using multiple coils. *Magn Reson Med*, 44:495–499, 2000.

[148] R. Watts and Y. Wang. k-space interpretation of the Rose model: Noise limitation on the detectable resolution in MRI. *Magn Reson Med*, 48(3):550–554, 2002.

[149] J. B. Weaver and D. M. Healy. Acquisition of the Karhunen-Loeve expansion to reduce MR imaging times. In *IEEE Proc Int Conf Image Processing*, volume 3, pages 35–39, 1994.

[150] J. B. Weaver, D. M. Healy, and J. R. Driscoll. Wavelet encoded MR imaging. *Magn Reson Med*, 24:275–287, 1992.

[151] J. B. Weaver and D. M. Healy Jr. Signal to noise ratios and effective repetition times for wavelet and adapted wavelet encoding. *J Magn Reson Series A*, 113:1–10, 1995.

[152] F. W. Wehrli. Fast-scan magnetic resonance: Principles and applications. *Magn Reson Quarterly*, 6:165–236, 1990.

[153] E. B. Welch, A. Manduca, R. C. Grimm, H. A. Ward, and C. R. Jack Jr. Spherical navigator echoes for full 3D rigid body motion measurement in MRI. *Magn Reson Med*, 47:32–41, 2002.

[154] A. H. Wilman, S. J. Riederer, B. F. King, J. P. Debbins, P. J. Rossman, and R. L. Ehman. Fluoroscopically triggered contrast-enhanced three-dimensional MR angiography with elliptical centric view order: application to the renal arteries. *Radiology*, 205:137–146, 1997.

[155] G. A. Wright. Magnetic resonance imaging. *IEEE Signal Processing Magazine*, 14:56–66, 1997.

[156] S. M. Wright. Sensitivity limits in MRI - signal and hardware issues. *Proceedings of the 10th ISMRM Weekend Educational Course*, pages 418–424, May 2002.

[157] Q.-S. Xiang and M. R. Henkelman. k-space description for MR imaging of dynamic objects. *Magn Reson Med*, 29:422–428, 1993.

[158] G. Z. Yang, P. Burger, P. D. Gatehouse, and D. N. Firmin. Locally focused 3D coronary imaging using volume-selective RF excitation. *Magn Reson Med*, 41:171–178, 1999.

[159] E. Yudilevich and H. Stark. Spiral sampling in magnetic resonance imaging - the effect of inhomogeneities. *IEEE Trans Med Imaging*, 6:337–345, 1987.

[160] E. Yudilevich and H. Stark. Spiral sampling: theory and an application to magnetic resonance imaging. *Journal of the Optical Society of America A*, 5(4), April 1988.

[161] L. Zhao, A. K. Venkatesh, M. S. Albert, and L. P. Panych. Signal-to-noise ratio comparison of encoding methods for hyperpolarized noble gas MRI. *J Magn Reson*, 148(2):314–326, 2001.

[162] Y. Zhu. Acceleration of focused excitation with a transmit coil array. In *Proc 10th ISMRM*, page 190, Hawaii, USA, May 2002.

[163] G. P. Zientara. Advanced non-Fourier imaging. In *Proc. ISMRM Fast MRI Workshop, Methodological Perspectives and Advances in Cardiac, Neuro, Angiography and Abdominal Imaging*, pages 149–152, Monterrey, CA, USA, October 1997.

[164] G. P. Zientara, L. P. Panych, and F. A. Jolesz. Dynamically adaptive MRI with encoding by singular value decomposition. *Magn Reson Med*, 32:268–274, 1994.

[165] G. P. Zientara, L. P. Panych, and F. A. Jolesz. Keyhole SVD encoded MRI. In *Proceedings* 2^{nd} *SMR*, page 778, San Francisco, USA, 1994.

[166] G. P. Zientara, L. P. Panych, and F. A. Jolesz. Lanczos spatial encodings for dynamically adaptive MRI. In *Proc* 3^{rd} *ISMRM*, page 664, Nice, France, August 1995.

[167] G. P. Zientara, L. P. Panych, and F. A. Jolesz. Applicability and efficiency of near-optimal spatial encoding for dynamically adaptive MRI. *Magn Reson Med*, 39:204–213, 1998.

[168] G. P. Zientara, L. P. Panych, and F. A. Jolesz. Near-optimal encoding for dynamically adaptive MRI: Mathematical principles and computational methods. *Int J Imaging Syst and Technol*, 10:151–165, 1999.

[169] G. P. Zientara, C. F. Westin, L. P. Panych, and F. A. Jolesz. Singular value decompositions of multivariate kernels and multidimensional arrays. 1999.